不規則波與離岸潛沒結構物
交互作用之模擬

Simulation of Irregular Waves and Their Interactions
with Submerged Offshore Structures

研究生：沈茂霖 Mao-Lin Shen

指導教授：黃清哲 Ching-Jer Huang

國 立 成 功 大 學

水 利 及 海 洋 工 程 研 究 所

博 士 論 文

A Dissertation Submitted to the Graduate Faculty of

Department of Hydraulic and Ocean Engineering

In Partial Fulfillment of

the Requirements for the Degree of

Doctor of Philosophy

In

National Cheng Kung University

中 華 民 國 九 十 七 年 七 月 四 日

4 July 2008

國立成功大學

博士論文

不規則波與離岸潛沒結構物交互作用之模擬
Simulation of Irregular Waves and Their
Interactions with Submerged Offshore
Structures.

研究生：沈茂霖

本論文業經審查及口試合格特此證明

論文考試委員：

吳永照　　許泰文

林進川　　廖世樟

吳清哲　　董志明

指導教授：吳清哲

系(所)主管：許泰文

中　華　民　國　97　年　7　月　4　日

Simulation of Irregular Waves and Their Interactions with Submerged Offshore Structures

by Mao-Lin Shen

A Dissertation Submitted to the Graduate Faculty of
Department of Hydraulic and Ocean Engineering
In Partial Fulfillment of
the Requirements for the Degree of

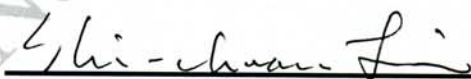**Doctor of Philosophy**

In

National Cheng Kung University

Approved by:

4 July 2008

Dedication

    This work is dedicated to the memory of my bright, attentive and conscientious friend, Chin-Hao Huang (黃致豪, 1982/08-2007/08) who died while this work was almost given up. Four year ago he knew his brain tumor were consuming his life, and continued his lasting fight until the day he cannot have furthermore conversation with all of his beloved family and friends. I wrote this paragraph down as a memento of Huang' existence and make myself have no regrets about his leaving.

Mao-Lin Earnest Shen

2008/07/09

Abstract

This work presents the simulation of irregular waves interacting with submerged offshore structures. By generating the incident irregular waves in a numerical wave flume and solving the unsteady two-dimensional Navier-Stokes equations with the fully nonlinear free surface boundary conditions for the fluid flows in the flume, the viscous flows are determined and the bed shear stress as well as vortex circulation can be obtained. Four topics were focus: irregular waves with the associated bed shear stress were studied linearly and nonlinearly, vortex formed beneath irregular waves around a submerged breakwater and ripples.

Irregular waves were generated by the wavemaker adopting deterministic spectral amplitude method implemented using the fast Fourier transform algorithm. The accuracy of the generated irregular waves and the viscous flows was confirmed by comparing the predicted wave spectrum with the target spectrum and by comparing the numerical transfer function between the shear stress and the surface elevation with the theoretical transfer function, respectively. Additionally, characteristics of the wave spectra and the associated shear stress spectra were discussed in terms of the spectral frequency, the zeroth spectral moment and the spectral bandwidth parameter. The maximum bottom shear stress caused by irregular waves, computed by this wave model, was compared with that obtained using Myrhaug's model (1995). The transfer function method was also employed to determine the maximum shear stress, and was demonstrated to be accurate.

Nonlinear properties of irregular waves are preliminary presented using the formula of the second-order bound waves, subharmonics and superharmonics, which deduced by Dean and Sharma (1981). As the associated phases changed, bound waves of the synthesized results show irregularity in spectrum and form randomness in spatial-varied skewness. Similar phenomena were found in the numerical results, although the magnitude of spectral higher harmonic components and the skewness are larger. The spatial-varied skewness of the surface elevation and the bed shear stress shows bound components indeed present, and indicate that the phase difference of surface elevation and bed shear stress has to be considered for building the associated statistical model.

Of the repeatable properties of the present numerical scheme, the incident waves and reflected waves from the submerged breakwater were separated without any assumption. A reliable time duration for analysis was confirmed by the comparison of reflected coefficients in order to ensure that the wave reflected from wavemaker would not affect the interesting duration. A vorticity-based method with a vorticity threshold were developed and made the automatic recognition of vortex become possible, in which the threshold was confirmed for well describing the vortex region. Both the circulations and the selected vortex region were shown in flow fields and vorticity contours. The interaction of the vortices was evidenced and showed the succeed-formed vortices above breakwater increased the breakdown rate of the vortices next to the breakwater three times. Of the irregular-wave train, the vortex of large wave followed by small one lasted longer.

Applying body-fitted boundary, different hydraulic conditions were studied about on

and off equilibrium ripple pattern beneath regular and irregular waves. While concerning only the region beneath twice the ripple wave height, the present numerical scheme was verified with the experiment and has a good agreement within the transitional regime. The vortices formed beneath regular waves reached a limited circulation if the bed-orbital-displacement amplitude is larger than the ripple wavelength. The limitation can furthermore be evidenced by the trajectories of the vortex center. The vortices formed beneath irregular waves were recognized automatically as well, although the number of the zero-upcrossing waves and the vortices was not matched.

Abstract in Chinese

　　本文主旨為探討不規則波與離岸潛沒結構物之交互作用。藉由數值水槽中生成不規則波與求解非線性自由液面邊界條件下之二維時變 Navier-Stokes 方程，可獲得不規則波動下完整黏性流流況、底床剪應力與渦流環流。文中涵蓋四個主題：不規則波與其底床剪應力的線性與非線性特徵；潛堤週圍渦流的性質；渦流砂漣所引致的渦流特性。

　　本研究中生成不規則波的方式，係採用快速傅立葉轉換架構下的定譜振幅模式決定成份波，再於黏性數值造波水槽中造出各波浪成份。以此數值造波結果與靶譜比對下，證實本模式可精準地生成所要求的不規則波波譜。線性條件下水位變化與底床剪應力間的轉換函數可由理論求得，其與數值結果的一致性可知本黏性流模式可準確無誤的模擬黏性流流況。此外，水位譜與其相對應之底床剪力譜分別以主頻、譜的零階動差和譜寬參數討論之。數值結果的底床剪應力最大值則與 Myrhaug (1995) 的模式進行比對。黏性水槽所求得的底床剪應力與採用轉換函數所求得的結果十分符合。

　　為明瞭不規則波的非線性特徵，採用 Dean and Sharma (1981)所推導的二階強制波模式—包含次諧波和超諧波—所合成的非線性不規則波進行初步探討。變化合成波中各成份波的相位，其波譜與偏度的空間變化都呈現出不規則的變動。數值模擬的不規則波在高非線性下，亦顯示出

類似的現象。非線性條件下數值結果所求得的轉換函數與線性條件下的理論解比對，可發現非線性效應對轉換函數的影響不大。線性條件下的轉換函數仍可用於應床剪應力的推估。藉由數值結果，比較水位與底床剪應力的偏度空間變化，可發現兩者有一相位差，同時意謂著兩者的相位差在架構統計模式中不容忽視。

由於數值模式可精準重複，本模式在沒有任何假設下便可以分離入射波與反射波。從反射係數的分析中，可決定出一段不受造波板處二次反射波浪影響的時段，並進行渦流分析。本文提出一渦流自動辨識系統，其中以渦度為判斷為基礎，且須決定一適切的渦度門檻值。本文中以流場和渦流場確認渦度門檻值能完整描述渦流的範圍。環流和所選取的渦流區域以流場與渦度場的方式呈現出不同時間點的差異。從渦流的交互作用中可以發現，生成於潛堤側的渦流受接續生成於潛堤上方渦流的影響，其的衰減率提升為原來的三倍。不規則波作用下，大波後跟隨小波時，大波所產生的渦流能持續較長的時間。

運用邊界配適法，規則波與不規則波作用下與砂漣的互制分成平衡態和非平衡態的情況進行探討。在二倍砂漣高度以內的區域（砂漣邊界層），本數值模式模擬過渡段流況的結果與實驗有很好的一致性。前述的渦流自動辨識模式在此用以判斷砂漣上方形成的渦流特性。平衡態或非平衡態下，如果底床水粒子軌跡的振幅大於砂漣漣長，規則波下生成的環流強度因受限於漣長而有一最大值。渦流中心的運動軌跡也反應出類似的特性。不規則波下所生成的渦流數量與零上切所求得的波數並不一

致，顯示並非任意大小的波動都能引致渦流的產生。

Contents

Table Caption

Figure Caption

List of Acronym

ARMA   autoregressive moving average

ADV   acoustic Doppler velocimetry

CIC   cloud-in-cell

DS   Dean and Sharma's

DSA   deterministic spectral amplitude

DSA-FFT   deterministic spectral amplitude performed by fast Fourier transform

FA   finite-analytic

FFT   fast Fourier transform

LDV   laser Doppler velocimetry

LES   large-eddy simulation

LHS   left hand side

LWR   long wave ripple

MAV   maximum absolute value of vorticities

MAC   mark-and-cell

MH   Myrhaug and Holmedal

NLS   nonlinear Schrödinger

NSA   nondeterministic spectral amplitude

NSA-FFT   nondeterministic spectral amplitude performed by fast Fourier transform

PIV   particle image velocimetry

RANS   Reynolds-averaged Navier-Stokes equations

RHS   right hand side

RMS   root-mean-square

SIMPLE   semi-implicit method for pressure-linked equations

SIMPLER   semi-implicit method for pressure-linked equations revised

SUMMAC   the Stanford-University-Modified MAC

SWR   short wave ripple

List of Symbols

Symbol	Quantity	SI Unit
A, B	Convection coefficients in the linearized convective-transport equation (in Chapter 3)	—
A_B	submergence-orbital-displacement amplitude at $y = (1-q)h_o$	m
$\widetilde{A}_i^n$	weighting area of point i in the curvilinear coordinate (ξ, ζ) at the n-th iteration	—
A_k	the k-th Fourier component of surface elevation	m
A_k^*	complex conjugate of A_k	m
A_o	bed-orbital-displacement amplitude	m
A_{rms}	root-mean-square of bed orbital amplitude	m
A_φ, B_φ	convection coefficients in the transport equation for φ	—
$A_{\Omega i}$	area of i-th element within a vortex	—
a	amplitude of a simple harmonic wave	m
$a^{(2-)}$	the amplitude of a subharmonic by the DS model	m
$a^{(2+)}$	the amplitude of a superharmonic by the DS model	m

(*continued on next page*)

Symbol	Quantity	SI Unit
a^*, b^*, C^*	coefficient of finite-analytic method, in Eq. (3.16)	—
a_e, a_w, etc.	finite-analytic coefficients for pressure and pressure-correction Equations, in Chapter 3	—
$\tilde{a}_i^n$	weighting area of point i in the Cartesian coordinate (x, y) at the n-th iteration	—
a_k	amplitude of the k-th wave component	m
B_k	the k-th Fourier component of bottom shear stress	$\mathrm{kg \cdot m^{-1} s^{-2}}$
B_k^*	complex conjugate of B_k	$\mathrm{kg \cdot m^{-1} s^{-2}}$
b_i^j	i-th component of the j-th contravariant base vector	—
C	A closed curve	m
$\bar{C}_p, \widetilde{C}_p$, etc.	finite-analytic coefficients	—
C_ψ	admissibility coefficient of wavelet transform	—
c	wave phase velocity	$\mathrm{ms^{-1}}$
c_g	group velocity	$\mathrm{ms^{-1}}$
c_o	dimensionless phase velocity of long wave	—
$\hat{D}$	source function in pressure Eq. (3.36)	—
D^*	Mass source term in pressure-correction Eq. (3.43)	—

Symbol	Quantity	SI Unit
D_1	partial mass source term defined in Eq. (3.35)	—
Diff	difference between the values of τ_{max}	—
d_{50}	medium grain size	m
d_e, d_w, etc.	finite-analytic coefficients for pressure and pressure-correction equations	—
e_k	amplitude of the k-th displacement function $\xi_k(t)$ of the wavemaker	m
$F_i = F(\vec{k}_i,\, t)$	energy for i-th wave component with wavenumber $\vec{k}_i$	m^2
Fr	the Froude number	—
Fr_d	the particle Froude number	—
$f(t)$	an arbitrary time series	—
Δf	frequency interval	s^{-1}
f^i	grid-control function, in Chapters 2 and 3	s^{-1}
f_c	cut-off (Nyquist) frequency	s^{-1}
f_k	frequency of the k-th wave component	s^{-1}
f_m	frequency of wavelet energy density	s^{-1}
f_p	spectral-peak frequency	s^{-1}

Symbol	Quantity	SI Unit
$f_{p\tau}$	spectral peak frequency of shear stress spectrum	s^{-1}
f_s	sampling frequency	s^{-1}
$G(\vec{k_1}, \cdots, \vec{k_4})$	the coupling coefficient of $\vec{k_1}, \cdots, \vec{k_4}$	—
G_f	source terms of the linerized convective-transport equation	—
g	gravitational acceleration	s^{-1}
g^{ij}	conjugate metric tensor in the general curvilinear coordinates	—
$H_{1/3}$	given significant wave height	m
H_i	incident wave height	m
H_r	ripple height	m
H_s	measured significant wave height defined by IAHR	m
$H_\tau(\omega_k)$	transfer function between the shear stress and the surface	
h'_e, h'_w, h'_n, h'_s	grid size for finite-analytic local element	—
h_o	still water depth	m
J	Jacobian	—
K_B	coefficient defined in Eq. (3.21)	—

Symbol	Quantity	SI Unit
k	wave number	m^{-1}
$\overline{k}$	mean wave number	m^{-1}
$\vec{k}$	the directional wave number	m^{-1}
k_p	spectral-peak wavenumber	m^{-1}
k_s	the Nikuradse roughness	m
k_s'	skin roughness	m
L_p	spectral-peak wavelength	m
L_r	ripple wavelength	m
m_o	the zeroth spectral moment	m^2
m_{o2DS}	the zeroth spectral moment of the bound waves determined by the model of Dean and Sharma (1981)	m^2
m_{ou}	the zeroth spectral moment of bed orbital velocity	m^2
$m_{o\eta}$	the zeroth spectral moment of wave elevation	m^2
$m_{o\tau}$	the zeroth spectral moment of shear stress	kg^{2}m^{-2}s^{-4}
m_r	the spectral moment of order r	m^{2}s^{-r}
N	length of a discrete sequence	—

(*continued on next page*)

Symbol	Quantity	SI Unit
N_M	number of the maximum value in the time-series data of the shear stress	—
N_w	number of zero-upcrossing waves	—
n, s, e, w	describing four surrounding elements	—
n_i	a unit vector normal to the free surface in Eqs. (2.5) and (2.6).	—
O_b	guessed location of a vortex	(m, m)
$P(\hat{\tau})$	cumulative distribution function of $\hat{\tau}$	—
p	Pressure	—
p'	dimensionless hydrodynamic pressure, $p' = p / \rho u_p^2$	—
p_o'	dimensionless hydrodynamic pressure at the free surface	—
p^*	guessed pressure field	—
$\tilde{p}$	pressure-correction	—
p_s'	dimensionless hydrostatic pressure	—
p_t'	dimensionless total pressure	—
$Q(\hat{\tau})$	exceedance probability of $\hat{\tau}$	—
Q_{DS}	the ratio of nonlinearity defined in Eq. (5.2)	—

Symbol	Quantity	SI Unit
Q_p	spectral bandwidth parameter	—
q	submergence ratio	—
Re	the Reynolds number of wave tank, $Re = u_p h_o / \upsilon$	—
Re_B	the submergence Reynolds number, $Re_B = U_B A_B / \upsilon$	—
Re_d	the particle Reynolds number, $Re_d = U_o d_{50} / \upsilon$	—
Re_o	the bed orbital Reynolds number, $Re_o = U_o A_o / \upsilon$	—
Re_{rms}	the bed-orbital Reynolds number of irregular waves, $Re_{rms} = U_{rms} A_{rms} / \upsilon$	—
Re_s	coefficient of sponge layer, $Re_s = \rho u_p h_o / \mu_s$	—
Δr	the estimated pace of a vortex within a time step Δt_r	—
$S(\omega)$, $S(f)$	spectral density function of a random series	—
S_o	stroke of the wavemaker	m
S^*	finite-analytic coefficients	—
S_k	stroke of the wavemaker for generating the k-th wave component	m
S_φ, s_φ	source terms, $\varphi = u,\ v$	—
S_η	spectral density of surface elevation	$m^2 s$

Symbol	Quantity	SI Unit
S_τ	spectral density of shear stress	$\mathrm{kg^2 m^{-2} s^{-3}}$
s	specific density	$\mathrm{kg^2 m^{-2} s^{-3}}$
s_w	dilation scale of wavelet transform	s
T	period	s
T_p	spectral-peak period	s
T_R	record length or time duration of an irregular-wave train	s
T_{R1}, T_{R2}, etc.	the time period with different beginning	s
Ta	Taylor number, $Ta = \sqrt{\omega/\upsilon}\, A_o^2 H_r \big/ 2L_r^2$	—
t	time	s
t'	dimensionless time	—
Δt	time interval	s
Δt_r	the time step of vortex analysis	s
t_o	non-dimensionalized parameter of time	s
t_n	discrete time	s
t_w	time translating range of wavelet transform	s
U', V'	mean values of u' and v' in a computational element	—

Symbol	Quantity	SI Unit
U_B	the submergence-orbital-velocity amplitude at $y = (1-q)h_o$	ms^{-1}
U_o	the orbital-velocity amplitude on the bed or the bed orbital velocity	ms^{-1}
U_{rms}	root-mean-square of bed orbital velocity	ms^{-1}
U_s	significant bottom velocity, $U_s = 4m_{ou}^{1/2}$	ms^{-1}
u , v	Velocities	m
u' , v'	dimensionless velocities, $u' = u/u_p$, $v' = v/v_p$	—
u^* , v^*	velocities obtained from guessed pressure field p^*	—
$\hat{u}'$, $\hat{v}'$	pseudo velocities	—
$\tilde{u}$, $\tilde{v}$	contravariant velocities	—
u_p	velocity amplitude of wavemaker	ms^{-1}
Ur	Ursell number	—
Ur_s	Ursell number defined by significant wave height and wave length of spectral peak wave	—
W_B	width of breakwater	m/s
$Wf(t_w, s_w)$	wavelet transform of $f(t)$	m

Symbol	Quantity	SI Unit
$WS(t_w, f_m)$	the time-frequency wavelet energy density	m^2
w_s	settling velocity	m/s
x, y	Cartesian coordinates	m
Δx, Δy	grid size in a computational element	—
x', y'	dimensionless cartesian coordinates, $x' = x / h_o$, $y' = y / h_o$	—
x_c, y_c	center of vortex circulation	m
x_{min}	location of the piston-type wavemaker	m
x_s, x_{s1}, x_{s2}	the width of spatially varying region of a sponge layer	m
$x_{\Omega i}$, $y_{\Omega i}$	the location of an element within a vortex	m
α	spectral shape parameter in Goda-JONSWAP spectrum	—
δ	Stokes layer thickness of regular wave	m
δ_{ij}	Kronecker delta	—
δ_p	Peak spectral characteristic thickness of the bottom boundary layer	m
ϕ_k	phase of k -th wave component	—
Γ, Γ_{95}, Γ_{99}	vortex circulation	$m^2 s^{-1}$

Symbol	Quantity	SI Unit
Γ_i	vortex circulation of an element	$m^2 s^{-1}$
γ	peak enhancement factor	—
γ_1	skewness	—
γ_{1DS}	skewness of the synthesized results using the DS model	—
$\eta(t),\ \eta(x, t)$	water wave elevation	m
$\eta(t_n)$	discrete wave elevation	m
$\eta^{(1)}$	the linear component of nonlinear random waves	m
$\eta^{(2)}$	the second-order component of nonlinear random waves	m
η_{DS}	the nonlinear irregular wave obtained by the DS model	m
$\eta_{DS}^{(2)}$	the second-order component of nonlinear irregular waves obtained by the DS model	m
η_k	the k-th wave component	m
φ	stand-in quantities. ($\varphi = u, v$)	—
μ	dynamic viscosity of fluid	$kg \cdot m^{-1} s^{-1}$
μ_3	the skewness of surface elevation	—
μ_{3DS}	the skewness of results of the DS model	—

Symbol	Quantity	SI Unit
μ_r	the r-th moment, $\mu_r = \int (x - \bar{x})^r p(x) dx$	$[x]^r$
μ_s	damping factor of a sponge	—
$\mu_{s\,max}$	maximum damping factor of a sponge	—
υ	kinematic viscosity of fluid	m^2s^{-1}
θ'	the maximum Shields number	—
θ'_c	the critical Shields number	—
θ'_r	the ripple-adjusted Shields number	—
ρ	density of water	$\text{kg} \cdot \text{m}^{-3}$
ρ_s	density of sand particle	$\text{kg} \cdot \text{m}^{-3}$
σ_{ij}	the i-th component of the stress tensor acting on the surface with constant x_j	—
τ	bottom shear stress	$\text{kg} \cdot \text{m}^{-1}\text{s}^{-2}$
$\tau(t_n)$	discrete bottom shear stress	$\text{kg} \cdot \text{m}^{-1}\text{s}^{-2}$
$\hat{\tau}$	normalized shear stress, $\hat{\tau} = \tau_{max} / \tau_{rmsM}$	—
τ_i	a unit vector normal and tangential to the free surface	—
τ_{max}	maximum bottom shear stress	$\text{kg} \cdot \text{m}^{-1}\text{s}^{-2}$

Symbol	Quantity	SI Unit
$(\tau_{\max})_{1/N_M}$	$\tau_{\max}$ which is exceeded by the probability $1/N_M$	$kg \cdot m^{-1}s^{-2}$
$\tau_{\max M}$	maximum bottom shear stress determined by Myrhaug's model	$kg \cdot m^{-1}s^{-2}$
$\tau_{\max T}$	$\tau_{\max}$ obtained using transfer function	$kg \cdot m^{-1}s^{-2}$
τ_s	significant shear stress	$kg \cdot m^{-1}s^{-2}$
Ω, Ω_i	vorticity	s^{-1}
$\|\Omega\|_{\max}$	the global MAV	s^{-1}
Ω_T	the threshold for determing the region of a vortex	s^{-1}
ω	angular frequency	s^{-1}
ω_k	discrete angular frequency of k-th wave component	s^{-1}
ω_p	angular frequency of spectral peak	s^{-1}
ω_z	zero-crossing frequency of bed displacement	s^{-1}
ω_ψ	frequency of mother wavelet	s^{-1}
ξ, ζ	curvilinear coordinates	—
$\xi(t)$	displacement function of a piston-type wavemaker	m
ξ', ζ'	dimensionless curvilinear coordinates	—

Symbol	Quantity	SI Unit
ξ^*, ζ^*	coordinate-stretching functions of ξ and ζ	—
ξ_o	the shape factor used to describe the ripple shape	m
$\xi_k(t)$	displacement function of a piston-type wavemaker for generating k-th wave component	m
Ψ	Fourier transform of the mother wavelet	—
ψ	mother wavelet	—
ψ^*	complex conjugate of the mother wavelet ψ	—
ψ_m	mobility parameter	—

Chapter 1 Introduction

"Science is organized knowledge. Wisdom is organized life."

—Immanuel Kant,
German philosopher

1.1 Research Background

On a natural sea, waves are irregular with high uncertainty. The researchers in about 1960 were tried ensuring the equilibrium state for wind-wave spectrum and establishing some simple parameterizations using "equivalent parameters", e.g. the significant wave height, the significant-associated period, and wavelength. Many experiments, theories and numerical studies were done by applying equivalent parameters as the realistic sea state in practical applications. However, taking equivalent parameters as true sea state leads to some misunderstandings about the realistic sea state, because multi-component introduced properties (e.g. wave-wave interaction, phase difference, and the occurrence of freak waves) were ignored when only significant wave properties are considered. Simulation and studying the effects of irregular waves interacting with itself or structures is inevitable for coastal study.

A measure of irregular waves in a particular location can be considered as stochastic process. Spectral and statistical processing are practical methods to determine properties of any stochastic process. Applying spectral method can reveal the energy distribution of each component and the dominant frequency. Applying statistical method can realize the probability distribution and obtain a forecasting about single event or long-term statement. In the present study, both methods were applied to extract the information of irregular waves and the associated effects. Four different subjects were studied. The first subject studied linear irregular waves and the associated shear tress; the second the nonlinear properties beneath irregular waves; the third the vortex dynamics around a submerged breakwater; the fourth the region from ripple trough to two times ripple height, which was dominated by ripple-induced vortices.

1.2   Linear irregular waves and the associated properties

The bottom shear stresses caused by irregular waves are very important in the sediment transports and the pipeline stability in the nearshore region. However, determining the shear stresses in response to irregular waves in the field and in the laboratory is difficult. Measurements of the velocity of the oscillatory boundary-layer flows over smooth and rough walls have already been made by Jonsson (1963, 1980) and Jonsson and Carlsen (1976) using a large oscillating water tunnel. Other measurements and theoretical models have also been reported (Kamphuis, 1975; Justesen, 1988; Jensen et al. 1989; Fredsøe et al., 2003). The maximum shear stresses, the friction factors and the boundary layer thickness of the laminar, smooth turbulent and rough turbulent flows

induced by a simple harmonic motion over a fixed bed have been discussed in detail. Lambrakos (1982) and Myrhaug et al. (1992) provided field measurement data of flows in wave boundary layers. Grant and Madsen (1986), Sleath (1995), and Blondeaux and Vittori (1999) reviewed articles in the boundary layer on the seabed.

Although the characteristics of the boundary layer induced by a simple harmonic motion or general waves have been elucidated in detail, the boundary layer or the shear stress under irregular waves has been less studied. Myrhaug (1995) proposed a model to calculate the maximum bottom shear stress induced by irregular waves. The surface elevation was assumed to be a stationary Gaussian narrow-band process. Simple explicit friction coefficient formulas for sinusoidal waves, such as Jonsson's formula (1980), were assumed to be valid for irregular waves as well. The coefficients of the proposed formulas were not constant and varied with the sea state parameters. The reliability of Myrhaug's model has not been tested. Myrhaug et al. (1998), Holmedal et al. (2000 and 2003) and Myrhaug and Holmedal (2001 and 2003) extended Myrhaug's approach (1995) for different applications. Samad et al. (1998) examined experimental shear stress results by comparing them with those obtained using the transfer function between the shear stress and the surface elevation. Tanaka and Samad (2006) solved the linearized boundary layer equation and the $k - \varepsilon$ equations to compute turbulent bottom shear stress induced by irregular waves with a Bretschneider-Mitsuyasu spectral density. Comparison of the model results with experimental data verifies their numerical model.

This study proposes a new approach for determining the shear stresses induced by

irregular waves. The viscous flow fields and the shear stresses induced by the desired irregular waves can be computed by generating the desired irregular waves in a numerical wave flume, in which the viscosity of the fluid is considered.

Various methods have been developed to simulate the irregular waves with the spectral and statistical properties of realistic ocean waves. Most such methods can be separated into two main categories: deterministic spectral amplitude (DSA) methods and nondeterministic spectral amplitude (NSA) methods. The former determine the spectral amplitude of each wave component precisely to match the theoretical or measured one-sided target wave spectrum, while in the latter, the simulated wave spectrum randomly fluctuates about the target wave spectrum. Rice (1955) originally developed these two methods for modeling Gaussian, white-noise, electronic signals. Ploeg and Funke (1980), Funke and Mansard (1987), Hughes (1993) and Goda (2000) reviewed irregular wave generation techniques in detail.

Borgman (1969) applied both the wave superposition method and the linear filtering method to simulate irregular waves. The wave spectra of the simulated irregular waves by these two methods coincide with the given target spectra, but lack sufficient randomness as in the real sea states. Goda (1970) demonstrated that in the wave superposition approach, the component frequencies should not be harmonics of each other and the amplitudes of the component waves should be approximately equal. Therefore, he treated the spacing between dividing frequencies as increasing with frequency, and the synthesized frequencies were selected randomly in the respective sub-ranges. The phase

of each component was selected at random and distributed uniformly in the interval $[0, 2\pi]$.

Tuah and Hudspeth (1982) compared the spectral moments, spectral bandwith, skewness and peakedness of the simulated waves obtained by the DSA and NSA methods. Their comparison indicated that the statistical properties of irregular waves simulated by the NSA method were closer to the realistic sea states. This difference was attributed to the fluctuating spectra obtained using the NSA method, which differs from the smooth spectra obtained from the DSA method. Tucker et al. (1984) and Miles and Funke (1988) made similar comparisons, with the same results as were reported by Tuah and Hudspeth (1982). However, Elgar et al. (1985) showed that if the number of spectral components suffices, then both DSA and NSA approaches simulate waves without a significant difference in the wave group statistics.

The autoregressive-moving average model (ARMA) used by Medina et al. (1985) has been considered to be one of the most general approaches for generating random signals. However, applying this model to simulate waves for any given spectra is rather difficult. Miles and Funke (1988) chose 16 sea state parameters, such as the significant wave height and the peakedness factor, to compare seven wave synthesis methods. The seven synthesis methods are the wave superposition method (Borgman, 1969), that of Goda (1970), the random amplitude and frequency method, the linear filtering method, the method of Fryer et al. (1973), ARMA and the random Fourier coefficients method. Miles and Funke (1988) concluded that all of these synthesis methods could generate realistic

5

Gaussian wave records. They noted also that the peak of the spectrum obtained by ARMA is lower than that of the target spectrum and, that the NSA-FFT (fast Fourier transform) was required for correct short-term variability. They showed that any finite duration wave record generated by a wave synthesis method could be approximated by the equivalent FFT time series.

1.3 Nonlinear properties beneath irregular waves

Nonlinear properties of irregular waves has been studied by experiencing much progress in the past half century. Since nonlinear irregular wave is complex and has huge affection about near shore phenomena, different methodologies (such as spectral or statistical method, field measurements, and experiments) were applied to survey the fundamental properties of nonlinear irregular wave and the associated dynamics. Some of the famous properties of nonlinear irregular wave are energy transfer beneath resonant or non-resonant condition, presence of subharmonics and superharmonics, increase of skewness, change of dispersion relation and phase velocities.

1.3.1 Spectral properties

By the assumption of stationary in time and in space, the Fourier-Stieltjes transform was applied to deal with the second order spectral properties of irregular waves in deep sea (Phillips, 1960; Longuet-Higgins, 1962; Longuet-Higgins and Phillips, 1962; Tick, 1963; Huang and Tung, 1976 and 1977; Zhang and Chen, 1999) as well as in finite depth (Hasselmann, 1962; Laing, 1986). Two major properties of nonlinear irregular wave

were found: existence of subharmonics and superharmonics; and energy transfer due to resonant interactions among wave components. Subharmonics and superharmonics are both bound waves. The former affect slow-drift motion of moored vessels, generation and evolution of sand bars, and surf-beat mechanism. The latter sharpen the wave crests and flatten the wave troughs, which consequently increases the skewness of surface elevation and occurrence of freak waves.

The wave-wave interaction beneath resonant condition for deep gravity waves was first derived by Phillips (1960), whereas Hasselmann (1962) treated of the problem by perturbation method and obtained a result of the nonlinear resonant interaction of free waves in a random sea. An example is for four waves with directional wavenumbers $(\vec{k_1}, \vec{k_2}, \vec{k_3}, \vec{k_4})$ and the angular frequencies $(\omega_1, \omega_2, \omega_3, \omega_4)$ satisfied or close to being satisfied the resonant conditions, say $\vec{k_1} + \vec{k_2} = \vec{k_3} + \vec{k_4}$ and $\omega_1 + \omega_2 = \omega_3 + \omega_4$, there is a direct energy transfer between these four waves and this is satisfied the action density spectrum $F(\vec{k}, t)$ at time t (Hasselmann, 1962):

$$
\begin{aligned}
\frac{\partial F(\vec{k_1}, t)}{\partial t} = \int_{-\infty}^{\infty} \cdots \int G(\vec{k_1}, \vec{k_2}, \vec{k_3}, \vec{k_4}) \delta(\vec{k_1} + \vec{k_2} - \vec{k_3} - \vec{k_4}) \\
\delta(\omega_1 + \omega_2 - \omega_3 - \omega_4)] d\vec{k_2} d\vec{k_3} d\vec{k_4}
\end{aligned}
\tag{1.1}
$$

where $F_i = F(\vec{k_i}, t)$ is the spectrum of energy in terms of wavenumber, $G(\vec{k_1}, \vec{k_2}, \vec{k_3}, \vec{k_4})$ is the coupling coefficient, $\vec{k}$ is the directional wavenumber which agrees the dispersion relation $\omega_i = \sqrt{g|\vec{k_i}|}$ in deep sea with the gravitational acceleration g. The exchange of energy is slow (Benny, 1962), and thus agrees with the assumption of nonlinear transfer that the action density spectrum is a slowly varying function of time.

Further theoretical advances were made by Longuet-Higgins (1976). He applied Davey and Stewartson's model (1974) for wave group evolution and considered the linear dispersion relation for waves in deep water. Physical meaning of each term of energy transfer equation was built up by the author and showed that the coupling coefficient $G(\vec{k_1}, \vec{k_2}, \vec{k_3}, \vec{k_4})$ between four nearly equal wave numbers $\vec{k_1}, \vec{k_2}, \vec{k_3}, \vec{k_4}$ is finite and not zero, and it is implied that the energy transfer within the spectral peak itself is of supreme importance. The author also noticed that the energy from an isolated peak in the spectrum tends to spread outwards along two characteristic lines, in which has the angle $\pm\tan^{-1}(\frac{1}{\sqrt{2}})$ with the main direction. This work was extended by Dungey and Hui (1979) with considering the effect of bandwidth of wave spectra. The secondary spectral peak was produced if the second-order spectrum was considered and $k_p h_o$ smaller than 0.6 (Laing, 1986), where k_p is the spectral-peak wavenumber and h_o the still water depth.

Wave amplitudes and random phases are two fundamental elements for building a synthesized irregular wave train more realistic as mentioned in Sector 1.2. In the afore-mentioned works, the properties of wave amplitude, such as energy transfer and the higher harmonics, were considered, but the effects of phase difference were seldom taken into account. A second-order directional wave theory for the case of infinite depth including the random phases was developed by Longuet-Higgins (1963), and later extended by Sharma (1979) and Sharma and Dean (1981) to the case of finite depth. Different case conditions of surface elevation were tested based on the assumption that the linear wave components are with the amplitude satisfied the Bretschneider spectrum and

with random phases. The higher harmonics, both subharmonics and superharmonics, were synthesized and presented produced with huge irregularity, which was resulted by the random phases of the linear waves.

While the spectral properties are known, the vital point for engineering use is to determine the dispersion relation, and thus gain the understanding about the phase velocity or the group velocity of waves. Many researchers (Longuet-Higgins and Phillips, 1962; Huang and Tung, 1976; Webber and Barrick, 1977; Barrick and Webber, 1977; Masuda et al., 1977; Mitsuyansu et al., 1979; Laing, 1986) have tried working it out. Since the bound wave were composed by the distribution of linear free waves with random phases, as synthesized results of Dean and Sharma (1981), the dispersion relation in deep sea is also random as a function of time and space, when the second order of irregular wave is considered. This was confirmed by Huang and Tung (1976), who ensured there was no single form of the dispersion relation for nonlinearity irregular waves. The recent experiments reconfirmed this phenomenon were made by Baldock et al. (1996), who tried surveying the wave evolution and flow velocity by experimental study. A particular wave group was test and compared the spectral amplitudes and phases. Of their work, the wave group velocity was increase as increasing nonlinearity and high nonlinearity of irregular waves introduces a permanent phase change. It indicates there is no permanent wave pattern for irregular waves if the nonlinearity is present.

Resonant interaction is good for describing the energy transfer of directional waves in deep sea. However, the energy transfer is rather slow and only weak nonlinearity is

considered (Dommermuth and Yue, 1987). Another drawback is the afore-mentioned method cannot deal with the energy transfer of unidirectional waves. For resonant conditions fitted only when ($\overrightarrow{k_1} = \overrightarrow{k_3}$, $\overrightarrow{k_2} = \overrightarrow{k_4}$) or ($\overrightarrow{k_1} = \overrightarrow{k_4}$, $\overrightarrow{k_2} = \overrightarrow{k_3}$) in unidirectional wave, the action density function showed in Eq. (1.1) tends to zero and appears no more energy transfers as the propagating of wave trains. For most studies about unidirectional waves, the existence of energy transfer is found, such as the case of Benjamin-Feir instability (Benjamin and Feir, 1967, also called as side-band modulation or non-resonant interaction), because the resonant condition are no longer satisfied. Most of these studies were performed by applying the nonlinear Schrödinger (NLS) equation and the Zakharov integral equation, which is another type of method to study the nonlinear effect of spectra.

The carrier waves of NLS were assumed to be linear and symmetric sinusoidal waves. Such a solution was good at analyzing the energy transfer of waves over large distance and long time span, but limited on dealing with the local wave profile asymmetry due to higher harmonic terms (Huang and Tung, 1976). The evolution of the wave train obtained by the nonlinear Schrödinger equation will tend to broaden the wave spectrum through side-band instability. For narrow-bandedness requirement, which is the main disadvantage of NLS, the time span of the NLS simulation is limited while the bandwidth reaches the broaden limit. For wave evolution governed by the NLS equation, Dysthe et al. (2003) showed the spectra followed a power-law behavior ω^{-4}. Another application performed by the NLS equation is to figure out the appearance of freak waves. Janssen (2003), Onorato et al. (2005) as well as Gramstan and Trulsen (2007) tried presenting the increased occurance

of freak waves using the NLS equation to implement the evolution of nonlinear multi-component waves, although the occurance was evidenced by the increased kurtosis. However, only the trend can be obtained because of the neglect of phase difference.

1.3.2 Statistical properties

The statistical properties of the realistic sea state are mostly concerned as Gaussian statistics for linear wave fields as summarized by Phillips (1977). However, the linear approximation can only hold true when the steepness approaches zero, which is the linear condition for deep water waves. Many laboratory data and field measures clearly show that surface elevation deviates from Gaussian (Kinsman, 1965; Huang and Long, 1980; Tayfun, 1980; Huang et al., 1983; Hatori, 1984; Goda, 1988; Tayfun and Lo, 1989; Mori and Yasuda, 1996 and 2002), and the statistical model of nonlinear surface waves was built by numerous methods. In generally, there are two ways for obtaining the non-Gaussian statistical models. One is applying an existed non-Gaussian formula to describe the statistical properties of wave elevation (Longuet-Higgins, 1963; Ochi, 1986; Cherneva et al. 2005). Another is extended the Gaussian statistics with the properties of nonlinear waves, e.g. the Stokes wave theory (Tayfun, 1980; Huang et al., 1983, Dawson, 2004), or the subharmonics and superharmonics (Tayfun, 1994; Song and Wu, 1999 a & b; Song et al., 2002).

The non-Gaussian property of irregular waves was first derived by Longuet-Higgins (1963). He applied Edgeworth's form of Gram-Charlier series and described the nonlinear properties by skewness and flatness of wave elevation. However, probability

11

density function formed by the Gram-Charlier series has some drawbacks for describing

sea state.   The major drawback is the Gram-Charlier approximation gives negative

probability density values for some range of wave elevation, especially in the cases of

steep waves.   The negative values obviously disagree with the axiom of a probability

density function, which should be always positive.   Another is the Gram-Charlier

approximation calls for the skewness and the flatness value to determine the nonlinear

statistical properties.   But these two parameters are not directly perceived through the

senses of statistical parameters.

Huang et al. (1983) used the second type of the afore-mentioned method to form a

nonlinear statistical formula in order to describe nonlinear random waves by extending

Gaussian distribution with Stokes wave property.   Formulas for deep sea and for finite

depth wave were built up.   The probability function for the deep water case was specified

by two parameters: the root-mean-square value of wave elevation and the significant slope.

For water of finite depth, an additional depth parameter is involved.   Of the formula, no

negative density value was given as the Gram-Charlier was.

1.3.3   Experimental treatment

For many researches and field applications, experiments are applied to build

preliminary knowledge about realistic phenomena.   It is doubtless that nonlinear irregular

waves have major affections about coastal structures and shore line protection, and

generating nonlinear waves with desired realistic sea state in wave flume is of inevitable

for experiments.   The basic concept of generating a nonlinear irregular wave train is to

satisfy the spectral properties, which the secondary spectral peak is appeared about two times the spectral-peak frequency. For lack of the knowledge about separating the linear components and the bound waves of a nonlinear-irregular-wave train, an alternative method is to apply an equilibrium spectrum (e.g. PM spectrum by Pierson and Moskowitz, 1964; JONSWAP by Hasselmann et al., 1973; Bretschneider-Mitsuyasu, etc.) with bound waves, which can be obtained following the formula of Phillips (1960), Hasselmann (1962), Laing (1986) or Dean and Sharma (1981).

Tuah and Hudspeth (1982) first synthesized the nonlinear irregular waves by this manner and corrected the spectrum to the second-order by applying the nonlinear interaction matrix in finite water depth given by Hasselmann (1962). In spite of the spectral property was similar with the nonlinear one, the results determined by the deterministic spectral amplitude method (DSA) was totally linear, and no bound waves generated. The statistical properties of nonlinear irregular waves thus are not satisfied, since the wave profile is still symmetric. For overcoming this drawback, a wavemaking theory for nonlinear irregular waves, in which fitted the boundary conditions and the nonlinear surface elevation, is inevitable. This manner seems to be first concerned by Sand and Mansard (1986), who solved the problem with second-order irregular waves in deep sea. A good agreement was obtained when the model was applied to generate the second-order Stokes waves and compared with the theoretical one. However, there were discrepancies when field data were simulated.

Similar works were done by Sulisz and Hudspeth (1993), Duncan and Drake (1995),

and Schäffer (1993, 1996). Klopman and Van Leeuwen (1990) as well as Van Leeuwen and Klopman (1996) used the narrow-band approximation to develop a nonlinear irregular wave generator. The random-amplitude/random-phase (similar to NSA-FFT) method proposed by Tucker et al. (1984) was applied to determine the linear components. The second-order spectra determined by the multiple-scales perturbation-series method (Mei, 1989) and by the full second-order theory (Laing, 1986) were compared.

Different methods were carried out for a nonlinear irregular wave generator, but only Sand and Mansard (1986) has verified their results by making comparison with theoretical Stokes waves, and the field spectrum. Sulisz and Paprota (2008) denoted that the nonlinear-waves generator can only provide a wave train satisfied the target spectrum within a very short distance form wavemaker, if the wave generator is considered weakly nonlinear formula only. The authors deduced another formula in order to predict the propagating waves and compared the predicted results with the wave packet of different nonlinearities. However, the wave packet stated the interaction of only few composite components and does not suffice the banded irregular wave spectrum.

1.3.4 Properties beneath nonlinear irregular waves

For many coastal applications, the dynamic property beneath irregular waves is a fundamental knowledge for the design of coastal structures and a basis to realize the stability about the structures. A study was done by Borgman (1969), who applied a transfer function of linear waves and the associated flow velocity to perform the understanding of the dynamics beneath irregular waves. More works were done by

statistical manner, which can be used both regarding single event and long-term statement, such as the extreme state or the significant properties for coastal structure design.   Tung (1975) built up an initial work about the dynamics based on linear irregular waves and Tung and Hunag (1984) extended the formula to nonlinear one.   Cieślikiewicz and Gudmestad (1993) combined the nonlinear model of Longuet-Higgins (1963), the linear concepts of Tung (1975) and considered the emergence properties to obtain a statistical formula satisfied nonlinear surface elevation and to fix the statistical results close to the surface.

The bed shear stresses caused by the nonlinear irregular waves are less studied since the theoretical formula for nonlinear surface elevation is not unique and no transfer function suitable for use.   The statistical work is made by Myrhaug and Holmedal (2003), who extended Myrhaug's approach (1995) using asymmetric property of the second-order Stokes waves to have that of the bed shear stress, which was formulated by Myrhaug and Holmedal (2001) for laminar flow.   Similar to Myrhaug (1995), no more verification was made, but a simplified procedure for practical application was stated clearly.

1.4 Interaction of irregular waves and a submerged breakwater

There are various coastal structures, such as reef, detached breakwater and submerged breakwater, built to prevent wave attack.   The major purpose of such structures is to introduce wave reflection or breaking and reduce wave transmission.   So that estimation

of wave motions with coastal structures in nearshore zone is an important subject of coastal engineering. Since a submerged breakwater has the potential to protect wave attack, against beach erosion, and for creation of artifical fishing grounds (Dattatri et al., 1978), many researchers experienced different methods to figure out its efficiency, stability and performance. Experiments, analytic and numerical models are variations of methods performed to study about waves propagating over a submerged breakwater. Reflected and transmitted coefficient, nonlinear effects or higher harmonic generation, wave breaking, vortex dynamics and scour around breakwater are the essential properties that introduced by the interaction of waves and submerged breakwaters.

Many experimental studies focused on wave reflections and transmissions induced by a submerged breakwater. Determining the reflected coefficients accurately is the major subject for such studies (e.g. Stamos and Hajj, 2001). Several methods have been proposed to determine the reflected characteristic. Goda and Suzuki (1976) applied two measured wave heights and phase difference to obtain reflected coefficient. Mansard and Funk (1980) used three probes and the least-square method to correct the bias of experimental results and to get the reflected coefficients more accurate. Lin and Huang (2004) adopted the least-square method and four measured surface elevation to determine the reflected coefficient and higher harmonics. These methods are all based on the Fourier transform with the assumptions that surface elevations are stationary in time, and homogeneous in space, and wave-wave interaction or energy loss are not allowed. These assumptions limit experimental studies on far off breakwaters, where waves are not

affected by the nonlinear effects and more stationary. Stamos and Hajj (2001) applied wavelet method to determine reflected waves from the variations in the amplitude as well as phase of the wave in only one measured result. However, this method can only be applied on regular waves.

Properties of surface elevations in the vicinal region of breakwater are vital for the performance and stability of breakwaters. The generation of higher harmonics above breakwaters is one of the properties. Johnson et al. (1951) noticed there are higher harmonics as a wave propagating over a submerged obstacle. Similar phenomena were found in experiments by Young (1989). Earlier researchers have tried to predict the generation of higher harmonics by applying nonlinear shallow-water wave theories, such as the Boussinesq and KdV equations. Since the derivation of the Boussinesq equations is based on the assumptions of both weak nonlinearity and weak dispersivity of waves, these equations may not be valid for the prediction on the lee side of a submerged breakwater, where harmonics may arise in the form of deep-water waves.

In order to overcome this defect, improvements on the Boussinesq equations have been developed. Peregrine (1967) developed equations of motion for long waves in water of varying depth. These equations can be viewed as the Boussinesq equations for water of varying depth. Witting (1984), Madsen and Sorensen (1992), Nwogu (1993) and Beji and Battjes (1994) improved the Boussinesq equations by adding a term to improve its dispersion characteristics and extended its applications. There are many studies employed the same equations to study the deformation of waves. However the

term for improving dispersion includes an unknown variable and not rigorous mathematically. Numerical results applied the extended Boussinesq equations are also found to overestimate the amplitude of higher harmonics and the total averaged energy flux on the lee side of a submerged breakwater (Ting et al., 2005). The KdV equations are also applied to deal with the deformation of waves (Ishida and Takahashi ,1981; Yasuda et al., 1982), and have the same limitations with the Boussinesq equations.

An experimental study about interaction of waves with a submerged trapezoidal breakwater was conducted by Beji and Battjes (1993), who investigated the deformation of waves around the breakwater. Ohyama and Nadaoka (1994) used potential theory to perform similar studies. Single and multiple wave components were considered. The results of single wave component were at a good agreement with that of experiments by Kojima et al. (1990), and the beat length introduced by higher harmonics were compared. Two irregular waves with different phases were compared by numerical experiments and results totally different transmitted patterns. Further verification was done by Ohyama et al. (1994). The experimental results of Beji and Battjes (1993) were applied to justify their model and had a good agreement in the comparison of regular wave.

The performance of impermeable and permeable breakwaters were revealed by Rambabu and Mani (2005), who used potential theory as governing equation and Green's function as boundary treatment to deal with waves over trapezoidal and rectangular breakwaters. After verifying the numerical results with experiments of permeable structures, the authors suggested several optimal conditions using parameterized

18

coefficients: submergence ratio q; steepness factor H_i / gT^2; the ratio of breakwater width and water depth W_B / h_o; and breakwater spacing parameter, where H_i was the incident wave height, g the gravitational acceleration, T the wave period, W_B the width of breakwater, and h_o the still water depth.

Detailed spectral deformation of multi-component waves was studied by Yoshida et al. (1996), who applied the Stokes series expansion and Green's second theory to solve the interactions over a submerged obstacle.   The results were compared with experiment one and were good enough to describe the spectral deformation when the wave amplitudes were small and wave breaking did not take place.

Vortices generated about a submerged breakwater have subtle effects on wave energy loss and the stability of breakwaters (Ting and Kim, 1994).   However, vortex dynamics strongly affect the mixing process of energy or nutrient, sediment transport, and also the introduced toe scour.   It is known that potential theory can deal with flow motions far from boundaries very well.   For studying vortex dynamics, flow viscous is inevitable, and thus only numerical models included viscous effects or experiments can handle this problem well.

In order to realize the effects introduced by vortex, Ting and Kim (1994) made a measure on vortex by numerical integrating the vorticity over the region of eddy motion. No more details about the numerical integrating were stated and the region of eddy motion was not clearly identified.   Dong (2000) and Huang (2004) followed the same manner to study vortices.   They numerically integrated vorticities over a fixed-rectangular region, in

which vortices formed.   However, the region was not moved with vortices and the results probably lead to misconceptions.

Another method was used by Chang et al. (2001, 2005), who chose the extreme value magnitude of vorticities as the measure of vortex strength.   With comparing the nearest horizontal velocity and the extreme vorticity obtained by numerical experiments, the authors found that the extreme vorticity was driven by the nearest horizontal velocity, and thus a simple model was built to have a prediction of the extreme vorticity around breakwater.

1.5   Vortex dynamics above rigid vortex ripples

Plenty of sea bed is covered by sand and forms soft bottom.   The bedform can be easily changed beneath energetic hydraulic conditions and is different to be measured in field.   However, knowledge of bedform geometry is vital in several interesting areas to the coastal and marine environment, e.g. in continental shelf area, which are known as the principal fishing ground of the world (Nybakken and Bertness, 2005).   Hence, different methods were carried out to reveal fundamental understanding about the formation process and equilibrium state and non-equilibrium state of bedform, especially wave-induced ripples.

1.5.1   The general conditions of ripples

Ripples is a general pattern of soft bottom.   Since large part of sea bed is covered by ripples, the properties and functions of ripples are important factors of many applications. Sediment transport process, ripple morphology, vortex dynamics over ripples and near-bed drift are most important, especially in storms or other kind of energetic hydraulic conditions.   After a storm, the relic ripples are dominate in determining the bed roughness, which is a parameter in bottom boundary condition for modeling waves (Mathisen and Madsen, 1996 a and b, 1999; Zhang et al., 2004) during moderate hydraulic conditions, in which the ripple form has less change.   The nutrient distribution, biological and chemical process can also be changed with different ripple patterns.   An important mechanism for exchanges of nutrients was carried out by pore water flow through ripples (Precht and

Huettel, 2004).

The bed flow properties are usually expressed as a function of bed orbital Reynolds number, say $Re_o = U_o A_o / \upsilon$, where U_o is the bed-orbital-velocity amplitude and A_o the bed-orbital-displacement amplitude. When bed orbital Reynolds does not suffice large, ripples were formed with small shape angles and flat, plane trough. This ripple form was recognized as rolling-grain ripples. As the bed orbital Reynolds number reached $O(10^3)$, separation bubbles form against both slopes of ripples and increase ripple steepness exceeds over $H_r/L_r > 0.1$, in which H_r is the ripple height and L_r the ripple wavelength. Thus, organized vortex structures form and dominate the region within $y < 2H_r$ (Ranasoma and Sleath, 1992; Davies and Thorn, 2005), so that sands are picked-up by vortices and settling when the vortices tend to breakdown. A new form of ripples are built by this process with the triangular shape and the steepness about $H_r/L_r = 0.17$. Since the ripple form was made by vortices, it is called vortex ripple. However, if the bed orbital Reynolds number exceeds $O(10^5)$, the form of ripples was washed out and became near flat bed with large suspension.

If the sand properties were taken into account, the particle Reynolds number, $Re_d = U_o d_{50} / \upsilon$, and the Froude number, which states the velocity ratio of flow and particle, $Fr_d = U_o / \sqrt{(s-1)g d_{50}}$, or the maximum Shields parameter, $\theta' = \tau_{\max} / \rho g (s-1) d_{50}$ should be considered, where s is the specific density ρ_s / ρ, d_{50} the medium grain size, and $\tau_{\max}$ the maximum shear stress. These parameters are usually used to defined the sediment properties in flat bed condition. While the Shields parameter exceeds the

critical value, say $\theta_c' \approx 0.05$ (Nielsen, 1992), the sands were moving by the flow.

1.5.2　The flow motion and vortex dynamics

Of preliminary study, the flow motion above ripples can be carried out theoretically when the ripple steepness is very small (Lyne, 1971; Kaneko and Honji, 1979; Matsunaga et al., 1981; Vittori, 1989; Hara and Mei, 1990; Blondeaux, 1990; Blondeaux and Vittori, 1991). With the assumption of small steepness for the ripple form, only rolling-grain ripple can be studied and with no vortex generated.

For achieving the understanding of the properties and functions of vortex ripples, the flow motion and vortex dynamic are matters of concern. Considerable amount of laboratory works has been performed to investigate the boundary layer flow above sand ripples. In the earlier, Tunstall and Inman (1975) used the hydrogen bubble technique to measure the circulation of vortices generated as the oscillating flow passes over rippled surface. It was found that the circulation is proportional to the horizontal flow velocity near the bottom and the height of sand ripples. Du Toit and Sleath (1981) employed the laser Doppler velocimetry (LDV) to measure the flow fields near the crest and trough sections of the wavy wall and showed that the significant increase of turbulent intensities was induced by the vortices. Sato et al. (1984 and 1987) performed the experiments by LDV and obtained the spatial distributions of the Reynolds stress, the eddy viscosity, and the characteristics of turbulent energy production rate and dissipation rate in the boundary layer. Similar measurement was also performed by Ikeda et al. (1989 and 1991) and found that the generation of the Reynolds stress is limited within the vortices and the

associated eddy viscosity showed sinusoidal variation.

The particle image velocimetry (PIV) was used to acquire the knowledge of regional velocities around ripples (Hudson et al., 1996; Earnshaw and Greated, 1998; Jespersen et al., 2004; Marin, 2004; Admiraal et al., 2006; Van der Werf et al., 2006). Hudson et al. (1996) focused on turbulent effects and calculated Reynolds shear stress and turbulent kinetic energy. Comparing to LDV or acoustic Doppler velocimetry (ADV), the PIV provides large spatial resolution. Therefore, the regional results of vortex properties (e.g. circulation, trajectory and vortical size) can be calculated by vorticity-weighting methods and by summing local properties over a vortex, and the region of vortex was determined by a particular threshold of the extreme vorticity.

Earnshaw and Greated (1998) as well as Admiraal et al. (2006) recognized the location with vorticity exceed 10% of the extreme one as the region of a vortex, and Jespersen et al. (2004) chose 20%. However, the vorticity threshold, either 10% or 20%, were satisfied only if the extreme vorticity is large. When the vorticities diffused and were convected, the region of vortex extended and with a smaller extreme vorticity, and the threshold, 10% or 20% of the extreme vorticity, led to misunderstanding about the properties of vortex. Admiraal et al. (2006) changed the threshold to 50% of the extreme vorticity when the extreme vortices is small. Moreover, the results were strongly affected by the selection of the threshold, and it should not be change within the interesting duration. By comparing the near-bed and free stream velocities, Van der Werf et al. (2006) stated the time-lag and reveal its contribution to sand concentration. The authors also revealed that

the peak concentrations were associated with vortex dynamics.

The fluid motion under waves is different from that of oscillatory flow. In the region above the rippled bed, flow motion in waves is elliptic type but only the streamwise component of the elliptical motion appeared in oscillating flow. The flow fields in waves above any two adjacent ripples are different because of different phase beneath the wave elevation and form a near-bed steady drift, which was responsible to the near-bed high-concentration sediment motion (Marin, 2004; Ourmières and Chaplin, 2004). On the contrary, the flow fields in oscillatory flow are exactly the same above any ripples and with no drift.

By PIV examination beneath single wave condition, Earnshaw and Greated (1998) found that negative vortices generated by onshore-directed flow were stronger than positive vortices generated by offshore-directed flow. Fredsøe et al. (1999) used laser Doppler anemometry (LDA) to measure the velocity profile above a fixed rippled bed with combined wave and current. Marin (2004) used similar methodology to study the Eulerian drift of waves over rippled beds. Another visualization of wave-induced flow was performed by Ourmières and Chaplin (2004), who applied a fluorescent dye filmed by a digital high speed video camera to capture flow over a rigid ripple bed. Vortex patterns were separated into rolls, rolls plus jets, first flow separation and vortex ejection, and also the patterns, ring and brick, of three-dimensional vortex were defined and distinguished by Taylor number, which defined as following.

$$Ta = \frac{A_o^2 H_r}{2L_r^2} \sqrt{\frac{\omega}{\upsilon}} = \frac{H_r}{2L_r^2} \sqrt{\frac{\upsilon}{\omega}} Re_o \qquad\qquad (1.2)$$

By the improvement of computing technique, many solvers (solving Navier-Stokes equations or vorticity equations with a turbulence model) are able to reveal the interaction of oscillating flow with ripples clearly. De Angelis et al. (1997) applied pseudospectral method and coordinate transformation technique to study regular oscillatory flow over a rippled bed. Turbulent effects and velocity profile were studied. Malarkey and Davies (2002, 2004) used two discrete vortex models, a simple inviscid model (with no diffusion of vorticity) and a cloud-in-cell (CIC) (with diffusion of vorticity), to study oscillating flow above rippled beds. The special case of a round-crested symmetric ripple used by Sleath (1984) and a sharp-crest symmetric ripple were considered. Chang and Scotti (2004) made a comparison of two turbulence models, the Reynolds-averaged Navier-Stokes equations (RANS) and the large-eddy simulation (LES), for simulating oscillating flow over ripples. Comparing with the experiments of Hudson et al. (1996), the authors found that only the numerical model with the LES is able to deal with the problems well.

Zedler and Street (2006) numerically studied the flow motion and the associated sediment concentration on long wave ripples. The Taylor number is extremely high $Ta \approx 127$ so that three dimensional pattern of flow motion was studied.

1.5.3 The equilibrium state of wave formed ripples

The equilibrium state of ripple is an important factor to determine the stability of sea bed or to evaluate the sediment transport, and also can be applied to estimate the associated

sea state if no measurements were set up.

An oscillating plate covered with a layer of sand in static water was usually used to produce ripple structure in laboratory (Bagnold, 1946; Hansen, 2001; Hansen et al., 2001; Scheibye-Knudsen et al., 2005). While the sand motion at the end of the oscillating plate may introduce instability, cylindrical tanks were applied to establish a quasi-one-dimensional system and avoid end effects (Betat et al., 1999; Stegner and Wesfreid, 1999; Andersen et al, 2000 and 2002; Rousseaux et al., 2004; Rousseaux, 2006). For the sake of realizing ripple patterns beneath waves, natural formed ripples with only waves or combined waves and current were carried out in experiments (Khelifa and Ouellet, 2000; Davis, 2005; Testik et al., 2005; Cataño-Lopera and García, 2006 a & b; Landry et al., 2007).

Experiments revealed two equilibrium patterns: rolling-grain ripples and vortex ripples. The rolling-grain ripples are small patterns with grains moving back and forth along the water-sand interface. The wavelength of rolling-grain ripples are nearly independent of bed orbital amplitude with small steepness $H_r / L_r < 0.1$ (Wiberg and Harris, 1994; O'Donoghue et al. 2006). Therefore, the rolling-grain ripples is also called anorbital ripples. The steepness of vortex ripples is larger than that of rolling-grain ripples and with vortices surrounding and picking-up sands from trough to crest. The wavelength of vortex ripples are proportional to bed orbital amplitude and also called orbital ripples (Wiberg and Harris, 1994; O'Donoghue et al. 2006). Comparing numerous data of experiments and field measurements, Wiberg and Harris (1994) distinguished these

two ripple forms by bed orbital properties and the oscillating rough turbulent layer thickness. However, the authors found that the oscillating rough turbulent layer thickness is not satisfied to describe the ripple patterns without the knowledge of flow motion.

Bagnold (1946) found that the wavelength of ripples was not affected by the frequency of the oscillatory flows. By changing the frequencies and last for a rather long duration, Scherer et al. (1999) and Stegner and Wesfreid (1999) found that rolling-grain ripples are transient stage and vortex ripples the true final stage of ripple form. Rousseaux et al. (2004) and Rousseaux (2006) confirmed the statement and revealed that the final stage can be quickly reached if the oscillating frequency was higher. The author also noted that some misunderstanding may introduce by the observation of "the pseudo-stability zone."

Cataño-Lopera and García (2006a) focus on the long wave ripple and called it sandwaves. The natural formed ripple beneath waves with 3.4 s in period was worked over 100 hrs. The authors performed the experiments on the sandwaves formation. While the sandwaves were formed, at about 8 hrs, the sandwave vertical growth rate was at about 0.2 cm/hr and went on smaller. The higher growth rate was at about 1 hr (0.76 cm/hr). And clear sandwaves formed after about 100 min. The migration rate of the short wave ripples, about 0.65 cm/min, is smaller than that at flat bed. This phenomena can only be carried out by waves. While standing wave formed, the sandy bed was formed with crests beneath the surface wave nodes and flat plateaus flanked by mounds under the antinodes (Landry, 2007). Cataño-Lopera and García (2006b) experimentally

studied the ripple migration and ripple formation above sandwaves. The results are similar to literature data. The authors also built the relation of ripple wavelength and ripple height with the Reynold number for $L_r/A_o = 277.3 Re_o^{-0.55}$ and $H_r/A_o = 155.2 Re_o^{-0.68}$ valid for $16 \times 10^3 < Re_o < 5 \times 10^5$.

For the sake of having the knowledge about ripple form beneath irregular wave motion, Mathisen and Madsen (1999) experimentally studied irregular waves with five wave component over a fixed ripples, and focused on the hydraulic roughness resulted by ripples. Scheibye-Knudsen et al. (2005) used oscillating plate with a set of multi-component wave motion to form natural ripples. The authors found that the selected wavelength is dominated by the largest wave.

Beneath the natural sea, bed form can be changed by the presence of wave groups, the distribution of grain size, and the wave direction, although experiments support simple parameterizations using "equivalent parameters", e.g. medium grain size, bed orbital diameter and the Shields number based on the significant wave height. However, there is difficult to determine the relation of ripples and wave condition in field since historical measurement of waves may not present. Traykovski et al. (1999) used sector-scanning sonar and acoustic backscattering system to perform bedform observation at the sandy LEO-15 site located on Beach Haven ridge off southern New Jersey. Ardhuin et al. (2002) used directional waverider buoys and side-scan sonar to measure the wave envelope and bed form on the North Carolina continental shelf. The observed ripple characteristics are consistent with wave-generated vortex ripple, in which the ratio of wave orbital amplitude

and ripple wavelength is about $A_o / L_r \approx 1$. Another field study was performed by William et al. (2004) and focused on suborbital ripples, which has the properties between orbital and anorbital ripples.

Grasmeijer and Kleinhans (2004) have compared many field and laboratory measurements and concluded the relation of bed forms and suspended sand concentrations. The field measurements were subdivided into two groups: short wave ripples (SWR) with wavelength of about $0.19 \sim 0.35$ m and long wave ripples (LWR) with wavelength of about $0.37 \sim 2.0$ m. The SWR and LWR associated respectively to low and high mobility parameter $\psi_m = U_o^2 / (s-1) g d_{50}$ of sand. The authors suggested a new bed form predictor that better collapsed the measure field and laboratory data. It included nondimensional ripple height H_r / A_o and ripple steepness H_r / L_r. However, the effects of relative proceeding wave were not considered. Different bottom concentration models were also tested against field measurements by the authors. Note that the information about the wave environment can be extracted from the preserved stratigraphy, if there are orbital ripples. If ripples are with anorbital pattern, the wave environment remained unknown while no wave gage was installed and extracting the wave environment from the preserved stratigraphy is impossible.

1.5.4 The non-equilibrium state and ripple migration

The final stage or the equilibrium stage of sand ripples can be reached if the hydraulic conditions last for a sufficient duration (Rousseaux, 2006, and among others). The sufficient duration, about $O(10^5) \sim O(10^6)$ cycles, is about $O(10)$ days for field or

realistic sea state, if $T_p \approx 10$ s .　　However, it is rarely for a storm or an energetic hydraulic condition last so long.　　The ripple migration, dynamic ripple pattern and non-equilibrium were studied with spectral or statistical manners by Becker et al. (2007) and Traykovski (2007).　　However, the non-equilibrium state is very difficult for any model to implement and this part is not considered herein.

1.6　Research Objectives

The overall objective of the research is to attempt to figure out the associated phenomena beneath irregular waves by applying a viscous numerical wave tank.　　This was to be achieved through the use of spectral and statistical methods about irregular waves and the associated properties, i.e. surface elevation and flow dynamics.　　Under the overall objective the study focuses on the properties which potential theory can not reveal, and set a number of objectives:

● Generating a stochastic wave train that satisfied the properties of linear or nonlinear irregular waves;

● Extract the information of bottom shear stress introduced by linear or nonlinear waves in viscous wave tank and verified the transfer function as well as the statistical formulas for engineering use;

● Build some fundamental understanding about the spectral and statistical properties of linear or nonlinear irregular waves and the associated flow dynamics;

● Applied a measure to determine the vortex characteristics, such as vortex circulation

(or called vortex strength), center of vortex motion and the relative vortex extent, of the cases both of wave interacting with submerged breakwater and wave propagating over rippled beds.

1.7   Layout and Contents of Dissertation

This dissertation is structured to provide a logical progression and series studies through the work that has been completed regarding irregular waves and the associated effects.   Each of the following paragraphs outline the specifics of each chapter.

Chapter 2 presents the theoretical treatment of water waves in a wave tank. Two-dimensional continuity equation and incompressible Navier-Stokes equations were consider as governing equations.   The boundary conditions that must be satisfied were applied.   The governing equations and boundary conditions are both described in Cartesian coordinate and in curvilinear coordinate.

Chapter 3 outlines the numerical model using in this study.   The finite-analytic (FA) method was applied to discretize the unsteady two-dimensional Navier-Stokes equations. The SIMPLER algorithm was used to calculate the coupled velocity and pressure fields. The Marker and Cell method (MAC) and its modified version SUMMAC were used in combination to calculate the free surface boundary.   The numerical model was expressed in both Cartesian coordinate and curvilinear coordinate.

Chapter 4 shows the generation of irregular waves and the associated results.   The deterministic spectral amplitude method based on the fast Fourier transform (DSA-FFT)

was adopted to generate a stochastic wave train that satisfies a target spectrum in amplitude and was with random-distributed phases.   Measure was made on sea bed and surface to realize the relation between surface elevation and bottom shear stress.   The accuracy of the numerical scheme was confirmed by comparing the measured wave spectrum with the target spectrum and by comparing the numerical transfer function between the shear stress and the surface elevation with the theoretical linear transfer function.   Velocity fields throughout the depth of the water and near the bottom, associated with irregular waves, were presented to elucidate the correlation between the water surface elevation and the bottom shear stress.   The Wavelet transform was also employed to obtain a full time-frequency representation of the wave and shear stress spectra.   The maximum bottom shear stresses obtained by this wave model are compared with those obtained using Myrhaug's statistical model (1995) and those obtained using transfer function method.

Chapter 5 reveals an extended studies of Chapter 4 on the nonlinear properties of surface elevation and the associated bed shear stress.   Since the nonlinear waves are without a permanent form, the model of Dean and Sharma (1981) was used as a qualitative comparison.   The statistical properties were presented spatially in order to elucidate the changes of nonlinearity of both the surface elevation and the bed shear stress.   A statistical model of the bed shear stress developed by Myrhaug and Holmedal (2003) were compared.

Chapter 6 presents an environment for studying the interaction of irregular wave and

a submerged breakwater. For simplicity, the real geometry and the permeability of a rubble-mound submerged breakwater, turbulent effects, and the stability of armour units are not considered herein. A reliable processing period was confirmed by comparing reflected coefficients. A procedure was carried out in order to study vortex dynamics around the breakwater. The region of vortex was selected by a threshold of the extreme vorticity. The flow field and vorticity contours were shown in sequence within the lifecycle of a counterclockwise vortex and a clockwise vortex. Circulations of the vortices formed within the reliable period around the breakwater were shown.

Chapter 7 uses the procedure in Chapter 6 to analysis the vortex dynamics above ripples. An ripple form agrees with the equilibrium state and the natural shape was used. The circulations and trajectories of the vortices were compared with the wave conditions on and off the equilibrium state. Statistical properties of the circulation of the vortices beneath irregular waves were also carried out.

Chapter 8 presents the major conclusions drawn from the four related subjects of this research and highlights a number of recommendations for future work in the associated phenomena about irregular waves.

Chapter 2 Governing Equations and Boundary Conditions

"If you don't learn to think when you are young , you may never learn."

—Thomas A. Edison,
American inventor

2.1 Cartesian Coordinate System
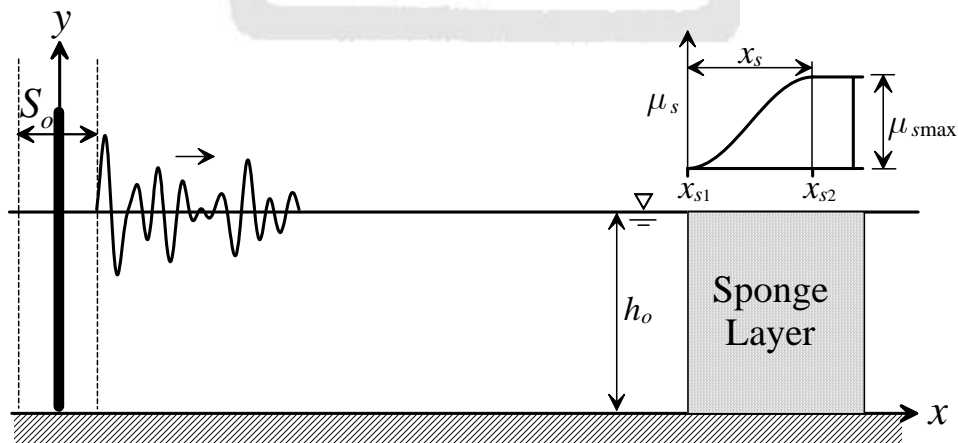
Figure 2.1: Schematic diagram of a numerical wave flume with a piston-type wavemaker and a sponge layer for generating irregular waves.

A schematic diagram of a two-dimensional numerical wave flume for generating

random waves is shown in Figure 2.1. The x-axis is measured horizontally in the direction of wave propagation and the origin is set at the initial location of the piston-type wave generator with stroke S_o. The y-axis is measured vertically upwards from bottom. The still water depth is h_o. In the present case, u_p and h_o are used to non-dimensionalize the velocity and length, while $t_o = h_o/u_p$ is chosen to non-dimensionalize the time, where u_p is the velocity-amplitude of the wave generator for producing the random waves with a spectral-peak frequency f_p. Furthermore, the pressure is non-dimensionalized by ρu_p^2. For incompressible, viscous fluid, the dimensionless continuity equation in the Cartesian coordinate system is

$$\frac{\partial u'}{\partial x'} + \frac{\partial v'}{\partial y'} = 0 \tag{2.1}$$

and the dimensionless Navier-Stokes equations are given by

$$\frac{\partial u'}{\partial t'} + u'\frac{\partial u'}{\partial x'} + v'\frac{\partial u'}{\partial y'} = -\frac{\partial p'}{\partial x'} + \frac{1}{Re}(\frac{\partial^2 u'}{\partial x'^2} + \frac{\partial^2 u'}{\partial y'^2}) \tag{2.2}$$

and

$$\frac{\partial v'}{\partial t'} + u'\frac{\partial v'}{\partial x'} + v'\frac{\partial v'}{\partial y'} = -\frac{\partial p'}{\partial y'} + \frac{1}{Re}(\frac{\partial^2 v'}{\partial x'^2} + \frac{\partial^2 v'}{\partial y'^2}) \tag{2.3}$$

where u' and v' are the horizontal and vertical velocity components, t' is the time, p' is the hydrodynamic pressure, which is defined as taking hydrostatic pressure p'_s off the total pressure p'_t ($p' = p'_t - p'_s$), and the apostrophe marks denote the dimensionless variables. The Reynolds number Re is defined as $Re = u_p h_o / \upsilon$, where υ is the kinematic viscosity of the fluid.

For obtaining the solution of Eqs. (2.1) to (2.3), it is necessary to provide appropriate

boundary conditions at all boundaries of the solution domain, as well as the initial conditions at $t = 0$ in the whole domain. The boundary conditions that must be satisfied are: (1) the kinematic and the dynamic free surface boundary conditions, (2) the no-slip boundary condition on the bottom, (3) the upstream boundary condition against the wavemaker, and (4) the non-reflected condition of the downstream. The initial conditions of the velocities, hydrodynamic pressure, and surface elevation are set to zero at time $t = 0$. Conditions (1), (3), and (4) mentioned above are explained in more detail in the following subsections.

2.1.1 Free surface boundary conditions

The kinematic condition states that fluid particles at free surface remain on the free surface, and can be expressed as

$$\frac{\partial \eta'}{\partial t'} + u' \frac{\partial \eta'}{\partial x'} = v' \tag{2.4}$$

where $\eta' = \eta'(x', t')$ is the surface elevation.

The dynamic condition requires that, along the free surface, the normal stress is equal to the atmospheric pressure and the tangential stress is zero. These conditions can be expressed as the following:

$$n_i \sigma_{ij} n_j = 0 \tag{2.5}$$

$$\tau_i \sigma_{ij} n_j = 0 \tag{2.6}$$

in which n_i and τ_i is the x_i component of a unit vector normal and tangential to the free surface, and σ_{ij} the i-th component of the stress tensor acting on the surface with

constant x_j. The x and y components of the normal and tangential unit vectors at the free surface are, respectively

$$n_1 = \frac{-\frac{\partial \eta'}{\partial x'}}{\sqrt{1+(\frac{\partial \eta'}{\partial x'})^2}} , \quad n_2 = \frac{1}{\sqrt{1+(\frac{\partial \eta'}{\partial x'})^2}}$$ (2.7)

$$\tau_1 = \frac{1}{\sqrt{1+(\frac{\partial \eta'}{\partial x'})^2}} , \quad \tau_2 = \frac{\frac{\partial \eta'}{\partial x'}}{\sqrt{1+(\frac{\partial \eta'}{\partial x'})^2}}$$ (2.8)

The stress tensor σ_{ij} is defined by

$$\sigma_{ij} = -(p' - \frac{y'-1}{Fr^2})\delta_{ij} + \frac{1}{Re}(\frac{\partial u'_i}{\partial x'_j} + \frac{\partial u'_j}{\partial x'_i})$$ (2.9)

where the Kronecker delta δ_{ij} is defined by

$$\delta_{ij} = \begin{cases} 1 & , \text{ for } i = j \\ 0 & , \text{ for } i \neq j \end{cases}$$ (2.10)

and Fr is the Froude number, defined as

$$Fr = \frac{u_p}{\sqrt{gh_o}}$$ (2.11)

where g is the gravitational acceleration. Substituting Eqs. (2.7) to (2.10) into (2.5) and (2.6), the dynamic free surface boundary conditions become

$$p'(x', \eta') = p'_o = \frac{\eta'}{Fr^2} + \frac{2[(\frac{\partial \eta'}{\partial x'})^2 \frac{\partial u'}{\partial x'} - (\frac{\partial u'}{\partial y'} + \frac{\partial v'}{\partial x'})\frac{\partial \eta'}{\partial x'} + \frac{\partial v'}{\partial y'}]}{Re[1+(\frac{\partial \eta'}{\partial x'})^2]}$$ (2.12)

$$2(\frac{\partial u'}{\partial x'} - \frac{\partial v'}{\partial y'})\frac{\partial \eta'}{\partial x'} + (\frac{\partial u'}{\partial y'} + \frac{\partial v'}{\partial x'})\left[(\frac{\partial \eta'}{\partial x'})^2 - 1\right] = 0$$ (2.13)

After substitution of equations (2.1) and (2.13) into equation (2.12), we obtain

$$p_o' = \frac{\eta'}{Fr^2} + \frac{2[1+(\frac{\partial \eta'}{\partial x'})^2]}{Re[1-(\frac{\partial \eta'}{\partial x'})^2]} \frac{\partial v'}{\partial y'} \qquad (2.14)$$

where $p_o' = p'(x', \eta')$ is the hydrodynamic pressure at the free surface η'. From Eq. (2.13), we obtain

$$\frac{\partial u'}{\partial y'} = -\frac{\partial v'}{\partial x'} + \frac{4}{(\frac{\partial \eta'}{\partial x'})^2 - 1} \frac{\partial v'}{\partial y'} \frac{\partial \eta'}{\partial x'} \qquad (2.15)$$

In numerical computations, Eq. (2.14) is used to determine the pressure at the free surface and Eq. (2.15) is used to extrapolate the horizontal velocity at the free surface from the flow domain. The vertical velocity component v' is then calculated from the continuity equation using the known velocity component u', obtained from Eq. (2.15).

2.1.2   The upstream boundary condition

The upstream conditions have two constrains: one is the flow motion against the piston-type wavemaker has identical velocity with the wavemaker; the other is no-slip condition along the wavemaker. However, strick no-slip condition makes the contact point of the free surface on the wavemaker unmovable in numerical performance. The detailed treatment is described in the last paragraph of Section 3.4.

2.1.3   The downstream boundary condition

The downstream boundary condition requires that, at a large distance from the wavemaker, the wave is outgoing. A numerical sponge layer, or sometimes referred to as "numerical beach" was applied at the downstream of the tank to dissipate wave energy and to eliminate possible reflected waves. The numerical beach has been shown to be very efficient for dissipating high frequency waves, provided the beach length is longer than the

typical wavelength of the incident waves (Clément, 1996). Details of the numerical beach will be discussed in the following chapter. With the sponge layer applied, only waves with wavelength longer than the width of the sponge layer remain at the end of the sponge layer, which are indeed long waves with the phase speed $\sqrt{gh_o}$. Such components are allowed to pass through the wave tank by utilizing the outgoing boundary condition applied on the downstream boundary. According to the wave equation and continuity equation, the downstream boundary conditions were set as follows (Dong and Huang, 2004).

$$\frac{\partial p'}{\partial t'} + c_o' \frac{\partial p'}{\partial x'} = 0 , \quad \frac{\partial u'}{\partial t'} + c_o' \frac{\partial u'}{\partial x'} = 0 , \quad \frac{\partial u'}{\partial x'} + \frac{\partial v'}{\partial y'} = 0 \qquad (2.16)$$

where $c_o' = \sqrt{gh_o} / u_p$ is the phase velocity of the long waves.

2.2 Curvilinear Coordinate System

For achieving the study about the interaction of waves and ripples, the body-fitted coordinate system is used. The curvilinear grid system is generated using algebraic coordinate method (Thompson, 1982). The Cartesian coordinate system (x, y) is transformed into the curvilinear coordinate system (ξ, ζ). To transform the equations of motion from the familiar orthogonal coordinates (x, y) to the new coordinate system (ξ, ζ) partial transformation was used. This means that only the independent coordinate variables were transformed, leaving the dependent variables, i.e. the velocity components, in the original orthogonal coordinates. This approach has the advantage that the resulting equations are relatively simple and the results can be easily interpreted.

The variables are next transformed from Cartesian space (x', y', t') into the curvilinear space (ξ', ζ', t'), where

$$\xi' = \xi'(x', y', t') \tag{2.17a}$$

$$\zeta' = \zeta'(x', y', t') \tag{2.17b}$$

From the chain rule of differential calculus, we have

$$\frac{\partial}{\partial x'} = \frac{\partial}{\partial \xi'}\frac{\partial \xi'}{\partial x'} + \frac{\partial}{\partial \zeta'}\frac{\partial \zeta'}{\partial x'} \tag{2.18a}$$

$$\frac{\partial}{\partial y'} = \frac{\partial}{\partial \xi'}\frac{\partial \xi'}{\partial y'} + \frac{\partial}{\partial \zeta'}\frac{\partial \zeta'}{\partial y'} \tag{2.18b}$$

$$\frac{\partial^2}{\partial x'^2} = \frac{\partial}{\partial \xi'}\frac{\partial^2 \xi'}{\partial x'^2} + \frac{\partial}{\partial \zeta'}\frac{\partial^2 \zeta'}{\partial x'^2} + \frac{\partial^2}{\partial \xi'^2}\left(\frac{\partial \xi'}{\partial x'}\right)^2$$
$$+ \frac{\partial^2}{\partial \zeta'^2}\left(\frac{\partial \zeta'}{\partial x'}\right)^2 + 2\frac{\partial^2}{\partial \zeta'\partial \xi'}\frac{\partial \zeta'}{\partial x'}\frac{\partial \xi'}{\partial x'} \tag{2.18c}$$

$$\frac{\partial^2}{\partial y'^2} = \frac{\partial}{\partial \xi'}\frac{\partial^2 \xi'}{\partial y'^2} + \frac{\partial}{\partial \zeta'}\frac{\partial^2 \zeta'}{\partial y'^2} + \frac{\partial^2}{\partial \xi'^2}\left(\frac{\partial \xi'}{\partial y'}\right)^2$$
$$+ \frac{\partial^2}{\partial \zeta'^2}\left(\frac{\partial \zeta'}{\partial y'}\right)^2 + 2\frac{\partial^2}{\partial \zeta'\partial \xi'}\frac{\partial \zeta'}{\partial y'}\frac{\partial \xi'}{\partial y'} \tag{2.18d}$$

The Cartesian derivatives in Eqs. (2.1) to (2.3) are replaced by Eqs. (2.18) to yield:

$$\frac{\partial}{\partial \xi'}\left(u'\xi'_{x'} + v'\xi'_{y'}\right) + \frac{\partial}{\partial \zeta'}\left(u'\zeta'_{x'} + v'\zeta'_{y'}\right) = 0 \tag{2.19}$$

$$g^{11}u'_{\xi'\xi'} + g^{22}u'_{\zeta'\zeta'} + 2g^{12}u'_{\xi'\zeta'} + f^1 u'_{\xi'} + f^2 u'_{\zeta'}$$
$$= \frac{Re}{J}\left[u'\left(b_1^1 u'_{\xi'} + b_1^2 u'_{\zeta'}\right) + v'\left(b_2^1 u'_{\xi'} + b_2^2 u'_{\zeta'}\right)\right] + Re \cdot u'_{t'} + s_u \tag{2.20}$$

$$g^{11}v'_{\xi'\xi'} + g^{22}v'_{\zeta'\zeta'} + 2g^{12}v'_{\xi'\zeta'} + f^1 v'_{\xi'} + f^2 v'_{\zeta'}$$
$$= \frac{Re}{J}\left[u'\left(b_1^1 v'_{\xi'} + b_1^2 v'_{\zeta'}\right) + v'\left(b_2^1 v'_{\xi'} + b_2^2 v'_{\zeta'}\right)\right] + Re \cdot v'_{t'} + s_v \tag{2.21}$$

Where the subscript (x', y'), (ξ', ζ') or t' on u' and v' denote the partial derivatives with respect to these variables, and

$$s_u = Re\left[\frac{1}{J}\left(b_1^1 p'_{\xi'} + b_1^2 p'_{\zeta'}\right)\right] \tag{2.22a}$$

$$s_v = Re\left[\frac{1}{J}\left(b_2^1 p'_{\xi'} + b_2^2 p'_{\zeta'}\right)\right] \tag{2.22b}$$

The Jacobian J is defined as follows

$$J = x'_{\xi'} y'_{\zeta'} - y'_{\xi'} x'_{\zeta'} = b_1^1 b_2^2 - b_1^2 b_2^1 \tag{2.23}$$

and the contravariant base vectors b_i^j are

$$\begin{cases} b_1^1 = y'_{\zeta'} = J\xi'_{x'} \\ b_1^2 = -y'_{\xi'} = J\zeta'_{x'} \\ b_2^1 = -x'_{\zeta'} = J\xi'_{y'} \\ b_2^2 = x'_{\xi'} = J\zeta'_{y'} \end{cases} \tag{2.24}$$

The conjugate metric tensor g^{ij} in the general curvilinear coordinates are defined as

$$\begin{cases} g^{11} = \xi'^2_{x'} + \xi'^2_{y'} = \frac{1}{J^2}\left(\left(b_1^1\right)^2 + \left(b_2^1\right)^2\right) = \frac{1}{J^2}\left(y'^2_{\zeta'} + x'^2_{\zeta'}\right) \\ g^{22} = \zeta'^2_{x'} + \zeta'^2_{y'} = \frac{1}{J^2}\left(\left(b_1^2\right)^2 + \left(b_2^2\right)^2\right) = \frac{1}{J^2}\left(x'^2_{\xi'} + y'^2_{\xi'}\right) \\ g^{12} = \xi'_{x'}\zeta'_{x'} + \xi'_{y'}\zeta'_{y'} = \frac{1}{J^2}\left(b_1^1 b_1^2 + b_2^1 b_2^2\right) = -\frac{1}{J^2}\left(x'_{\xi'}x'_{\zeta'} + y'_{\xi'}y'_{\zeta'}\right) \end{cases} \tag{2.25}$$

The grid-control function f^i are defined as

$$\begin{cases} f^1 = \xi'_{x'x'} + \xi'_{y'y'} = \frac{1}{J}\frac{\partial}{\partial\xi'}\left(Jg^{11}\right) + \frac{1}{J}\frac{\partial}{\partial\zeta'}\left(Jg^{21}\right) \\ f^2 = \zeta'_{x'x'} + \zeta'_{y'y'} = \frac{1}{J}\frac{\partial}{\partial\xi'}\left(Jg^{12}\right) + \frac{1}{J}\frac{\partial}{\partial\zeta'}\left(Jg^{22}\right) \end{cases} \tag{2.26}$$

In curvilinear coordinates (ξ', ζ'), the dynamic free surface boundary conditions (2.13) and (2.14) are rewritten as:

$$p_o' = \frac{\eta'}{Fr^2} + \frac{2\left[1 + (\frac{1}{J}b_1^1\eta_{\xi'}' + \frac{1}{J}b_1^2\eta_{\zeta'}')^2\right]}{Re\left[1 - (\frac{1}{J}b_1^1\eta_{\xi'}' + \frac{1}{J}b_1^2\eta_{\zeta'}')^2\right]}\left[\frac{1}{J}b_2^1v_{\xi'}' + \frac{1}{J}b_2^2v_{\zeta'}'\right] \qquad (2.27)$$

$$\left[\frac{1}{J}b_2^1u_{\xi'}' + \frac{1}{J}b_2^2u_{\zeta'}'\right] = -\left[\frac{1}{J}b_1^1v_{\xi'}' + \frac{1}{J}b_1^2v_{\zeta'}'\right]$$
$$+ \frac{4\left(\frac{1}{J}b_1^1\eta_{\xi'}' + \frac{1}{J}b_1^2\eta_{\zeta'}'\right)\left(\frac{1}{J}b_2^1v_{\xi'}' + \frac{1}{J}b_2^2v_{\zeta'}'\right)}{\left(\frac{1}{J}b_1^1\eta_{\xi'}' + \frac{1}{J}b_1^2\eta_{\zeta'}'\right)^2 - 1} \qquad (2.28)$$

Chapter 3 Numerical Methods

"Never make a calculation until you know the answer."

—John Wheeler's first moral principle,
American theoretical physicist

3.1 Staggered grid system

A difficulty in solving the Navier-Stokes equations using primitive variables is the discretization of the pressure gradient and the continuity equation. A highly non-uniform pressure and velocity field can probably be generated by a non-staggered grid system. This can be resolved by using a staggered grid system, in which velocities are calculated on the surface of control volumes, and pressures are calculated at the central of the control volumes. The locations for u', v', and p' are shown in Figure 3.1, where the subscripts n, s, e, w denote the four surroundings and c denotes the one calculated.
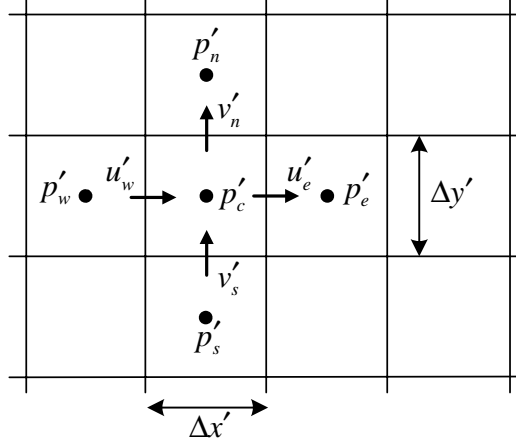
Figure 3.1: Staggered grid system for u', v', and p'.

3.2 Finite-analytic method

In general, equations (2.1) through (2.3) for unsteady two-dimensional flow can be transformed into the following form

In Cartesian coordinate:

$$\varphi_{x'x'} + \varphi_{y'y'} = Re \cdot U' \varphi_{x'} + Re \cdot V' \varphi_{y'} + Re \cdot \varphi_{t'} + s_{\varphi} \tag{3.1}$$

In curvilinear coordinate:

$$\begin{aligned}
&g^{11}\varphi_{\xi'\xi'} + g^{22}\varphi_{\zeta'\zeta'} + 2g^{12}\varphi_{\xi'\zeta'} + f^{1}\varphi_{\xi'} + f^{2}\varphi_{\zeta'} \\
&= \frac{Re}{J}[U'(b_1^1\varphi_{\xi'} + b_1^2\varphi_{\zeta'}) + V'(b_2^1\varphi_{\xi'} + b_2^2\varphi_{\zeta'})] + Re \cdot \varphi_{t'} + s_{\varphi}
\end{aligned} \tag{3.2}$$

where the subscripts (x', y'), (ξ', ζ') or t' on $\varphi(= u', v')$ denote the partial derivatives with respect to these variables. U' and V' are the mean values of u' and v' in a given computational element. Note that Eq. (3.2) depends upon g^{ij}, b_i^j, and the Jacobian. All of these quantities are only coordinate functions. The source terms s_{φ}

are defined as

In Carteian coordinate:

$$s_u = Re \cdot p'_{x'} \tag{3.3a}$$

$$s_v = Re \cdot p'_{y'} \tag{3.3b}$$

In Curvilinear coordinate:

$$s_u = Re \left[\frac{1}{J} \left(b_1^1 p'_{\xi'} + b_1^2 p'_{\zeta'} \right) \right] \tag{3.4a}$$

$$s_v = Re \left[\frac{1}{J} \left(b_2^1 p'_{\xi'} + b_2^2 p'_{\zeta'} \right) \right] \tag{3.4b}$$

Equations (3.1) and (3.2) can be rearranged into a general convective-transport equation of the following formula

In Cartesian coordinate:

$$\varphi_{x'x'} + \varphi_{y'y'} = 2A\varphi_{x'} + 2B\varphi_{y'} + Re \cdot \varphi_{t'} + S_\varphi \tag{3.5}$$

where the coefficient A_φ, B_φ and the source term S_φ are

$$\begin{cases} 2A_\varphi = Re \cdot U' \\ 2B_\varphi = Re \cdot V' \\ S_\varphi = s_\varphi \end{cases} \tag{3.6}$$

In Curvilinear coordinate:

$$g^{11}\varphi_{\xi'\xi'} + g^{22}\varphi_{\zeta'\zeta'} = 2A_\varphi \varphi_{\xi'} + 2B_\varphi \varphi_{\zeta'} + Re \cdot \varphi_{t'} + S_\varphi \tag{3.7}$$

where

$$\begin{cases} 2A_\varphi = \dfrac{Re}{J}\left(b_1^1 U' + b_2^1 V'\right) - f^1 \\[2mm] 2B_\varphi = \dfrac{Re}{J}\left(b_1^2 U' + b_2^2 V'\right) - f^2 \\[2mm] S_\varphi = s_\varphi - 2g^{12}\varphi_{\xi'\zeta'} \end{cases} \tag{3.8}$$

If we introduce the coordinate-stretching functions

$$\tilde{\xi}' = \frac{\xi'}{\sqrt{g^{11}}}, \quad \tilde{\zeta}' = \frac{\zeta'}{\sqrt{g^{22}}} \tag{3.9}$$

Eq. (3.7) can be written as

$$\varphi_{\tilde{\xi}'\tilde{\xi}'} + \varphi_{\tilde{\zeta}'\tilde{\zeta}'} = \frac{2A_\varphi}{\sqrt{g^{11}}}\varphi_{\tilde{\xi}'} + \frac{2B_\varphi}{\sqrt{g^{22}}}\varphi_{\tilde{\zeta}'} + Re\cdot\varphi_{t'} + S_\varphi \tag{3.10}$$

Let $2A = \dfrac{2A_\varphi}{\sqrt{g^{11}}}; \quad 2B = \dfrac{2B_\varphi}{\sqrt{g^{22}}}$ \tag{3.11}

Equation (3.10) reduces to the standard two-dimensional convective-transport equation described in Chen and Chen (1982 and 1987), i.e.,

$$\varphi_{\tilde{\xi}'\tilde{\xi}'} + \varphi_{\tilde{\zeta}'\tilde{\zeta}'} = 2A\varphi_{\tilde{\xi}'} + 2B\varphi_{\tilde{\zeta}'} + Re\cdot\varphi_{t'} + S_\varphi \tag{3.12}$$

It is convenient to rewrite the governing stand-in equations (3.5) and (3.12) in the following form

$$\varphi_{x_1'x_1'} + \varphi_{x_2'x_2'} = 2A\varphi_{x_1'} + 2B\varphi_{x_2'} + Re\cdot\varphi_{t'} + S_\varphi \tag{3.13}$$

Equation (3.13) can be rewritten as

$$\varphi_{x_2'x_2'} = 2B\varphi_{x_2'} + G_f \tag{3.14}$$

where

$$G_f = 2A\varphi_{x_1'} + Re \cdot \varphi_{t'} + S_\varphi - \varphi_{x_1' x_1'} \tag{3.15}$$

Of an element as shown in Figure 3.2, it is found that a general solution for equation (3.14) is a linear combination of exponential and linear functions of x_2', i.e.

$$\varphi = a^* \left(e^{2Bx_2'} - 1 \right) + b^* x_2' + C^* \tag{3.16}$$
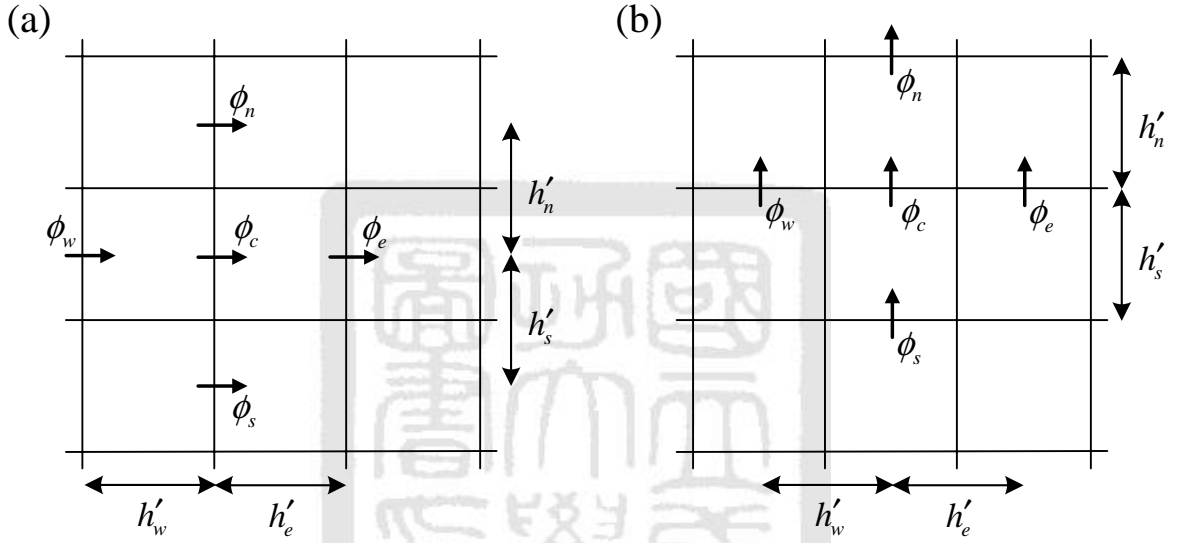
Figure 3.2: A schematic of the solving variable with four neighbors: (a) for $\varphi = u'$; (b) for $\varphi = v'$.

The coefficients, a^*, b^*, and C^* are determined by the boundary conditions

$$x_2' = \begin{cases} h_n' & , \text{ if } \quad \varphi = \varphi_n \\ 0 & , \text{ if } \quad \varphi = \varphi_c \\ -h_s' & , \text{ if } \quad \varphi = \varphi_s \end{cases} \tag{3.17}$$

i.e.

$$a^* = \frac{h_n' \varphi_s + h_s' \varphi_n - \left(h_n' + h_s' \right) \varphi_c}{h_n' e^{-2Bh_s'} + h_s' e^{2Bh_n'} - h_n' - h_s'} \tag{3.18a}$$

$$b^* = \frac{\left(-e^{2Bh'_n}+1\right)\varphi_s + \left(e^{2Bh'_s}-1\right)\varphi_n + \left(e^{2Bh'_n}-e^{-2Bh'_s}\right)\varphi_c}{h'_n e^{-2Bh'_s} + h'_s e^{2Bh'_n} - h'_n - h'_s} \tag{3.18b}$$

$$C^* = \varphi_c \tag{3.18c}$$

Substituting Eq. (3.16) into Eq. (3.14), we obtain

$$2Bb^* + G_f = 0 \tag{3.19}$$

Substituting Eq. (3.18b) into Eq. (3.19), we have

$$
\begin{aligned}
G_f &= \frac{1}{\overline{C}_c}\varphi_c - \frac{\overline{C}_s}{\overline{C}_c}\varphi_s - \frac{\overline{C}_n}{\overline{C}_c}\varphi_n \\
&= \frac{2B\left(e^{-2Bh'_s}-e^{2Bh'_n}\right)}{K_B}\varphi_c + \frac{2B\left(e^{2Bh'_n}-1\right)}{K_B}\varphi_s + \frac{2B\left(1-e^{-2Bh'_s}\right)}{K_B}\varphi_n \\
&= \tilde{C}_c\varphi_c + \tilde{C}_s\varphi_s + \tilde{C}\varphi_n
\end{aligned}
\tag{3.20}
$$

where

$$K_B = h'_n e^{-2Bh'_s} + h'_s e^{2Bh'_n} - h'_n - h'_s \tag{3.21}$$

$$\overline{C}_s = \frac{e^{2Bh'_n}-1}{e^{2Bh'_n}-e^{-2Bh'_s}} \tag{3.22a}$$

$$\overline{C}_n = \frac{1-e^{-2Bh'_s}}{e^{2Bh'_n}-e^{-2Bh'_s}} \tag{3.22b}$$

$$\overline{C}_p = \frac{1}{2B}\frac{-h'_s e^{2Bh'_n} - h'_n e^{-2Bh'_s} + h'_n + h'_s}{e^{2Bh'_n}-e^{-2Bh'_s}} \tag{3.22c}$$

$$\tilde{C}_c = \frac{1}{\overline{C}_c} \tag{3.22d}$$

$$\tilde{C}_s = -\frac{\overline{C}_s}{\overline{C}_c} = -\overline{C}_s\tilde{C}_c \tag{3.22e}$$

$$\tilde{C}_n = -\frac{\overline{C}_n}{\overline{C}_c} = -\overline{C}_n\tilde{C}_c \tag{3.22f}$$

$$\tilde{C}_s + \tilde{C}_n = -\tilde{C}_c = \tilde{C}_c^* \tag{3.22g}$$

Similarly, it yields

$$
\begin{aligned}
& 2A\varphi_{x_1'} - \varphi_{x_1'x_1'} + Re \cdot \varphi_{t'} + S_\varphi \\
& = -(\overline{C}_w + \overline{C}_e)\varphi_c + \overline{C}_w\varphi_w + \overline{C}_e\varphi_e + Re \cdot \varphi_{t'} + S_\varphi \\
& = G_f \\
& = \tilde{C}_c\varphi_p + \tilde{C}_s\varphi_s + \tilde{C}_n\varphi_n
\end{aligned}
\tag{3.23}
$$

where $\overline{C}_w$ and $\overline{C}_e$ are

$$
\overline{C}_w = 2A \frac{1 - e^{2Ah_e'}}{h_e'e^{-2Ah_w'} + h_w'e^{2Ah_e'} - h_w' - h_e'}
\tag{3.24a}
$$

$$
\overline{C}_e = 2A \frac{e^{-2Ah_w'} - 1}{h_e'e^{-2Ah_w'} - h_w'e^{2Ah_e'} - h_w' - h_e'}
\tag{3.24b}
$$

Equation (3.23) can be rewritten as

$$
(\overline{C}_w^* + \overline{C}_e^* + \tilde{C}_s + \tilde{C}_n)\varphi_c = \tilde{C}_s\varphi_s + \tilde{C}_n\varphi_n + \overline{C}_w^*\varphi_w + \overline{C}_e^*\varphi_e - Re \cdot \varphi_{t'} - S_\varphi
\tag{3.25}
$$

where $-\overline{C}_w = \overline{C}_w^*$, $-\overline{C}_e = \overline{C}_e^*$. If we approximate $\varphi_{t'}$ using a backward-difference scheme and let $S^* = \overline{C}_w^* + \overline{C}_e^* + \tilde{C}_s + \tilde{C}_n$, the local analytic solution at the central node c of the element is obtained

$$
\begin{aligned}
\varphi_c &= \frac{\widetilde{C}_s}{S^* \cdot D}\varphi_s + \frac{\widetilde{C}_n}{S^* \cdot D}\varphi_n + \frac{\overline{C}_w^*}{S^* \cdot D}\varphi_w + \frac{\overline{C}_e^*}{S^* \cdot D}\varphi_e + \frac{Re}{S^* \cdot D \cdot \Delta t'}\varphi_c^{n-1} - \frac{S_\varphi}{S^* \cdot D} \\
&= \sum_{nb=1}^{4} C_{nb}\varphi_{nb} + \frac{Re}{S^* \cdot D \cdot \Delta t'}\varphi_c^{n-1} - \frac{S_\varphi}{S^* \cdot D}
\end{aligned}
\tag{3.26}
$$

where $D = 1 + Re/(S^* \cdot \Delta t')$. The subscript nb represents the "neighboring" nodes of c. Equation (3.26) is the four-point finite-analytic formula for the momentum equations.

3.3 Solution algorithm

If the pressure field is known, Eq. (3.26) can be used to solve the convective-diffusion

equation (3.13) for u and v. However, in practice, the pressure is a priori unknown and has to be determined with the velocity field satisfying the continuity equation. In the present study the SIMPLER algorithm developed by Patankar (1979) was used to calculate the coupled velocities and pressure field.

In the staggered grid system, the arrangement of the velocity and pressure nodes is shown in Figure 3.1. The velocity u on the east side of the control volume is represented, from Eq. (3.26), by

$$u'_e = \hat{u}'_e - d_e(p'_e - p'_c) \tag{3.27}$$

where the pseudo-velocity $\hat{u}'_e$ and the coefficient d_e are defined as

In Cartesian coordinate:

$$\hat{u}'_e = (\sum_{nb=1}^{4} C_{nb} u'_{nb}) \Big|_e + (\frac{Re}{S^* \cdot D \cdot \Delta t'}) \Big|_e u'^{n-1}_e \tag{3.28a}$$

$$d_e = (\frac{Re}{S^* \cdot D \cdot \Delta x'}) \Big|_e \tag{3.28b}$$

In curvilinear coordinate:

$$\hat{u}'_e = (\sum_{nb=1}^{4} C_{nb} u'_{nb} - \frac{1}{S^* \cdot D} \frac{Re}{J} b_1^2 p'_{\zeta'} + \frac{1}{S^* \cdot D}(2g^{12})u'_{\xi'\zeta'}) \Big|_e + (\frac{Re}{S^* \cdot D \cdot \Delta t'}) \Big|_e u'^{n-1}_e \tag{3.29a}$$

$$d_e = (\frac{1}{S^* \cdot D \cdot \Delta \xi'} \frac{Re}{J} b_1^1) \Big|_e \tag{3.29b}$$

Similarly, the velocities at the west, north, and south sides are, respectively

$$u'_w = \hat{u}'_w - d_w(p'_c - p'_w) \tag{3.30a}$$

$$v'_n = \hat{v}'_n - d_n(p'_n - p'_c) \tag{3.30b}$$

$$v'_s = \hat{v}'_s - d_s(p'_c - p'_s) \tag{3.30c}$$

where

In Cartesian coordinate:

$$\hat{u}'_w = (\sum_{nb=1}^{4} C_{nb} u'_{nb})\bigg|_w + (\frac{Re}{S^* \cdot D \cdot \Delta t'})\bigg|_w u'^{n-1}_w \tag{3.31a}$$

$$\hat{v}'_n = (\sum_{nb=1}^{4} C_{nb} v'_{nb})\bigg|_n + (\frac{Re}{S^* \cdot D \cdot \Delta t'})\bigg|_n v'^{n-1}_n \tag{3.31b}$$

$$\hat{v}'_s = (\sum_{nb=1}^{4} C_{nb} v'_{nb})\bigg|_s + (\frac{Re}{S^* \cdot D \cdot \Delta t'})\bigg|_s v'^{n-1}_s \tag{3.31c}$$

$$d_w = (\frac{Re}{S^* \cdot D \cdot \Delta x'})\bigg|_w , \quad d_n = (\frac{Re}{S^* \cdot D \cdot \Delta y'})\bigg|_n , \quad d_s = (\frac{Re}{S^* \cdot D \cdot \Delta y'})\bigg|_s \tag{3.31d}$$

In curvilinear coordinate:

$$\hat{u}'_w = (\sum_{nb=1}^{4} C_{nb} u'_{nb} - \frac{1}{S^* \cdot D} \frac{Re}{J} b_1^2 p'_{\zeta'} + \frac{1}{S^* \cdot D}(2g^{12}) u'_{\xi'\zeta'})\bigg|_w + (\frac{Re}{S^* \cdot D \cdot \Delta t'})\bigg|_w u'^{n-1}_w \tag{3.32a}$$

$$\hat{v}'_n = (\sum_{nb=1}^{4} C_{nb} v'_{nb} - \frac{1}{S^* \cdot D} \frac{Re}{J} b_2^1 p'_{\xi'} + \frac{1}{S^* \cdot D}(2g^{12}) v'_{\xi'\zeta'})\bigg|_n + (\frac{Re}{S^* \cdot D \cdot \Delta t'})\bigg|_n v'^{n-1}_n \tag{3.32b}$$

$$\hat{v}'_s = (\sum_{nb=1}^{4} C_{nb} v'_{nb} - \frac{1}{S^* \cdot D} \frac{Re}{J} b_2^1 p'_{\xi'} + \frac{1}{S^* \cdot D}(2g^{12}) v'_{\xi'\zeta'})\bigg|_s + (\frac{Re}{S^* \cdot D \cdot \Delta t'})\bigg|_s v'^{n-1}_s \tag{3.32c}$$

$$d_w = (\frac{1}{S^* \cdot D \cdot \Delta \xi'} \frac{Re}{J} b_1^1)\bigg|_w , \quad d_n = (\frac{1}{S^* \cdot D \cdot \Delta \zeta'} \frac{Re}{J} b_2^2)\bigg|_n , \quad d_s = (\frac{1}{S^* \cdot D \cdot \Delta \zeta'} \frac{Re}{J} b_2^2)\bigg|_s$$

$$\tag{3.32d}$$

The pressure-gradient terms in the above equations were evaluated using the pressure field at the previous time step or iteration. The continuity equations (2.1) and (2.19) within the element can be discretized as

In Cartesian coordinate:

$$[u'_e - u'_w]\Delta y' + [v'_n - v'_s]\Delta x' = 0 \tag{3.33}$$

In curvilinear coordinate:

$$[(b_1^1 u')_e - (b_1^1 u')_w]\Delta \zeta' + [(b_2^2 v')_n - (b_2^2 v')_s]\Delta \xi' + D_1 = 0 \tag{3.34}$$

where

$$D_1 = [(b_2^1 v')_e - (b_2^1 v')_w]\Delta \zeta' + [(b_1^2 u')_n - (b_1^2 u')_s]\Delta \xi' \tag{3.35}$$

An equation for the pressure is then obtained by substituting Eqs. (3.26), (3.29) through (3.31) into Eq. (3.34) or (3.35), i.e.,

$$a_c p'_c = a_e p'_e + a_w p'_w + a_n p'_n + a_s p'_s - \hat{D} \tag{3.36}$$

where

In Cartesian coordinate:

$$\begin{cases} a_e = d_e \Delta y' \\ a_w = d_w \Delta y' \\ a_n = d_n \Delta y' \\ a_s = d_s \Delta y' \\ a_c = a_e + a_w + a_n + a_s \end{cases} \tag{3.37a}$$

$$\hat{D} = [\hat{u}'_e - \hat{u}'_w]\Delta y' + [\hat{v}'_n - \hat{v}'_s]\Delta x' \tag{3.37b}$$

In curvilinear coordinate:

$$\begin{cases} a_e = b_{1e}^1 d_e \Delta \zeta' \\ a_w = b_{1w}^1 d_w \Delta \zeta' \\ a_n = b_{2n}^2 d_n \Delta \zeta' \\ a_s = b_{2s}^2 d_s \Delta \zeta' \\ a_c = a_e + a_w + a_n + a_s \end{cases} \tag{3.38a}$$

54

$$\hat{D} = [(b_1^1 \hat{u}')_e - (b_1^1 \hat{u}')_w]\Delta\zeta' + [(b_2^2 \hat{v}')_n - (b_2^2 \hat{v}')_s]\Delta\xi' + D_1 \tag{3.38b}$$

Although the guessed pressure field can be updated directly by Eq. (3.36), the updated pressure field probably produces a velocity field which does not satisfy the continuity equation. An iterative procedure is therefore required to correct this erroneous velocity field for achieving more rapid convergence. A velocity-correction formula, similar to that used in the SIMPLE algorithm, is derived. If we denote the dimensionless imperfect velocities and pressure by u^*, v^*, and p^*, respectively, the resulting velocities at the calculated locations are

$$u_e^* = \hat{u}_e^* - d_e(p_e^* - p_p^*) \tag{3.39a}$$

$$u_w^* = \hat{u}_w^* - d_w(p_p^* - p_w^*) \tag{3.39b}$$

$$v_n^* = \hat{v}_n^* - d_n(p_n^* - p_p^*) \tag{3.39c}$$

$$v_s^* = \hat{v}_s^* - d_s(p_p^* - p_s^*) \tag{3.39d}$$

After subtracting these from the exact expressions, i.e. Eqs. (3.26) and (3.30), we obtain

$$u_e' - u_e^* = \hat{u}_e' - \hat{u}_e^* - d_e(\tilde{p}_e - \tilde{p}_c) \tag{3.40a}$$

$$u_w' - u_w^* = \hat{u}_w' - \hat{u}_w^* - d_w(\tilde{p}_c - \tilde{p}_w) \tag{3.40b}$$

$$v_n' - v_n^* = \hat{v}_n' - \hat{v}_n^* - d_n(\tilde{p}_n - \tilde{p}_c) \tag{3.40c}$$

$$v_s' - v_s^* = \hat{v}_s' - \hat{v}_s^* - d_s(\tilde{p}_c - \tilde{p}_s) \tag{3.40d}$$

where $\tilde{p} = p' - p^*$ is the pressure correction, and $(u' - u^*)$ and $(v' - v^*)$ are the corresponding velocity corrections. It is not necessary to retain such a complicated

formulation because both the pressure- and velocity-corrections become trivial when the solution converges. It is possible to omit that part of the velocity-corrections, $\hat{u}' - \hat{u}^*$ and $\hat{v}' - \hat{v}^*$. Patankar (1979) used this critical approximation in his SIMPLER algorithm. With this approximation, the velocity-corrections are expressed as

$$u'_e = u^*_e - d_e(\tilde{p}_e - \tilde{p}_c) \tag{3.41a}$$

$$u'_w = u^*_w - d_w(\tilde{p}_c - \tilde{p}_w) \tag{3.41b}$$

$$v'_n = v^*_n - d_n(\tilde{p}_n - \tilde{p}_c) \tag{3.41c}$$

$$v'_s = v^*_s - d_s(\tilde{p}_c - \tilde{p}_s) \tag{3.41d}$$

As the velocity field satisfying the continuity equation, a pressure-correction equation is obtained

$$a_c\tilde{p}_c = a_e\tilde{p}_e + a_w\tilde{p}_w + a_n\tilde{p}_n + a_s\tilde{p}_s - D^* \tag{3.42}$$

where

In Cartesian coordinate:

$$D^* = [u^*_e - u^*_w]\Delta y' + [v^*_n - v^*_s]\Delta x' \tag{3.43}$$

In curvilinear coordinate:

$$D^* = [(b^1_1 u^*)_e - (b^1_1 u^*)_w]\Delta\zeta' + [(b^2_2 v^*)_n - (b^2_2 v^*)_s]\Delta\xi' + D_1 \tag{3.44}$$

and the coefficients a_e, a_w, a_n, a_s, and a_c are exactly the same as those in equation (3.36). After the pressure correction is obtained by equation (3.42), we substituted it into Eq. (3.41) to update the velocity field, which are used in Eq. (3.36) to renew the pressure

field. This procedure repeated until the convergent condition $\left\| \varphi - \varphi^* \right\|_\infty < 10^{-4}$ was satisfied, where $\left\| \cdot \right\|_\infty$ denotes the infinite norm.

3.4 Free surface boundary

A difficult aspect of flow problems with a free surface is the accurate location of the free surface, which forms an integral part of the solution. The boundary conditions that must be satisfied at the free surface are the kinematic and the dynamic free surface boundary conditions. The former condition is used to determine the location of the free surface after the velocity components are obtained. In addition to the free surface location, there are three remaining unknowns: the velocity components u' and v' and the pressure p'; while there are only two remaining boundary conditions, namely, the dynamic free surface boundary conditions in the normal and tangential directions. To obtain a unique solution of the problem, one more condition is inevitable. The additional condition is the equation of continuity, which requires the conservation of mass everywhere in the flow domain.

In the present model, the SUMMAC method was used to deal with the free surface boundary. The major concept underlying this method is the use of marker particles to identify the location of the free surface. By tracking the positions of these marked particles, the transient location of the free surface can be determined, namely

$$x_k^n = x_k^{n-1} + u_k \Delta t \,; \;\; y_k^n = y_k^{n-1} + v_k \Delta t \tag{3.45}$$

where the subscript k denotes the k-th marked particle on the free surface.

For the curvilinear coordinate, the afore-mentioned method has to be changed as following.   Consider an element with points 1, 2, 3, 4 and a marker M located within it, as shown in Figure 3.3.   A weighting coefficient $\tilde{A}_i$ is equal to the weighting area of the point i.   The Cartesian velocity can be evaluated at the points 1, 2, 3, and 4 in the computational domain.   The contravariant velocity $(\tilde{u}', \tilde{v}')$ must be evaluated in these points in order to find the successive position of the free surface.   The transform formulas between Cartesian velocities and contravariant velocities are

$$\tilde{u}' = u'\xi'_{x'} + v'\xi'_{y'} = \frac{b_1^1}{J}u' + \frac{b_2^1}{J}v' \tag{3.46a}$$

$$\tilde{v}' = u'\zeta'_{x'} + v'\zeta'_{y'} = \frac{b_1^2}{J}u' + \frac{b_2^2}{J}v' \tag{3.46b}$$
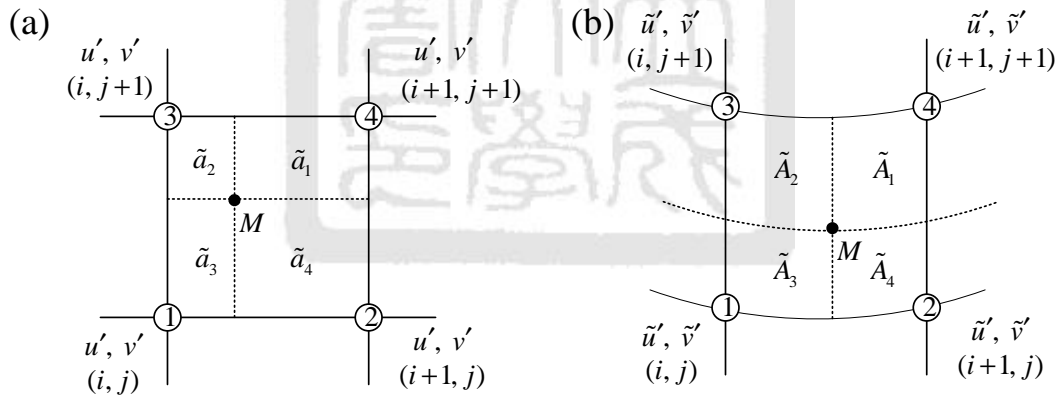
Figure 3.3: Marker M in the Cartesian coordinate system and the curvilinear coordinate system with the surrounding points and the weighting areas.

When the contravariant velocities at points 1 to 4 are known, the contravariant velocity at the marker M can be evaluated by interpolation.

$$\tilde{u}'^n_M = \left(\tilde{u}'^n_{i,j}\tilde{A}_1^n + \tilde{u}'^n_{i+1,j}\tilde{A}_2^n + \tilde{u}'^n_{i+1,j+1}\tilde{A}_3'^n + \tilde{u}'^n_{i,j+1}\tilde{A}_4^n \right) \Big/ \left(\tilde{A}_1^n + \tilde{A}_2^n + \tilde{A}_3^n + \tilde{A}_4^n \right) \tag{3.47a}$$

$$\tilde{v}'^n_p = \left(\tilde{v}'^n_{i,j} \tilde{A}^n_1 + \tilde{v}'^n_{i+1,j} \tilde{A}^n_2 + \tilde{v}'^n_{i+1,j+1} \tilde{A}^n_3 + \tilde{v}'^n_{i,j+1} \tilde{A}^n_4 \right) / \left(\tilde{A}^n_1 + \tilde{A}^n_2 + \tilde{A}^n_3 + \tilde{A}^n_4 \right) \tag{3.47b}$$

Where the subscript M denotes the variables were at the marked location M.

Thus the new free surface in the curvilinear coordinate system (ξ, ζ) can be calculated by

$$\xi'^{n+1}_M = \xi'^n_M + \tilde{u}'^n_M \Delta t \tag{3.48a}$$

$$\zeta'^{n+1}_M = \zeta'^n_M + \tilde{v}'^n_M \Delta t' \tag{3.48b}$$

The new location $(\xi'^{n+1}_p, \zeta'^{n+1}_p)$ of the marker M are certainly located with an element in the Cartesian coordinate system and surrounded by the four points $\left(\xi'_{i,j}, \zeta'_{i,j} \right)$, $\left(\xi'_{i+1,j}, \zeta'_{i+1,j} \right)$, $\left(\xi'_{i+1,j+1}, \zeta'_{i+1,j+1} \right)$, and $\left(\xi'_{i,j+1}, \zeta'_{i,j+1} \right)$. In the Cartesian coordinate system, the four weighting areas, as shown in Figure 3.3(b), are $\tilde{a}^{n+1}_1$, $\tilde{a}^{n+1}_2$, $\tilde{a}^{n+1}_3$, and $\tilde{a}^{n+1}_4$, respectively. Hence, the location of the marker M in the Cartesian coordinate system is calculated by

$$x'^{n+1}_M = \frac{\left(x'^{n+1}_{i,j} \tilde{a}^{n+1}_1 + x'^{n+1}_{i+1,j} \tilde{a}^{n+1}_2 + x'^{n+1}_{i+1,j+1} \tilde{a}^{n+1}_3 + x'^{n+1}_{i,j+1} \tilde{a}^{n+1}_4 \right)}{\left(\tilde{a}^{n+1}_1 + \tilde{a}^{n+1}_2 + \tilde{a}^{n+1}_3 + \tilde{a}^{n+1}_4 \right)} \tag{3.49a}$$

$$y'^{n+1}_M = \frac{\left(y'^{n+1}_{i,j} \tilde{a}^{n+1}_1 + y'^{n+1}_{i+1,j} a'^{n+1}_2 + y'^{n+1}_{i+1,j+1} \tilde{a}^{n+1}_3 + y'^{n+1}_{i,j+1} \tilde{a}^{n+1}_4 \right)}{\left(\tilde{a}^{n+1}_1 + \tilde{a}^{n+1}_2 + \tilde{a}^{n+1}_3 + \tilde{a}^{n+1}_4 \right)} \tag{3.49b}$$

The pressure at the free surface is calculated by the normal dynamic free surface boundary condition [equation (2.12) or (2.27)] with the known velocities u' and v'. By means of the tangential dynamic boundary condition [equation (2.13) or (2.28)], the velocity component u' on the free surface is calculated from the velocity of the main body of the fluid. By choosing a simple control volume beneath the free surface, as

shown in Figure 3.4, the vertical velocity v_2' can be calculated by the discretized continuity equation as follows.

$$\frac{u_2' - u_1'}{\Delta x'} + \frac{v_2' - v_1'}{\Delta y'} = 0 \tag{3.50}$$

In Figure 3.4, the velocity components u_1' and u_2' were interpolated from the known-neighboring horizontal velocities, $u_{i,j}'$ and $u_{i+1,j}'$ as well as $u_{i+1,j+1}'$, and $u_{i,j+1}'$ respectively. The velocity components u_k' and v_k' of the k-th marked particle were then interpolated from the neighboring velocities u' and v' as in the SUMMAC method. A method (Chan and Street, 1970), which satisfies the discretized Poisson equation for the pressure, called "irregular star" was applied to determine the pressure at the element near the free surface.
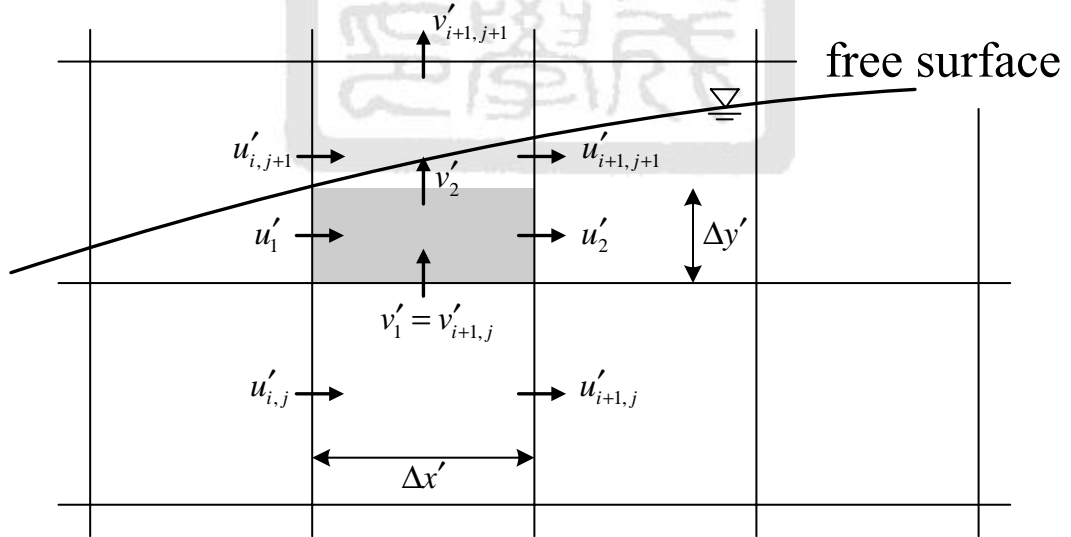
Figure 3.4: A simple control volume (shaded area) beneath free surface.

If strict no-slip boundary condition were held on the contact point of the free surface

on the wavemaker, the free surface on the wavemaker will be unmovable and be against physical flow motion. For overcoming this deviation, the no-slip boundary condition at the wavemaker is released at two nodal points beneath the free surface. The slip velocities v along the wavemaker are extrapolated from the flow inside the domain (Tang et al., 1990).

3.5 Numerical sponge layer

A numerical sponge layer (Ohyama, 1991) was used for eliminating wave energies. An artificial viscous term was added as energy damper in the momentum equations, i.e. equations (2.2) and (2.3), and of the following form:

$$\frac{\partial u'}{\partial t'}+u'\frac{\partial u'}{\partial x'}+v'\frac{\partial u'}{\partial y'}=-\frac{\partial p'}{\partial x'}+\frac{1}{Re}(\frac{\partial^2 u'}{\partial x'^2}+\frac{\partial^2 u'}{\partial y'^2})-\frac{1}{Re_s}u' \tag{3.51a}$$

$$\frac{\partial v'}{\partial t'}+u'\frac{\partial v'}{\partial x'}+v'\frac{\partial v'}{\partial y'}=-\frac{\partial p'}{\partial y'}+\frac{1}{Re}(\frac{\partial^2 v'}{\partial x'^2}+\frac{\partial^2 v'}{\partial y'^2})-\frac{1}{Re_s}v' \tag{3.51b}$$

where $Re_s=\rho u_p h_o/\mu_s$ and μ_s the damping factor of sponge layer, which should change smoothly along onshore direction to avoid sudden disturbance in the numerical domain. Normally, three kinds of function were used to perform the smooth change of the damping factor: rational, cosine and exponential function. According to Troch and Rouck (1998), using cosine function has the smallest reflected coefficient over the three. Such that, the cosine function was used to connect $\mu_s=0$ and $\mu_s=\mu_{s\max}$ smoothly and has the following form.

$$\mu_s = \begin{cases} 0 & , \ x < x_{s1} \\ 0.5\left(1-\cos\left(\dfrac{\pi}{x_s}(x-x_{s1})\right)\right)\mu_{s\max}, & x_{s1} < x < x_{s2} \\ \mu_{s\max} & , \ x > x_{s2} \end{cases} \qquad (3.52)$$

Note that the damping factor μ_s varies within the region $\left[x_{s1}, \ x_{s2}\right]$ with the width x_s.

The deployment of the sponge layer was shown in Figure 2.1.

To examine the efficiency of the sponge layer, Fig. 2 compares the surface elevation

of the random waves with the peak-spectral period, $T_p = 1.6 \text{ s}$, significant wave height

$H_{1/3} = 1 \text{ cm}$, time duration $T_R = 16 \text{ s}$, and still water depth $h_o = 20 \text{ cm}$ produced in the

numerical wave tank with and without the numerical sponge layer. When there is no

sponge layer deployed, the numerical wave flume was simply extent so far that the waves

will not touch the downstream boundary of the flume and no waves are reflected. In

Figure 3.5, the surface elevation η is normalized to the significant wave height $H_{1/3}$ and

the time is normalized to T_p. The results illustrated in Figure 3.5 indicate that no waves

were reflected from the sponge layer. Hence, in this study, the numerical sponge layer, or

so-called numerical beach was deployed to avoid the wave reflection from the downstream

boundary.
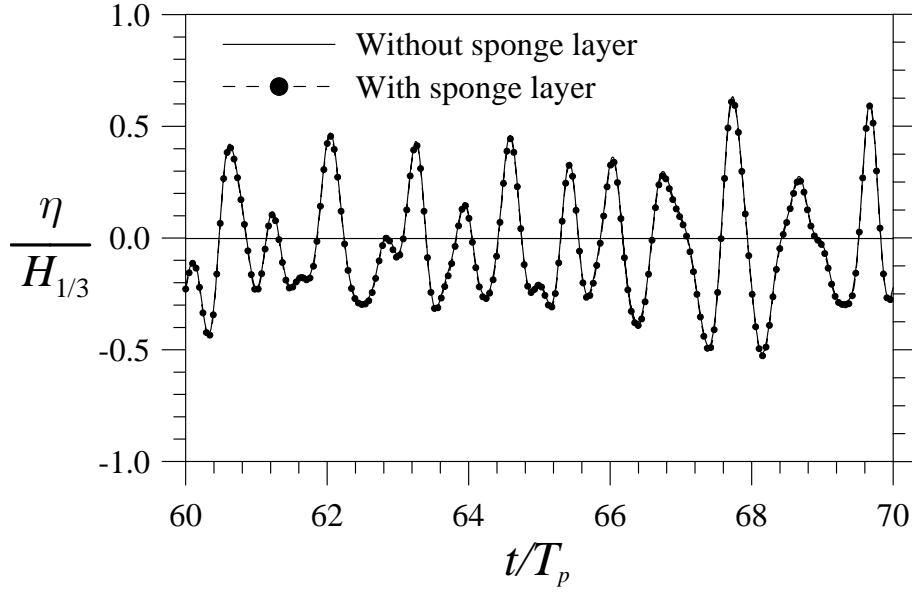
Figure 3.5: An irregular-wave train with peak-spectral period $T_p = 1.6\,\text{s}$, significant wave height $H_{1/3} = 1\,\text{cm}$, time duration $T_R = 16\,\text{s}$, and still water depth $h_o = 20\,\text{cm}$ in the numerical wave flume with (dot line and solid circle) and without (solid line) the numerical sponge layer.

While the case without sponge layer was taken as a pure incident irregular wave, the attenuation of spectral energy within the sponge layer can be quantified and shown in Figure 3.6. Comparing with the normalized damping factor $\mu_s / \mu_{s\max}$, the spectral energy is found approximately zero before the damping factor reaches its maximum, although it costs about $3L_p$ to have this results. In this case, the associated parameters of the sponge layer are $Re_s = 21.46$ and $x_s = 3.77L_p$. For assuring a robust non-reflected downstream boundary, the sponge layer was given as $\mu_{s\max}\sqrt{h_o / g} = 0.04$, $x_s \approx 4L_p$, and the length longer than $5L_p$ in subsequent computations.
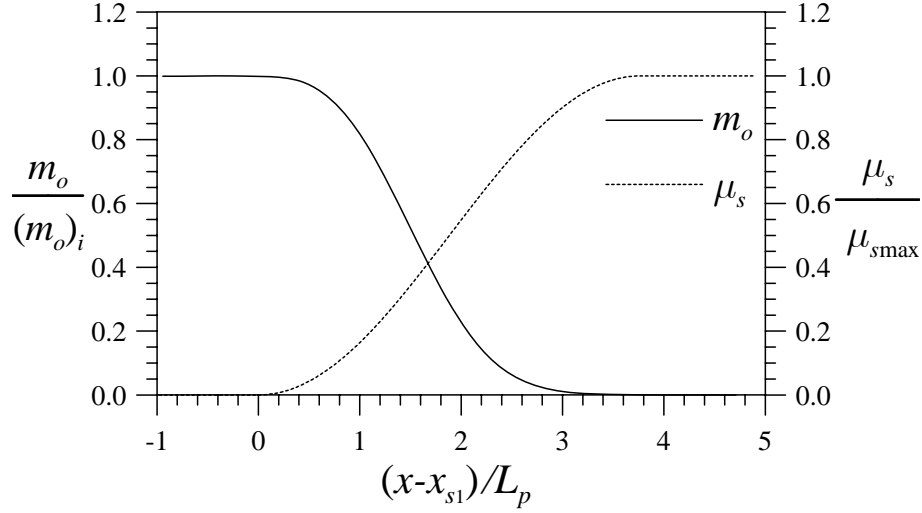
Figure 3.6: The attenuation of spectral energy within the sponge layer, which has the parameters: $Re_s = 21.46$, $x_s = 3.77L_p$. The case without the numerical sponge layer was chosen as the incident irregular wave.

3.6   Calculating of shear stress

Shear stress is studied in the present in present work, and can be obtained using numerical implement.   The shear stress is defined as following.

$$\tau_{j+1/2} = \mu(u_{j+1} - u_j)/\Delta y_j \quad \text{at} \quad y = y_{j+1/2} \quad \text{for} \quad j = 1, 2, 3 \tag{3.63}$$

where Δy_j is the distance of y_j and y_{j+1}, which is the location of the horizontal velocities, and $y_o = 0$ m is located on the bed boundary.   However, the results $\tau_{1/2}$ has a distance $y_{1/2}$ from the bed, and an extrapolation method, the spline function in the Matlab toolbox, was used to obtain the bed shear stress τ_o.   Consequently, the results is strongly dominated by the grid resolution along y-axis.   In the present study, the near-bed vertical grid size Δy_o is set to be $\delta_p/16$, where δ_p is the spectral-peak Stokes layer thickness, i.e. $\delta_p = \sqrt{\upsilon/\omega_p}$ with the spectral-peak angular frequency ω_p.

3.7 The solution procedure

The complete solution procedure of the present method is summarized in Figure 3.7.

Program Start

Assign the initial conditions and boundary conditions

Calculate the FA coefficients

Solve the momentum equations to have u^*, v^*, D^*

Solve the pressure-correction equation to obtain p'

Use the velocity-correction formula to correct the velocity u', v'

Calculate the velocity u', v' at the free surface

No

Calculate the u', v'

Next time step

Solve the pressure equation to have the pressure p'

If the absolute error smaller than 10^{-4}

Yes

Calculate the locations of free surface and the wavemaker

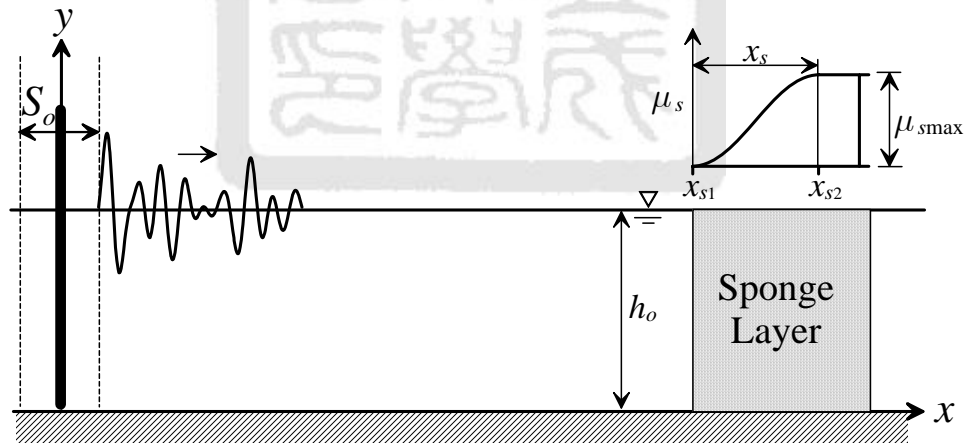Program End while all time steps are done

Figure 3.7: The solution procedure.

Chapter 4 Linear irregular waves and the associated properties

"A theory is something nobody believes, except the person who made it. An experiment is something everybody believes, except the person who made it."

—Albert Einstein,
German-born theoretical physicist

Figure 4.1: Numerical wave flume with a piston-type wavemaker and a sponge layer for generating irregular waves.

A schematic diagram of a two-dimensional numerical wave flume for generating irregular waves is shown in Figure 4.1. The x-axis is measured horizontally in the

direction of wave propagation and the origin is set at the initial location of a piston-type wave generator with stroke S_o. The y-axis is measured vertically upwards from bottom. The still water depth is h_o.

4.1 Generation of irregular waves

In the present work, the deterministic spectral amplitude method based on the fast Fourier transform (DSA-FFT) was applied to generate irregular waves. Simulation of a time sequence $\eta(t)$ requires the independent time variable t, to be discretized as $t_n = n\Delta t$ $(n = 0,1,2,...)$, where Δt is the time interval. This discrete time sequence $\eta(t_n)$ represents a continuous time series of water surface elevation with a total record length of T_R, and a total number of discrete values N, which satisfies

$$N = T_R / \Delta t \tag{4.1}$$

The reciprocal of Δt is the sampling frequency $f_s = 1/\Delta t$, and $f_c = 1/(2\Delta t)$ is the cut-off (Nyquist) frequency. The discrete Fourier transform pair is defined as

$$A_k = \sum_{n=0}^{N-1} \eta(t_n) e^{-i2\pi nk/N}, \quad k = 0,1,2,...,N-1 \tag{4.2}$$

$$\eta(t_n) = \frac{1}{N} \sum_{k=0}^{N-1} A_k e^{i2\pi nk/N}, \quad n = 0, 1, 2,..., N-1 \tag{4.3}$$

where $i = \sqrt{-1}$ and A_k is the discrete Fourier transform of $\eta(t_n)$ or the k-th Fourier component. The frequency interval between any two successive frequencies is

$$\Delta f = f_k - f_{k-1} = 1/T_R \tag{4.4}$$

For the identical frequency interval, this method can be identified as equal-frequency

superposition method.

   When the target wave spectral density S_η of surface elevation is specified, the k-th Fourier component of the real time series $\eta(t)$ can be represented by a complex variable A_k ($k = 0, 1, ..., N/2 - 1$) with an amplitude of $\sqrt{S_\eta(f_k)\Delta f / 2}$, a phase of ϕ_k and $A_k = A_{N-k}^*$ ($k = N/2, N/2+1, ..., N-1$), where the superscript asterisk means complex conjugate.   The phase ϕ_k ($k = 0, 1, ..., N-1$) are independent random variables, distributed uniformly over the interval $[0, 2\pi]$.   The time sequence of the surface elevation was then determined by applying the inverse Fourier transform to A_k, as indicated in Eq. (4.2).   Alternatively, with the known amplitude of each Fourier component, the surface elevation of linear irregular waves can be superposed by $N/2$ components of discrete waves as follows.

$$\eta(t) = \sum_{k=0}^{N/2-1} a_k \cos(\omega_k t - \phi_k) \tag{4.5}$$

$$a_k = 2|A_k| = \sqrt{2S_\eta(f_k)\Delta f} \tag{4.6}$$

where $\omega_k = 2\pi f_k$ is the discrete angular frequency.   Thus, wave synthesis of any duration can be performed without leakage.   However, this limitation is inefficient in the present numerical model for irregular wave generation.   In ocean engineering practice, the cut-off frequency is generally less than 1 Hz (Medina et al., 1985).   In the numerical simulation, for the sake of accuracy, the time marching steps are typically $10^{-3} \sim 10^{-4}$ seconds, and the cut-off frequency can be up to $5\times10^2 \sim 5\times10^3$ Hz.   If the duration of wave synthesis is 1000 s, then 5×10^5 wave components are required, given $\Delta t = 10^{-3}$ s.   Since waves with frequencies of over 1 Hz seem to be redundant in reality, for simplicity,

wave components with frequencies higher than 4 Hz are neglected in the numerical model of irregular wave generations.

When the wave components are known,

$$\eta_k(x,t) = a_k \cos(k_k x - \omega_k t + \phi_k)$$ (4.7)

the displacement function of a piston-type wavemaker used to generate this wave is determined using linear wavemaker theory, as follows (Dean and Dalrymple, 1984).

$$\xi_k(t) = e_k \sin(\omega_k t - \phi_k)$$ (4.8)

with $e_k = a_k \dfrac{\sinh 2k_k h_o + 2k_k h_o}{2(\cosh 2k_k h_o - 1)}$ (4.9)

where $e_k = S_k/2$ and S_k is the stroke of the wavemaker for generating the k-th wave component. The displacement function of the wavemaker used to generate irregular waves is then obtained by linearly superposing the displacements to generate the k-th wave component as follows.

$$\xi(t) = \sum_{k=0}^{N/2-1} \xi_k(t) = \sum_{k=0}^{N/2-1} e_k \sin(\omega_k t - \phi_k)$$ (4.10)

The Goda-JONSWAP spectral density (Goda, 1988) was chosen as the target wave spectrum, and is given by

$$S_\eta(f) = \beta H_{1/3}^2 T_p^{-4} f^{-5} \exp[-1.25(T_p f)^{-4}] \gamma^{\exp[-(T_p f - 1)^2/2\alpha^2]}$$ (4.11)

$$\alpha = \begin{cases} 0.07, \ for \ f \le f_p \\ 0.09, \ for \ f > f_p \end{cases}$$ (4.12)

$$\beta = \frac{0.06238 \times (1.094 - 0.01915 \ln \gamma)}{0.230 + 0.0336\gamma - 0.185(1.9 + \gamma)^{-1}}$$ (4.13)

where $T_p = 1/f_p$, f_p is the peak-spectral frequency; $H_{1/3}$ the significant wave height

assigned initially, and γ is the peak enhancement factor, which usually varies between 1 and 10.

4.2 Transfer function between shear stress and surface elevation

Since the surface elevation of irregular waves can be constructed by superposing linear waves of various wave heights and frequencies, the shear stress exerted on the bottom by irregular waves can be synthesized similarly. The shear stress on the bottom is $\tau = \mu(\partial u / \partial y)$, at $y = 0$. The horizontal velocity within the boundary layer under linear waves with surface elevation $\eta = a\cos(kx - \omega t)$ is (Dean and Dalrymple, 1984)

$$u = \frac{\omega a}{\sinh kh_o}\left[1 - e^{-(1-i)\,y\sqrt{\omega/2\upsilon}}\right]e^{i(kx-\omega t)} \tag{4.14}$$

where $y = 0$ is set at the bottom. The shear stress on the bottom is then

$$
\begin{aligned}
\tau|_{y=0} &= \operatorname{Re}\left[\mu\frac{\omega a}{\sinh kh_o}(1-i)\sqrt{\frac{\omega}{2\upsilon}}e^{i(kx-\omega t)}\right] \\
&= \frac{\mu\omega a}{\sinh kh_o}\sqrt{\frac{\omega}{\upsilon}}\cos(kx - \omega t - \frac{\pi}{4}) \\
&= \frac{\mu\omega}{\sinh kh_o}\sqrt{\frac{\omega}{\upsilon}}\eta(x, t + \frac{\pi}{4\omega})
\end{aligned}
\tag{4.15}
$$

Equation (4.15) reveals that a phase shift exits between the shear stress and the water surface elevation and that the shear stress can be directly obtained from the surface elevation by multiplying it by the term $\sqrt{\omega/\upsilon}\mu\omega/\sinh kh_o$. This term represents the transfer function or the response function between the shear stress and the surface elevation and equals the square root of the ratio between the shear stress spectrum and the

wave spectrum (Samad et al., 1998);

$$H_\tau(\omega) = \sqrt{\frac{S_\tau(\omega)}{S_\eta(\omega)}} = \frac{\mu\omega}{\sinh kh_o}\sqrt{\frac{\omega}{\upsilon}} \qquad (4.16)$$

The angular frequency and the wavenumber follow the dispersion relations, $\omega^2 = gk \tanh kh_o$.

Incident irregular waves of uniform spectral density (a Gaussian white noise) were generated and propagated in the numerical wave flume at a still water depth $h_o = 40$ cm to confirm that the shear stress under irregular waves, computed by this numerical wave model, is correct. The wave height of each wave component is $H = 2.683 \times 10^{-2}$ cm.

The numerical results obtained by $\sqrt{S_\tau/S_\eta}$ were compared with the theoretical one and shown in Figure 4.2. The comparison reveals that the numerical results are identical to the theoretical values. Experiments carried out by Samad et al. (1998) are compared and shown in Figure 4.2(b). The experimental results have good agreement while the frequency is larger than unit hertz. When the frequency is smaller than unit hertz, the discrepancy of the experiments are shown and indicates there is still difficult for measuring bottom shear stress using experiment.
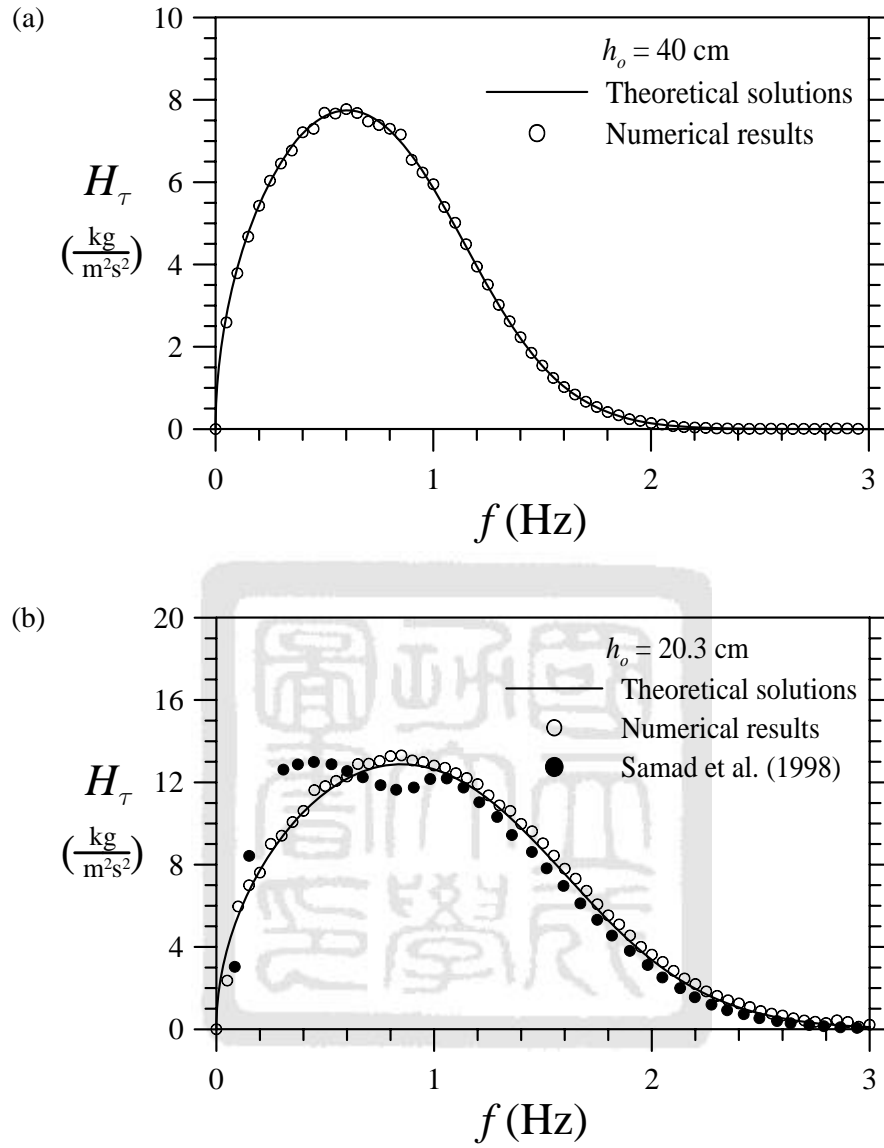
Figure 4.2: The numerical results and theoretical transfer function between the shear stress and the surface elevation: (a) the case with $h_o = 40$ cm; (b) the case with $h_o = 20.3$ cm and comparing with the experiments of Samad et al. (1998).
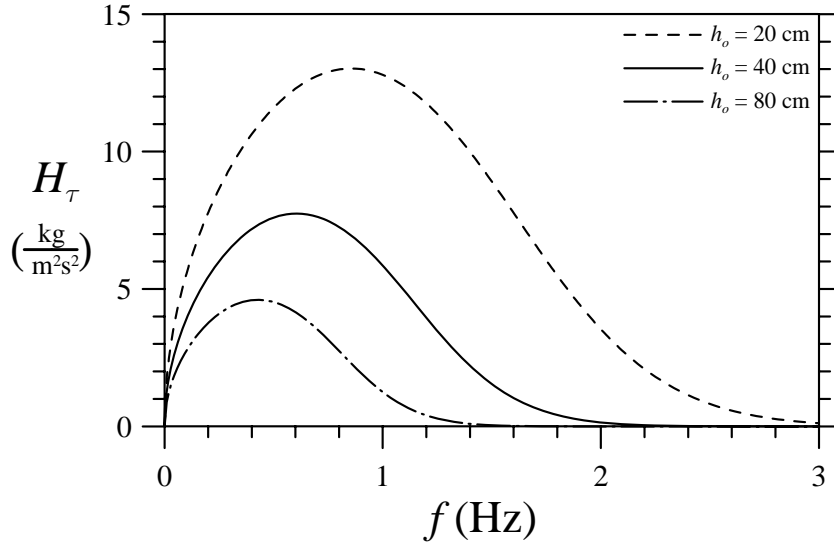
Figure 4.3: Variation of transfer functions with depth of still water.

Figure 4.3 plots the variation of the transfer function $H_\tau(f)$ as a function of the still water depth. It shows that the main responsible frequency band shifts to a lower frequency as the water depth increases. The spectral-peak frequencies of the transfer function are 0.8521 Hz, 0.6015 Hz, and 0.4311 Hz for still water depths of $h_o = 20$ cm, 40 cm and 80 cm, respectively.

4.3 Relation between wave and shear stress spectra

The accuracy of the numerical scheme was confirmed by comparing the wave spectrum of the simulated irregular waves with the target wave spectrum. After the accuracy of this wave model was verified, the wave spectra and the associated shear stress spectra were discussed with reference to the spectral frequency, the zeroth moment and the spectral bandwidth parameter.

**Table 4.1:** Numerical conditions of simulated irregular waves.

Case	T_R	h_o	$H_{1/3}$	f_p	γ	Ur_s
	(s)	(cm)	(cm)	(Hz)		
4.1	128	40	1.0	0.625	1.0	1.257
4.2	128	40	1.0	0.500	1.0	2.133
4.3	128	40	1.0	0.800	1.0	0.658
4.4	128	40	1.0	1.000	1.0	0.335
4.5	128	20	1.0	0.625	1.0	5.635
4.6	128	80	1.0	0.625	1.0	0.246
4.7	128	40	1.0	0.625	3.3	1.257
4.8	128	40	1.0	0.625	7.0	1.257
4.9	256	40	1.0	0.625	1.0	1.257

Table 4.1 presents the numerical conditions studied in this work. The characteristics of irregular waves were specified in terms of duration T_R, the significant wave height $H_{1/3}$, the peak spectral frequency f_p and the peak enhancement factor γ. The significant Ursell number, which is often used to judge the nonlinearity of regular waves, is defined as

$$Ur_s = H_{1/3}L_p^2 / h_o^3 \tag{4.17}$$

where L_p $(=2\pi/k_p)$ is the peak-spectral wavelength and can be determined from the dispersion relation.

Figure 4.4 shows an excellent agreement between the simulated wave spectrum and the target wave spectrum in Case 4.1. The target spectrum is the Goda-JONSWAP spectrum, which is described by Eq. (4.11). The spectral density is normalized by the zeroth spectral moment $m_{o\eta}$, which will be presented in the following section.
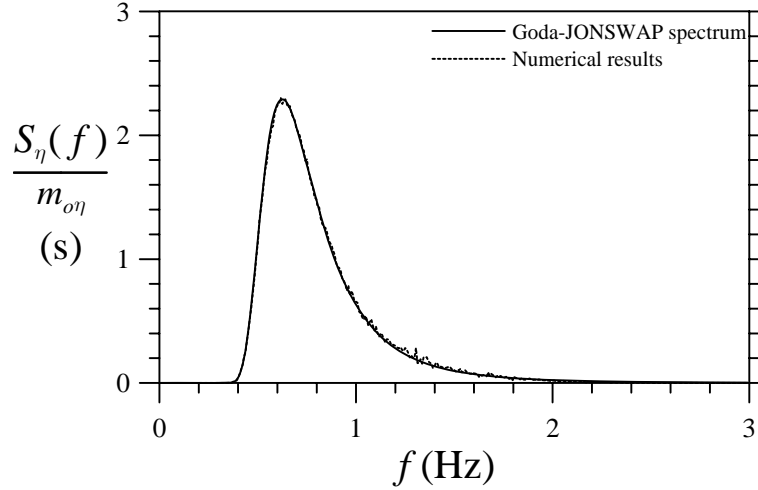
Figure 4.4: Comparison of spectrum of simulated waves and target wave spectrum in Case 4.1.

Since this wave model takes into account the viscosity of the fluid, the viscous flow fields and the bottom shear stress can be determined. Dong and Huang (2004) demonstrated the accuracy of this wave model by comparing the numerical results for wave and velocity profiles, including those in the bottom boundary layer, with the analytical solutions. Figures 4.5(a) and 4.5(b) present the temporal variation of surface elevation at $x/h_o = 10$ and the horizontal velocity profiles near the bottom at different wave phases, respectively, to elucidate viscous flows induced by the irregular waves in Case 4.1. The significant bottom velocity U_s was calculated by the definition of the significant property, say $U_s = 4m_{ou}^{1/2}$, where m_{ou} is the zeroth spectral moment of bed orbital velocity.
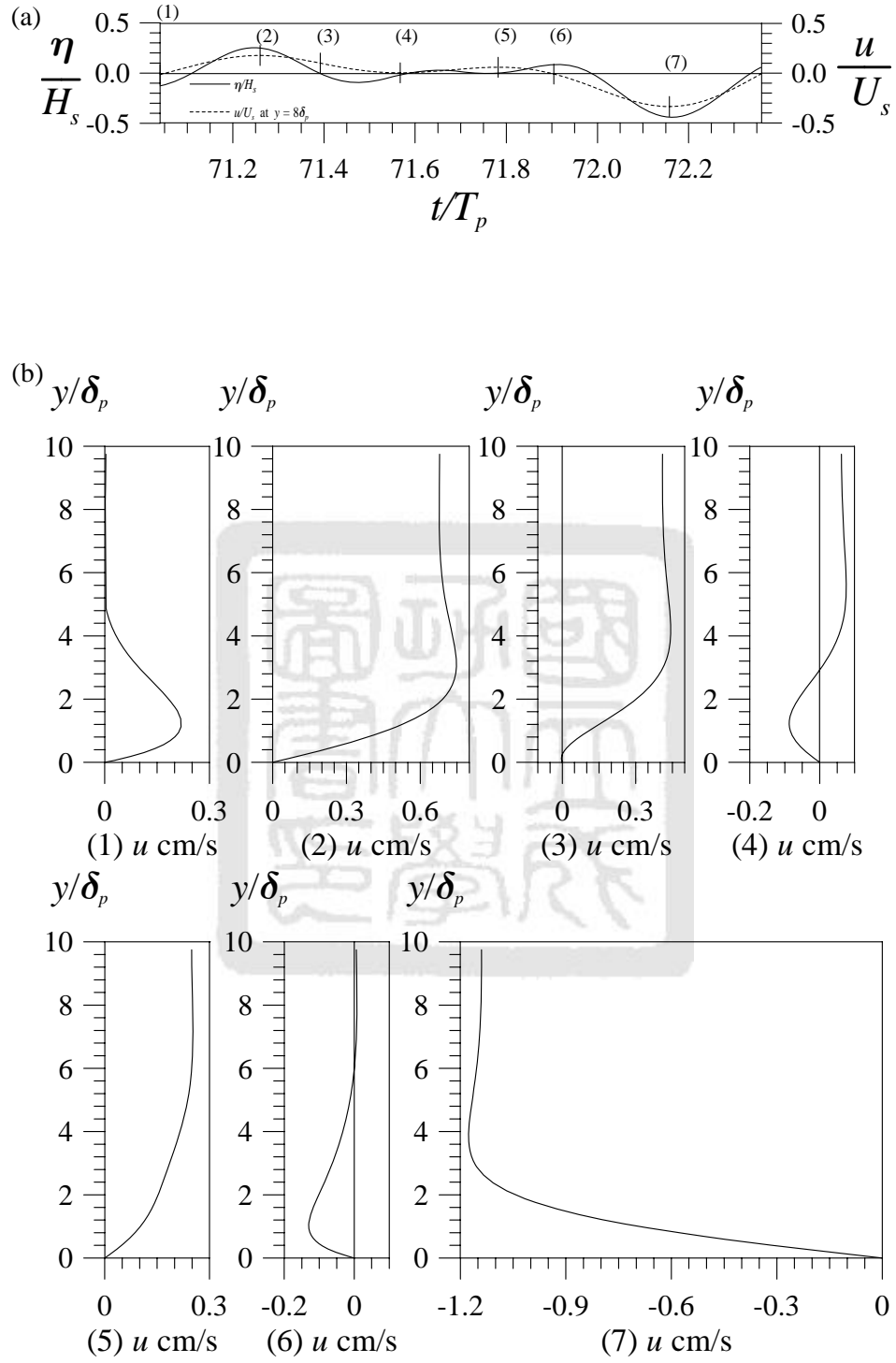
Figure 4.5: (a) Temporal variation of surface elevation at $x/h_o = 10$ and (b) horizontal velocity profile near the bottom at different wave phases of irregular waves in Case 4.1 ($\delta_p = 5.064 \times 10^{-4}$ m).
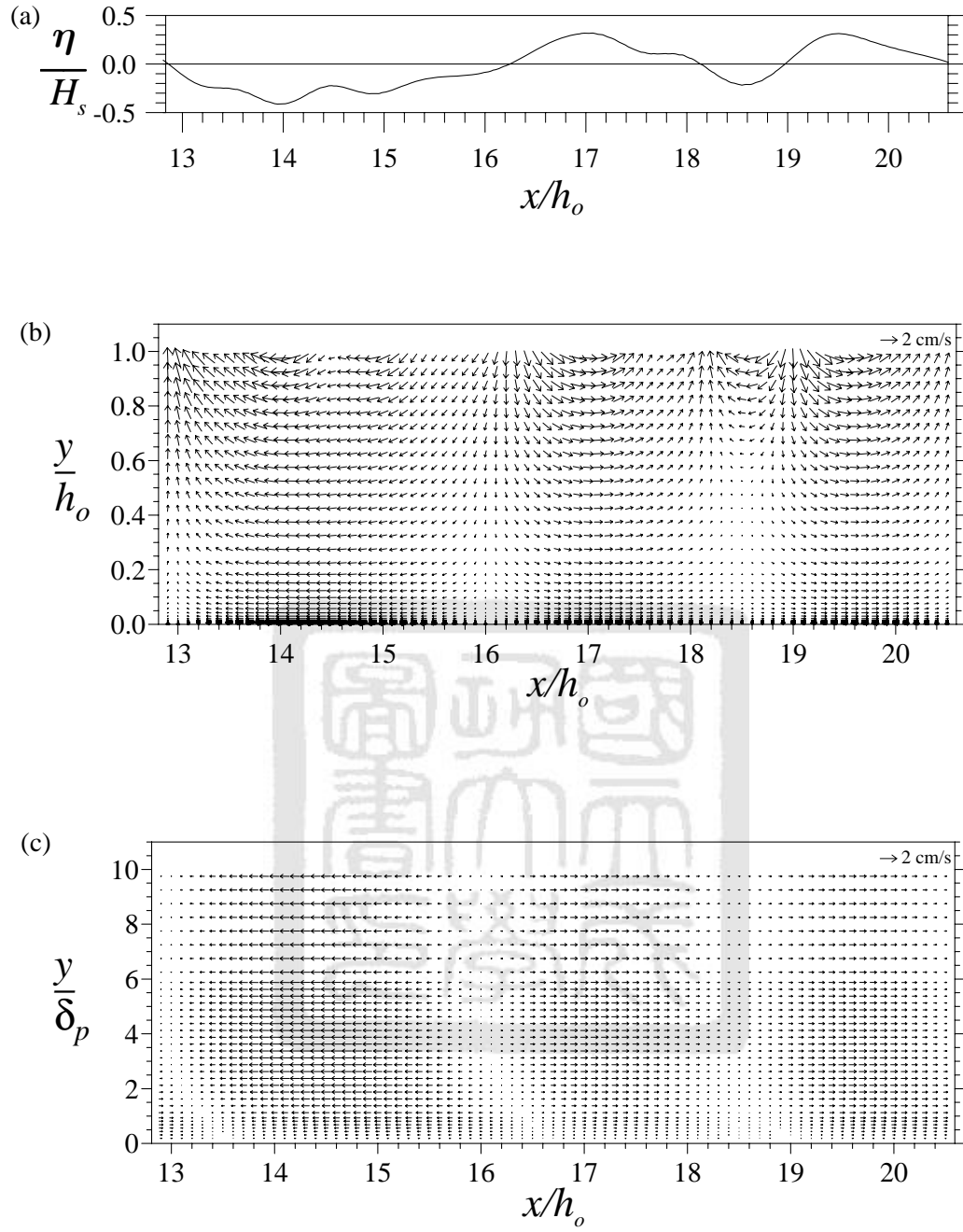
Figure 4.6: (a) Water surface elevation, (b) velocity fields throughout the depth and (c) near the bottom beneath two zero-downcrossing waves induced by the irregular waves in Case 4.1.

Figure 4.6 plots the corresponding water surface elevation and velocity fields throughout the depth and near the bottom beneath two zero-upcrossing waves. Figure 4.5(a) also plots the temporal variation of the horizontal velocity component at $y/\delta_p = 8$, where is far from the boundary layer and the velocity can be regarded as the free stream velocity. Figure 4.5 reveals that the wave phase (1) with negative surface elevation induces a zero horizontal velocity beyond the boundary layer, instead of a negative horizontal velocity component, as for small-amplitude waves or Stokes waves (Dong and Huang, 2004). Similarly, at the wave phase (3) with zero water elevation, a rather large positive horizontal velocity component instead of a zero horizontal velocity, was induced, because, although the higher frequency components are manifest in the wave profile, their effect does not reach close enough to the bottom. Near the bottom, the velocities induced by the low-frequency components cover those induced by the higher-frequency components. Accordingly, the wave components with very low frequencies dominated the flow behavior near the bottom. Figure 4.6 also displays this phenomenon. The negative surface elevation of a high-frequency component, located between $x/h_o = 18.2$ and 19.0 in Figure 4.6(a), is responsible for the negative horizontal velocity only to a certain depth, as shown in Figures. 4.6(b) and 4.6(c). Below that depth, a positive velocity component exists, which is associated with other waves of lower frequencies. Figure 4.5(b) reveals also that the thickness of the boundary layer is about $6\delta_p$, if the thickness of the boundary layer is defined as the location where the flow velocity approaches 1.01 times the potential flow velocity of the spectral peak frequency. Based on this definition, the thickness of the boundary layer for regular waves is about 4δ

($\delta = \sqrt{v/\omega}$) (Dong and Huang, 2004).   Figure 4.7 compares the wave spectrum with the shear stress spectrum for irregular waves in Case 4.1.   It shows that the spectral width of the shear stress spectrum is less than that of the wave spectrum and that the peak frequency of the shear stress spectrum is slightly lower than that of the wave spectrum.
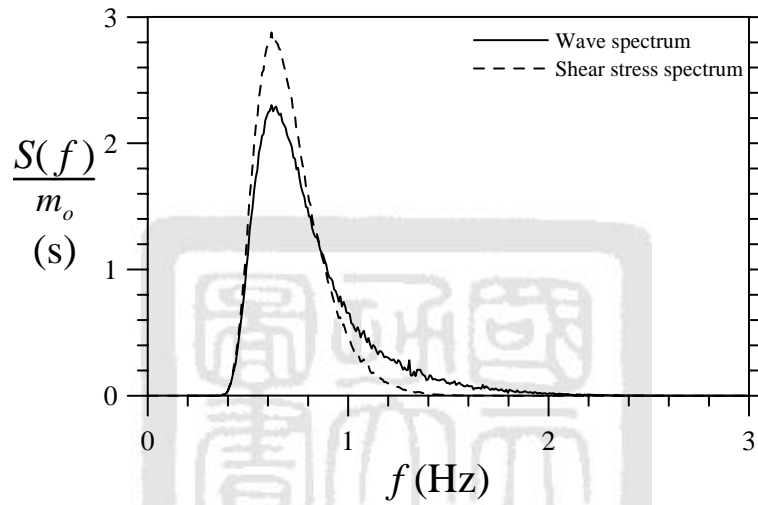
Figure 4.7: Comparison of wave spectrum and shear stress spectrum for irregular waves in Case 4.1.

4.4 Wavelet transform and effects of different spectral parameters

The wavelet transform is also applied to yield a full time-frequency representation of the random water surface elevation and the associated shear stress.   The wavelet transform allows localization in the time domain via translations of the so-called mother wavelet and in the frequency domain via dilations.   Massel (2001) and Huang (2002) and several others successfully applied it to the analysis of wave data.   The wavelet

transform of a time series $f(t)$ is defined as

$$Wf(t_w, s_w) = \int_{-\infty}^{\infty} f(t)\psi_{t_w, s_w}^*(t)dt = \int_{-\infty}^{\infty} f(t)\frac{1}{\sqrt{s_w}}\psi^*(\frac{t-t_w}{s_w})dt \qquad (4.18)$$

where ψ^* is the complex conjugate of the mother wavelet ψ; t_w is the time translating range and s_w is the dilation scale. One of the most often used mother wavelets is the Morlet wavelet, which is given by

$$\psi(t) = \exp(-t^2/2)\exp(i\omega_\psi t) \qquad (4.19)$$

where $\omega_\psi = 5.5$ is the frequency of mother wavelet. The time-frequency wavelet energy density is defined as

$$WS(t_w, f_m) = \frac{2|Wf(t_w, s_w)|^2}{T_R C_\psi s_w f_m} \qquad (4.20)$$

where $s_w \cdot 2\pi f_m = \omega_\psi$ and C_ψ is the admissibility coefficient, defined as

$$C_\psi = \int_0^\infty (|\Psi(\omega)|^2/\omega)d\omega \qquad (4.21)$$

where $\Psi(\omega)$ is the Fourier transform of the mother wavelet. Figures 4.8(a) and 4.8(b) present the time-frequency analysis of the water surface elevation and shear stress at $x/h_o = 10$, respectively, for the irregular waves in Case 4.1. The values of the wavelet coefficient, $WS(t_w, f_m)$, were normalized by the corresponding zeroth spectral moment, $m_{o\eta}$ and $m_{o\tau}$ (Table 4.2). Notably from Figure 4.8, throughout the duration of wave progression, the spectral width of the shear stress is less than that of the wave elevation. This property is consistent with that presented in Figure 4.7. The maximum values of the water surface elevation and the shear stress occurred in the period between $50 \sim 55T_p$

with a sharp energy rise and a small frequency band.
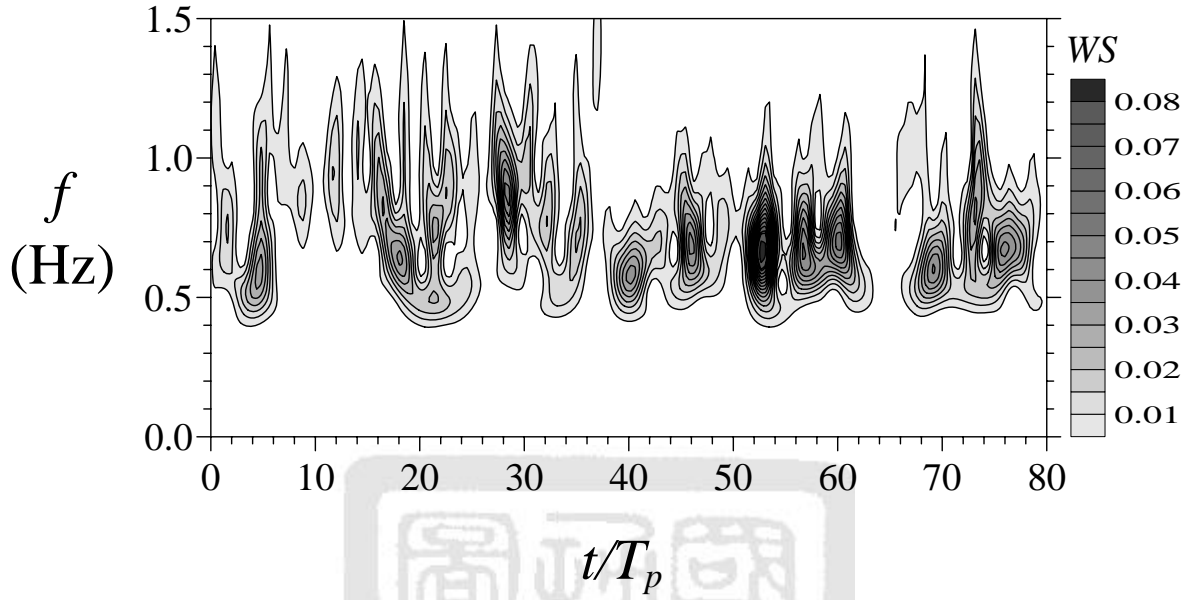
(a) time-frequency analysis of the surface elevation.
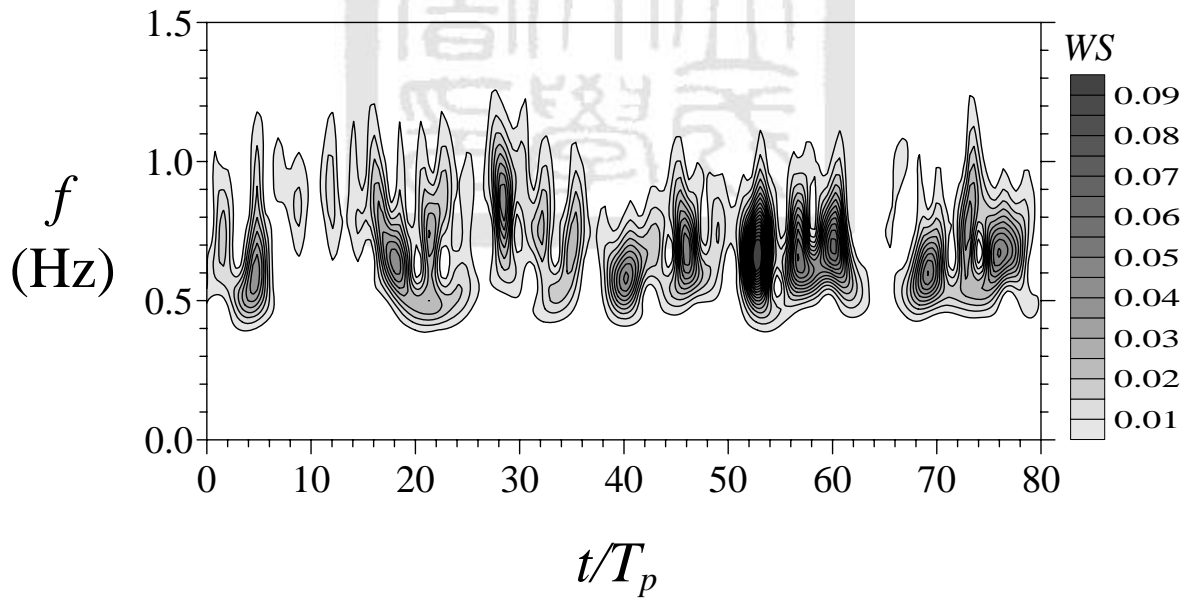
(b) time-frequency analysis of the bed shear stress.

Figure 4.8: Comparison of the surface elevation and shear stress in time-frequency domain for irregular waves in Case 4.1; the values of wavelet coefficient, $WS(t_w, f_m)$ were normalized to the corresponding zeroth spectral moments, $m_{o\eta}$ and $m_{o\tau}$.

Table 4.2: Comparison of different spectral parameters for cases in Table 4.1.

Case	f_p (Hz)	$m_{o\eta}$ ($\times 10^{-6}$ m^2)	H_s (cm)	$Q_{p\eta}$	$f_{p\tau}$ (Hz)	$m_{o\tau}$ ($\times 10^{-4}$ kg^{2}m^{-2}s^{-4})	$Q_{p\tau}$
4.1	0.625	6.790	1.042	1.981	0.617	3.547	2.562
4.2	0.500	7.079	1.064	1.923	0.500	3.854	2.291
4.3	0.800	6.377	1.010	2.165	0.750	2.565	2.983
4.4	1.000	7.394	1.088	2.143	0.906	1.678	3.419
4.5	0.625	5.913	0.973	2.219	0.773	9.553	2.345
4.6	0.625	7.433	1.095	1.950	0.594	0.797	3.184
4.7	0.625	6.900	1.050	3.044	0.625	3.715	3.885
4.8	0.625	6.865	1.048	4.499	0.625	3.862	5.462
4.9	0.625	6.978	1.056	1.966	0.613	3.479	2.553

The characteristics of the simulated wave spectra and the associated shear stress spectra can also be examined in terms of the zeroth spectral moment m_o and the spectral bandwidth parameter Q_p. When these parameters referred to the wave spectra or the shear stress spectra, an extra subscript η or τ was added.

The spectral moments of order r are defined as

$$m_r = \int_0^\infty \omega^r S(\omega) d\omega \tag{4.22}$$

where $S(\omega)$ is the spectral density function of the random variable. The significant wave height recommended by IAHR (1989) is defined as

$$H_s = 4 m_{o\eta}^{1/2} \tag{4.23}$$

The spectral bandwidth parameter, Q_p can be determined using various approaches. The spectral bandwidth parameter proposed by Goda (1970) is adopted here. It is defined as

$$Q_p = \frac{2}{m_{o\eta}^2} \int_0^\infty f S_\eta^2(f) df \tag{4.24}$$

Based on this definition, a higher value of Q_p corresponds to a narrower spectral bandwidth.

Table 4.2 lists the values of the spectral peak frequency, f_p, the zeroth spectral moment, m_o, and the spectral bandwidth parameter, Q_p, for the irregular waves and the associated shear stresses given in Table 4.1. The results in Table 4.2 indicate that for $f_p = 0.625 \, \text{Hz}$ as the water depth increases, from $h_o = 20 \, \text{cm}$ through 40 cm to 80 cm (Cases 4.5, 4.1 and 4.6), the spectral peak frequency of the shear stress $f_{p\tau}$ declines from 0.773 Hz through 0.617 Hz to 0.594 Hz, respectively. The zeroth spectral moment $m_{o\eta}$ is a measure of the energy associated with the random variables. Notably, although the zeroth spectral moments of the waves in Cases 4.1 to 4.9 are about the same since the $H_{1/3}$ values are identical, the values of $m_{o\tau}$ in these cases differ markedly and drop as f_p increases. This fact implies that less energy is transferred to the bottom shear stress if the main frequency band of the waves shifts to higher frequencies. Furthermore, the zeroth spectral moment of the shear stress increases rapidly as the water depth decreases. The bandwidth of the wave and the shear stress spectra becomes narrower as γ increases.

4.5 Determination of shear stresses using the transfer function method

The shear stresses caused by irregular waves can also be directly estimated using the transfer function between the shear stress and the surface elevation, as given by Eq. (4.16). When the target spectral density function of the waves is specified, the k-th Fourier

component A_k of the surface elevation, can be determined as stated in Section 4.1. The discrete time-series data of the shear stress were then obtained by superposing the shear stress due to each wave component, which can be determined from the shear stress in the frequency domain by applying the inverse discrete Fourier transform. Therefore

$$\tau(t_n) = \frac{1}{N}\sum_{k=0}^{N-1} B_k e^{i2\pi nk/N} \ , \quad n = 0,1,2,..., N-1 \tag{4.25}$$

where

$$B_k = \begin{cases} H_\tau(\omega_k)|A_k|e^{i(\phi_k + \pi/4\omega)} \ , & k = 0,1,..., N/2-1 \\ B_{N-k}^* & , & k = N/2, N/2+1,..., N-1 \end{cases} \tag{4.26}$$

where B_k is the k-th Fourier component of the bottom shear stress. Figure 4.9 shows the comparison of the free surface of Case 4.1 and the bottom shear stress calculated by using Eq. (4.25) base on the free surface. Both free surface and bottom shear stress were normalized by its significant value. The results indicates not only the magnitude but also the phase difference can be well-quantified by Eq. (4.25). Note that the phase difference between surface elevation and bottom shear stress is not exactly $\pi/4\omega$, since the time series shows the overall change contributed by each wave component, not reveals the change of single component.

Figures 4.10(a), 4.10(b) and 4.10(c) exhibit excellent agreement between the shear stresses obtained from this nonlinear wave model and those determined from Eqs. (4.25) and (4.26) for the irregular waves in Cases 4.1, 4.3 and 4.6 in Table 4.1, respectively. The shear stresses are normalized with respect to the significant bottom shear stress τ_s, which is defined as $\tau_s = 4(m_{o\tau})^{1/2}$.
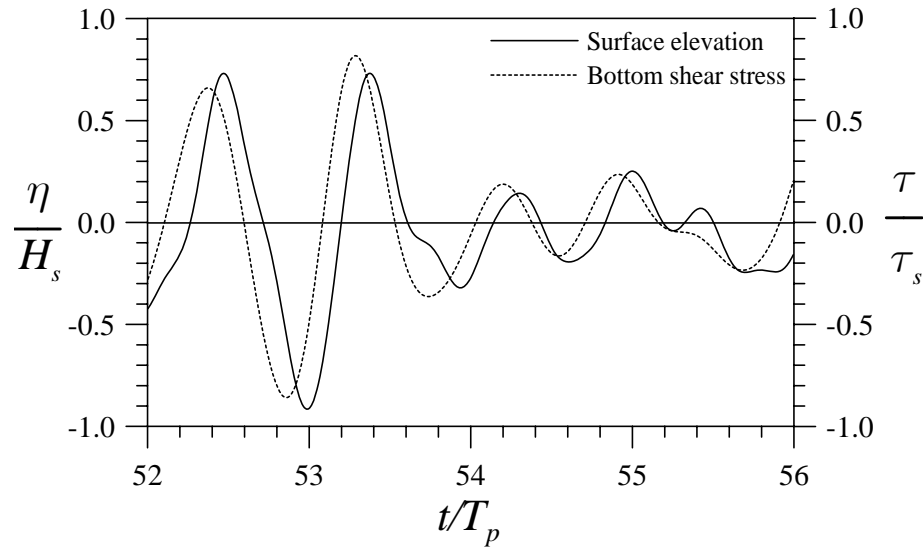
Figure 4.9: The free surface of Case 4.1 and the associated bottom shear stress determined using Eq. (4.25). The phase difference between the free surface and the bottom shear stress can be found clearly.
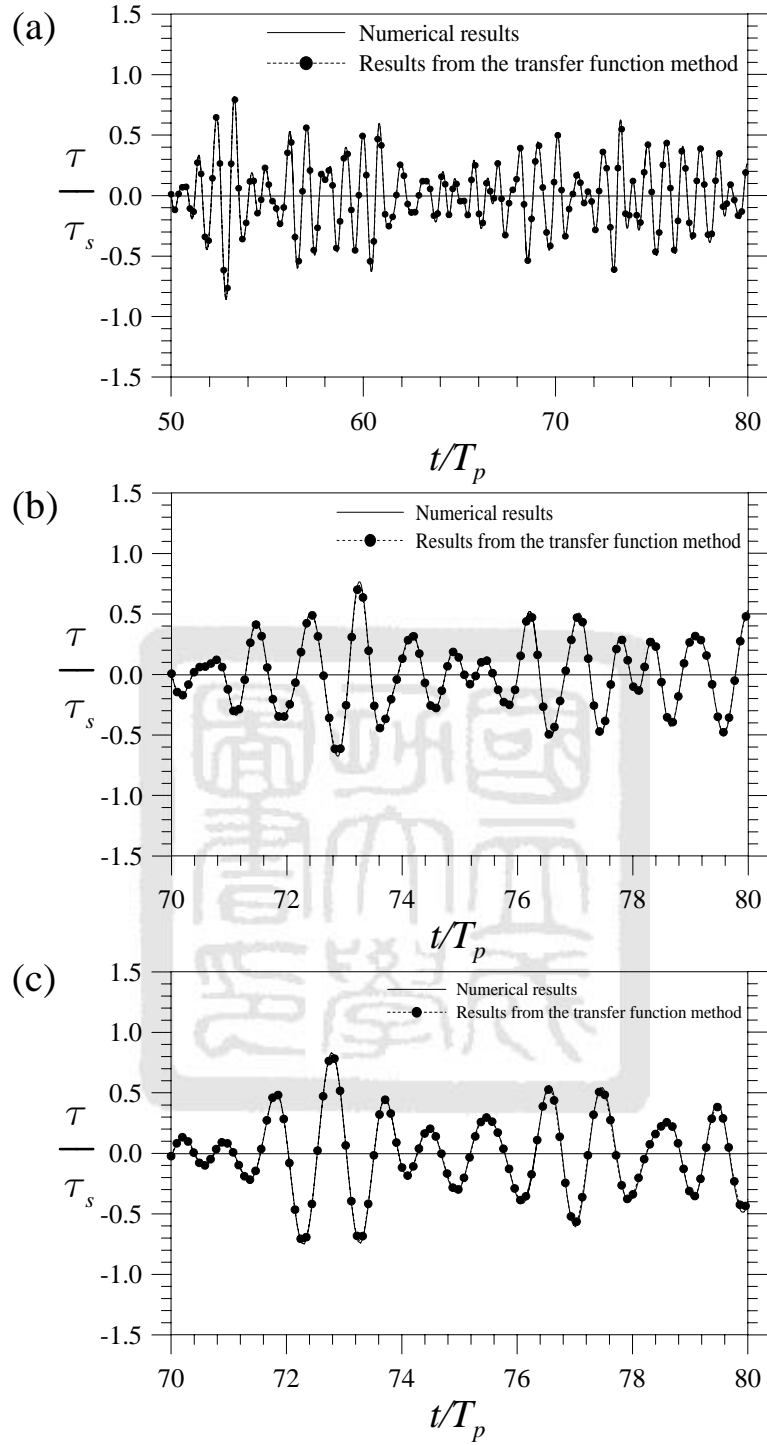
Figure 4.10: Comparison of shear stresses obtained from the numerical wave model and the transfer function method , using Eqs. (4.25), for irregular waves in (a) Case 4.1, (b) Case 4.3 and (c) Case 4.6.

4.6 Bed shear stress induced by irregular waves

The maximum shear stress is an important factor in the initial motion of the sediments and is difficult to determine in the field. Myrhaug (1995) proposed a model for calculating the maximum bottom shear stress based on the assumption that the surface elevation is a stationary Gaussian narrow-band random process with zero expectation and the one-sided spectral density S_η. Both the orbital displacement amplitude on the sea bed A_o, and the orbital velocity amplitude on the seabed U_o are then Rayleigh-distributed.

Let $\tau_{\max}$ denote the maximum bottom shear stress and $(\tau_{\max})_{1/N_M}$ denote the value of $\tau_{\max}$ which is exceeded by the probability $1/N_M$, Myrhaug (1995) proposed the following equation to determine $(\tau_{\max})_{1/N_M}$ for laminar flows.

$$(\tau_{\max})_{1/N_M} = (\ln N_M)^{0.5} \rho Re_{rms}^{-0.5} U_{rms}^2 \tag{4.27}$$

where N_M is the number of the crested value in the time-series data of the shear stress and U_{rms} is the root-mean-square of U_o and is defined as

$$U_{rms}^2 = 2 \int_0^\infty \frac{\omega^2 S_\eta(\omega)}{\sinh^2 kh_o} d\omega \tag{4.28}$$

The Reynolds number is defined as

$$Re_{rms} = U_{rms} A_{rms} / \upsilon \tag{4.29}$$

where A_{rms} is the root-mean-square of A_o and is defined as

$$A_{rms}^2 = 2 \int_0^\infty \frac{S_\eta(\omega)}{\sinh^2 kh_o} d\omega \tag{4.30}$$

Table 4.3 lists the values of the maximum bottom shear stress for the incident irregular waves shown in Table 4.1, as determined by Myrhaug's model, denoted by $\tau_{\max M}$, and those determined using the present numerical wave model. The value of N_M must be provided to determine $\tau_{\max}$ using Eq. (4.27). In this study, the zero-upcrossing method was used to determine the number of zero-upcrossing waves, N_w, and let this number be N_M. Table 4.3 also presents this value. The difference between the values of $\tau_{\max}$ obtained using these two approaches was evaluated as a percentage as follows.

$$Diff = \left| \tau_{\max M} - \tau_{\max} \right| / \tau_{\max} \tag{4.31}$$

Table 4.3 demonstrates that Myrhaug's model underestimates the maximum bottom shear stresses and at least with the $Diff > 0.1$.

Table 4.3: Maximum bottom shear stress obtained by Myrhaug's model and the present numerical wave model.

Case	N_w	U_{rms}	A_{rms}	$\tau_{\max M}$	$\tau_{\max}$	$Diff$
		(cm/s)	(cm)	($\times 10^{-2}$ kg·m^{-1}s^{-2})	($\times 10^{-2}$ kg·m^{-1}s^{-2})	(%)
4.1	108	1.563	1.000	4.235	6.146	31.09
4.2	94	1.800	1.040	5.052	6.768	25.35
4.3	125	1.209	1.105	2.782	4.911	43.35
4.4	165	0.907	1.688	1.505	4.112	63.40
4.5	103	2.521	0.654	10.668	9.572	11.45
4.6	109	0.774	0.314	2.639	3.005	12.18
4.7	104	1.639	1.251	4.049	6.421	36.94
4.8	98	1.683	0.979	4.731	6.128	22.80
4.9	224	1.561	0.418	7.027	6.152	14.21

Another possible approach for determining the maximum bottom shear stress associated with irregular waves is to use the transfer function between the shear stress and the surface elevation, given by Eq. (4.25). Table 4.4 compares the value of $\tau_{\max}$

obtained using Eq. (4.25), named $\tau_{\max T}$, and those obtained using the present numerical

model. Notably, the results are in good agreement.

Table 4.4: Maximum bottom shear stress obtained by utilizing transfer function and the present wave model.

Case	$\tau_{\max T}$ ($\times 10^{-2}$ kg·m^{-1}s^{-2})	$\tau_{\max}$ ($\times 10^{-2}$ kg·m^{-1}s^{-2})	$Diff$ (%)
4.1	5.989	6.146	2.55
4.2	6.596	6.768	2.54
4.3	4.713	4.911	4.03
4.4	3.935	4.112	4.30
4.5	9.580	9.572	0.08
4.6	2.926	3.005	2.63
4.7	6.176	6.421	3.78
4.8	5.987	6.128	2.30
4.9	6.361	6.152	3.39

4.7 Chapter remark

The main conclusions from the study of this chapter can be summing up briefly:

1. The wave spectrum of the generated irregular waves was in good agreement with the target spectrum; and the numerical and theoretical transfer functions coincide with each other. This testified the accuracy of this numerical wave model.

2. For a given depth of water, less wave energy is transferred to the bottom shear stress if the main frequency band of the waves is shifted to higher frequencies.

3. The comparison of the maximum bottom shear stress obtained by this wave model with that obtained by Myrhaug's model indicates that Myrhaug's model underestimates the maximum bottom shear stress caused by laminar irregular waves, except when the water

is shallow.

4. The bottom shear stresses obtained from this wave model agree closely with those obtained from the transfer function between the wave spectrum and the shear stress spectrum.

Chapter 5 Nonlinear properties beneath irregular waves

> *"Twenty years from now you will be more disappointed by the things you didn't do than by the ones you did do. So throw off the bowlines. Sail away from the safe harbor. Catch the trade winds in your sails. Explore. Dream. Discover."*
>
> —*Mark Twain, American writer*

5.1   The properties of Dean and Sharma's formula

The nonlinear free surface boundary conditions introduce the bound wave components, subharmonics and superharmonics, to irregular waves. For achieving a basic understanding of the nonlinear phenomenon, a model deduced by Dean and Sharma (1981) was introduced in this section.

The formula of Dean and Sharma's model (shorten as the DS model) with a known linear unidirecitional irregular-wave train η is prescribed as follows.

$$\eta = \eta^{(1)} + \eta^{(2)}_{DS} \tag{5.1a}$$

$$\eta^{(1)} = \sum_{k=0}^{N/2-1} a_k \cos\psi_k \tag{5.1b}$$

$$\eta_{DS}^{(2)} = \frac{1}{4}\sum_{k=0}^{N/2-1}\sum_{l=0}^{N/2-1} a_{kl}^{(2-)}\cos(\psi_k - \psi_l) + \frac{1}{4}\sum_{k=0}^{N/2-1}\sum_{l=0}^{N/2-1} a_{kl}^{(2+)}\cos(\psi_k + \psi_l) \tag{5.1c}$$

where

$$a_{kl}^{(2-)} = a_k a_l \left[\frac{D_{kl}^- - (k_k k_l + R_k R_l)}{\sqrt{R_k R_l}} + (R_k + R_l)\right] \tag{5.1d}$$

$$a_{kl}^{(2+)} = a_k a_l \left[\frac{D_{kl}^+ - (k_k k_l - R_k R_l)}{\sqrt{R_k R_l}} + (R_k + R_l)\right] \tag{5.1e}$$

$$D_{kl}^- = \begin{cases} \dfrac{(\sqrt{R_k} - \sqrt{R_l})(\sqrt{R_l}(k_k^2 - R_k^2) - \sqrt{R_k}(k_l^2 - R_l^2))}{(\sqrt{R_k} - \sqrt{R_l})^2 - k_{kl}^- \tanh k_{kl}^- h_o} \\ \quad + \dfrac{2(\sqrt{R_k} - \sqrt{R_l})^2(k_k k_l + R_k R_l)}{(\sqrt{R_k} - \sqrt{R_l})^2 - k_{kl}^- \tanh k_{kl}^- h_o} & ,\ kl \neq l \\ 0 & ,\ k = l \end{cases} \tag{5.1f}$$

$$D_{kl}^+ = \frac{(\sqrt{R_k} + \sqrt{R_l})(\sqrt{R_l}(k_k^2 - R_k^2) + \sqrt{R_k}(k_l^2 - R_l^2))}{(\sqrt{R_k} + \sqrt{R_l})^2 - k_{kl}^+ \tanh k_{kl}^+ h_o}$$
$$\quad + \frac{2(\sqrt{R_k} + \sqrt{R_l})^2(k_k k_l - R_k R_l)}{(\sqrt{R_k} + \sqrt{R_l})^2 - k_{kl}^+ \tanh k_{kl}^+ h_o} \tag{5.1g}$$

$$k_{kl}^- = k_k - k_l \tag{5.1h}$$

$$k_{kl}^+ = k_k + k_l \tag{5.1i}$$

$$\psi_k = k_k x - \omega_k t + \phi_k \tag{5.1j}$$

$$R_k = k_k \tanh k_k h_o \tag{5.1k}$$

where the subscript DS denotes the results of the DS model, and N is number of the time sequence. The term $\eta_{DS}^{(2)}$ in Eq. (5.1a) is the second-order component of the nonlinear irregular wave. The first term of the left hand side in Eq. (5.1c) is the second-order subharmonics and the second the second-order superharmonics.

In Eq. (5.1c), the phase of each second-order component, with the amplitude $a_{kl}^{(2-)}$ or

$a_{kl}^{(2+)}$, was a composition of the phase of the first order waves. Furthermore, a bound wave component with frequency f is constituted by the associated first-order waves, i.e. subharmonics with frequency $f = f_k - f_l$, and superharmonics with frequency $f = f_k + f_l$ (k, $l = 0, 1,..., N/2 - 1$). Although the amplitude of each second-order harmonic, $a_{kl}^{(2-)}$ or $a_{kl}^{(2+)}$, was constant if the linear irregular waves and the still water depth were held, the constituted results varies with phases, which changes temporally and spatially. This denotes that there are no equilibrium state or permanent spectral form for nonlinear irregular wave when the second-order nonlinearity was considered. Similar phenomenon were found by Huang and Tung (1976) as well as Baldock et al. (1996).

Table 5.1: The conditions of studied cases.

Case	h_o (cm)	$H_{1/3}$ (cm)	T_R (s)	Ur_s	Q_{DS}
5.1	40	1	128	1.257	0.0005
5.2	40	4	128	5.027	0.008
5.3	40	8	128	10.05	0.033
5.4	40	10	128	12.57	0.051
5.5	20	1	128	5.635	0.005
5.6	20	2	128	11.27	0.020
5.7	20	4	128	22.54	0.077
5.8	20	5	128	28.18	0.115
5.9	20	6	128	33.81	0.187

Table 5.1 lists the numerical conditions studied in the present study. The cases with different wave height and water depth were studied for verifying the effects of nonlinearities. The characteristics of nonlinear irregular waves were specified in terms of the time duration $T_R = 128\,\mathrm{s}$, the significant wave height $H_{1/3}$, the spectral-peak frequency $f_p = 0.625\,\mathrm{Hz}$, and the peak enhancement factor $\gamma = 3.3$ of Goda-JONSWAP

spectral density in Eq. (4.11).

The significant Ursell number was defined as Eq. (4.17).

$$Ur_s = H_{1/3}L_p^2 / h_o^3 \tag{4.17}$$

Ursell number is regarded as a nonlinear factor, which denotes the ratio of the first-order to the second-order wave component, and the significant Ursell number Ur_s were applied for this manner. A similar parameter can be defined by taking square of the ratio of linear energy $m_{o\eta^{(1)}}$ to the energy of the second-order component $m_{o\eta^{(2)}}$, say $\sqrt{\left(m_{o\eta^{(2)}} / m_{o\eta^{(1)}}\right)}$. However, there is lack of techniques that can separate linear and nonlinear irregular waves successfully. The DS model was applied to generate a synthesized results for comparison and denotes as following.

$$Q_{DS} = \sqrt{\left(m_{o\eta^{(2)}} / m_{o\eta^{(1)}}\right)_{DS}} \tag{5.2}$$

The subscript DS of each parameter denotes the parameter was obtained from the synthesized results which synthesized by the DS model with the conditions in Table 5.1.
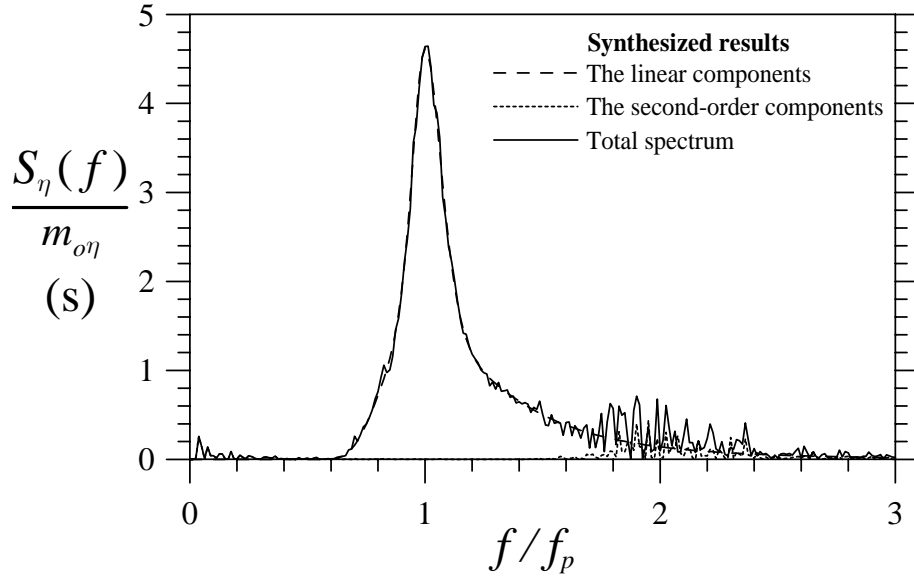
Figure 5.1: Synthesized nonlinear irregular wave spectrum applied the conditions of Case 5.7, in which the linear components satisfied the Goda-JONSWAP spectrum and the second-order spectrum are formed by the DS model.

Figure 5.1 shows the synthesized results of Case 5.7, which is synthesized by the linear irregular waves and the second-order components. The linear waves was satisfied the Goda-JONSWAP spectrum with the specified condition, and the second-order components were formed by Eq. (5.1), the DS model. The second-order subharmonics and superharmonics were clearly shown in Figure 5.1, in which the magnitude of subharmonics is smaller than that of superharmonics. Note that the total spectrum cannot be determined by the sum of the spectra of the linear part and the second-order one, say

$S_\eta \neq S_{\eta^{(1)}} + S_{\eta_{DS}^{(2)}}$ (Sand and Mansard, 1986).
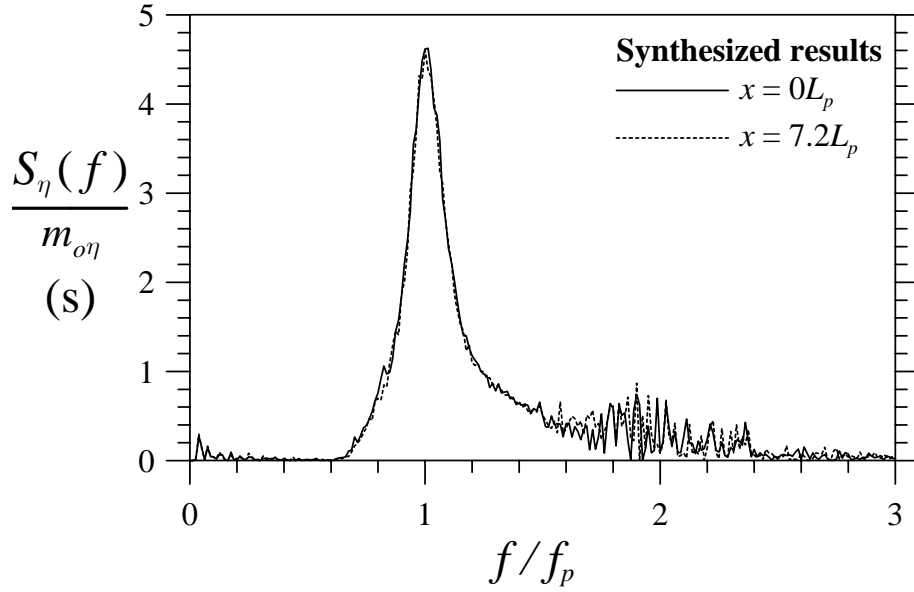
Figure 5.2: Synthesized results under identical condition with Case 5.7 with different applied locations, which introduced the phases difference of each component.

Figure 5.2 shows the another synthesized results of Case 5.7 but with different phases. Although the random phase ϕ_k of the linear components $\eta^{(1)}$ was without change, the phase of the second-order harmonics varied temporally and spatially as shown in Eq. (5.1), while the phase difference was formed by applying different locations, i.e. $x = 0$ and $x = 7.2\,L_p$. The results reveal that there is no identical spectral form of nonlinear irregular waves if time or location changes.

To identify the phase difference by the variation of zeroth moment is diffcult since the energy ration of the second-order components to the linear one is small. A statistical properties, skewness γ_1, the third standardized moment, is defined as

$$\gamma_1 = \frac{\mu_3}{\mu_2^{3/2}} \tag{5.3}$$

$$\mu_r = \int (x - \bar{x})^r\, p(x)dx \tag{5.4}$$

where $\bar{x}$ is the mean value of variable x, $p(x)$ the probability of x, and μ_r the r-th moment of x. The statistical properties can offer comprehensions about the tendency of the bound waves. It is believed that linear irregular waves with random phases are normal distributed (or called Gaussian distributed), and nonlinear properties make the statistical properties deviating from Gaussian distribution. An important parameter for determining the symmetric of wave crest and trough is the skewness, which is close to zero if surface elevation is symmetric, or the upper-envelop and the lower-envelop are identical or near identical. Otherwise, skewness is far from zero if surface elevation is asymmetric. Since the present of subharmonics and superharmonics introduce sharp-narrow crests and broad-flat troughs, the asymmetric of the surface elevation is increased and the skewness as well.

For wave train with identical random phase ϕ, and time duration T_R, the skewness γ_{1DS} of the synthesized results of Case 5.1 to 5.4 can thus be compared spatially and draw in Figure 5.3. The random variation of the skewness γ_{1DS} was resulted by the random phases, and the identical randomness of these four cases denotes the random phase of the four cases were identical. Within the same locations the skewness increases as the increasing of the significant wave height. Note that in different locations the skewness of Case 5.1 ($H_s = 1$ cm) can probably larger than that of Case 5.1 ($H_s = 8$ cm). Although the phase difference changes the skewness, the larger positive skewness can indicate the larger nonlinearity of the surface elevation.
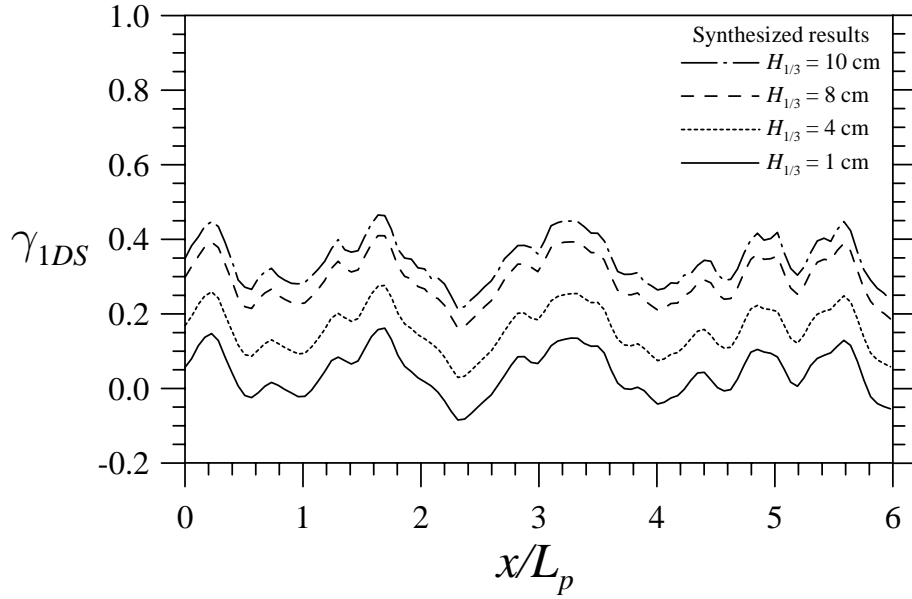
Figure 5.3: Spatial-varied skewness of the synthesized results with four different significant wave heights, Cases 5.1 to 5.4.

If the subharmonic components and wave-wave interaction were not considered, the first-order and the second-order components of a nonlinear-irregular-wave train can be separated using the method suggested by Sand and Mansard (1986). The authors pointed the separation process can start from the lowest-frequency component with assuming it is fully linear, and eliminating the associated second-order component using a formula prescribed superharmonics. When the sequential work is done, the linear components and the second-order components are separated. However, subharmonics are clearly found in the synthesized results in Figure 5.2, and thus the suggestion of Sand and Mansard was not satisfied. Henceforth, the comparison and further study used only the total spectrum S_η and the separation of linear and nonlinear irregular waves were not considered herein.

5.2 Generation of irregular waves and the numerical conditions

A nonlinear-irregular-wave train can be combined by a linear-irregular-wave train and the associated higher order components.   Similar manner was used to generate nonlinear irregular waves by Shen and Huang (2005), who applied the second-order Stokes waves generator to each wave component and formed the nonlinear-irregular-wave train. However, only the second-order components satisfied the superharmonic $k = l$ in Eq. (5.1) were generated and none of the subharmonics.   Since the nonlinear-irregular-wave generator based on weakly nonlinearity cannot have the agreement with the target spectrum far from the wavemaker (Sulisz and Paprota, 2008), it is not considered herein.

In the present work, the irregular-wave generator in Chapter 4 was used to form the waves.   Although the incident waves are without subharmonics and superharmonics, the nonlinear bound waves are supposed to be automatically formed by the fluid mechanics and can be found of the following discussions.

5.3   Spectral properties

With simply increasing the assigned significant wave height $H_{1/3}$, the nonlinear properties of the irregular-wave train was increased but was no robust confirmation.   The following process was applied to have the knowledge about the nonlinearity of irregular waves.   Figure 5.4 compares the numerical results and the Goda-JONSWAP spectral

density within identical conditions.   Of Case 5.2 shown in Figure 5.4(a), the components at about $1.8f_p$ of the numerical results have larger magnitudes than that of Goda-JONSWAP spectrum, in which only presents linear components.   The similar phenomena is noticed in Figure 5.4(b), a comparison with the conditions on Case 5.7.   Of this condition, not only superharmonics but also subharmonic were formed in the numerical flume.

Without nonlinear-irregular-wave generator, the higher-order harmonics, either subharmonics or superharmonics, are not generated by the wavemaker but by the nonlinear fluid mechanics.   Since the present numerical model considers the free surface conditions given in Eqs. (2.12) and (2.13) as well as the conservation equations, the numerical flume has the ability to simulate the fully nonlinear fluid mechanics.   Thus, the wave energy transferred in the progress of wave propagating and the change of the higher harmonics were introduced.
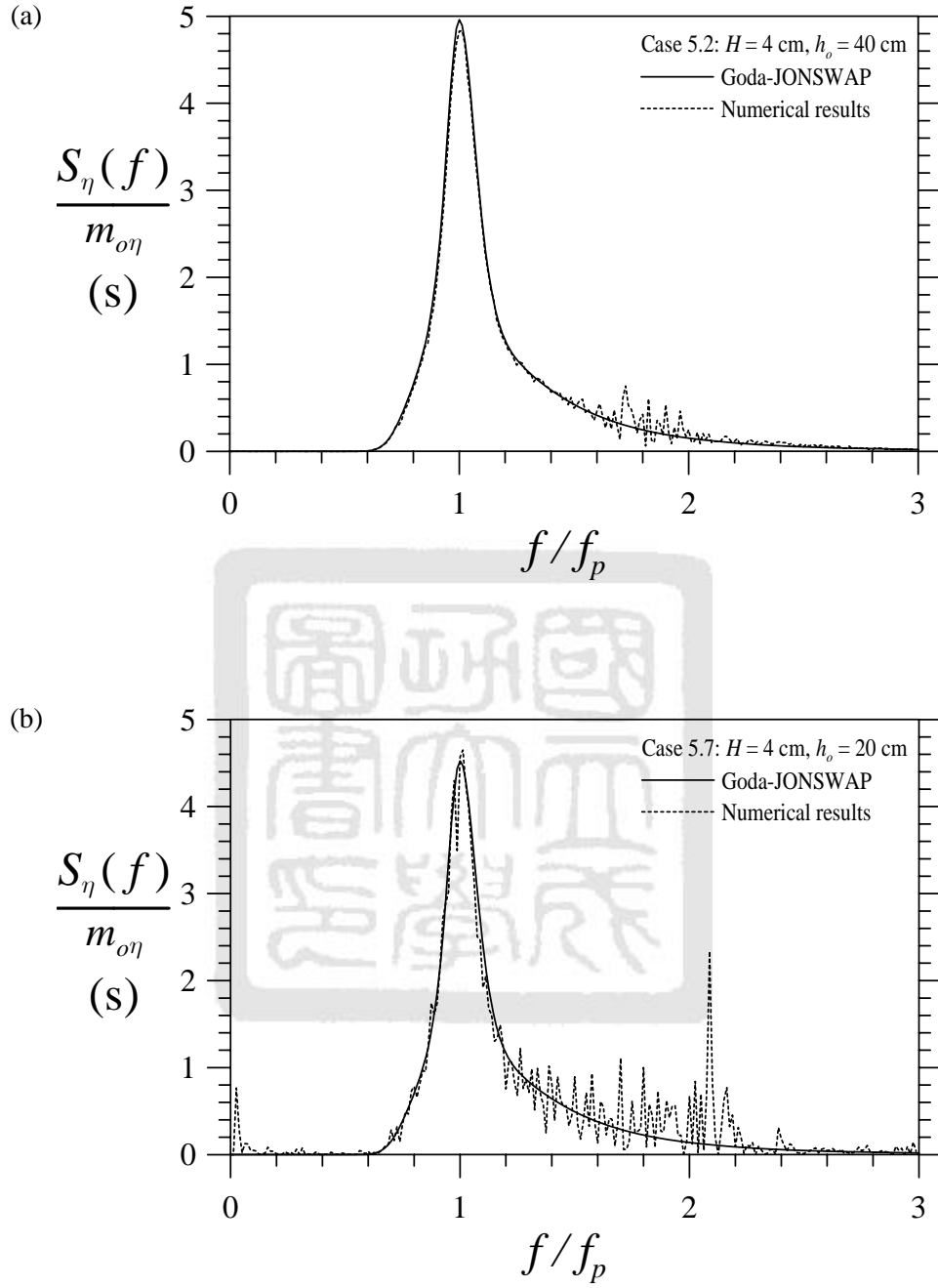
Figure 5.4: Spectrum of the numerical results (dot line) and the Goda-JONSWAP spectral density (solid line): (a) of Case 5.2; (b) of Case 5.7.

On the other hand, for a surface elevation, such as the DS model, considered only the weakly nonlinearity in the stationary state can not well describe the realistic nonlinear sea state. Furthermore, a nonlinear-irregular-wave generator prescribes such surface elevation as free surface boundary has less the ability to form the irregular-wave train even to satisfy the target surface elevation. This is indeed a very difficult problem.

When generating a regular wave with a large Ursell number using linear wavemaking theory, the bound waves and free waves are both formed in the wave flume. Similar phenomenon was expected for irregular waves. It means not only the bound waves, subharmonics and superharmonics, but also free waves were formed as wave propagating. Since it is not possible to recognized whether the spectral density around the frequency $2f_p$ were bound waves or no, the statistical properties have to be introduced. The results will not present in this section but in the following one, and make a comparison with the skewness of the bed shear stress.

5.4   The properties of the transfer function

In Chapter 4, the transfer function of surface elevation and the associated bed shear stress is identical with the numerical results and is good at estimating the bed shear stress beneath linear irregular waves. In this section, the same procedure was applied to reveal the properties of the transfer function beneath nonlinear irregular waves. The Gaussian white noises were used again to gain the characteristics of transfer function beneath nonlinear irregular waves.

Figure 5.5 shows the comparison of the theoretical transfer function (Eq. (4.16)) and numerical results of the Gaussian white noise with different wave heights. The results show the property of transfer function beneath the white noise with still water depth $h_o = 20$ cm and wave height 0.067, 0.2, 0.267, 0.4 cm, in which the nonlinear properties of free surface take place. The results in Figure 5.5 show that the transfer function of the numerical results is slightly departed from the theoretical one if the wave heights of the white noise were large. However, the tests of the white noise with different wave heights are limited by the physical and numerical limitation. The physical limitation is that wave breaking may appear because the frequency band is so wide that the occurance of freak waves are increase. The numerical limitation is the wavelength of high frequency components is not long enough for the present grid resolution to simulate it.

Of these four white noise, the numerical results indicate the theoretical transfer function can be used with surface elevation to estimate bed shear stress well enough it small disturbance is allowable.
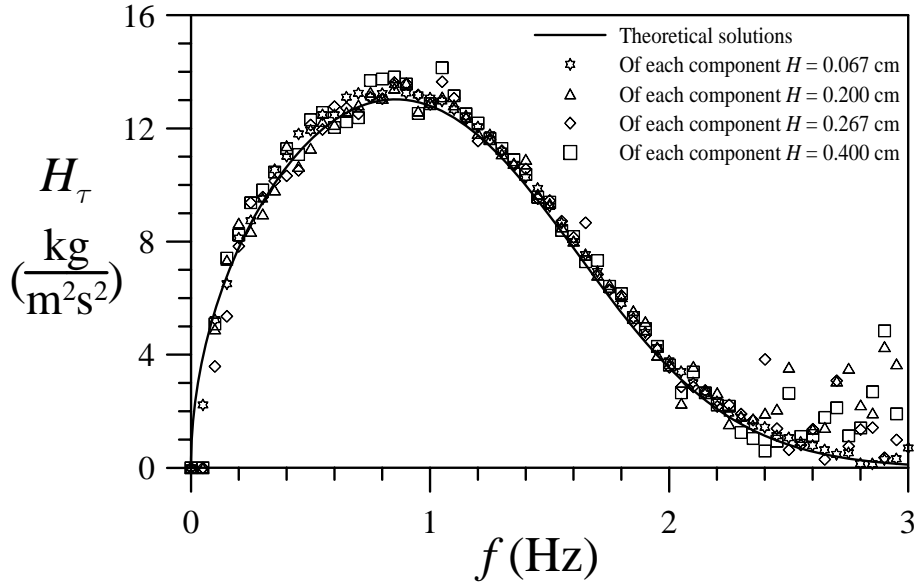
Figure 5.5: Theoretical transfer function and the transfer function of white noises with different wave height, which was assigned for each wave component within $0 \sim 4 \; \text{Hz}$. In the present case, the still water depth is $h_o = 20 \; \text{cm}$.

5.5 The statistical properties of the nonlinear bed shear stress

The statistical properties of a nonlinear irregular wave train is well-known of the skewness departed from the Gaussian distribution, in which the skewness is zero. The distribution of nonlinear surface elevations can be obtained by extending the linear one with the Stokes wave model. This manner was used for nonlinear shear stress by Myrhaug and Holmedal (2003), who deduced the probability distribution of the crested value of bed shear stress using the second-order Strokes theory.

Myrhaug and Holmedal (2003) found the cumulative distribution was with the form:

$$P(\widehat{\tau}) = 1 - \exp\left[-\frac{(\sqrt{1+4\Delta_{rms}\widehat{\tau}} - 1)^2}{4\Delta_{rms}^2} \right], \quad \widehat{\tau} \geq 0 \tag{5.5}$$

and the probability of exceedance as following.

$$Q(\widehat{\tau}) = 1 - P(\widehat{\tau}), \quad \widehat{\tau} \geq 0 \tag{5.6}$$

where the normalized root-mean-square of bed shear stress:

$$\widehat{\tau} = \tau_{\max} / \tau_{rmsM} \tag{5.7}$$

the root-mean-square of bed shear stress maxima:

$$\frac{\tau_{rmsM}}{\rho} = Re_{rms}^{-0.5} U_{rms}^2 \tag{5.8}$$

The bed orbital Reynolds numbers of irregular waves:

$$Re_{rms} = U_{rms} A_{rms} / \upsilon \tag{5.9}$$

The root-mean-square of bed-orbital-displacement amplitude:

$$A_{rms}^2 = 2 \int_0^\infty \frac{S_\eta(\omega)}{\sinh^2 k h_o} d\omega \tag{5.10}$$

The root-mean-square of bed-orbital-velocity amplitude:

$$U_{rms}^2 = 2 \int_0^\infty \frac{\omega^2 S_\eta(\omega)}{\sinh^2 k h_o} d\omega \tag{5.11}$$

According to Myrhaug and Holmedal (2001), an adjusted factor Δ_{rms}, which consisted with the second-order Stokes theory, can be defined as:

$$\Delta_{rms} = \left[2 - 2 \left(1 - \frac{1}{\pi} \right) \right] \frac{3 \bar{k} H_{rms}}{8 \sinh^3 \bar{k} h_o} \tag{5.12}$$

where the root-mean-square of wave height:

$$H_{rms}^2 = 8 \int_0^\infty S_\eta(\omega) d\omega = 8 m_{o\eta} = H_s^2 / 2 \tag{5.13}$$

the average wave number satisfying the distribution relation with ω_z:

107

$$\omega_z^2 = g\,\bar{k}\,\tanh\bar{k}h_o \tag{5.14}$$

in which the angular frequency is defined by

$$\omega_z = \left(\frac{m_{2A}}{m_{oA}}\right)^{1/2} = \frac{U_{rms}}{A_{rms}} \tag{5.15}$$

where the m_{oA} and m_{2A} are the zeroth momentum and the second momentum of bed-orbital-displacement amplitude.

For the cumulative distribution function (Eq. (5.5)), the results were dominated by two parameters: the root-mean-square of bed shear stress and the adjusted factor Δ_{rms}. The former one determined the magnitude of normal distribution of the linear bed shear stress, and the letter modifies the distribution to satisfy the second-order property. According to the results of Myrhaug's model (1995), which present in Chapter 4 and vary with the root-mean-square of bed shear stress only, we know that the RMS of bed shear stress determined by the simple explicit formula as shown in Eq. (5.8) cannot have a good estimation about the real bed shear stress. Since the model of Myrhaug and Holmedal (2003) is strongly based on the estimation of the RMS of the bed shear stress, the probability of exceedance in Eq. (5.6) using τ_{rmsM} obviously has none of the ability to describe the statistics of bed shear stress very well.

For having a comparison about the probability of exceedance, the τ_{rmsM} in Eq. (5.7) was replaced by the numerical results τ_{rms}, so that we can have a knowledge about the nonlinear adjustment of the statistical results. Figure 5.6 shows the probability of exceedance of normal distribution (solid line), nonlinear adjustment with Δ_{rms} (the

dashed line), and the numerical results of Case 5.6 (solid circle).   The results, numerical

one or adjustment one, are both departed from the normal distribution when the surface

elevation is nonlinear.   With the nonlinear adjustment Δ_{rms}, the probability of

exceedance can deviate from Gaussian distribution, although the results do not satisfy with

the numerical one or the one using the transfer function.
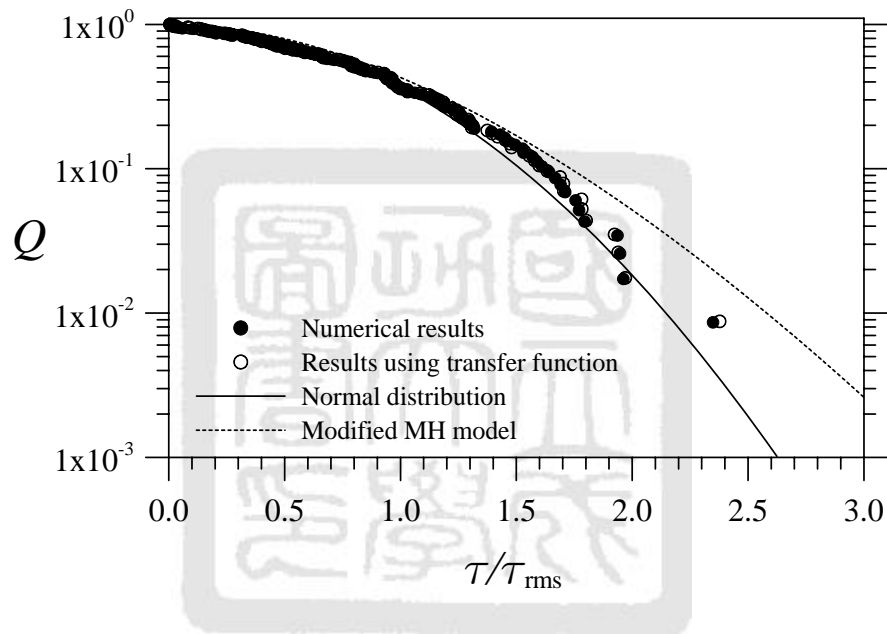
Figure 5.6: The probability of exceedance of the normal distribution (solid line), the modified nonlinear model results (dot line), the numerical results (solid circles), and the results by applying theoretical transfer function.

5.6   Skewness of surface elevation and bed shear stress

Of Figure 5.3, the skewness is known that changes with the phase of composite waves.

Figure 5.7 shows two cases, Cases 5.7 and 5.9, and compares the skewness of both the

surface elevation and the bed shear stress.   The skewness varies with the location, and the

of Case 5.9 is always larger than that of Case 5.7. It indicates the generated irregular wave were with bound waves so that the skewness is remained positive and has large value. In comparison to the skewness of the surface elevation, the skewness of the two bed shear stress shows similar variation. The found is the skewness has a phase different between the one of the surface elevation and of the bed shear stress. It indicates a forecasting using statistical formula will fail if only the associated magnitudes of the surface elevation and the bed shear stress are considered and ignore the phase difference.
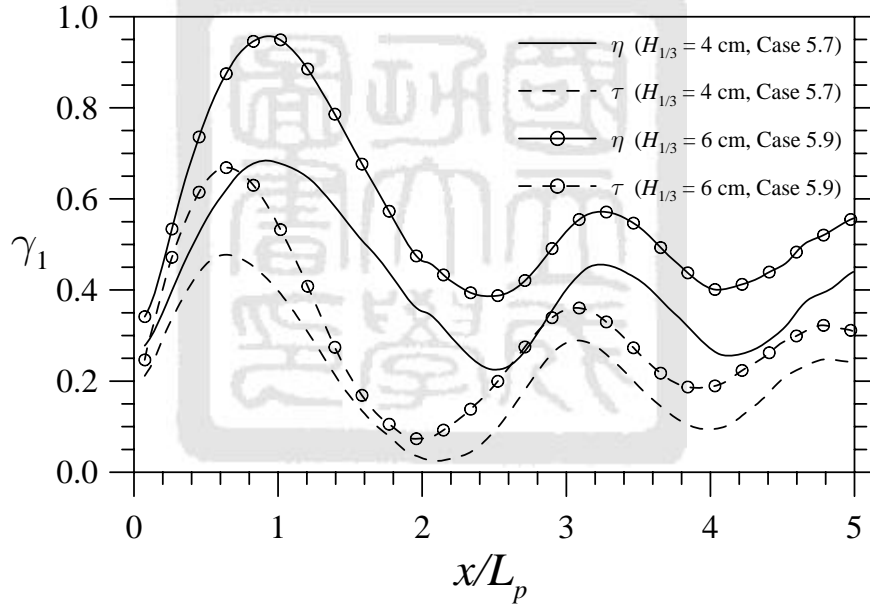
Figure 5.7: Skewness of the surface elevation η and the bed shear stress τ of Cases 5.7 and 5.9.

5.7 Chapter remark

The main conclusions from the study of this chapter can be summing up briefly:

1. Applying identical linear components with different phases, the synthesized results of

the DS model present irregular wave propagating with no identical spectral form, even though the change of phase velocity is not consider in the DS model.

2. For the waves propagating in the numerical flume, the subharmonics and superharmonics were generated automatically.

3. Increasing the wave height of the white noise increases only slight scatter of the transfer function obtained by the numerical results from the theoretical one. It indicates the theoretical transfer function is capable for predicting the associated bed shear stress from the surface elevation.

4. The skewness of both the surface elevation and the bed shear stress denotes there are bound waves within the numerical results. Of the spatial-varied skewness, the comparison evidences that the skewness of the bed shear stress has a phase difference between that of the surface elevation. This may result the statistical forecasting about the bed shear stress is malfunction if the phase shift is without concerned.

Chapter 6 Interaction of irregular waves and a submerged breakwater

> *"The important thing in science is not so much to obtain new facts as to discover new ways of thinking about them."*
>
> —*William H. Bragg,*
> *British physicist*
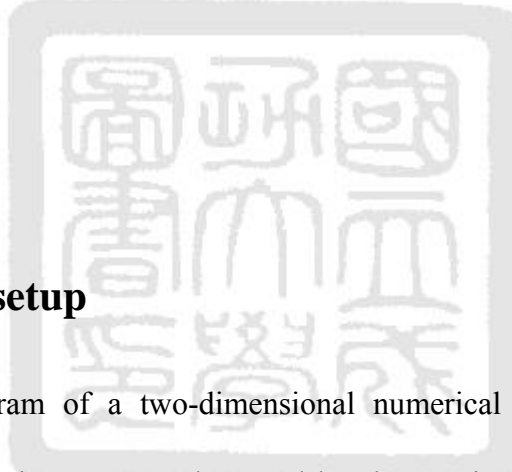
6.1 Numerical setup

A schematic diagram of a two-dimensional numerical wave flume for studying irregular waves propagating over a submerged breakwater is shown in Figure 6.1. The x-axis is measured horizontally in the direction of wave propagation and the origin is set at the weather side of the breakwater. The piston-type wavemaker with stroke S_o is located at $x = x_{\min}$. The y-axis is measured vertically upwards from bed. The still water depth is h_o, the height of the submerged breakwater $(1-q)h_o$, the width of the breakwater W_B, and the submergence ratio q.

113
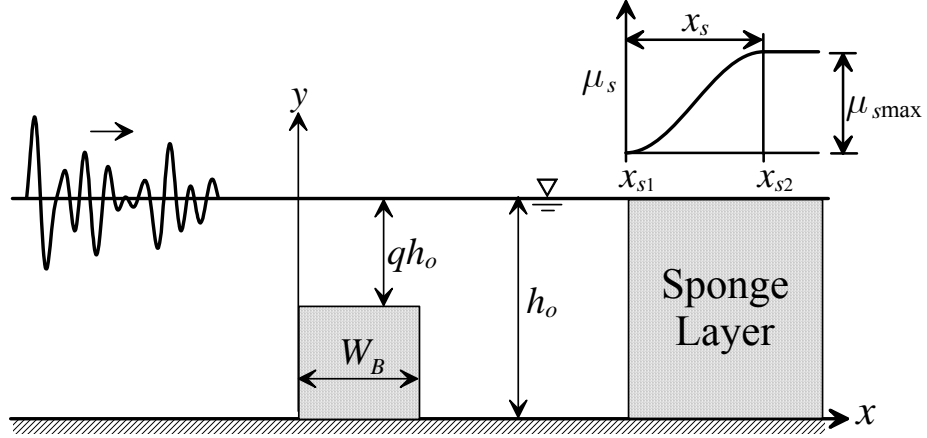
Figure 6.1: Schematic diagram of the numerical wave tank for studying the interaction of irregular waves propagating over a submerged breakwater.

The numerical scheme, which was with no sponge layer and capable of generating regular waves only, was once used by Huang and Dong (1999) to study the interaction of waves and a submerged breakwater and has been verified the accuracy of wave transformation and the associated nonlinear effects.   For the purpose of studying irregular waves, the irregular wave generator, which has verified in Chapter 4, was used, and the sponge layer was add to provide a non-reflected downstream.

Table 6.1 presents numerical conditions of the irregular waves and the submerged breakwater studied here.   The Goda-JONSWAP spectrum (Eq. (4.11)), was chosen as the target spectrum of the incident irregular waves with spectral-peak frequency $f_p = 0.625 \text{ Hz}$, the peak enhancement factor $\gamma = 3.3$, the spectral-peak wavelength is $L_p = 2.84 \text{ m}$, and the still water depth $h_o = 40 \text{ cm}$.   The duration of each wave train is $T_R = 16 \text{ s}$ and the location of wavemaker is $x_{\min} = -16 \text{ m}$.   The submergence Reynolds number at the depth $y = (1-q)h_o$ is simply defined by the

submergence-orbital-displacement amplitude A_B and the submergence-orbital-velocity

amplitude U_B as follows.

$$Re_B = U_B A_B / \upsilon \tag{6.1}$$

$$A_B = \frac{H_{1/3}}{2} \frac{\cosh[k_p(1-q)h_o]}{\sinh(k_p h_o)} \tag{6.2}$$

$$U_B = \omega_p A_B \tag{6.3}$$

where k_p is the spectral-peak wavenumber followed the dispersion relation

$\omega_p = g k_p \tanh k_p h_o$. In Case 6.1 no breakwater was in the numerical wave flume.

Hence, the measures of Case 6.1 are purely incident waves. Effects of different

submergence depths and widths of the breakwater were compared.

Table 6.1: Tested conditions with the rest are $T_p = 1.6$ s, $H_{1/3} = 4$ cm, $\gamma = 3.3$, $h_o = 40$ cm, $L_p = 2.84$ m and $T_R = 16$ s.

Case	q	W_B $(\times L_p)$	Re_B
6.1	----	----	1549
6.2	0.50	0.5	1874
6.3	0.50	1.0	1874
6.4	0.25	0.5	2341
6.5	0.25	1.0	2341

Of regular waves, it is known that the propagation of waves over a submerged

breakwater generates higher harmonics (Beji and Battjes, 1993; Ohyama and Nadaoka,

1994; Huang and Dong, 1999; and among others). When the incident waves are irregular,

the propagation of waves over a submerged breakwater, which will be expounded further

in following section, will produce the subharmonics and superharmonics as well as energy

transfer, due to the nonlinear properties in shallow water. Since the properties of subharmonics and superharmonics depend on the amplitude and phase of their constituent wave components, to obtain reliable results for examining these two types of waves, the random seed for generating the randomness of phases for each wave component was held the same and thus random sequence was identical. The effects of the height and width of the submerged breakwater were studied on the vortex dynamics, which were measured in the vicinity at the weather side and the lee side of the breakwater.

The interaction of waves and the breakwater results wave reflection. Reflected waves have to be quantify in order to ensure the result reliable. In most experiments, wave separation methods or an active water-wave absorber were used to deal with reflected waves. The wave separation method which uses measures at different locations is functional if surface elevation of the measures is stationary temporally and spatially. The active water-wave absorber works by generating waves, which are out of phase of the reflected one, to eliminate the measured reflected waves. Thus, the efficiency of eliminating the reflected waves is up to the determination of reflected waves, and is also limited by the stationary constrain.

Base on the repeatable property of the present numerical method, incident waves and reflected waves can be separated whether the results are stationary or no. Figure 6.2 plots the temporal variation of surface elevation for Cases 6.1 and 6.2 at $x/L_p = -3$, which is in between the wavemaker and the weather side of the breakwater. Note that the surface elevation before $t/T_p = 7.40$ (denoted by a vertical dashed line) was not affected by the

reflected waves, such that the surface elevations for Case 6.1 and Case 6.2 are identical. After $t/T_p = 7.40$, the surface elevation in Case 6.2 contains the reflected waves from the weather side of the breakwater. The identity of the incident irregular waves in Cases 6.1 and 6.2 enables us to detach out the reflected waves by subtracting the incident waves from the surface elevation in Case 6.2, namely $\eta_{\text{Case } 6.2} - \eta_{\text{Case } 6.1}$. The reflected waves thus obtained for Case 6.2 are plotted in Figure 6.3. Notably the wave front of the reflected waves appeared at $t/T_p = 7.40$.
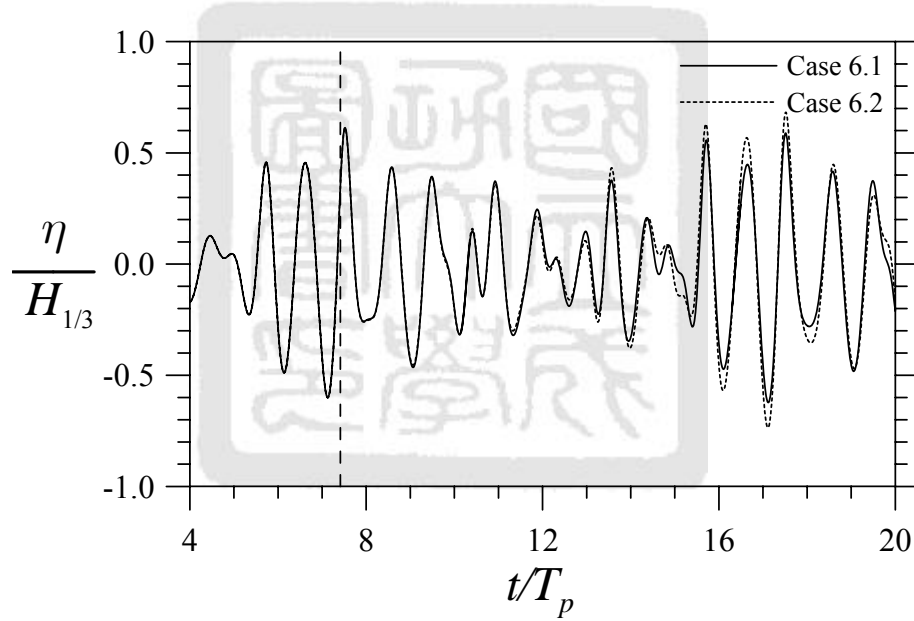
Figure 6.2: The surface elevation of Cases 6.1 and 6.2 at $x = -3L_p$. The changes made by the reflected waves are evident after the dashed line.
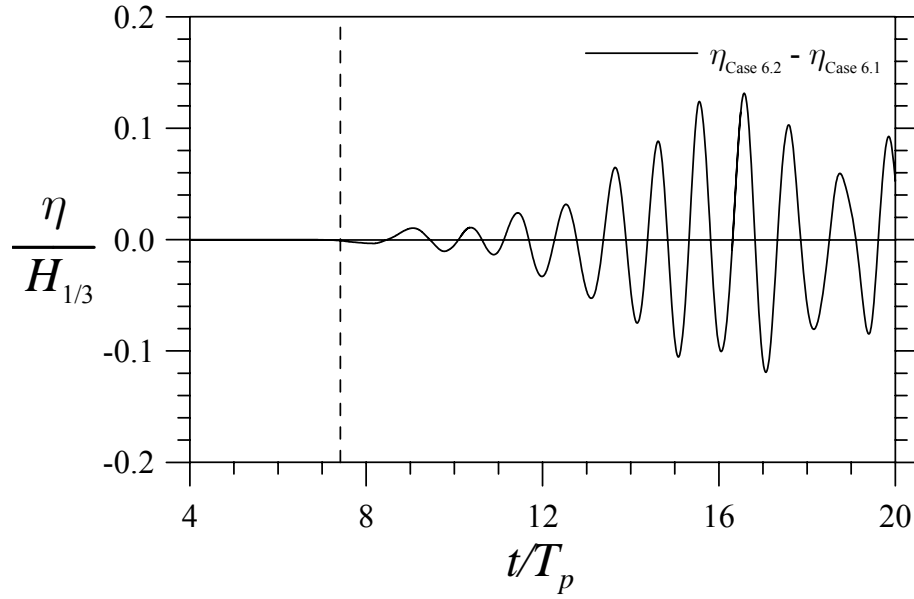
Figure 6.3: The reflected waves of Case 6.2 at $x = -3L_p$, obtained by $\eta_{Case\ 6.2} - \eta_{Case\ 6.1}$.

6.2 Duration for study

Athough the reflected waves can be well identified, they are accumulated in the flume because of lacking the non-reflecting boundary at the upstream.   A reliable duration for study has to be checked.   The reflected coefficients were analyzed spatially and temporally to verify the effects of reflected waves.   The reflected coefficient can be determined by

$$C_R = \frac{(H_s)_r}{(H_s)_i} = \sqrt{\frac{(m_{o\eta})_r}{(m_{o\eta})_i}} \qquad (6.4)$$

where

$$m_{o\eta} = \int_0^\infty S_\eta(\omega)d\omega \ \text{ and } \ H_s = 4\sqrt{m_{o\eta}} \qquad (6.5)$$

where $S_\eta(\omega)$ is the spectral density function of the surface elevation, the subscript r

denotes the reflected waves and the subscript i the incident one. Spatial variation of the reflected waves of Case 6.2 was shown in Figure 6.4. The location $x/L_p = 0$ is the leading side of the breakwater. Four different time periods of Case 6.2 were compared to examine their temporal difference. The four time periods, denoted as T_{R1}, T_{R2}, etc., differ in the beginning time, but have the same time duration of 16 seconds.
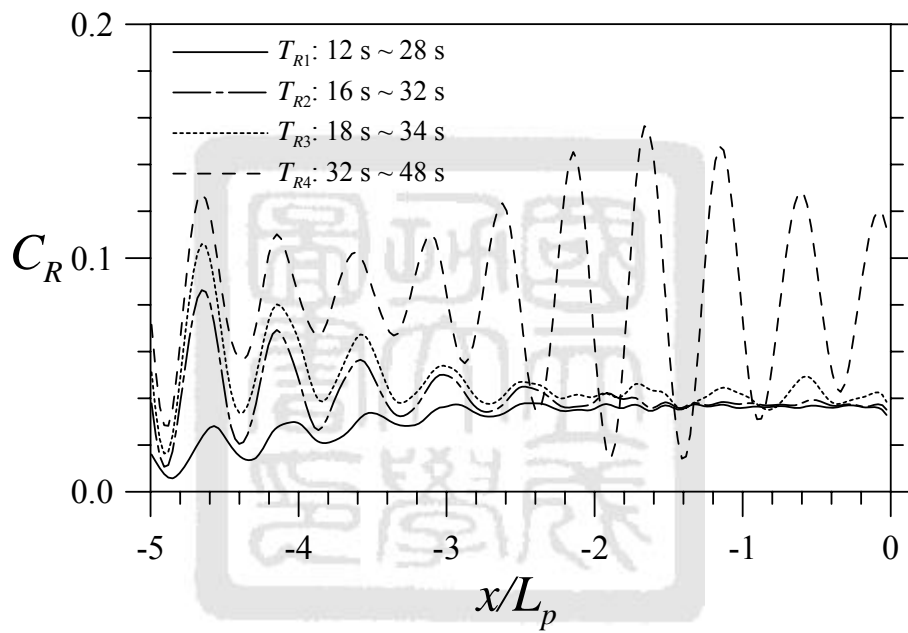
Figure 6.4: The reflected coefficient of Case 6.2 in different time period. The time duration, $T_R = 16\text{ s}$, was identical.

The results in Figure 6.4 indicate that the reflected coefficient increases with time. This is because that in our numerical wave flume no active water-wave absorber was installed at the wavemaker, such that when the reflected waves from the breakwater move back to the wavemaker, they will be reflected, and then combine with the new generated incident waves. This process repeats again and again and results in the continuous

increase of the reflected coefficient with time.   The results in Figure 6.4 indicate also that the reflected waves appear during T_{R1} is the justified ones, and the further study will focus on this period.

6.3   Nonlinear properties

Figure 6.5 compares the spectra, which is normalized by its own zeroth momentum $m_{o\eta}$, of the water surface elevation above the breakwater at $x/L_p = 0.50$ in Cases 6.1, 6.3 and 6.5.   The spectrum for Case 6.1 is the purely incident waves.   The breakwaters in Cases 6.3 and 6.5 have the same width ($W_B/L_p = 1.0$) but differ in the height.   As regular waves propagating over a submerged breakwater, the higher harmonics, which include bound waves and free waves, are generated in the shallow water region.   Irregular waves have similar phenomenon to regular waves.   In finite water depth or deep sea, the second order bound waves are introduced by nonlinear free surface boundary condition (Hasselmann, 1962; Laing, 1986; Dean and Sharma, 1981), and such bound waves are subharmonics and superharmonics, in which the amplitude and phases are determined by the linear constituent waves as shown in Eq. (5.1), and the amplitude of the bound waves can be described as

$$a_{f_i} \propto \sum_{f_a+f_b=f_i} a_{f_a} a_{f_b} \cos(\psi_a \pm \psi_b) \tag{6.6}$$

where a_{f_a} 、 a_{f_b} 、 ψ_a 、 ψ_b are the amplitudes and phases of the linear constituent waves respectively, and a_{f_i} is the amplitude of the bound waves.   The subharmonics are with the phase $(\psi_a - \psi_b)$, and the superharmonics with the phase $(\psi_a + \psi_b)$, and the detailed

properties are described in Chapter 5.   In Figure 6.5 the spectral form about the spectral

peak of Case 6.3 is similar to that of Case 6.1, with no observable difference.   However,

there are superharmonics of Case 6.3 observed at about $f/f_p = 2.1$ and 2.3 because of

the present of nonlinear properties in irregular waves.   The subharmonics of Case 6.3,

with the magnitude about $O\left(10^{-2}m_{o\eta}\right)$ are too small to be observed in Figure 6.5.

When submergence ratio decrease (Case 6.5, $q = 0.25$), the energy of the

components around the spectral peak (f_p, $f_1 = 1.1f_p$, and $f_2 = 1.2f_p$) are decrease

significantly, and the energy of higher harmonics, saying $f = 2.1f_p = f_p + f_1 = \cdots$,

$f = 2.3f_p = f_1 + f_2 = \cdots$, are increase observably.   Although the nonlinear properties can

be stated more clearly by analyzing about the numerical data, the results presented here

only figure out the phenomena for the following discussion about vortex dynamics.
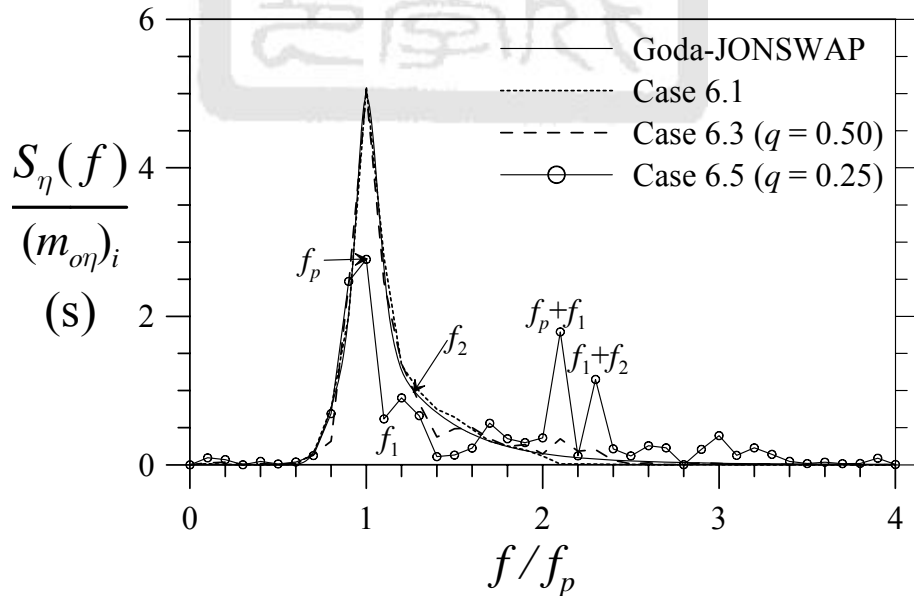
Figure 6.5: Wave spectra of Cases 6.1, 6.3 and 6.5 at $x = 0.5L_p$.

6.4 Properties of vortices around breakwater

Vortex dynamics are vital for many subtle applications, such as the mixing process, or nutrient transport. For achieving the goal of studying vortex dynamics, vorticities were calculated by the definition

$$\Omega = \nabla \times \underline{u} = \left(\frac{\partial v}{\partial x} - \frac{\partial u}{\partial y} \right) \tag{6.7}$$

Figures 6.6 (a) and (b) show the flow field with the vorticity contours of Case 6.4 at $t/T_p = 10.76$ and $t/T_p = 11.27$ respectively. A clockwise vortex above the breakwater was observed in Figure 6.6(a), and a counterclockwise vortex in front of the breakwater in Figure 6.6(b).

A vortex can be both found by observing the swirling velocity in flow field and by tracing the maximum absolute value of vorticities (condensed as MAV, the maximum vorticity for a counterclockwise vortex and the minimum vorticity for a clockwise one). However, as shown in Figure 6.6(b), the swirling center of the vortex, which is at about $(x/h_o,\ y/h_o) = (-0.10,\ 0.68)$ approximately, and the location of the MAV, which is at $(x/h_o,\ y/h_o) = (-0.10,\ 0.71)$, are not identical. In this chapter, the MAV was chosen to find the characteristics of a vortex because it can be traced automatically by numerical programming.
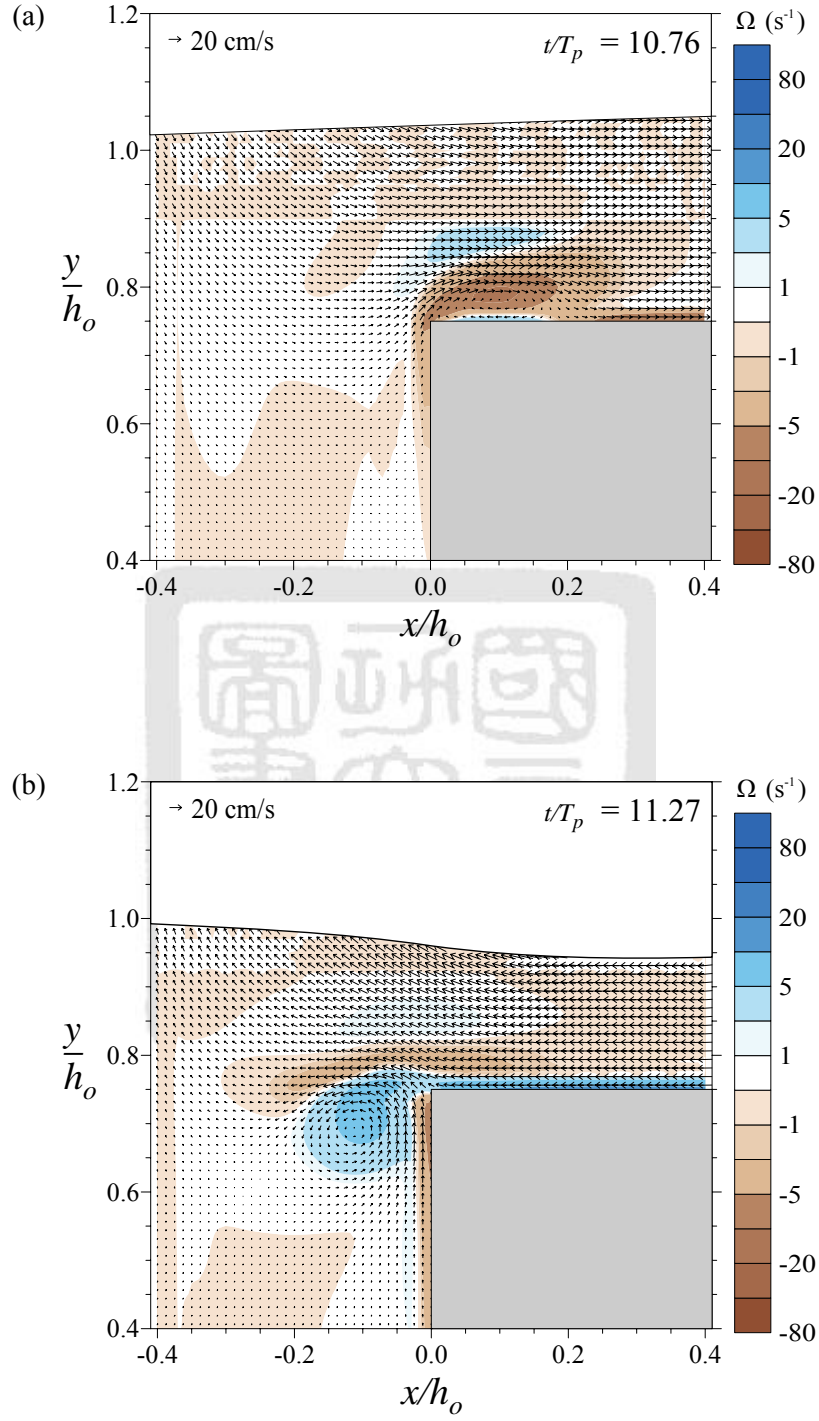
Figure 6.6: The flow field and the vorticity contours in Case 6.4: (a) $t/T_p = 10.76$ with a clockwise vortex above the breakwater; (b) $t/T_p = 11.27$ with a counterclockwise vortex in front of the breakwater.

Since there are no finer numerical elements close the boundaries to improve the resolution within boundary layer, the large-valued vorticities next to the boundaries are introduced by the no-slip condition and with no sense about vortex. Hence, the vorticities of the elements next to the boundaries were not taken into account.

For quantify a vortex, the following definition have to be made. A circulation Γ around a closed curve C is a scalar that gives a measure of the strength of a vortex, defined by Saffman (1992):

$$\Gamma = \oint_C \underline{u} \cdot d\underline{l} \tag{6.8}$$

From Stokes' theorem, Eq. (6.8) equivalent to the flux of vorticity through the surface s bounded by the curve C, so it can be rewritten as:

$$\Gamma = \int \Omega \cdot ds \tag{6.9}$$

Equation (6.9) has to be discretized for numerical use with the form (Earnshaw and Greated, 1998):

$$\Gamma = \sum_{i \in \text{vortex}}^{N_\Omega} \Gamma_i = \sum_{i \in \text{vortex}}^{N_\Omega} \Omega_i A_{\Omega i} \tag{6.10}$$

where Γ_i, Ω_i and $A_{\Omega i}$ are the circulation of a vortex, vorticity and the area of the i-th numerical element within a vortex respectively. N_Ω denotes the number of the numerical elemtnes of a vortex, and varies with the vortex strength and the definition of the vortical region. The center of a vortex can be defined as follows.

$$x_c = \frac{\sum_{i \in \text{vortex}}^{N_\Omega} \Gamma_i x_{\Omega i}}{\Gamma} \quad \text{and} \quad y_c = \frac{\sum_{i \in \text{vortex}}^{N_\Omega} \Gamma_i y_{\Omega i}}{\Gamma} \tag{6.11}$$

Since the circulation of a vortex is affected by the vorticities around it and the distance it can extent, the submergence-orbital-displacement amplitude A_B and the submergence-orbital-velocity amplitude U_B at the depth $y=(1-q)h_o$ were chosen as parameters to normalize the circulation of vortex.

6.4.2   The region of a vortex

Vertices can be traced automatically by searching the MAV of numerical results in each time step.   A procedure was stated here to identify the region of vortices.   The procedure is based on an assumption that the contour of the vorticities of a vortex was centralized on the MAV.   This also states that the absolute value of the vorticities in the region of a vortex is monotonous decreasing from center.   First of all, a guassed location O_b and an estimated pace Δr within a time step Δt_r of a vortex have to be calculated for performing a good searching.   The guassed location O_b was at $(x,\, y)=(\Delta r,\, (1-q)h_o+\Delta r)$ and $(x,\, y)=(-\Delta r,\, (1-q)h_o-\Delta r)$ for the clockwise vortices and the counterclockwise vortex at the weather side, and at $(x,\, y)=(W_B+\Delta r,\, (1-q)h_o-\Delta r)$ and $(x,\, y)=(W_B-\Delta r,\, (1-q)h_o+\Delta r)$ for the clockwise vortex and the counterclockwise vortex at the lee side respectively.   The estimated pace Δr can be obtained by assuming that the vortex was moved with the phase velocity of the surface elevation.   Thus the estimated pace Δr within the time step Δt_r for a vortex is predicted as following.

$$\Delta r = c_p \Delta t_r \qquad\qquad\qquad (6.12)$$

where $L_p = 2.84$ m is the spectral-peak wavelength, $T_p = 1.6$ s , $\Delta t_r = 1/64$ s , and

results $\Delta r = 2.7$ cm $\approx 5\Delta x$ in the present case. Since effects of viscous and no-slip boundary, the true pace of a vortex within time step Δt_r is smaller than the estimated one. The estimated space Δr makes the searching process focus on the same vortex.

The detail of the procedure for determining a vortex was described as follows:

1. Choose one type of the vortices (clockwise or counterclockwise, at the weather side on at the lee side) and assign the guessed location O_b;

2. Searching the MAV of the area $(2\Delta r) \times (2\Delta r)$ centralized on O_b;

3. Trace the MAV and find the global MAV, denotes as $|\Omega|_{max}$, over the time period T_{R1};

4. Define the vorticity threshold Ω_T as a ratio of the global MAV $|\Omega|_{max}$;

5. Find the location of the MAV of the area $(2\Delta r) \times (2\Delta r)$ centralized on O_b in the beginning of the time period T_{R1};

6. Record the location $(x_{\Omega i}, y_{\Omega i})$ of elements as the vortex if the vorticity in this location satisfies with the following contrains:

   (1) the vorticity of the element is larger than the vorticity threshold Ω_T;

   (2) the vorticity is smaller than that of the surrounding elements which is nearer O_b than the location $(x_{\Omega i}, y_{\Omega i})$;

   (3) the element is not isolated in the flow field;

7.   The properties of the vortex can thus be calculated and will be discussed later;

8.   The location of the MAV was assigned to be the new guessed location O_b of the searching process of the next time step;

9.   Repeat Step 5 to Step 8 for tracing the vortices and calculating the properties of the vortices.

   The flow field in Figure 6.6 was tested by the procedure and found the vortex region as shown in Figure 6.7.   Of the flow field only the elements within the selected vortex region were shown.   By this procedure, the vortex can be recognized automatically with an applied vorticity threshold.
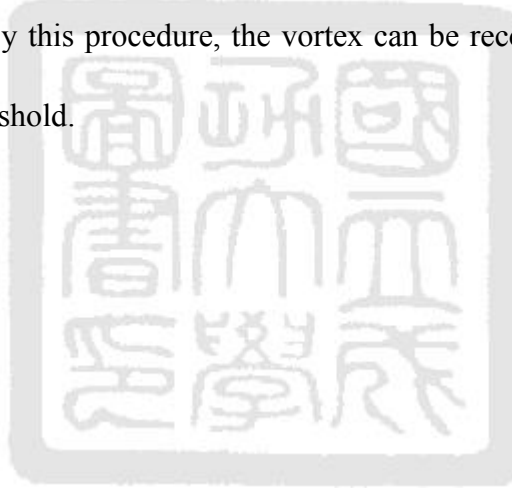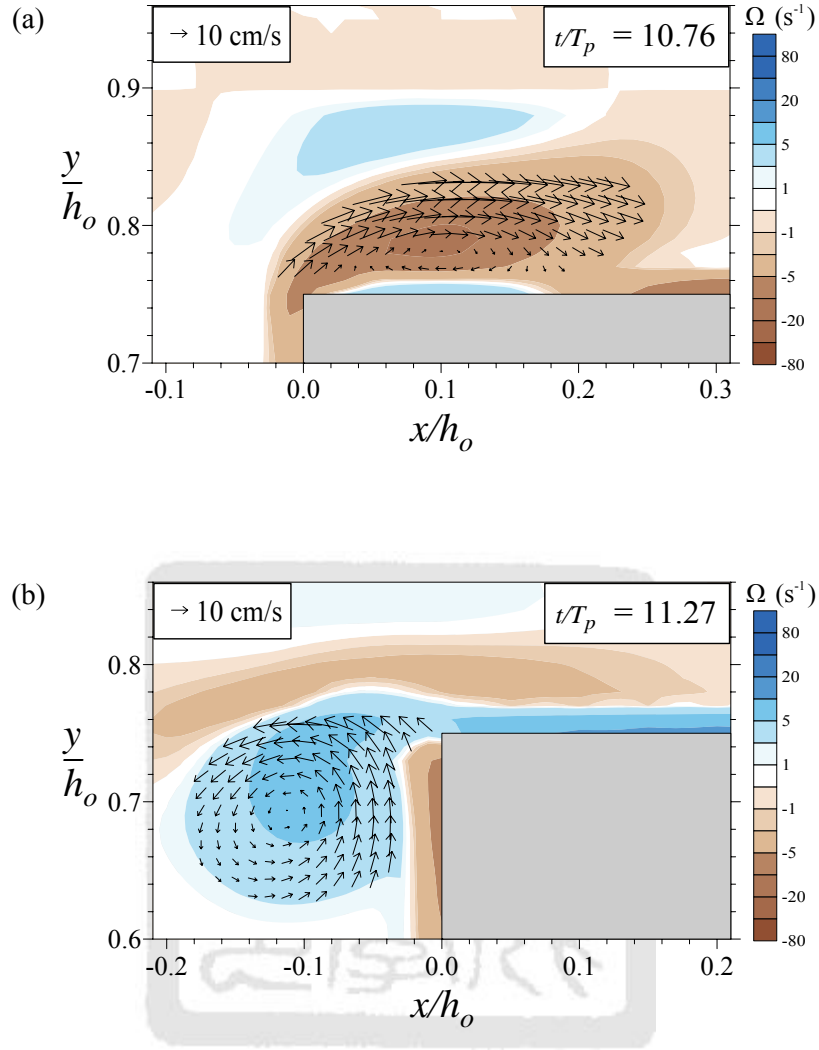
Figure 6.7: The selected region of vortices of Case 6.4: (a) the clockwise vortex at $t/T_p = 10.76$; (b) the counterclockwise vortex at $t/T_p = 11.27$. Only the flow field within the selected region of the vortices were shown.

6.4.3 Determining the threshold

Although the measure of vortex was defined in Eq. (6.10) and the procedure was clearly stated in Section 6.4.2, comparison is needed in order to define a particular threshold that makes the region of the vortices identically agrees with the swirling velocities of the flow field. Different thresholds, which are $\Omega_T = 0.5$, 0.2, 0.1, 0.05, 0.01, $0.001 \left| \Omega \right|_{max}$, were compared. The circulations of the clockwise vortex, in Figure 6.7(a), and the counterclockwise vortex, in Figure 6.7(b), were calculated using Eq. (6.10) with the vortical region selected by different thresholds and compared within a life cycle of the vortices.

Figure 6.8 shows the circulation and Figure 6.9 selected region of the counterclockwise vortex. The results of the clockwise vortex in Figure 6.7(a) were shown in Figure 6.8(a). When $\Omega_T = 0.5 \left| \Omega \right|_{max}$ was chosen as the vorticity threshold (denotes by dashed line with open circle), the maximum absolute circulation $\left| \Gamma \right|$ was only $3.2 U_B A_B$ and no measure were obtained after $t = 10.95 T_p$. When $\Omega_T = 0.2 \left| \Omega \right|_{max}$ was used, the maximum circulation $\left| \Gamma \right|$ is $5.3 U_B A_B$ with smoother results. By taking $\Omega_T = 0.1$, 0.05, 0.01, $0.001 \left| \Omega \right|_{max}$ as the vorticity threshold, the results show similar tendency but have slight difference of the magnitudes, and the selected region of the vortex in the flow field have to be compared for ensuring a reliable vorticity threshold.

The circulation of the clockwise vortex in Figure 6.7(b) were shown in Figure 6.8(b) with using different vorticity thresholds, and similar results were obtained. At about $t / T_p = 11.2$ the circulations of the clockwise vortex have a discrepance, which will be

discussed latter.
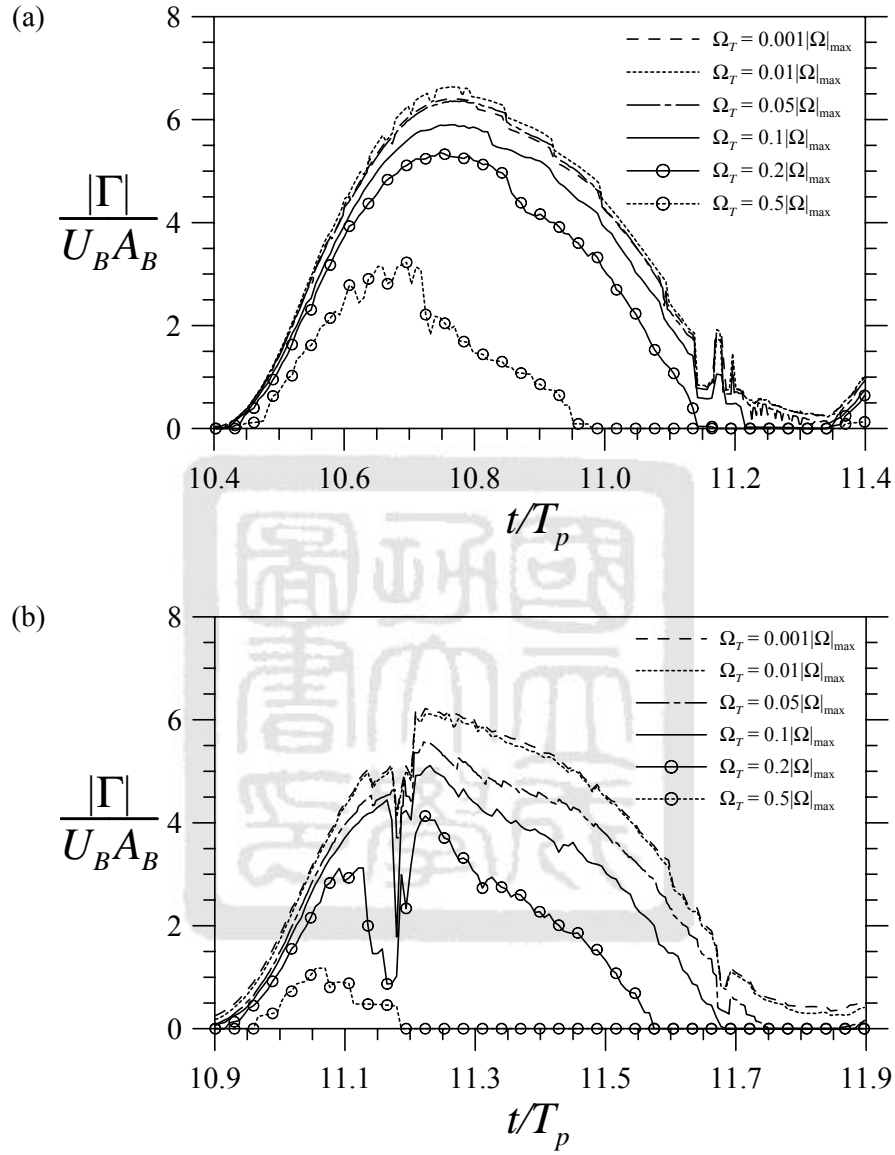
Figure 6.8: Circulations with different threshold: (a) the circulations of the clockwise vortex in Figure 6.7(a); and (b) the circulations of the counterclockwise vortex in Figure 6.7(b).

From the results of Figure 6.6 and the enlarged one of Figure 6.7, the vorticity contours of the vortex above the breakwater are so convex that the region of the vortex can be determined easily with the procedure described in Section 6.4.2. On the contrary, the vortex next to the breakwater is not so convex in the formation of the vortex, and is difficult to determine the region. Thus, the vortex in front of the submerged breakwater was chosen as the pattern to confirm a reliable threshold.

Figure 6.9 shows a sequence of plots, which include the flow fields, the vorticity contours and the selected region of the vortex, in order to verify the vortical region. The flow field within the selected region of the vortex was denoted by black arrows and otherwise gray. In Figure 6.7(b), swirling velocities centralize at $(x/h_o, y/h_o) = (-0.10, 0.68)$ were observed and the radius of the vertical is about $0.05 \sim 0.06 h_o$. Hence the threshold was chosen in order to select the elements in this region of the vortex with less misunderstanding. In Figure 6.9(a), the selected region is obviously not sufficient to be regarded as a vortex since only the swirling center was caught and other part of the vortex was lost by using the threshold $\Omega_T = 0.2 |\Omega|_{max}$. The selected region decided by $\Omega_T = 0.1 |\Omega|_{max}$ in Figure 6.9(b) has similar problem with that by $\Omega_T = 0.2 |\Omega|_{max}$. In general, the extent is larger when the smaller threshold was chosen. However, it can be found that the selected region obtained by the smallest threshold $\Omega_T = 0.001 |\Omega|_{max}$ in Figure 6.9(e) includes many elements that can not be regarded as part of the vortex, especially at about $x/h_o = -0.1$ and $y/h_o = 0.6$. The selected region determined by $\Omega_T = 0.05 |\Omega|_{max}$ and $0.01 |\Omega|_{max}$ are similar and good enough in describing the region of the vortex. In the present work, the threshold

$\Omega_T = 0.05|\Omega|_{max}$ was chosen as the one for determining the selected region of vortices and

the circulation calculated by Eq. (6.10) with this vorticity threshold is denoted as Γ_{95}.

(a) $\Omega_T = 0.2|\Omega|_{max}$
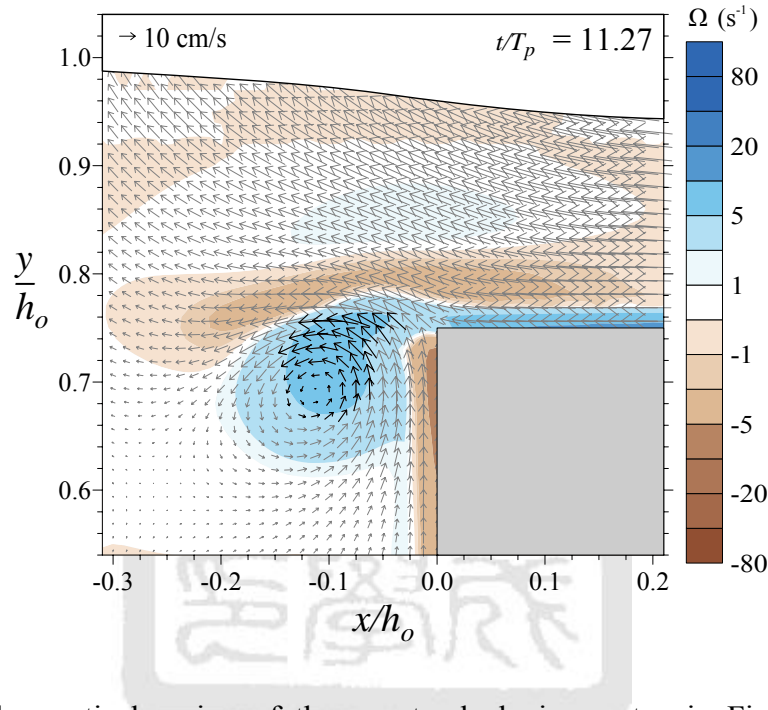
Figure 6.9: The vortical region of the counterclockwise vortex in Figure 6.6(b) with different vorticity thresholds: (a) $\Omega_T = 0.2|\Omega|_{max}$; (b) $\Omega_T = 0.1|\Omega|_{max}$; (c) $\Omega_T = 0.05|\Omega|_{max}$; (d) $\Omega_T = 0.01|\Omega|_{max}$; (e) $\Omega_T = 0.001|\Omega|_{max}$. The black arrows denote the selected region obtained by the vorticity threshold with the procedure in Section 6.4.2. (*continued on next page*)

(b) $\Omega_T = 0.1|\Omega|_{max}$

(c) $\Omega_T = 0.05|\Omega|_{max}$
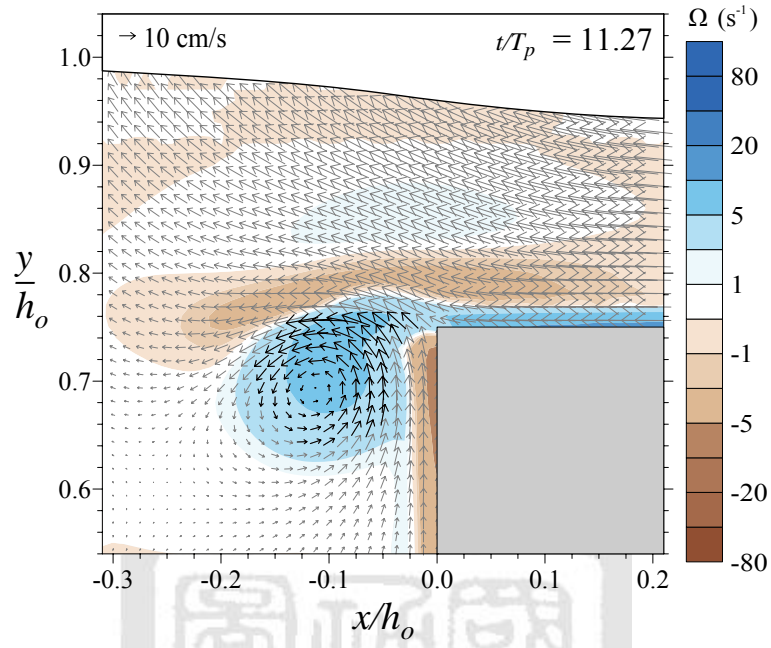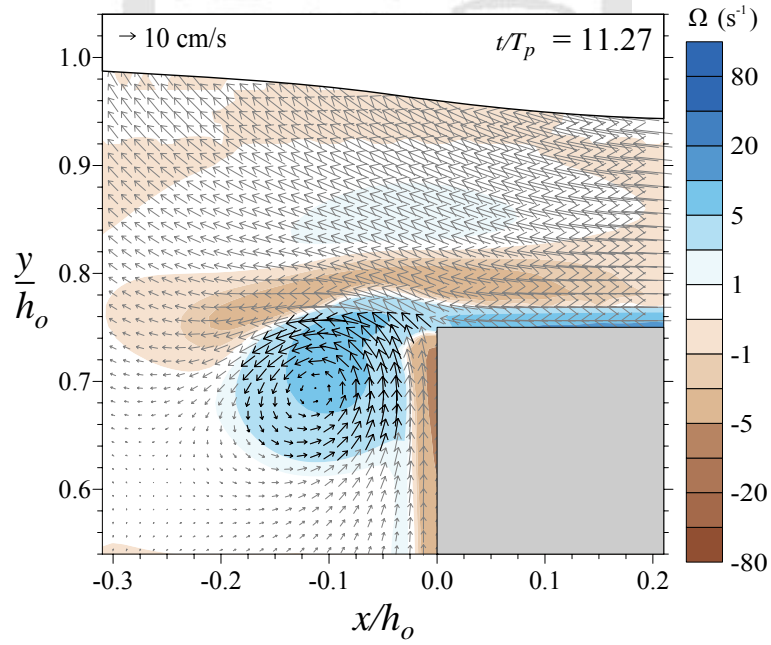
Figure 6.9: (*continued on next page*).

(d) $\Omega_T = 0.01 |\Omega|_{max}$

(e) $\Omega_T = 0.001 |\Omega|_{max}$
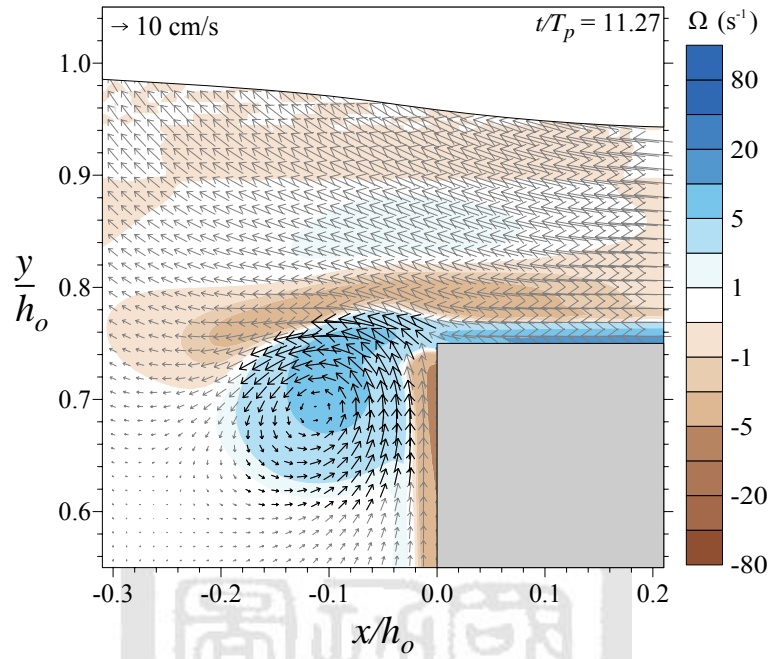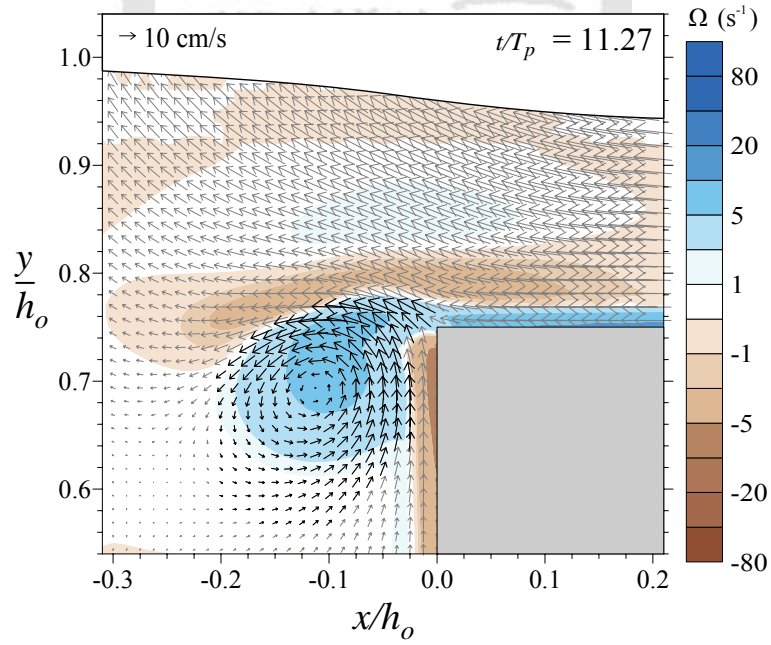
Figure 6.9: (*continued*).

6.4.4 Circulations at the weather side

By means of the threshold $\Omega_T = 0.05 \left.|\Omega|\right|_{max}$ and the procedure in Section 6.4.2, the vortex circulation and the associated properties of vortices can be measured. Figure 6.10 shows the circulations, in which contains the life cycles of two clockwise vortices $(-\Gamma)$ and one counterclockwise vortex $(+\Gamma)$ at the weather side, in which the clockwise vortices are formed above the breakwater and the counterclockwise vortex are formed in front of the breakwater.

The variation of the circulation $\left|\Gamma_{95}\right|$ can be compared with the surface elevation at $x/L_p = 0$. The maximum circulation of the clockwise vortex $(-\Gamma)$ in $t/T_p = 10.4 \sim 11.3$ was measured at $t/T_p = 10.76$ and has a time shift $\Delta t/T_p = 0.12$ with the wave crest, which is at $t/T_p = 10.64$. The maximum circulation of the counterclockwise vortex was measured at $t/T_p = 11.22$ and has a time shift $\Delta t/T_p = 0.07$ with the wave trough, which is at $t/T_p = 11.15$. The time shifts were obviously introduced by viscosity of fluid. Figure 6.10 also indicates that at the weather side the clockwise vortex $(-\Gamma)$ is driven by the positive horizontal velocities beneath the wave crest, and the counterclockwise vortex the negative horizontal velocities beneath the wave trough.

The circulation of the clockwise vortex $(-\Gamma)$ in $t/T_p = 11.3 \sim 12.0$ is shown to demonstrate that the counterclockwise vortex was affected by the clockwise vortex after $t/T_p = 11.44$, and further description and comparison were stated in Section 6.4.5. The discrepancy at $t/T_p = 11.18$ of the counterclockwise vortex at the weather side will be discussed later by the plots of flow fields with the vorticity contours.
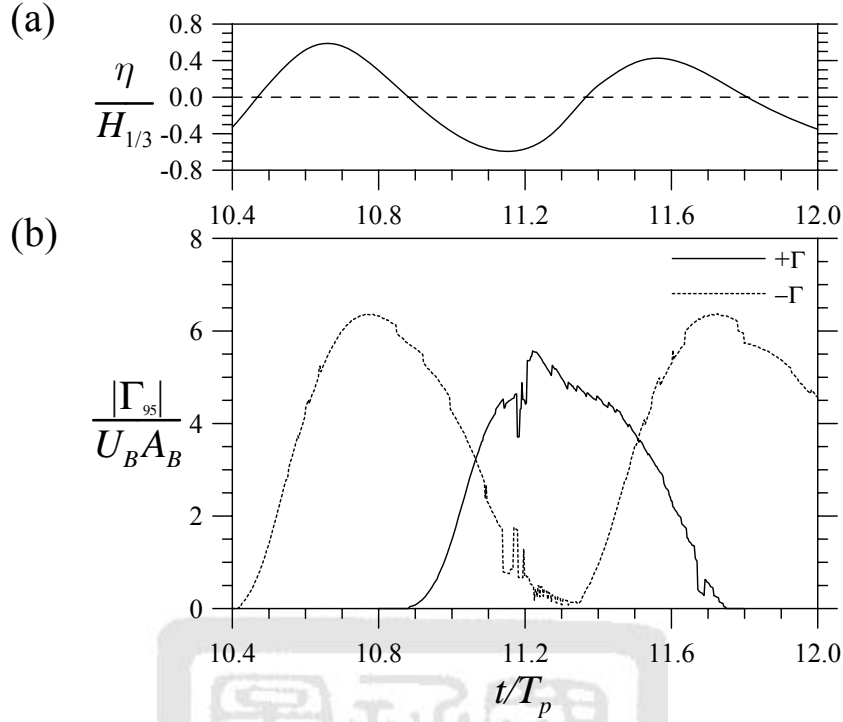
Figure 6.10: The circulations $|\Gamma_{95}|$ of the clockwise and counterclockwise vortices at the weather side in Case 6.4. The wave elevation was measured at $x/L_p = 0$.

6.4.5 Motions of the vortices at the weather side

Figure 6.11 and Figure 6.12 show sequences of plots of flow fields with the vorticity contours. The surface elevation at $x/L_p = 0$ and the circulation $|\Gamma_{95}|$ of the vortices were marked by cross and were presented within the breakwater. The flow fields were distinguished by colors: the black arrows denote the selected region of the vortex and the gray arrows otherwise.

Figure 6.11 shows the life cycle, from formation to breakdown, of the clockwise vortex, which has been presented in Figures 6.6(a) and 6.7(a). In Figure 6.11(a), the vortex formed as a result of the positive surface elevation and the associated positive

horizontal velocities.

(a) $\left(x_c / h_o, \ y_c / h_o\right) = \left(0.021, \ 0.787\right)$
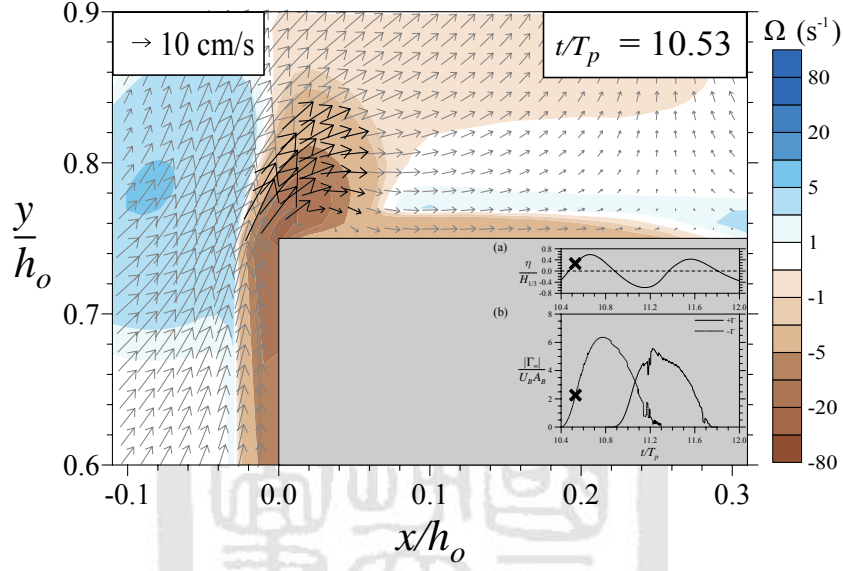
(b) $\left(x_c / h_o, \ y_c / h_o\right) = \left(0.063, \ 0.792\right)$
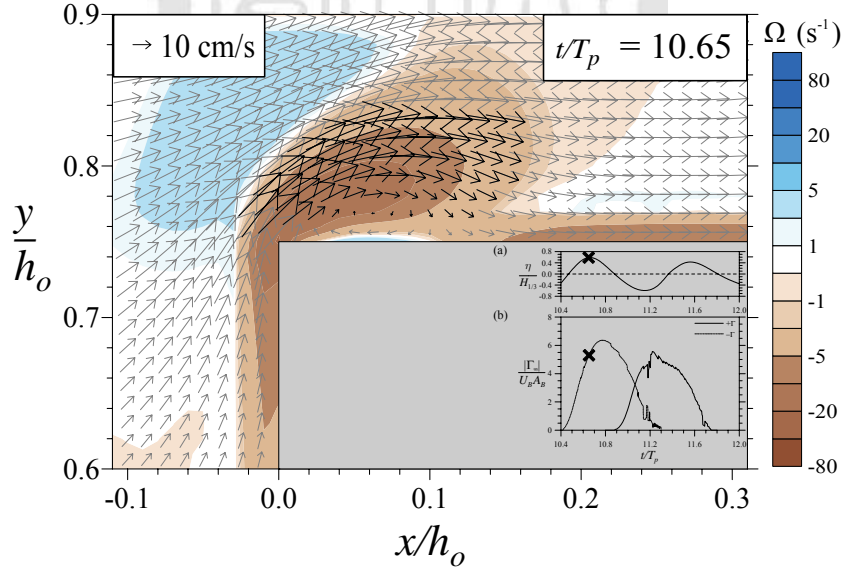

Figure 6.11: A sequence of flow fields with the vorticity contours shows the life cycle of the clockwise vortex indicated in Figure 6.6(a). The surface elevation and the circulation $\left|\Gamma_{95}\right|$ were denoted both in mark and the location of the vortical centers $\left(x_c / h_o, \ y_c / h_o\right)$ are shown. The phase of each flow fields is: (a) $t / T_p = 10.53$; (b) $t / T_p = 10.65$; (c) $t / T_p = 10.76$; (d) $t / T_p = 10.92$; (e) $t / T_p = 11.08$. (*continued on next page*)

(c) $\left(x_c/h_o,\ y_c/h_o\right)=\left(0.113,\ 0.794\right)$
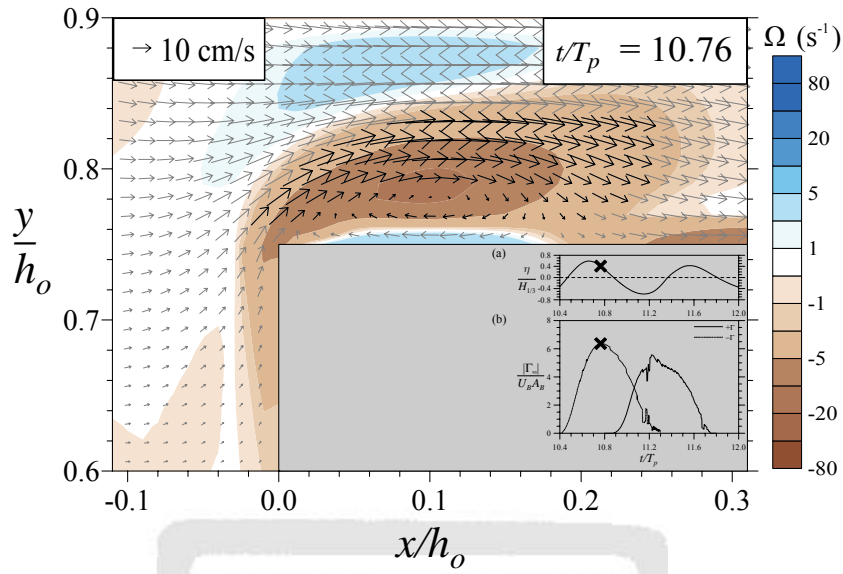
(d) $\left(x_c/h_o,\ y_c/h_o\right)=\left(0.135,\ 0.790\right)$
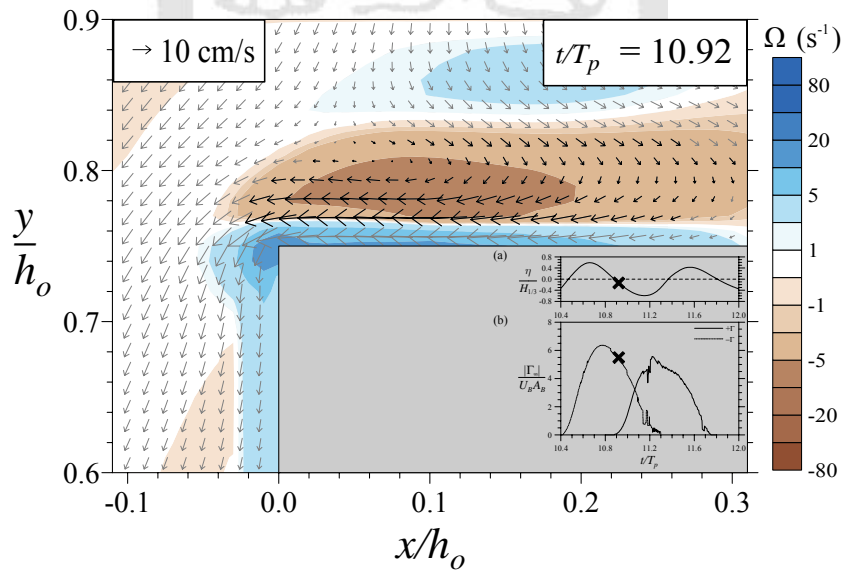
Figure 6.11: (*continued on next page*).

(e) $\left(x_c / h_o, \; y_c / h_o\right) = \left(0.067, \; 0.780\right)$
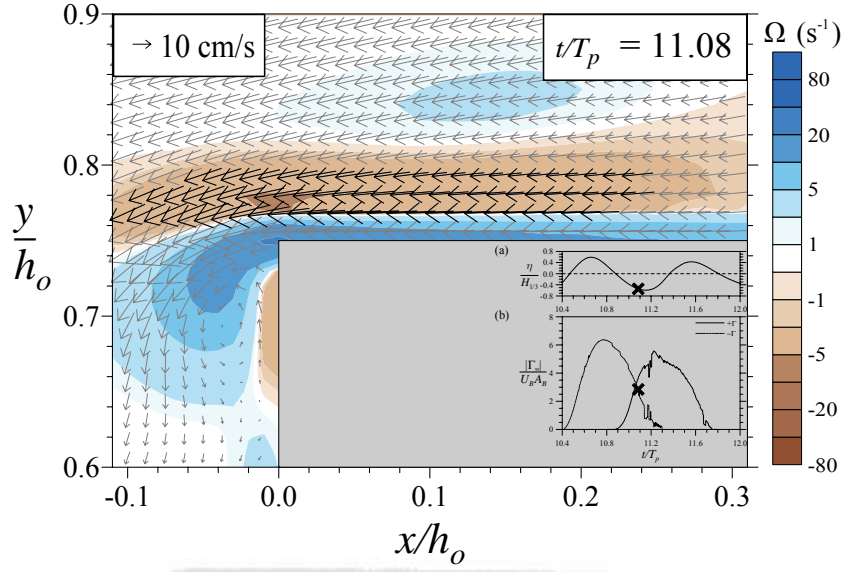
Figure 6.11: (*continued*).

When the wave crest arrived, the selected region of the vortex enlarged with higher circulation and the location of the MAV detached from the corner as shown in Figure 6.11(b). The vortex reached the maximum circulation $\left|\Gamma_{95}\right|$ at $t/T_p = 10.76$ in Figure 6.11(c) and centralized at $\left(x_c / h_o, \; y_c / h_o\right) = \left(0.113, \; 0.794\right)$. The extent of the vortex in Figure 6.11(d) is wider than that in Figure 6.11(c) and with the smaller MAV because the vorticity was convected by flow motion. The swirling center at about $x/h_o = 0.06$ in Figure 6.11(d) was parted from the location of the MAV. Although the circulation can be measured at the stage shown in Figure 6.11(e), there are no clockwise-vortical velocities. This denotes that the selected region of a vortex base on vorticity is not well-described if the vorticities are small.

(a) $\left(x_c / h_o, \; y_c / h_o\right) = \left(-0.048, \; 0.715\right)$
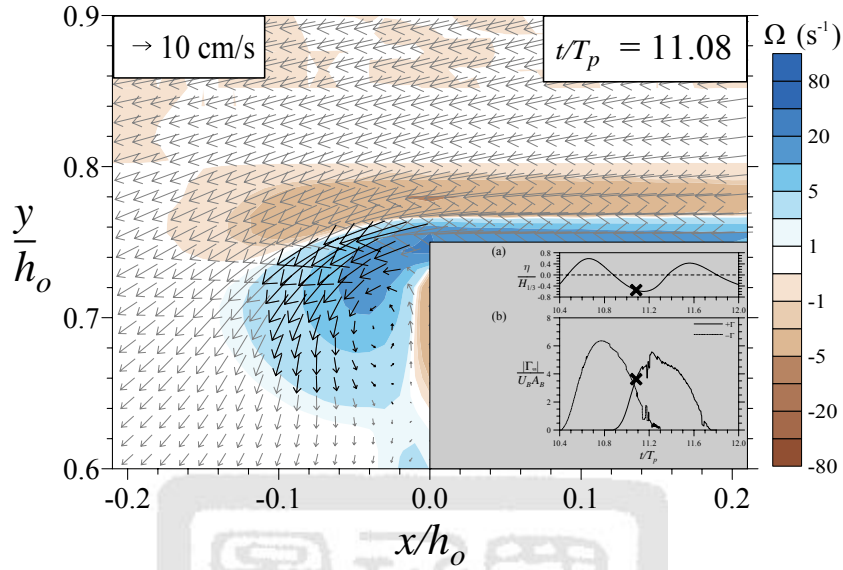
(b) $\left(x_c / h_o, \; y_c / h_o\right) = \left(-0.062, \; 0.710\right)$
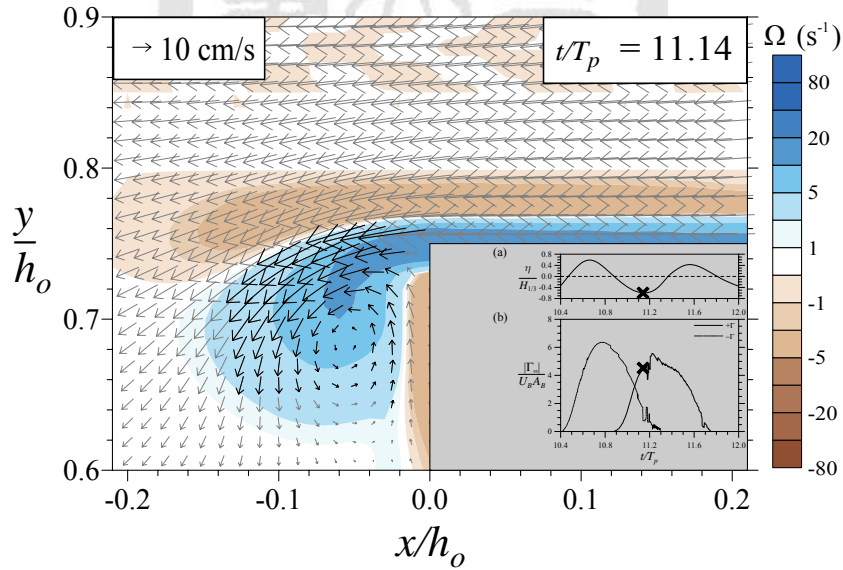
Figure 6.12: A sequence of flow fields with the contours of vorticities shows the life cycle of the counterclockwise vortex indicated in Figure 6.6(b). The surface elevation and the circulation $\left|\Gamma_{95}\right|$ were denote both in mark and the location of the vortical centers $\left(x_c / h_o, \; y_c / h_o\right)$ were showed. The phase of each flow fields is: (a) $t/T_p = 11.07$; (b) $t/T_p = 11.14$; (c) $t/T_p = 11.18$; (d) $t/T_p = 11.27$; (e) $t/T_p = 11.38$; (f) $t/T_p = 11.44$; (g) $t/T_p = 11.53$. (*continued on next page*)

(c) $\left(x_c/h_o, \ y_c/h_o\right) = \left(-0.070, \ 0.722\right)$
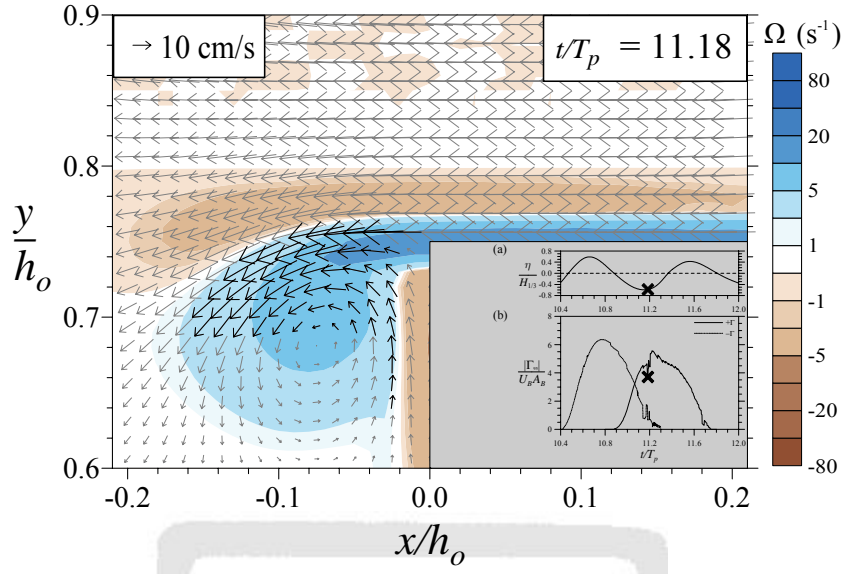
(d) $\left(x_c/h_o, \ y_c/h_o\right) = \left(-0.083, \ 0.708\right)$
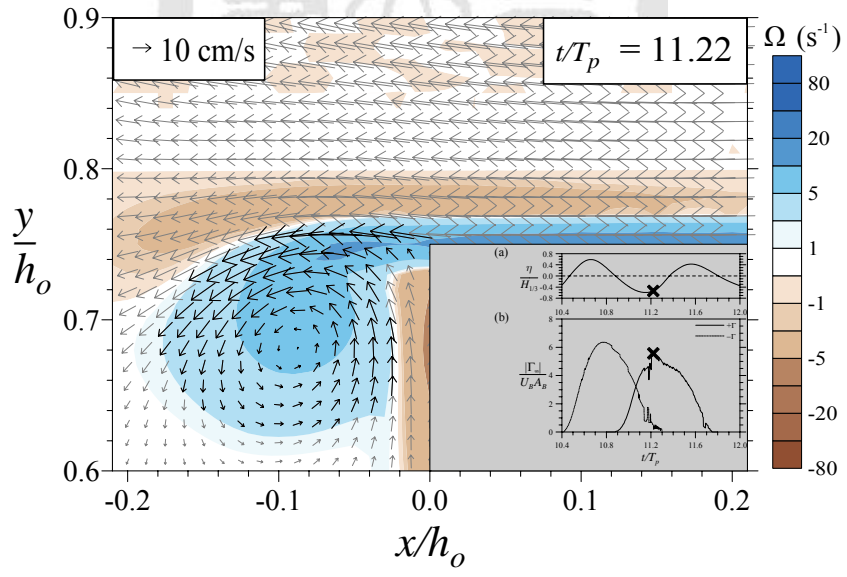
Figure 6.12: (*continued on next page*).

(e) $\left(x_c/h_o,\ y_c/h_o\right)=\left(-0.106,\ 0.733\right)$
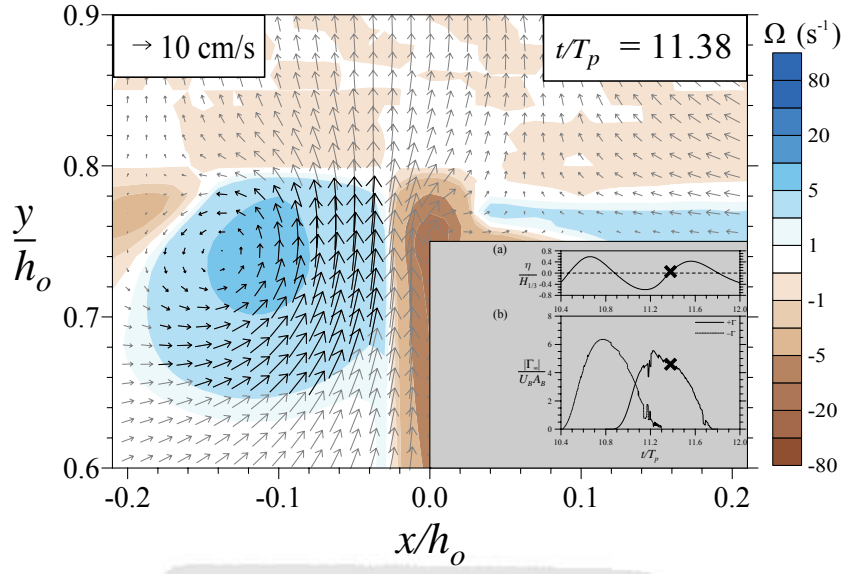
(f) $\left(x_c/h_o,\ y_c/h_o\right)=\left(-0.097,\ 0.755\right)$
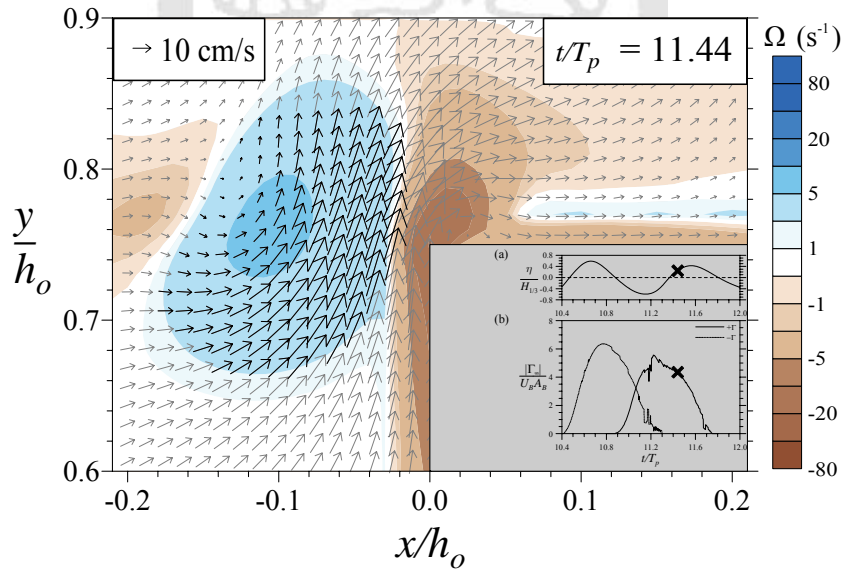
Figure 6.12: (*continued on next page*).

(g) $(x_c/h_o,\ y_c/h_o) = (-0.071,\ 0.789)$
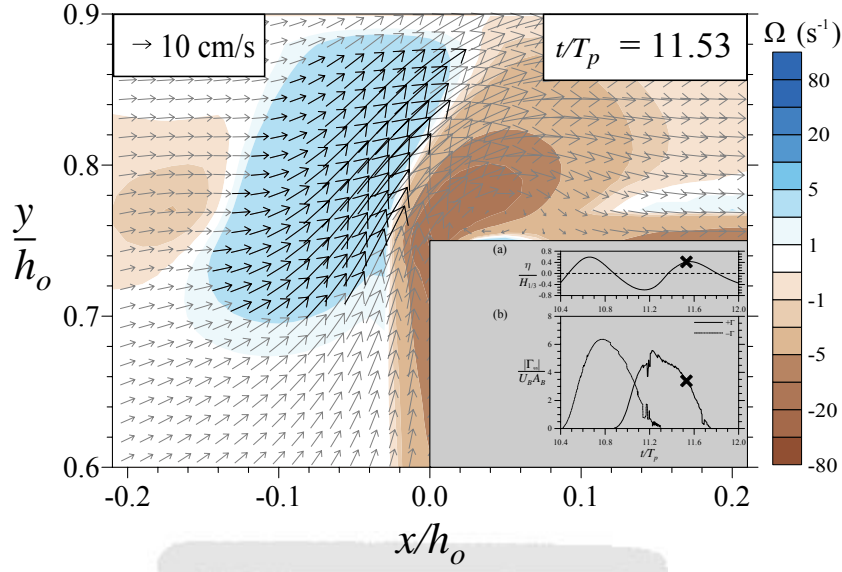
Figure 6.12: (*continued*).

The life cycle of the counterclockwise vortex, which has been presented in Figure 6.6(b) and Figure 6.7(b), is shown in Figure 6.12.   The counterclockwise vortex in Figure 6.12(a) was formed in front of the breakwater and introduced by the negative velocities which followed with the coming wave trough.   When the wave trough arrived in Figure 6.12(b), the location of the MAV, which is at the corner of the breakwater, differs from that of the swirling center, which was at about $(x/h_o,\ y/h_o) = (-0.5,\ 0.69)$.   This resulted the vorticity contour in Figure 6.12(b) are neither convex nor centralized at the location of the MAV.
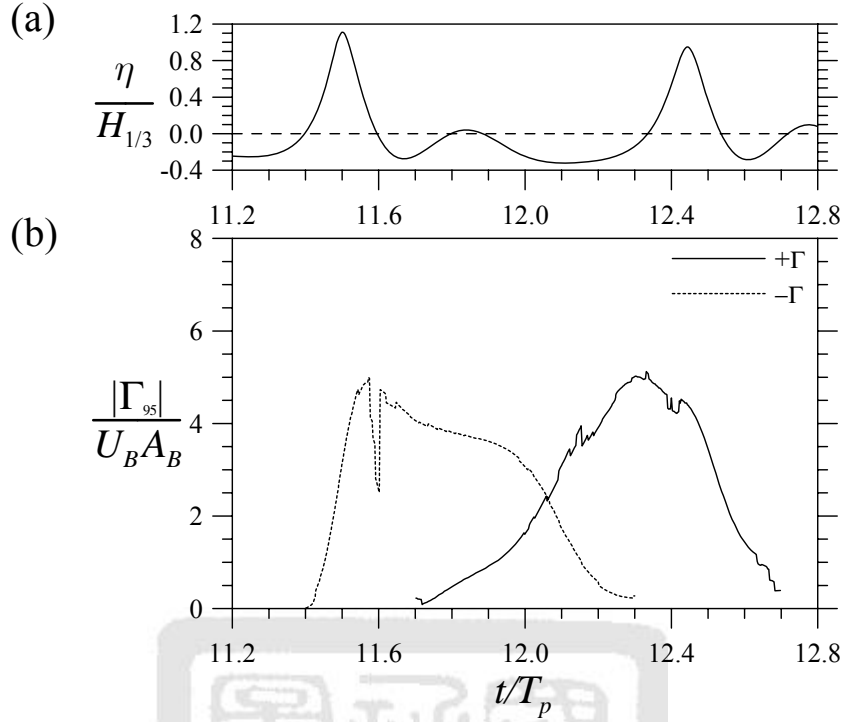
Figure 6.13: The circulations $|\Gamma_{95}|$ of the clockwise vortex and the counterclockwise vortex at the lee side in Case 6.4. The wave elevation was measured at $x/L_p = 0.5$.

In the case of the counterclockwise vortex at the weather side, large positive vorticities are initially induced by the negative horizontal velocities above the breakwater and convected into the deep water region in front of the breakwater. Thus, the vorticities convected downward and introduced the swirling velocities in the deep water. However, the velocities above the breakwater continuously decreasing until reaching the minimum at the wave trough and the MAV reaches its maximum value at the corner of the breakwater, and results the discrepancy at $t/T_p = 11.18$ of the circulation of the counterclockwise vortex in Figure 6.10. Figure 6.12(c) offers a clear view of the discrepancy, and shows that the procedure described at Section 6.4.2 cannot catch the all of the vortical region below $y/h_o = 0.69$ since the contours of the vorticities were not convex and not

centralized on the MAV.   Thus the lack of the selected elements introduces the circulation measured by using Eq. (6.10) has a value smaller than that at $t/T_p = 11.14$ or 11.22. The same phenomena appeared at the lee side of the breakwater when the positive velocities introduce a clockwise vortex behind the breakwater, and thus introduced a smaller measures within the life cycle of a vortex.   This distortions can be seen in Figure 6.10 at $t/T_p = 11.18$ of the counterclockwise vortex at the weather side and in Figure 6.13 at $t/T_p = 11.60$ of the clockwise vortex at the lee side.

Although the vorticity contours are not convex and the swirling center is parted from the location of the MAV in Figure 6.12(d), the maximum circulation was well-measured and the region of the vortex was well-described.   In Figure 6.12(e), the counterclockwise vortex was lifted by the upward vertical velocities and another clockwise vortex, which was with the circulation of duration $t/T_p = 11.3 \sim 12.0$ shown in Figure 6.10, was formed at the corner of the breakwater.   Swirling velocities of the counterclockwise vortex can be found at about $(x/h_o,\ y/h_o) = (-0.14,\ 0.74)$ and the vortical structure is near disappear, although the contours of the vorticities are convex enough and centralized at the location of the MAV.   In Figure 6.12(f) of the timing $t/T_p = 11.44$, the vorticity was strongly affected by the clockwise vortex at the corner.

In Figure 6.12(g), the vortical structure of the counterclockwise vortex was not observed and the contours of the positive vorticities were affected by the negative one, which introduced by the clockwise vortex at the corner.   Thus, the circulation of the region within the contours of the positive vorticities decreases in higher speed than that

before $t/T_p \approx 11.44$. The phenomenon can be revealed by measuring the decreasing rate

of the circulation of the counterclockwise vortex ($+\Gamma$) in Figure 6.10, where two

decreasing rate are clearly distinguished. Before $t/T_p = 11.44$, the counterclockwise

vortex was not affected by the clockwise vortex, which formed at about $t/T_p = 11.3$, and

was with a decreasing rate $d|\Gamma_{95}|/dt \approx -0.008$ m^{2}s^{-2}. After $t/T_p = 11.44$ as shown in

Figure 6.12(f) and 6.12(g), the clockwise vortex at the corner of the breakwater became

stronger and sped up the decreasing rate of the circulation of the counterclockwise vortex,

which is $d|\Gamma_{95}|/dt \approx -0.026$ m^{2}s^{-2}. It seems that the successive-formed clockwise

vortex increased the decreasing rate about three times the original decreasing rate.

6.4.6   Circulations at the lee side

At the lee side of the breakwater, clockwise vortices are formed behind the submerged

breakwater, and counterclockwise vortices are formed above the submerged breakwater.

Figure 6.13 shows the circulation of a clockwise vortex ($-\Gamma$) and a counterclockwise

vortex ($+\Gamma$) of Case 6.4 with the surface elevation at $x/L_p = 0.5$. The discrepancy at

$t/T_p = 11.60$ of the clockwise vortex at the lee side is caused by the same reason of that of

counterclockwise vortices at the weather side.

At the weather side, the circulation-decreasing rate of a counterclockwise vortex in

front of the breakwater was affected by the successive-formed clockwise vortex at the

corner of the breakwater. Similarly, the circulation-decreasing rate of the clockwise

vortex behind the breakwater was affected by the successive-formed counterclockwise

vortex. In the region of the lee side, typically counterclockwise vortices should be

formed and strengthened at the wave trough. However, the formation process of counterclockwise vortex in Figure 6.13(b) was diminished by the higher order free wave in the trough and results a longer formation process. It took about $t/T_p = 0.6$ for the counterclockwise vortex to reach the maximum circulation $|\Gamma_{95}|$.

The clockwise vortex $(-\Gamma)$ in Figure 6.13(b) formed with the higher increasing rate, which is about $d|\Gamma_{95}|/dt \approx 0.054 \text{ m}^2\text{s}^{-2}$, and was resulted by the sharpened wave crest. The breakdown process of the clockwise vortex has two decreasing rates separated at about $t/T_p = 12.0$, when the successive-formed counterclockwise vortex was strong enough. Before $t/T_p = 12.0$, the circulation of the counterclockwise vortex was with the decreasing rate $d|\Gamma_{95}|/dt \approx -0.006 \text{ m}^2\text{s}^{-2}$, and with the decreasing rate $d|\Gamma_{95}|/dt \approx -0.020 \text{ m}^2\text{s}^{-2}$ after $t/T_p = 12.0$. Similar with the results at the weather side, the successive-formed counterclockwise vortex increased the decreasing rate of the clockwise vortex about three times the original decreasing rate.

6.4.7　Properties beneath the irregular waves

Since the procedure in Section 6.4.3 was well-programmed and has the ability to automatically detect vortices, the circulations of the vortices around the breakwater in the period T_{R1} can be quantified and shown in Figure 6.14.

The life cycle of the vortices in $t/T_p = 10 \sim 14$ have similar pattern with that shown in Figure 6.11, in which four large waves were observed in the surface elevation. One of them has been discussed detailly in Sections 6.4.4 to 6.4.6. In $t/T_p = 8 \sim 10$, the vortices formed by the small waves can be distinguished by zero-valued circulation. In

$t/T_p = 10 \sim 14$, although the circulations were seldom zero, the clear pattern makes the life cycle of the vortices be identified with no difficult. However, after $t/T_p = 14$, the successive small waves resulted that the vortices lasted for longer duration since the associated velocities were not huge enough to eliminate the vortex. The clockwise vortex in $t/T_p = 16 \sim 18$ strongly evidenced this phenomena. Similar phenomena was appeared in the vortices at the lee side in Figure 6.14(b) if a large wave was followed by several small waves. It shows that the wave sequences or wave phases are important for determining the vortex pattern or the last duration of a vortex.

Figure 6.14(b) shows the circulations at the lee side with the surface elevation measured at $x/L_p = 0.5$. The shallow water region made the subharmonics and superharmonics take place, and resulted the sharpened crest and the floated trough. In $t/T_p = 11 \sim 15$, there are four large wave components, which has the wave crest exceed $0.7 H_{1/3}$ and three waves with small heights and shorter periods in between. The vortices formed in $t/T_p = 11 \sim 15$ were with similar pattern of the vortices discussed in Section 6.4.6. Note that the sharpened crests made the maximum circulations $\left|\Gamma_{95}\right|$ of the clockwise vortex $(-\Gamma)$ were near that of the counterclockwise vortex.

For studying irregular waves, the statistical manner is inevitable. Because the reflected waves in between the wavemaker and the breakwater has not been eliminated, the duration T_R of the irregular waves has only 16 s, which is not sufficient for a good statistical study. Hence, the statistical properties of vortex dynamics were not considered herein.
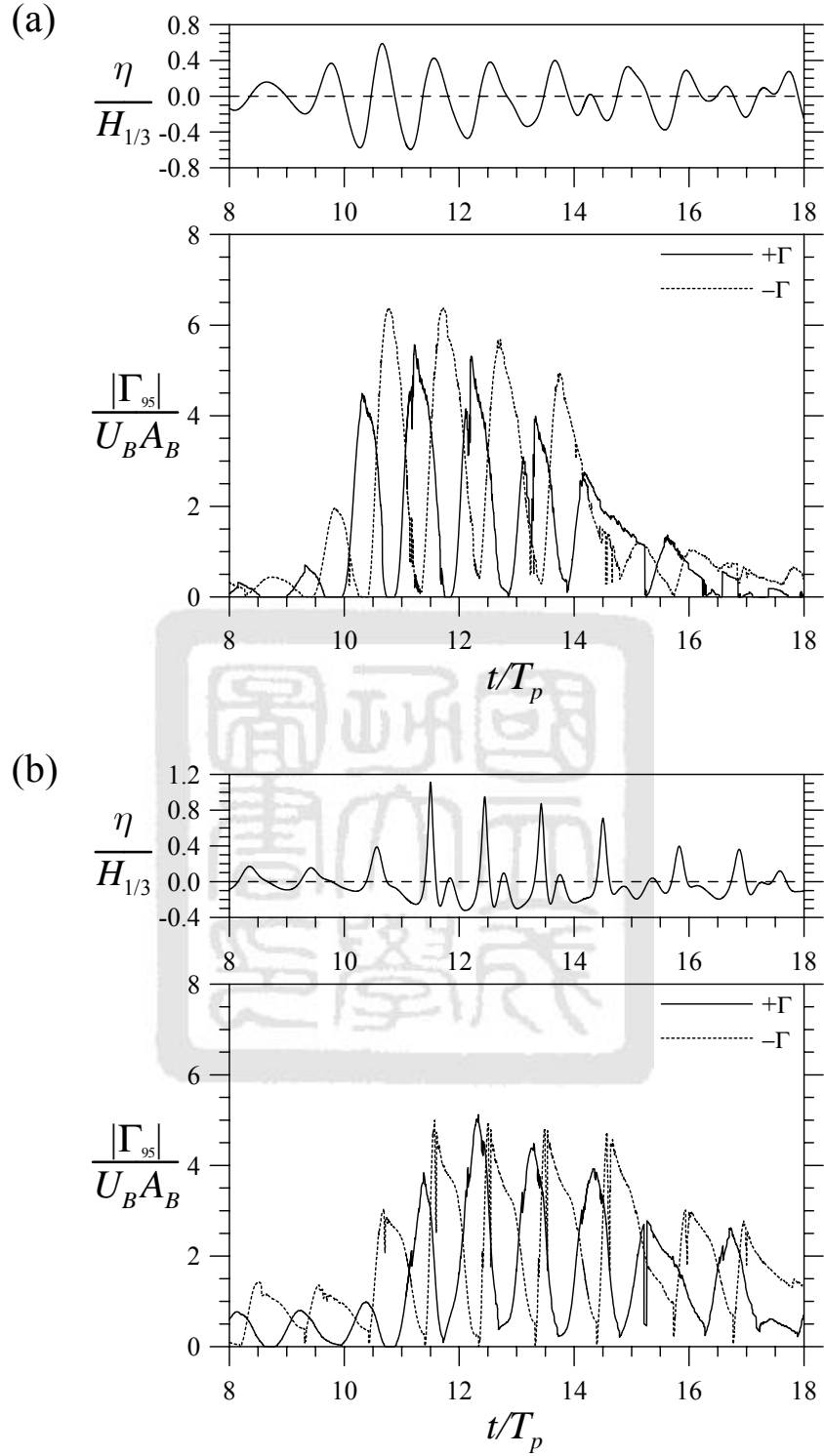
Figure 6.14: The variation of vortex circulation $\left|\Gamma_{95}\right|$: (a) at the weather side, and (b) at the lee side of the breakwater in Case 6.4. The wave elevation is measured at $x/L_p = 0$ and $x/L_p = 0.5$ respectively.

6.5   Chapter remark

The main conclusions from the study of this chapter can be summing up briefly:

1. Base on the repeatable property of the numerical wave tank, the reflected waves were identified by subtracting the surface elevation of Case 5.1, which was the pure incident waves, from that of Cases 5.2 to 5.5 without assumptions.

2. By comparing the reflected coefficients spatially, the time period $T_{R1} = 12 \sim 28 \text{ s}$ was without the reflected waves from the wavemaker with the spectral-peak phase velocity $c_p = 1.77 \text{ m/s}$ and the distance 16 m between the wavemaker and the breakwater.

3. The vorticity-major method were stated and the vorticity threshold $\Omega_T = 0.05|\Omega|_{max}$ applied.   By means of this method, the region of the vortices were selected automatically and the properties of the vortices can be calculated if the vortex centered on the location of the MAV.

4. The normal pattern of the lifecycle of the vortices were as results shown in Figures 6.10 and 6.13.   At the both sides of the breakwater, although the lifecycle of the vortices was different, the breakdown process of the vortices next to the breakwater was always affected by the formation process of that above the breakwater, and had two distinguishable breakdown rate.

5. The lifecycle within the irregular wave train had similar patterns before large wave packet, and differed while large wave followed by small waves, which induced the flow motion not sufficient to diminish the vortex formed by large waves.   Thus, the vortex

formed by large waves last for a longer duration.

Chapter 7 Vortex dynamics above rigid vortex ripples

"That is the essence of science: ask an impertinent question, and you are on the way to the pertinent answer."

—*Jacob Bronowski,*
British mathematician

7.1   Dimensional analysis

As bed flow moves back and forth above sandy bed with the Shields number (defined in Eq. (7.3)) larger than a critical value, the shear stress make sands roll over bed, pile together and then form several small bumps.   This is an initial stage of ripple formation. If the distance or wavelength of the bumps was large than the bed orbital amplitude, a steady streaming (Rousseaux et al., 2004), was formed between the bumps and rolling sands were transported by the shear stress of fluid.   In this stage, ripple pattern was dominant by sand properties, i.e. medium grain size d_{50}, particle density ρ_s, and fluid density ρ.

When the bump's height is large enough, the oscillating flow forms separation

bubbles of both sides of the bumps. Reversal flow of the separation bubbles introduces near-bed offshore (onshore) flow while the free stream is in onshore (offshore) direction. Consequently, the shear stress is increase of both slopes of the bumps and results sediment transport from the flat bed to the bumps' top. This procedure is treated as a steepening process, and goes on until the slopes of ripples reach the angle of repose, which is the maximum angle of a stable slope of particles.

While the same hydraulic condition last for only a short duration (less than about $O(10^3 tf)$, which was suggested by Rousseaux, 2006) and the steepness H_r/L_r less than 0.1, an equilibrium state is reached and named as rolling-grain ripples, in which the ripple form is only base on the grain properties and length of the almost horizontal troughs are always irregular since the initial piled locations are random.

While two rolling-grain ripples are close enough, with a distance or wavelength L_r, or the hydraulic condition are sufficiently huge, say $A_o/L_r > 0.4$, vortices form on the both slopes of the ripples. If the vortex is strong enough, sands are picked-up by the vortices and settle down when the vortex is weak. A new sharpening process is formed by the organized vortices until the new equilibrium state is reached, and named as vortex ripple.
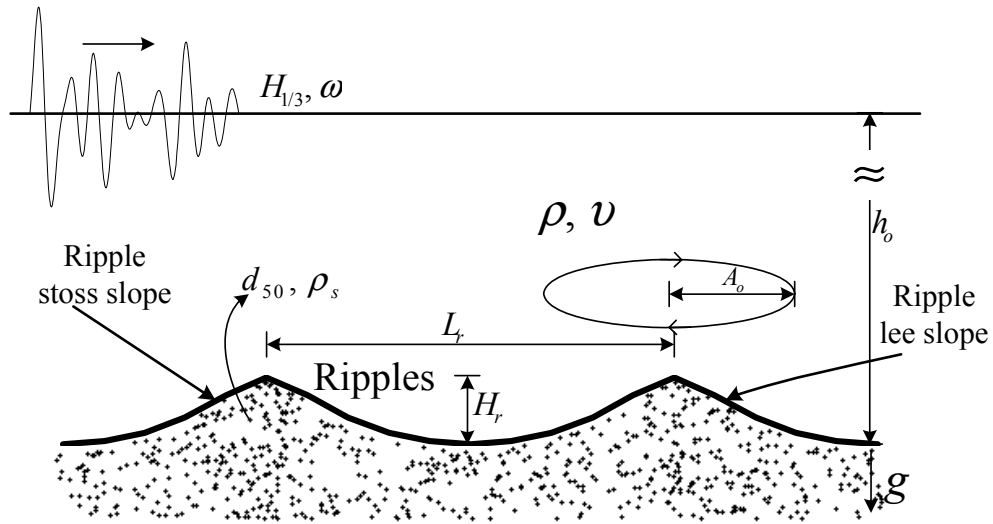
Figure 7.1: The ripple geometry (not to scale) and the associated parameters.

Regarding waves over vortex ripples as shown in Figure 7.1, the following dimensional quantities were considered:

H or $H_{1/3}$ —wave height or significant wave height ($[L]$)

ω or ω_p —angular frequency or spectral-peak angular frequency ($[T^{-1}]$)

υ —fluid kinematic viscosity ($[L^2 T^{-1}]$)

H_r —ripple height ($[L]$)

L_r —ripple wavelength ($[L]$)

A_o —bed-orbital-displacement amplitude ($[L]$)

U_o —bed-orbital-velocity amplitude ($[LT^{-1}]$)

h_o —still water depth ($[L]$)

k_s —the Nikuradse roughness ($[L]$)

where the bracket denotes the dimension, L the length, and T the time.

There are nine dimensional quantities and two fundamental dimensions, time and space, in such a problem. Hence, seven nondimensional quantities can be formed. Chosen ω as the reference of time and A_o as the reference of length, we have

$$\frac{\omega A_o^2}{\upsilon} = f\left(\frac{H}{A_o}, \ \frac{U_o}{\omega A_o}, \ \frac{h_o}{H_r}, \ \frac{H_r}{L_r}, \ \frac{A_o}{L_r}, \ \frac{A_o}{k_s} \right) \tag{7.1}$$

The parameter $U_o/\omega A_o$ is unit for linear regular waves, and $H/A_o = 2\sinh(kh_o)$ is determined when a frequency was chosen. For vortex ripples, the Nikuradse roughness was defined as $k_s = 20H_r^2/L_r$ (Van Rijn, 1993). Since the interaction of flow and ripples are major within the vortex layer beneath $y < 2H_r$ (Ranasoma and Sleath, 1992; Davies and Thorn, 2005) or $y < k_s$ (Marin, 2004), which is far smaller than the water depth h_o, the water depth became unimportant. The parameter $\omega A_o^2/\upsilon$ is defined as the bed-orbital Reynold number in the present study. The parameter A_o/k_s is used to confirm whether turbulent effects take a leading part in or ont. If $A_o/k_s > 30$, momentum transfer is no more dominated by vortex but by random turbulent process (Trowbridge and Madsen, 1984).

If sediment transport were considered, the dimensional analysis becomes more complex and four new dimensional quantities have to be concerned:

ρ —density of fluid ($[ML^{-3}]$)

d_{50} —medium grain diameter ($[L]$)

ρ_s —density of the sediment ($[ML^{-3}]$)

w_s —settling velocity ($[L^2T^{-1}]$)

where M denotes the mass. And implies three non-dimensional quantities: the specific density $s = \rho_s / \rho$; the ratio of bed-orbital-displacement amplitude to median grain size, A_o / d_{50}; and the normalized settling velocity w_s / U_o.

In general, the relative density s is about 2.65 for the density of glass spheres or quartz sand to that of water, and is constant in the present study. The ratio of bed-orbital-displacement amplitude to medium grain diameter is important for rolling-grain ripple, and not for vortex ripple. This quantity is replaced by the ripple-adjusted Shields parameter (Nielsen, 1986):

$$\theta_r = \frac{\theta'}{\left(1 + \pi \dfrac{H_r}{L_r}\right)^2} \tag{7.2}$$

where the maximum Shields parameter θ' and the maximum shear stress τ_{max} are:

$$\theta' = \frac{\tau_{max}}{\rho g(s-1)d_{50}} \tag{7.3}$$

and

$$\tau_b' = \frac{1}{2} \rho f_w U_o^2 \tag{7.4}$$

The coefficient f_w is the resistance factor and defined as follows.

For laminar flow over smoothed bed:

$$f_w = 2Re_o^{-0.5} \tag{7.5a}$$

For rough bed (Swart,1974):

$$f_w = \exp(-5.977 + 5.213(A_o / k_s')^{-0.194}) \quad \text{for} \quad A_o / k_s' > 1.59 \tag{7.5a}$$

The skin roughness $k_s' = 2.5d_{50}$ is the roughness along ripple surface. The ripple-adjusted Shields parameter was used for confirmed that no sediment transport was occurred beneath the tested hydraulic conditions physically. Since the present numerical model can simulate only rigid ripple, the numerical settling velocity, which used to identify sediment rate, was not considered herein.
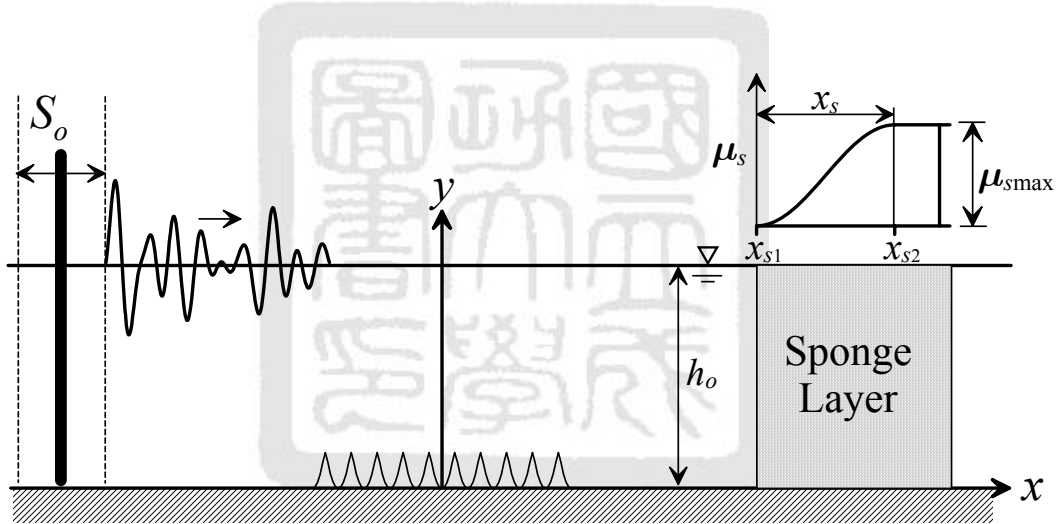
Figure 7.2: Schematic diagram (not to scale) of a numerical wave tank for studying irregular waves over rigid vortex ripples.

By means of the curvilinear coordinate mentioned in Chapters 2 and 3, this chapter examined the vortex dynamic of waves over ripples. Figure 7.2 shows the schematic of the numerical model for studying irregular waves over rigid vortex ripples. Ten ripples were set up. The x-axis is measured horizontally in the direction of wave propagation from the center of the ripples. So that the center of the ripples is $x = 0$ and two edges

are at $x = \pm 5L_r$. The distance between wavemaker and ripples is about $2L_p$, where L_p is the spectral-peak wavelength. The grids for studying waves over rippled beds are generated and shown in Figure 7.3. The y-axis is measured vertically upwards from ripple trough. The still water depth is h_o.

7.2 Ripple form

The natural shape of vortex ripple and the equilibrium state of ripple steepness H_r/L_r should be taken into account for a good simulation. The approximated form of natural sea ripples are suggested by many researchers, and the Sleath form (Sleath, 1984) were used

$$x = \xi_o - 0.5 H_r \sin\left(2\pi\xi_o/L_r\right) \tag{7.6a}$$

$$y = 0.5 H_r \left(\cos\left(2\pi\xi_o/L_r\right) + 1\right) \quad \text{for } |x| \leq L_r \tag{7.6b}$$

$$y = 0 \quad \text{for } |x| > L_r \tag{7.6c}$$

where ξ_o is a shape factor used to describe the ripple surface.

The bottom boundary in Figure 7.3 is the bed form generated by Eq. (7.6). The ripple shape with approximately triangular crest and flatten trough satisfies with the evidence obtained by the experiments of Stegner and Wesfreid (1999). The equilibrium state of ripple steepness H_r/L_r has been stated with different manner, experiments (Wiberg and Harris, 1994; Sistermans, 2002; Davis, 2005; Admiraal et al., 2006; Lacy et al., 2007), field measurements (Traykovski et al., 1999; Hanes et al., 2001; Ardhuin et al., 2002; Masselink et al., 2007; Traykovski, 2007). An acceptable pattern of vortex ripple is

that the ripple wavelength is about the bed-orbital-displacement amplitude, and the ripple steepness is about 0.17 (Wiberg and Harris, 1994). By using the formula of Khelifa and Ouellet (2000) with medium sand size $d_{50} = 242\,\mu\text{m}$, which is a finer sand case of Davis' (2005) study, we have

$$\psi = \frac{U_o^2}{(s-1)gd_{50}} = \frac{U_o^2}{3.92 \times 10^{-3}} \tag{7.7 a}$$

$$\frac{L_r}{A_o} = 1.9 + 0.08\left(\ln(1+\psi)\right)^2 - 0.74\ln(1+\psi) \tag{7.7 b}$$

$$\frac{H_r}{A_o} = 0.32 + 0.017\ln^2(1+\psi) - 0.142\ln(1+\psi) \tag{7.7 c}$$

Although the present numerical model is using for solid and impermeable bed only, these parameters, L_r/A_o and H_r/L_r, were referred to design reasonable test cases in this study.
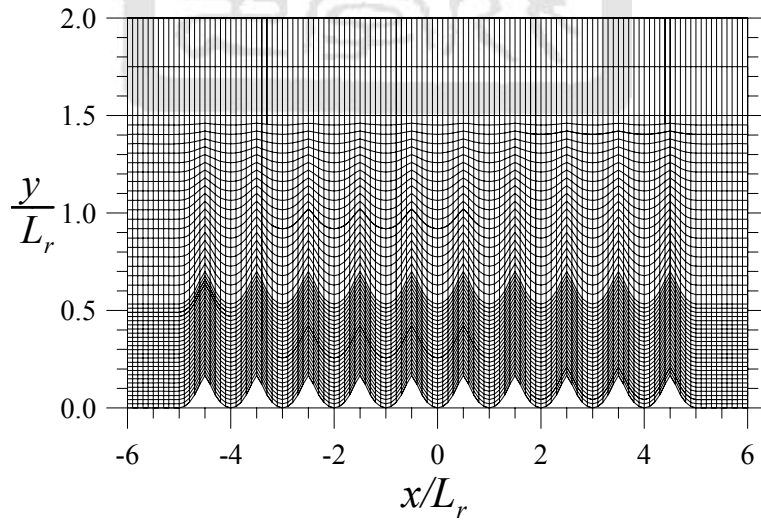
Figure 7.3: Numerical grids about the ripples.

7.3 Validation and numerical conditions

With applying curvilinear boundary to form rippled bed, as shown in Figure 7.3, the present numerical model can deal with the problem that waves propagating over ripples. For ensuring the accuracy of the present model, validation was carried out by comparing the numerical results with experimental one. Marin (2004) made a series of experiments ranged from transitional to full turbulent flow. Test 1, a transitional flow case, of Marin's tests was compared with the numerical results with the identical wave condition and was shown in Figure 7.4, where $\delta = \sqrt{\upsilon/\omega}$. The agreement in Figure 7.4 indicates the present numerical model is good in describing this problem within the transitional regime.
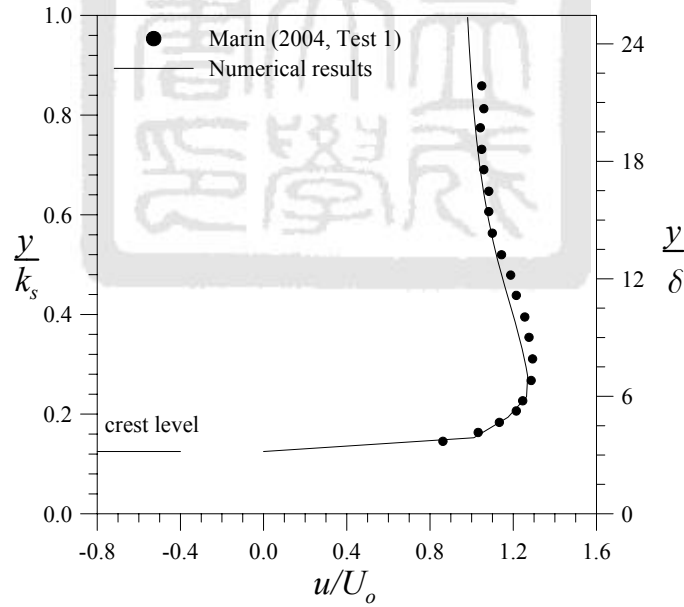
Figure 7.4: Comparison of numerical results (solid line) and the experimental one (solid circles) of Marin (2004, Test 1). The associated conditions are with $h_o = 27$ cm, $H = 4.8$ cm, $T = 1.08$ s, $Ur = 5.38$, $A_o/L_r = 0.947$, $H_r = 0.3$ cm, $L_r = 1.8$ cm.

The numerical conditions in this study were built base on this comparison and the equilibrium ripple pattern mentioned in Section 7.2. When a wave with period $T = 2.0$ s, wave height $H = 4$ cm propagates unidirectionally in water with the depth $h_o = 30$ cm, the bed orbital amplitude of this wave is $A_o = 3.27$ cm and thus the ripple wavelength was designed to be $L_r = 3$ cm to satisfy $A_o/L_r \approx 1$. By means of Eq. (7.7) with $A_o = 3.27$ cm, we have a steepness $H_r/L_r \approx 0.153$, hence the ripple height is about $H_r = 0.45$ cm. For the sake of simplicity, the ripple height $H_r = 0.5$ cm was selected, which led to the steepness $H_r/L_r \approx 0.167$ and still within the equilibrium state $H_r/L_r \approx 0.15 \sim 0.17$.

Table 7.1: List of wave conditions.

Case	Type	$H_{1/3}$ (cm)	A_o (cm)	A_o/L_r	Ur	Re_o	U_oL_r (cm^2/s)
7.1		1.5	1.23	0.41	5.90	469	11.6
7.2	Regular	4.0	3.27	1.09	15.72	3338	30.83
7.3		5.5	4.50	1.50	21.62	6311	42.39
7.4		1.5	1.02	0.41	5.90	333	9.8
7.5	Irregular	4.0	2.86	1.09	15.72	2432	25.7
7.6		5.5	4.12	1.50	21.62	4703	34.5

Three regular-wave cases, Cases 7.1 to 7.3 with $L_r/A_o = 0.41, 1.09, 1.50$ respectively, were tested to reveal the properties on and off the equilibrium state. Although some researchers stated that ripple form beneath irregular waves was differed from that of regular waves, the bedform was also used for irregular-wave cases in order to have an identical environment and comparable results. The bed orbital properties of irregular waves defined in Chapter 4 were applied herein:

$$U_o = U_{rms} = \sqrt{2\int_0^\infty \frac{\omega^2 S_\eta(\omega)}{\sinh^2 kh_o} d\omega}$$ (7.8 a)

$$A_o = A_{rms} = \sqrt{2\int_0^\infty \frac{S_\eta(\omega)}{\sinh^2 kh_o} d\omega}$$ (7.8 b)

The non-dimensional quantities, Re_o and A_o/k_s, of the listed cases are ploted in Figure 7.5 and are in transitional regime. This indicated that the present numerical model can simulate these flow motion very well. Since the parameter A_o/k_s were not exceeded over 30, the flow or momentum transfer were dominated by organized vortex, not by random turbulent process.
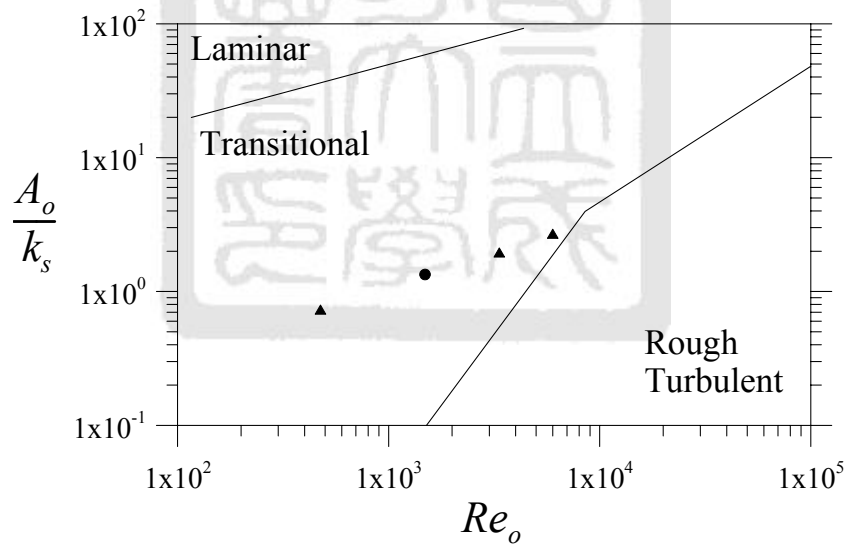
Figure 7.5: Delineation of flow regime proposed by Davies (1980), indicating the boundaries between laminar, transitional and rough turbulent oscillatory flow, in which solid circle denotes Marin (2004, Test 1), and solid triangles the listed cases.

7.4 Vortex properties above ripples

The well-defined properties of vortex were described in Chapter 6 and used here to reveal the vortex dynamics above ripples.   The vorticity is defined as

$$\Omega = \frac{\partial v}{\partial x} - \frac{\partial u}{\partial y} \tag{7.9}$$

The vorticity threshold $\Omega_T = 0.05|\Omega|_{max}$ in order to define the region of a vortex was confirmed in Section 6.4.3.   Applying the threshold, the circulation of a vortex can be defined as:

$$\Gamma_{95} = \sum_{i \in \text{vortex}} \Omega_i A_{\Omega i} \quad \text{for } |\Omega_i| \geq \Omega_T \tag{7.10}$$

where Γ_i, Ω_i and $A_{\Omega i}$ are the circulation of a vortex, vorticity and the area of the i-th numerical element within a vortex respectively.

7.4.1 Vortex circulation

Figure 7.6 shows the temporal variation of circulations of the three regular-wave cases. The surface elevation at $x/L_r = 0$ was shown to compare the phase difference of the surface elevation and the circulations.   The circulations can be regarded as the strength of vorticies, and the process from formation to breakdown of vortices can also be stated by the variation as well.

164
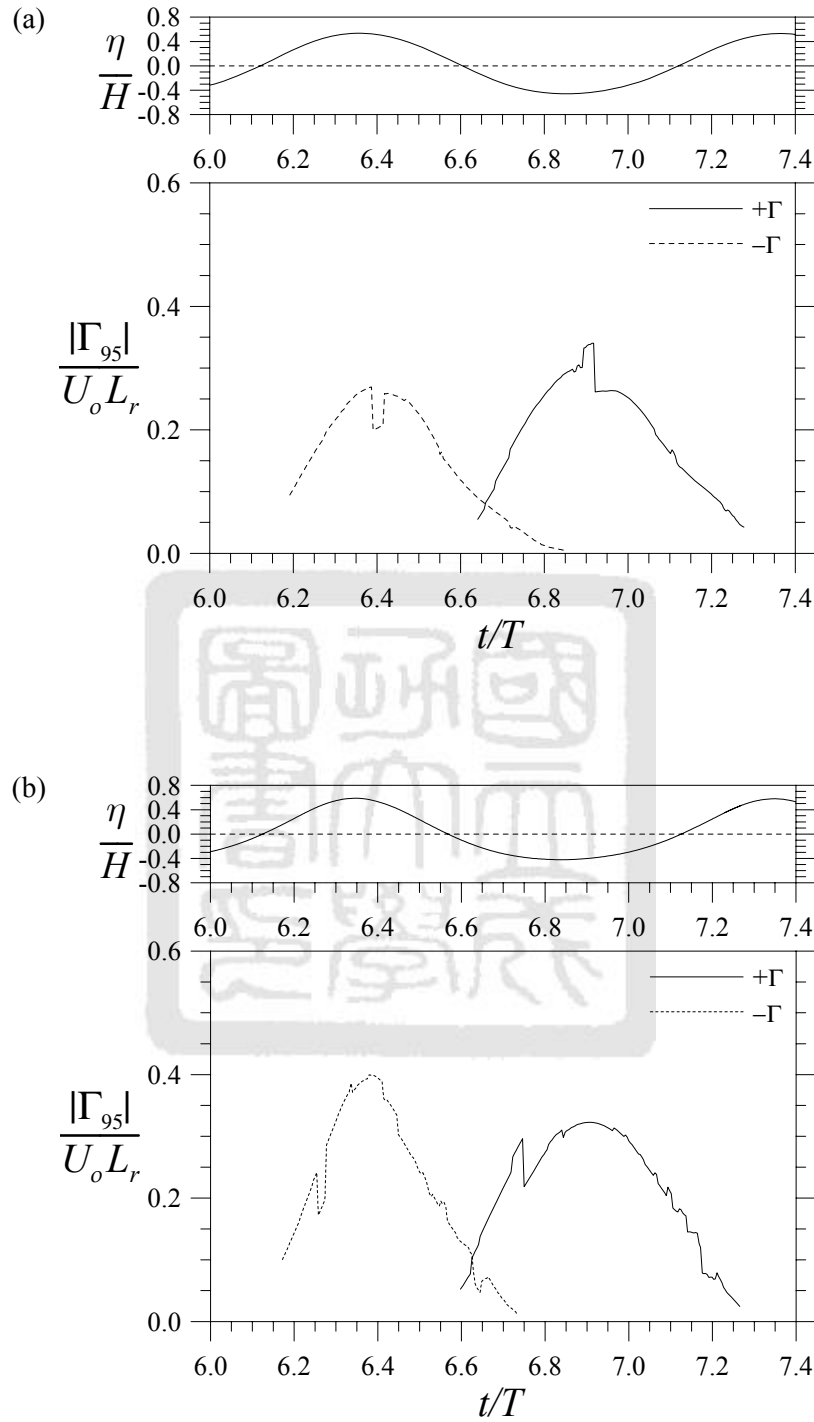
Figure 7.6: Circulations of counterclockwise vortices (+Γ, solid line) and clockwise vortices (−Γ, dashed line): (a) Case 7.1 ($U_oL_r = 1.16 \times 10^{-3}$ m^2/s); (b) Case 7.2 ($U_oL_r = 3.08 \times 10^{-3}$ m^2/s); (c) Case 7.3 ($U_oL_r = 4.24 \times 10^{-3}$ m^2/s). The surface elevation was measured at $x/L_r = 0$. (*continued on next page*)
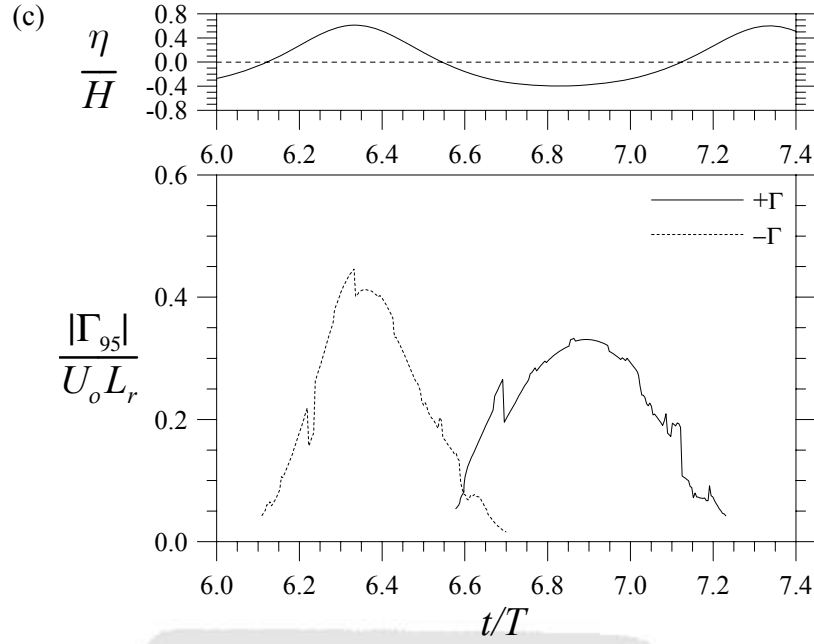
Figure 7.6: (*continued*).

Comparing to Chapter 6, the circulation of vortices above ripples are more disturbed. This disturbed was resulted by the grid resolution and by the vortex properties above ripples. Although it is good enough to describe the boundary layer above ripples, as shown in Figure 7.4, the grid resolution is not sufficiently good to describe the variation of vorticities, which changes quickly about ripple surface. Around a corner of a submerged breakwater, the vortices Within a large wave can be distinguished easily since only one vortex, either clockwise vortex or counterclockwise vortex, dominates the flow. However, series ripples introduce series vortices. When waves propagating over ripples, vortices were formed next to each other and were only with a phase difference about $\Delta\phi = \omega L_r / c$, where c is the phase velocity of waves. In the regular-wave cases, the time difference is about $\Delta\phi = 0.056$. Although the method described in Section 6.4.2 can identify the region of a vortex, the results in Figure 7.6 show the method still have some discrepancy of

vortex recognition.

As afore-mentioned, Case 7.2 was taken as the equilibrium state of regular waves in this hydraulic condition. Since the bedform prescribed by Eq. (7.6) is symmetric, the difference of circulation is determined by the asymmetric property of free stream, which is resulted by the Stokes wave. Consequently, the asymmetric property is increase if the Ursell number is large enough as Case 7.3, and it is nearly symmetric if the Ursell number is small as Case 7.1. Hence, the circulations of Case 7.3 shown in Figure 7.6(c) show large difference in magnitude, and that of Case 7.1 shown in Figure 7.6(a) only a bit difference.

The process of formation and breakdown of the vortices above ripples is similar since the major effects were dominated by oscillating flow motion. In Figure 7.6(b), maximum circulation of the clockwise vortex in equilibrium ripple form (Case 7.2) is about $0.4U_oL_r$. Similar phenomenon can be found in Figure 7.6(c). Although the bed-orbital-velocity amplitude is larger than that of Case 7.2, the maximum vortex strength is limited at $0.4U_oL_r$. The results denote that the vortex development was limited by the ripple form as well as the velocity of the free stream. Similar results can be observed in the following section with the velocity field and the vorticity contours.

7.4.2 Flow field and vorticity contours

Detailed flow motion above a ripple within oscillatory waves has been stated clearly by Van der Werf et al. (2007). In this study, we focus on the flow motion and the associated circulations of vortex, which strongly affects the picked-up and settling process

of sediment transport. Figure 7.7 shows different phases of the velocity field and vorticity contours beneath the surface elevation at $x/L_r = 0$ of Case 7.2 shown in Figure 7.6(b). Seven phases were selected for discussion. Because the surface elevation is in phase with the associated near-bed free stream velocity, we used the surface elevation to evidence the near bed flow motion.

The free-stream velocity was increase in $t/T = 6.281$ and shown in Figure 7.7(b), in which the large near-bed vorticities were introduced by the no-slip condition with large near-bed velocities. A separation bubble formed against ripple lee slope, and this is the first stage that a clockwise vortex can be measured by the procedure showed in Section 6.4.2. The free stream velocity reached the maximum in $t/T = 6.347$. After a while, the circulation of the vortex has its largest value $|\Gamma_{95}|/U_o L_r = 0.399$ at $t/T = 6.375$ shown in Figure 7.7(c). Note that the center of the vortex is close to the ripple lee slope and the extent of the vortex is small than the ripple wavelength. Comparing with Figure 7.7(b), the vortex was extended and shifted toward ripple center $x/L_r = 0$. Furthermore, the reversal flow induced by the separation bubble were on offshore direction and introduced the near bed positive vorticities, and the negative vorticities extended all over the ripple surface.

Pass the wave crest or the maximum circulation, the free stream velocity was decreasing but was not yet zero. At $t/T = 6.5$ shown in Figure 7.7(d), the negative vorticities were transferred to higher location and the swirling velocities had an extent about a ripple wavelength. Because the spatial phase difference introduced by wave

propagating, the magnitude of negative vorticities around the ripple crest at $x/L_r = 0.5$ is larger than that at $x/L_r = -0.5$.

Of Figure 7.6(e), the remained circulation dominated the flow, and the vortex became a weak swirl with large extent at higher location. As discussed in Section 6.4.5, the smaller magnitude of vorticity probably introduced the discrepancy of the calculated vortex center (x_c, y_c) and the swirling center. The calculated vortex center was at $(x_c/L_r, y_c/L_r) = (-0.21, 0.10)$, and the swirling center is at about $(x/L_r, y/L_r) = (-0.2, 0.25)$ by observing Figure 7.7(e), where x_c, y_c are the measured vortex center and defined in the following section. Clearly, the calculated vortex center is lower than the swirling center in this phase.

When the flow moves back, the counterclockwise vortex was formed and dominated the flow. The counterclockwise vortex at the maximum circulation $\left|\Gamma_{95}\right|$ is shown in Figure 7.7(f). The counterclockwise vortex was formed against the ripple stoss slope and centered at $(x_c/L_r, y_c/L_r) = (0.094, 0.140)$.
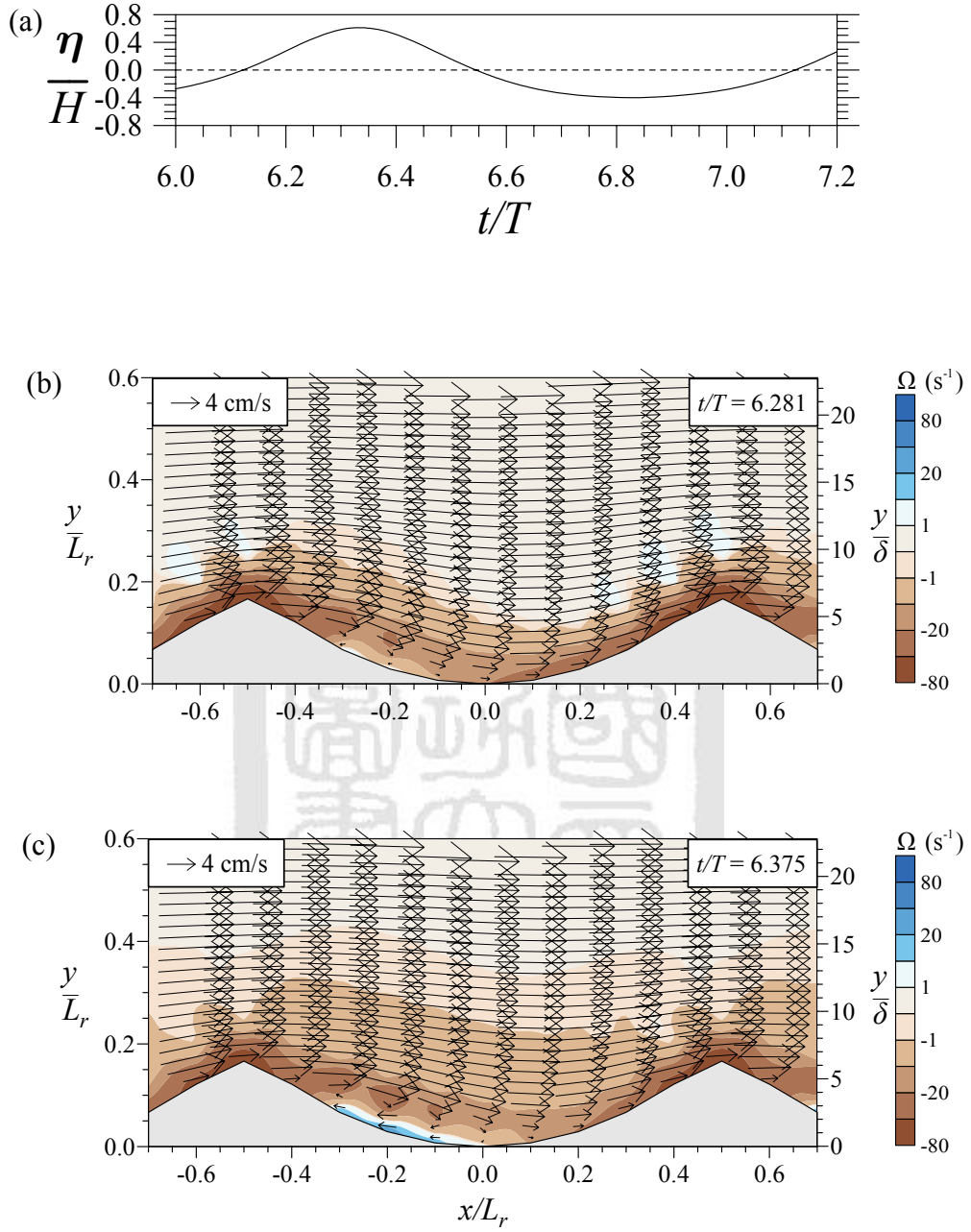
Figure 7.7: The surface elevation, the flow fields, and vorticity contours of Case 7.2 with (a) the surface elevation at $x/L_r = 0$, and flow field at (a) $t/T_p = 6.281$, (c) $t/T_p = 6.375$, (d) $t/T_p = 6.500$, (e) $t/T_p = 6.563$, (f) $t/T_p = 6.906$, (g) $t/T_p = 7.063$, as well as (h) $t/T_p = 7.125$. (*continued on next page*)
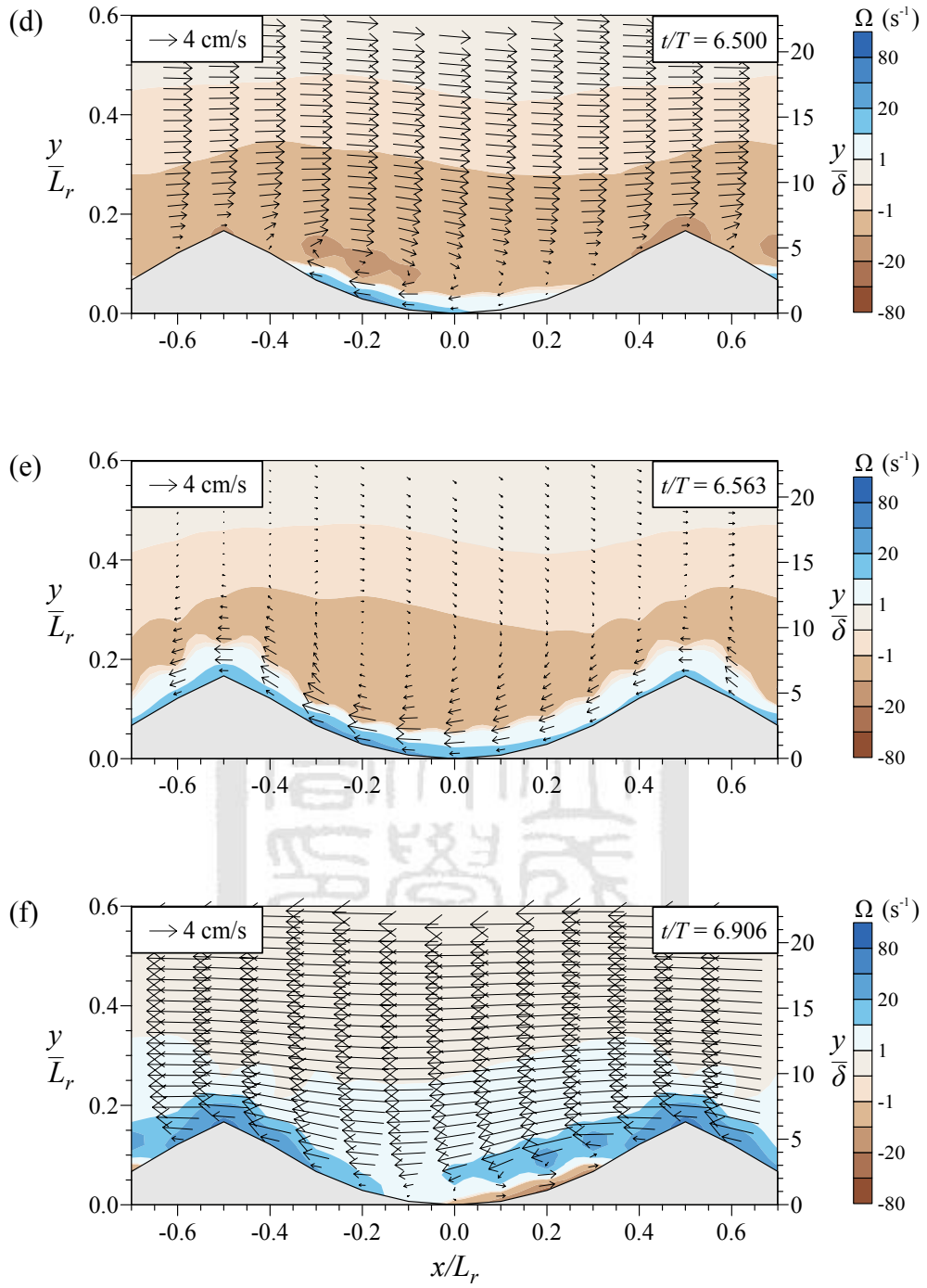
Figure 7.7: (*continued on next page*).
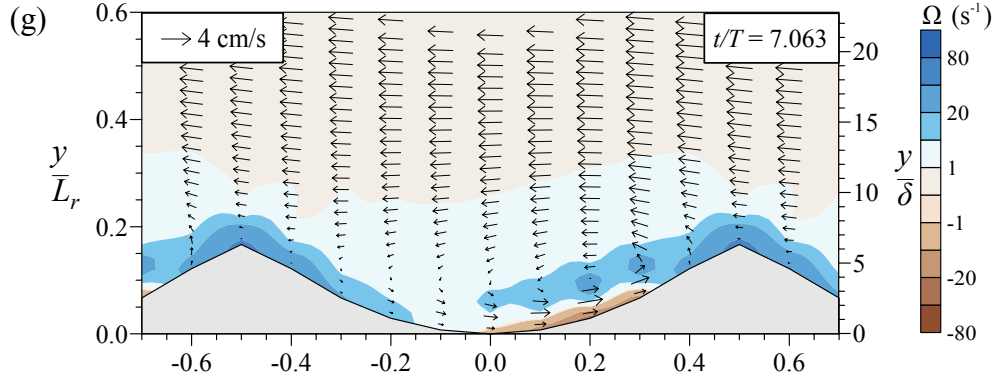
Figure 7.7: (*continued*).

Similar to the clockwise vortex, the circulation of the counterclockwise vortex is decreased but with larger extent in Figure 7.7(g). When the vortex was ejected to higher region in Figure 7.7(h), the counterclockwise vortex is almost disappeared.

7.4.3   Migration of vortex center and strength variation

By tracing the center of a vortex defined in Eq. (7.11), the trajectory of vortex is able to be established. The vortex trajectories can used to realize the vortex motion, the energy transfer, and the further study may reveal the equilibrium state if the process of sand transport is considered. Similar to circulations, the trajectories were also dominated by the selected region of vortex and the grid resolution. Although some discrepancy of trajectory is inevitable, the tendency can be stated.

Figure 7.8 shows the trajectories of the measured vortex center of the regular wave cases, Cases 7.1, 7.2 and 7.3. In Figure 7.8(b), three stages of vortex motion were marked by I_-, II_-, III_- and I_+, II_+, III_+ for the clockwise vortex and the counterclockwise vortex respectively. The center of a vortex can be defined as:

$$x_c = \frac{\displaystyle\sum_{i \in \text{vortex}} \Gamma_i x_{\Omega i}}{\Gamma_{95}} \tag{7.11a}$$

$$y_c = \frac{\displaystyle\sum_{i \in \text{vortex}} \Gamma_i y_{\Omega i}}{\Gamma_{95}} \tag{7.11b}$$

where Γ_i, $x_{\Omega i}$ and $y_{\Omega i}$ are the circulation of a vortex and the position of the i-th numerical element within a vortex respectively.

Of the first stage, I_- or I_+, the circulations of the vortices are from a small initial value to its maximum as the circulation shown in Figure 7.6, and the vortices were moved from ripple slope side toward ripple trough, which can be found at Figure 7.7. This stage can also be stated as the formation process. Of the beginning of the formation, the vortices formed near the ripple slope and moved toward the ripple trough as the increasing of the free stream velocity. Comparing the trajectories of vortex center, the maximum circulations do not appear at the trough but the slope side. This normally results sand picked-up process and change the ripple form.

Of the second stages, II_- and II_+, the vortices moved from the ripple slope side to the ripple center $x/L_r = 0$. Since the center of vortex were measured by weighting with vorticity, the results show the vorticities were convected and extended to cover all ripple region as shown in Figure 7.7(d). The vortex region were extended as well but limited by the ripple crest and by the vortices at $x/L_r = \pm 1$.

173
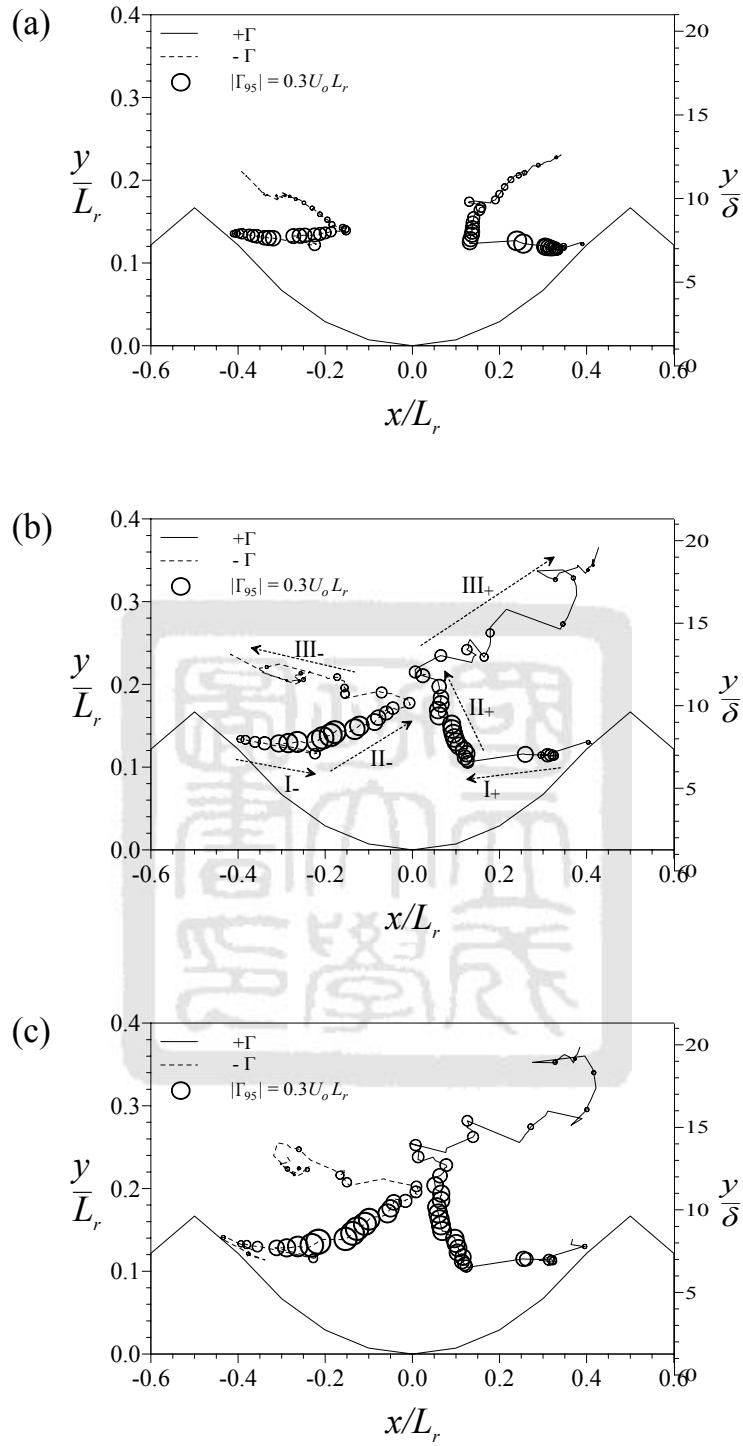
Figure 7.8: Trajectories of vortex center and the magnitude of circulations denoted by open circle with different size: (a) Case 7.1 ($U_o L_r = 1.16 \times 10^{-3}$ m^2/s); (b) Case 7.2 ($U_o L_r = 3.08 \times 10^{-3}$ m^2/s); (c) Case 7.3 ($U_o L_r = 4.24 \times 10^{-3}$ m^2/s). Solid and dashed line showed the trajectory of vortex center calculated by Eq. (7.11) and open circles denote the circulation determined by Eq. (7.10).

In the third stage, III_- and III_+, the circulation was small and moved toward ripple crest.   Note that in small vorticity the method underestimates the location of vortex center, which is lower than the swirling center as shown in Figure 7.7(e).   However, the small circulation denotes that vortices are about breakdown.

7.5   Statistics results of vortex strength beneath irregular waves

Cases 7.4, 7.5 and 7.7 cannot be processed only by the methods using to deal with the results of Cases 7.1, 7.2 and 7.3, because wave elevations are not periodic and the associated vortex characteristics are not regular.   Figure 7.9 states the randomness of irregular waves properly.   The circulations of counterclockwise vortices ($+\Gamma$) and clockwise vortices ($-\Gamma$) were measured automatically with the applied vorticity threshold. Since the ratio of ripple height to water depth can be ignored, the reflected waves introduced by ripples were neglected as well.   Hence, the irregular-wave tests can have longer time duration than that of Chapter 6, and the statistical properties can be measured. Note that of surface elevation there are 24 zero-upcrossing waves but only 22 counterclockwise vortices and 21 clockwise vorticex are counter in Figure 7.9.   Similar to Chapters 4 and 5, the statistical properties of surface elevation can not state the near bed phenomena directly.   Modification has to be made and to build an association.
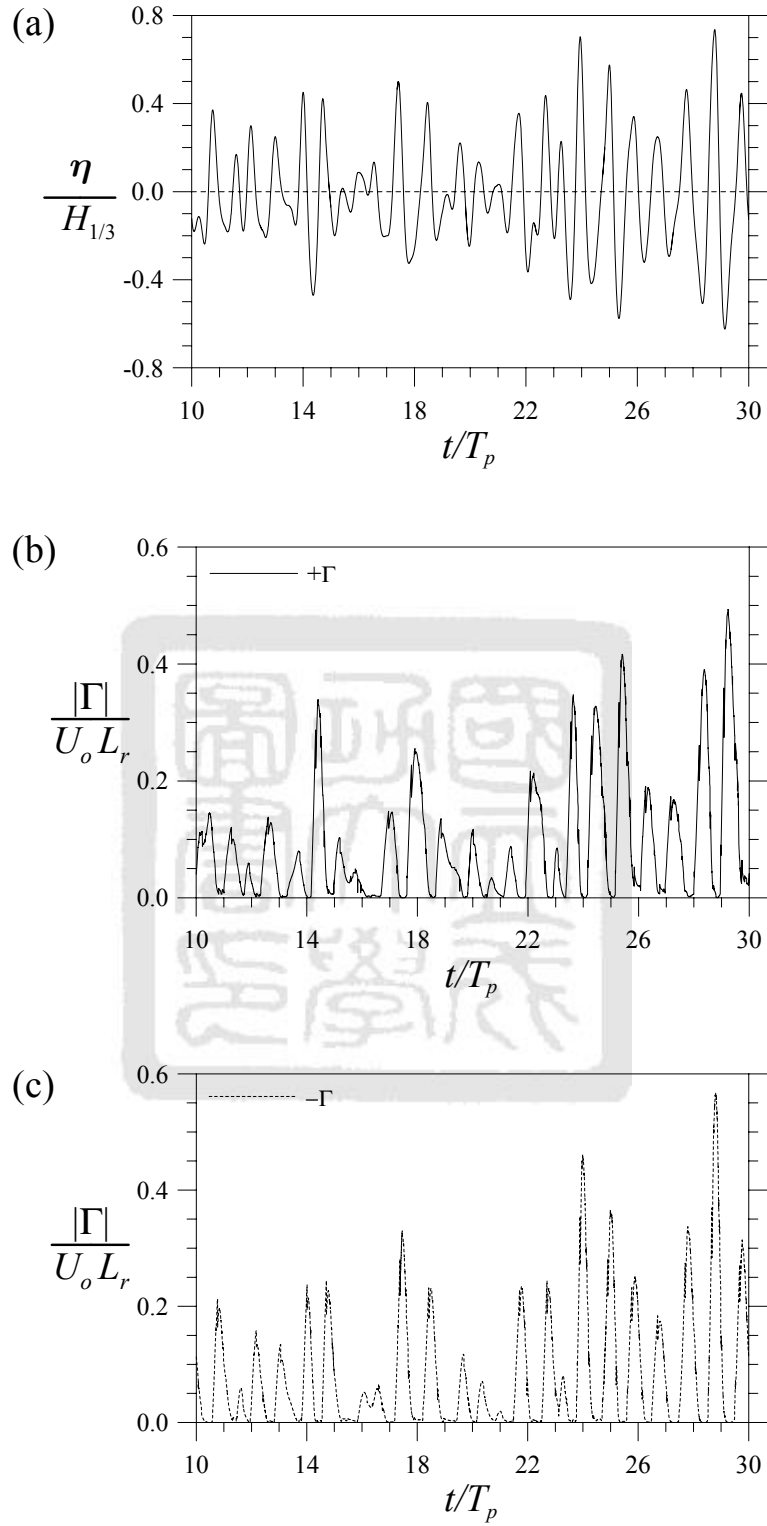
Figure 7.9: Surface elevation and circulations of Case 7.5 with $U_oL_r = 2.57 \times 10^{-3}$ m^2/s: (a) the surface elevation at $x = 0$; (b) the circulations of clockwise vortices, and (c) the circulations of counterclockwise vortices.

7.6 Chapter remark

With the results in this chapter, some remarks were carried out here briefly:

1. The present numerical model can simulate the flow within the transitional regime very well.

2. The circulation of the vortex above ripples were limited by ripple form and the free stream velocity. Of Cases 7.2 and 7.3 the maximum circulation $\left|\Gamma_{95}\right|$ was about $0.4 U_o L_r$. Of Case 7.1 the maximum circulation $\left|\Gamma_{95}\right|$ was smaller because it was not sufficiently large to be limited.

3. The asymmetric property of the surface elevation resulted the non-identical maximum circulation $\left|\Gamma_{95}\right|$ of the clockwise vortex and the counterclockwise vortex. With the sharp crest and flat trough of Cases 7.2 and 7.3, the circulation of the clockwise vortex was larger with shorter duration, and that of counterclockwise vortex was smaller with longer duration.

4. The circulations of irregular-wave cases were measured automatically and the different number of the surface elevation and the introduced vortices was found.

Chapter 8 Conclusions and Recommendations

"If you thought that science was certain—well, that is just an error on your part."

—Richard P. Feynman,
American physicist

8.1　Conclusions

8.1.1　Linear irregular waves and the associated properties

The deterministic spectral amplitude method performed by the fast Fourier transform was applied to generate irregular waves in the numerical viscous wave flume. The Goda-JONSWAP spectral density was chosen as the target wave spectrum. Characteristics of the wave spectra and the spectra of the bottom shear stresses caused by irregular waves were discussed in terms of the spectral frequency, the zeroth spectral moment and the spectral bandwidth parameter. Based on the numerical results the following conclusion can be drawn.

1. The wave spectrum of the simulated irregular waves was in good agreement with the target spectrum; and the numerical and theoretical transfer functions coincide with each

other.   This testified the accuracy of this numerical wave model.

2. The comparison of the maximum bottom shear stress obtained by this wave model with
    that obtained by Myrhaug's model indicates that Myrhaug's model underestimates the
    maximum bottom shear stress caused by laminar irregular waves.

3. The bottom shear stresses obtained from this wave model agree closely with those
    obtained from the transfer function between the wave spectrum and the shear stress
    spectrum.

8.1.2   Nonlinear properties beneath irregular waves

   Applying the method in Chapter 4, Chapter 5 focused on the nonlinear properties of
irregular waves.   The model deduced by Dean and Sharma (1981) was used to
demonstrate the irregularity of nonlinear waves and to provided a comparison.   With the
numerical results the following conclusions were carried out.

1. The bound waves, subharmonics and superharmonics, were found in the numerical
    results of the studied cases.

2. Despite the bound waves of the surface elevation are identified, the transfer function of
    the surface elevation and the associated bed shear stress are only departed from the
    theoretical one slightly.   The theoretical transfer function is satisfied for estimating the
    bed shear stress if the small bias is acceptable.

3. The spatial-varied skewness of surface elevation and bed shear stress is with a phase
    difference.   The phase difference evidences the statistical properties of bed shear

stress can not simply extent by that of the surface elevation, and it should have a roll in the shear stress forecasting using statistical manner.

8.1.3 Interaction of irregular wave s and submerged breakwater

The present numerical model with a rectangular submerged breakwater was used on the study of the vortex dynamics about the breakwatrer. Base on the repeatable properties of the numerical wave tank, the reflected waves were identified by subtracting the surface elevation of the pure incident waves from that of the listed cases without assumptions. Of the numerical results, the conclusions were stated as following.

1. The vorticity-major method were stated and utilized with the applied vorticity threshold $\Omega_T = 0.05|\Omega|_{max}$. By means of this method, the vortex region were found automatically and the properties of vortices can be obtained if the swirling velocities centered on the location of the MAV.

2. The normal pattern of the lifecycle of the vortices were as results shown in Figures 6.10 and 6.13. At the both corner of the breakwater, although the vortex pattern were different, the formation process of the vortices above breakwater increased the breakdown rate of the nearby counter-vortex about three fold.

3. The lifecycle within the irregular wave train had similar patterns before large wave packet, and had different patterns while a large wave followed by small waves, which induced the flow motion not sufficient large to diminish the vortex which formed by the large wave. Therefore, the vortex formed by the large wave last for a longer

duration.

8.1.4   Vortex dynamics above rigid vortex ripples

Using the curvilinear coordinate discussed in Chapters 2 and 3, Chapter 7 reveals the properties of vortices above ripples beneath regular waves and irregular waves.   The method for identifying the region of vortex in Chapter 6 was applied to have the vortex circulations and trajectories of the vortex center.   After verifying the reliable regime which the numerical model satisfied, the numerical results were carried out on and off the equilibrium ripple pattern, and can be concluded as following.

1. The circulation of the vortex above ripples were limited by ripple form and the free stream velocity.   Of the cases on or over the equilibrium state, the maximum circulation $\left|\Gamma_{95}\right|$ was limited about $0.4U_oL_r$.   Of the case with mild hydraulic condition, say $A_o < L_r$, the maximum circulation $\left|\Gamma_{95}\right|$ will not reach the limitation $0.4U_oL_r$.

2. The asymmetric property of the surface elevation resulted to the non-identical maximum circulation $\left|\Gamma_{95}\right|$ of the clockwise vorteies and the counterclockwise one. With the sharp crest and flat trough of the waves with larger Ursell number, say $Ur > 10$, the circulation of the clockwise vortex was larger with shorter duration, and that of counterclockwise vortex was smaller with longer duration.

3. By the vortex-automatic-recognition method, the vortex circulations beneath irregular-wave cases were studied.   Similar to the borrom phenomena of Chapters 4

and 5, the statistical pattern of vortex circulations can not be predicted directly with that of the surface elevation.

8.2 Recommendations for Future Research

The following recommendations were stated in the four topics studied herein.

8.2.1 Linear irregular waves and the associated properties

1. The study of Chapter 4 can be extended by generating an irregular-wave train with a longer duration, about $O(10^3 \text{ s})$ or longer for approaching the amount of field data, in order to have more rigorous statistical statement.

2. The transfer function of surface elevation and bed shear stress is only useful for a measured wave train or an artificial irregular waves. For estimating critical events or long term properties, a rigorous statistical model for bed shear stress is helpful.

3. The 1% difference with free stream velocity are usually applied to recognized the edge of boundary layer. However, the criterion is not satisfied for identifying the edge of boundary layer beneath irregular-wave motion. A new criterion is inevitable in order to determine boundary layer thickness by statistical manner.

4. Of time or space domain, the occurrence of freak waves can be calculated numerically with linear dispersion relation, if both amplitudes and phases of an irregular-wave train over a smooth-flat bed are identified. The results can provided a basic understanding about freak waves and help building the associated statistical model.

8.2.2   Nonlinear properties beneath irregular waves

1. The comparison of spatial-varied skewness of surface elevation and bed shear stress can provide good knowledge base to build a more robust statistical model about bed shear stress.

2. The statistical parameters of bed shear stress can be studied and compared with statistical formula of surface elevation.   Thus, the statistical results can be built and the true statistical relation can be revealed instead of using parametric estimation.

8.2.3   Interaction of irregular wave s and submerged breakwater

1. Vorticity-based method is easy to perform, but is with discrepancy about recognizing swirling center or the region of a vortex when the vorticity is small.   The invariant of velocity deformation can be used for further and detailed study (Kolář, 2007).

2. Since the width of the submerged breakwater is larger than the extent of vortex, the vortices formed above the submerged breakwater do not interact with each other.   A submerged breakwater with small width can be tested to study the interaction of vortices and have the knowledge about the effects of momentum transfer.

3. More cases have to be tested to build the relation of vortex circulation and the geometry of submerged breakwaters.

4. Since reflected waves are non-stationary, active wave absorber is malfunction.   A new boundary treatment to deal with offshore reflected waves is essentially important for having a wave train with longer duration, and therefore the statistical properties can be

built.

5. The procedure of determining the region of a vortex can be further refined to diminish the misunderstanding of the circulations of vortices next to a submerged breakwater, in which the un-convex distribution of vorticities makes the procedure in Section 6.4.2 have a long discontinuity.

8.2.4 Vortex dynamics above rigid vortex ripples

1. If the study of the momentum transfer above $y = 2H_r$ is inevitable, a turbulent model should be combined in the present numerical method. Base on the conclusion of Chang and Scotti (2004), only large-eddy simulation is suggested for the rippled bed problem.

2. The near-bed drift can be calculated numerically and make a comparison to improve the knowledge of ripple migration. However, the grid resolution have to be finer than the present study.

3. For further study, e.g. waves over a non-equilibrium ripples or irregular ripples, a more flexible boundary treatment or grid regenerated technique can be built in the present numerical model in stead of the body-fitted boundary.

4. Because of the no-slip boundary condition, the shear region near boundary is no sense about vortex core, and the near-boundary elements were excluded in this study to avoid misconception about vortex region. As studied cases in the present work, the maximum circulation appeared at near the ripple slope and taking-out the near-bed

elements probably introduce the underestimation about circulations. Similar with the

recommendation in Section 8.2.3, the invariant of velocity deformation are suggested

to implement the vortex recognition more accurate.

References

1. Admiraal, D., R. Musalem-Jara, M. Garcia, and Y. Nino (2006) "Vortex trajectory hysteresis above self-formed vortex ripples," *J. Hydraulic Res.*, Vol. 44, No. 4, pp. 437-450.

2. Andersen, K. H. (1999), *The Dynamics of Ripples Beneath Surface Waves and Topics in Shell Models of Turbulence*, Ph.D. Dissertation, Niels Bohr Institute, University of Copenhagen, Denmark.

3. Andersen, K. H., M. Abel, J. Krug, C. Ellegaard, L. R. Sondergaard, and J. Udesen (2002) "Pattern dynamics of vortex ripples in sand: Nonlinear modeling and experimental validation," *Phys. Rev. Letters*, Vol. 88, No. 234302.

4. Andersen, K. H., M.-L. Chabanol, and M. van Hecke (2001) "Dynamical models for sand ripples beneath surface waves," *Phys. Rev. E*, Vol. 63, No. 066308.

5. Ardhuin, F., T. G. Drake, and T. H. C. Herbers (2002) "Observations of wave-generated vortex ripples on the North Carolina continental shelf," *J. Geophysical Res.*, Vol. 107, No. C10, 3143.

6. Bagnold, R. A. (1946) "Motion of wave in shallow water interaction between waves and sand bottoms," *Proc. R. Soc. London, A*, Vol. 187, No. 1008, pp. 1-18.

7. Baldock, T. E., C. Swan and P. H. Taylor (1996) "A laboratory study of nonlinear surface waves on water," *Philosphical Transactions of the Royal Society: Mathematical, Physical and Engineering Sciences*, Vol. 354, pp. 649-676.

8. Barrick, D. E. and B. L. Weber (1977) "On the nonlinear theory for gravity waves on the ocean surface. Part 2: Interpretation and applications," *J. Phys. Oceanography*, Vol. 7, pp. 11-21.

9. Becker, J. M., Y. L. Firing, J. Aucan, R. Holman, M. Merrifield, and G. Pawlak (2007) "Video-based observations of nearshore sand ripples," *J. Geophysical Res.*, Vol. 112,

References

No. C01007, doi:10.1029/2005JC003451.

10. Beji, S. and J. A. Battjes (1993) "Experimental investigation of wave propagation over a bar," *Coastal Eng.*, Vol. 19, pp. 151-162.

11. Beji, S. and J. A. Battjes (1994) "Numerical simulation of nonlinear wave propagation over a bar," *Coastal Eng.*, Vol. 23, pp. 1-16.

12. Benjamin, T. B. and J. E. Feir (1967) "The disintegration of wave trains on deep water, Part 1. Theory," *J. Fluid Mech.*, Vol. 27, No. 3, pp. 417-430.

13. Benny, D. J. (1962) "Non-linear gravity wave interactions," *J. Fluid Mech.*, Vol. 14, pp. 577-584.

14. Betat, A., V. Frette, and I. Rehberg (1999) "Sand ripples induced by water shear flow in an annular channel," *Phys. Rev. Letters*, Vol. 83, No. 1, pp. 88-91.

15. Blondeaux, P. (1990) "Sand ripples under sea waves Part 1. Ripple formation," *J. Fluid Mech.*, Vol. 218, pp. 1-17.

16. Blondeaux, P. and G. Vittori (1991) "Vorticity dynamics in an oscillatory flow over a rippled bed," *J. Fluid Mech.*, Vol. 226, pp. 257-289.

17. Blondeaux, P. and G. Vittori (1999) "Boundary layer and sediment dynamics under sea waves," in: Liu, P. L.-F. (Ed.), *Advances in Coastal and Ocean Engineering*, Vol. 4, World Scientific, 133-190.

18. Borgman, L. E. (1969) "Ocean wave simulation for engineering design," *J. Waterways and Harbor Div.*, ASCE, **95**, 557-583.

19. Cataño-Lopera, Y. A. and M. H. García (2006a), "Geometry and migration characteristics of bedforms under waves and current. Part 1: Sandwave morphodynamics," *Coastal Eng.*, Vol. 53, pp. 767-780.

20. Cataño-Lopera, Y. A. and M. H. García (2006b), "Geometry and migration characteristics of bedforms under waves and current. Part 2: Ripples superimposed on sandwaves," *Coastal Eng.*, Vol. 53, pp. 781-792.

21. Chang, H.-H. (2004) *Interaction of Water Waves and Submerged Permeable Offshore Structures*, Ph.D. Dissertation, Department of Hydraulics and Ocean Engineering,

National Cheng Kung University, Taiwan (R.O.C.).

22. Chang, K.-A., T.-J. Hsu, and P. L.-F. Liu (2001) "Vortex generation and evolution in water waves propagating over a submerged rectangular obstacle: Part I. Solitary waves," *Coastal Eng.*, Vol. 44, No. 1, pp. 13-36.

23. Chang, K.-A., T.-J. Hsu, and P. L.-F. Liu (2005) "Vortex generation and evolution in water waves propagating over a submerged rectangular obstacle: Part II. Cnoidal waves," *Coastal Eng.*, Vol. 52, No. 3, pp. 13-36.

24. Chang, Y. S. and A. Scotti (2004) "Modeling unsteady turbulent flows over ripples: Reynolds-averaged Navier-Stokes equations (RANS) versus large-eddy simulation (LES)," *J. Geophysical Res.*, Vol. 109, C09012.

25. Chan, R. K.-C. and R. L. Street (1970) "A computer study of finite-amplitude water waves," *J. Comput. Physics,* Vol. 6, pp. 68-94.

26. Chen, C.-J. and H.-C. Chen (1982) *The finite-analytic method*, IIHR Report 232-IV, Iowa Institute of Hydraulic Research, The University of Iowa, Iowa City.

27. Chen, H.-C. and V. C. Patel (1987) "Laminar flow at the trailing edge of a flat plate," *AIAA J.*, Vol. 25, pp. 920-928.

28. Cherneva, Z., P. Petrova, N. Andreeva, and C. G. Soares (2005) "Probability distributions of peaks, troughs and heights of wind waves measured in the black sea coastal zone," *Coastal Eng.*, Vol. 52, No. 7, pp. 599-615.

29. Cieślikiewicz, W. and O. T. Gudmestad (1993) "Stochastic characteristics of orbital velocities of random water waves," *J. Fluid Mech.*, Vol. 255, pp. 275-299.

30. Clément, A. (1996) "Coupling of two absorbing boundary conditions for 2d time-domain simulations of free surface gravity waves," *J. Comput. Phys.,* Vol. 126, pp. 139-151.

31. Dattatri, J., H. Raman, and N. J. Shankar (1978) "Performance characteristics of submerged breakwaters," *Proc. 16th Int. Conf. Coastal Eng.,* ASCE, Hamburg, Germany, pp. 2153-2171.

32. Davey, A. and K. Stewartson (1974) "On three-dimensional packets of surface

References

waves," *Proc. R. Soc. Lond. A*, Vol. 338, pp. 101-110.

33. Davies, A. G. (1980) "Field observations of the threshold of sand motion in a transitional wave boundary layer" *Coastal Eng.*, Vol. 4, pp. 23-46.

34. Davis, J. P. (2005) *A spectral approach to the transient analysis of wave-formed sediment ripples*, Ph.D. Dissertation, School of Civil and Environmental Engineering, The University of Adelaide, Australia.

35. Dawson, T. H. (2004) "Stokes correction for nonlinearity of wave crests in heavy seas," *J. Waterw., Port, Coast., Ocean Eng.*, ASCE, Vol. 130, No. 1, pp. 39-44.

36. De Angelis, V., P. Lombardi, and S. Banerjee (1997) "Direct numerical simulation of turbulent flow over a wavy wall," *Phys. Fluids*, Vol. 9, No. 8, pp. 2429-2442.

37. Dean, R. G. and R. A. Dalrymple (1984) *Water Wave Mechanics for Engineers and Scientists*, Prentice-Hall, New Jersey.

38. Dean, R. G. and J. N. Sharma (1981) "Simulation of wave systems due to nonlinear directional spectra," *Proc. Int. Symp. Hydrodynamics in Ocean Eng.*, Trondheim, Norway, Vol. 2, pp. 1211-1222.

39. Dommermuth, D. G. and D. K. P. Yue (1987) "A high-order spectral method for the study of nonlinear gravity waves," *J. Fluid Mech.*, Vol. 184, pp. 267-288.

40. Dong, C.-M. (2000) *The Development of a Numerical Viscous Wave Flume and its Applications*, Ph.D. Dissertation, Department of Hydraulics and Ocean Engineering, National Cheng Kung University, Taiwan (R.O.C.).

41. Dong, C.-M. and C.-J. Huang (2004) "Generation and propagation of water waves in a two-dimensional numerical viscous wave flume," *J. Waterw., Port, Coast., Ocean Eng.*, ASCE, Vol. 130, pp. 143-153.

42. Du Toit, C. G. and J. F. A. Sleath (1981) "Velocity measurements close to rippled beds in oscillating Flow," *J. Fluid Mech.*, Vol. 112, pp. 77-96.

43. Duncan, P. E. and K. R. Drake (1995) "A note on the simulation and analysis of irregular non-linear waves," *Appl. Ocean Res.*, Vol. 17, No. 1, pp. 1-8.

44. Dungey, J. C. and W. H. Hui (1979) "Nonlinear energy transfer in a narrow

gravity-wave spectrum," *Proc. R. Soc. Lond. A*, Vol. 368, No. 1733, pp. 239-265.

45. Dysthe, K. B., K. Trulsen, H. E. Krogstad, and H. Socquet-Juglard (2003) "Evolution of a narrow-band spectrum of random surface gravirty waves," *J. Fluid Mech.*, Vol. 478, pp. 1-10.

46. Earnshaw, H. C. and C. A. Greated (1998) "Dynamics of ripple bed vortices," *Experiments in Fluid*, Vol. 25, pp. 265-275.

47. Elgar, S., R. T. Guza, and R. J. Seymour (1985) "Wave group statistics from numerical simulations of a random sea," *Appl. Ocean Res.*, Vol. 7, pp. 93-96.

48. Fredsøe, J., K. H. Andersen, and B. M. Sumer (1999) "Wave plus current over a ripple-covered bed," *Coastal Eng.*, Vol. 38, pp. 177-221.

49. Fredsøe, J., B. M. Sumer, A. Kozakiewicz, L. H. C. Chua, and R. Deigaard (2003) "Effect of externally generated turbulence on wave boundary layer," *Coast. Eng.*, Vol. 49, pp. 155-183.

50. Fryer, D. K., G. Gilbert, and M. J. Wilkie (1973) "A wave spectrum synthesizer," *J. Hydraul. Res.*, Vol. 11, pp. 193-204.

51. Funke, E. R. and E. P. D. Mansard (1987) "A rationale for the use of deterministic approach to laboratory wave generation," *Proc. IAHR Seminar Wave Analysis and Generation in Laboratory Basins*, Lausanne, pp. 153-195.

52. Goda, Y. (1970) "Numerical experiments on wave statistics with spectral simulation," *Report of the Port and Harbour Research Institute*, Vol. 9, pp. 3-57.

53. Goda, Y. (1988) "Statistical variability of sea state parameters as a function of wave spectrum," *Coastal Eng. in Japan,* Vol 31, pp. 39-52.

54. Goda, Y. (2000) *Random Seas and Design of Maritime Structures, Advances in Coastal and Ocean Engineering*, Vol. 15, World Scientific, Singapore.

55. Goda, Y. and Y. Suzuki (1976) "Estimation of incident and reflected waves in random wave experiments," *Proc. 15th Int. Conf. Coastal Eng.*, ASCE, Honolulu, pp. 828–845.

56. Gramstad, O., and K. Trulsen (2007) "Influence of crest and group length on the

References

occurrence of freak waves," *J. Fluid Mech.,* Vol. 582, pp. 463-472.

57. Grant, W. D. and O. S. Madsen (1986) "The continental-shelf bottom boundary layer," *Annu. Rev. Fluid Mech.,* Vol. 18, pp. 265-305.

58. Grasmeijer, B. T. and M. G. Kleinhans (2004) "Observed and predicted bed forms and their effect on suspended sand concentrations," *Coastal Eng.,* Vol. 51, pp. 351-371.

59. Hanes, D. M., V. Alymov, and Y. S. Chang (2001) "Wave-formed sand ripples at Duck, North Carolina," *J. Geophysical Res.,* Vol. 106(C10), pp. 22575-22592.

60. Hansen, J. L. (2001) *Pattern Formation of Sand Ripples and Polygons in the Hydraulic Jump* , Ph.D. Dissertation, Niels Bohr Institute, University of Copenhagen, Denmark.

61. Hansen, J. L., M. van Hecke, C. Ellegaard, K. H. Andersen, T. Bohr, A. Haaning, and T. Sams (2001) "Stability balloon for two-dimensional vortex ripple patterns," *Phys. Rev. Letters*, Vol. 87, No. 204301.

62. Hara, T. and C.-C. Mei (1990) "Oscillating flows over periodic ripples," *J. Fluid Mech.,* Vol. 211, pp. 183-209.

63. Hasselmann, K. (1962) "On the non-linear energy transfer in a gravity-wave spectrum. Part 1. General theory," *J. Fluid. Mech.,* Vol. 12, pp. 481-500.

64. Hasselmann, K., T. P. Barnett, E. Bouws, H. Carlson, D. E. Cartwright, K. Enke, J. A. Ewing, H. Gienapp, D. E. Haselmann, P. Kruseman, A. Meerburg, P. Muller, D. J. Olbers, K. Richter, W. Sell, and H. Walden (1973) "Measurements of wind-wave growth and swell decay during the Joint North Sea Wave Project (JONSWAP)," *Ergnzungsheft zur Deutschen Hydrographischen Zeitschrift Reihe (Deutsches Hydrogr. Zeit.)*, Vol. 12(A8), pp. 1-95.

65. Hatori, M. (1984) "Nonlinear properties of laboratory wind waves at energy containing frequencies. Part 1. Probability density distribution of surface elevation," *J. of the Oceangraphical Society of Japan*, Vol. 40, pp. 1-11.

66. Holmedal, L. E., D. Myrhaug, and H. Rue (2000) "Seabed shear stresses under irregular waves plus current from Monte Carlo simulations of parameterized

models," *Coastal Eng.*, Vol. 39, pp. 123-147.

67. Holmedal, L. E., D. Myrhaug, and H. Rue (2003) "The sea bed boundary layer under random waves plus current," *Continental Shelf Res.*, Vol. 23, No. 7, pp. 717-750, 2003.

68. Huang, N. E. and S. R. Long (1980) "An experimental study of the surface elevation probability distribution and statistics of wind-generated waves," *J. Fluid Mech.*, Vol. 101, pp. 179-200.

69. Huang, N. E., S. R. Long, C. C. Tung, Y. Yuan, and L. F. Bliven (1983) "A non-Gaussian statistical model for surface elevation of nonlinear random wave fields," *J. Geophysical Res.*, No. 3C0795, pp. 7597-7606.

70. Huang, N. E. and C.-C. Tung (1976) "The dispersion relation for a nonlinear random gravity wave field," *J. Fluid Mech.*, Vol. 75, No. 2, pp. 337-345.

71. Huang, N. E. and C.-C. Tung (1977) "The influence of the directional energy distribution on the nonlinear dispersion relation in a random gravity wave field," *J. Phys. Oceanography*, Vol. 7, No. 3, pp. 403-414.

72. Huang, C.-J. and C.-M. Dong (1999) "Wave deformation and vortex generation in water waves propagating over a submerged dike," *Coastal Eng.*, Vol. 37, pp, 123-148.

73. Huang, M.-C. (2002) "Wave parameters and functions in wavelet analysis," *Ocean Eng.*, Vol. 31, pp. 111-125.

74. Hudson, J. D., L. Dykhno, and T. J. Hanratty (1996) "Turbulence production in flow over a wavy wall," *Experiments in Fluid*, Vol. 20, pp. 257-265.

75. Hughes, S. A. (1993) *Physical models and laboratory techniques in coastal engineering*, Chap. 7. *Advances Series on Ocean Engineering*, Vol. 7, World Scientific, Singapore.

76. IAHR Working Group on Wave Generation and Analysis, (1989) "List of sea-state parameters," *J. Waterw., Port, Coast. Ocean Eng.*, ASCE, Vol. 115, pp. 793-808.

77. Ikeda, S., K. Horikawa, H. Nakamura, and K. Noguchi (1991) "Oscillatory boundary

References

layer over a sand ripple model," *Coastal Eng. In Japan*, Vol. 34, pp. 15-29.

78. Ikeda, S., S. Kizaki, S. Ishii, and S. Kuribayashi (1989) "Flow near sand ripples and dissipation of wave energy," *Coastal Eng. In Japan*, Vol. 32, pp. 15-36.

79. Ishida, A. and H. Takahashi (1981) "Numerical analysis of shallow water wave deformation in a constant depth region," *Coastal Eng. in Japan*, Vol. 24, pp. 1-18.

80. Janssen, P. A. E. M. (2003) "Nonlinear four-wave interactions and freak waves," *J. Phys. Oceanography*, Vol. 33, No. 4, pp. 863-884.

81. Jensen, B. L., B. M. Sumer, and J. Fredsøe (1989) "Turbulent oscillatory boundary layers at high Reynolds numbers," *J. Fluid Mech.,* Vol. 206, pp. 265-297.

82. Jespersen, T. S., J. Q. Thomassen, A. Andersen, and T. Bohr (2004) "Vortex dynamics around a solid ripple in an oscillatory flow," *Eur. Phy. J. B*, Vol. 38, pp. 127-138.

83. Johnson, J. W., R. A. Fuchs and JR Morison (1951) "The damping action of submerged breakwaters," *Trans. of Amer. Geophy. Union*, Vol. 32, No. 5, pp. 704-718.

84. Jonsson, I. G. (1963) "Measurements in the turbulent wave boundary layer," *Proc. 10th Congress Inter. Ass. Hydraul. Res*, London, Vol. 1, pp. 85-92.

85. Jonsson, I. G. (1980) "A new approach to oscillatory rough turbulent boundary layers," *Ocean Eng.,* Vol. 7, pp. 109-152.

86. Jonsson, I. G. and N. A. Carlsen (1976) "Experimental and theoretical investigations in an oscillatory turbulent boundary layer," *J. Hydraul. Res.,* Vol. 14, pp. 45-60.

87. Justesen, P. (1988) "Prediction of turbulent oscillatory flow over rough beds," *Coastal Eng.,* Vol. 12, pp. 257-284.

88. Kamphuis, J. W. (1975) "Friction factor under oscillatory waves," *J. Waterw., Harbor and Coast. Div.,* ASCE, Vol. 101, pp. 135-144.

89. Kaneko, A. and H. Honji (1979) "Double structures of steady streaming in the oscillatory viscous flow over a wavy wall," *J. Fluid Mech.*, Vol. 93, No. 4, pp. 727-736.

90. Khelifa, A., and Y. Ouellet (2000) "Prediction of sand ripple geometry under waves and currents," *J. Waterw., Port, Coast., Ocean Eng.*, ASCE, Vol. 126, No. 1, pp. 14-22.

91. Kim, H. (2004) "Effective Form Roughness of Ripples for Waves," *J. Coast. Res.*, Vol. 20, pp. 731-738

92. Kinsman, B. (1965) *Wind waves: their generation and propagation on the ocean surface*, Prentice-Hall.

93. Kojima, H., T. Ijima, and A. Yoshida (1990) "Decomposition and interception of long waves by a submerged horizontal plate" *22nd Coastal Eng. Conf.*, Delft, ASCE, New York, pp. 1228-1241.

94. Klopman, G. and P. J. Von Leeuwen (1990) "An efficient method for the reproduction of non-linear random waves," *Proc. 22nd Int. Conf. Coastal Eng.*, ASCE, Delft, The Netherlands, Vol. 1, pp. 478-488.

95. Kolář, V. (2007) "Vortex identification: New requirements and limitations," *International Journal of Heat and Fluid Flow*, Vol. 28, No. 4, pp. 638-652.

96. Lacy, J. R., D. M. Rubin, H. Ikeda, K. Mokudai, and D. M. Hanes (2007) "Bed forms created by simulated waves and currents in a large flume," *J. Geophysical Res.,* Vol. 112, C10018, doi:10.1029/2006JC003942.

97. Lambrakos, K. F. (1982) "Seabed wave boundary layer measurements and analysis," *J. Geophysical Res.,* Vol. 87(C6), pp. 4171-4189.

98. Laing, A. K. (1986) "Nonlinear properties of random gravity waves in water of finite depth," *Journal of Physical Oceanography*, Vol. 16, pp. 2013-2030.

99. Landry, B. J., M. J. Hancock, and C.-C. Mei, (2007), "Note on sediment sorting in a sandy bed unter standing water waves," *Coastal Eng.*, Vol. 54, pp. 694-699.

100. Lin, C.-Y. and C.-J. Huang (2004) "Decomposition of incident and reflected higher harmonic wavesusing four wave gauges," *Coastal Eng.*, Vol. 51, No. 5, pp. 395-406.

101. Longiet-Higgins, M. S. (1962) "Resonant interactions between two trains of gravity waves," *J. Fluid Mech.*, Vol. 12, No. 3, pp. 321-332.

References

102. Longuet-Higgins, M. S. (1963) "The effect of nonlinearities on statistical distribution in the theory of sea waves," *J. Fluid Mech.*, Vol. 17, pp. 459-480.

103. Longiet-Higgins, M. S. (1976) "On the nonlinear transfer of energy in the peak of a gravity-wave spectrum: a simplified model," *Proc. R. Soc. Lond. A: Mathematical and Physical Sciences*, Vol. 347, No. 1650, pp. 311-328.

104. Longuet-Higgins, M. S. and O. M. Phillips (1962) "Phase velocity effects in tertiary wave interactions," *J. Fluid Mech.*, Vol. 12, pp. 333-336.

105. Lyne, W. H. (1971) "Unsteady viscous flow over a wavy wall," *J. Fluid Mech.*, Vol. 50, No. 1, pp. 33-48.

106. Madsen, P. A. and O. R. Sorensen (1992) "A new form of the Boussinesq equations with improved linear dispersion characteristics (part 1)," *Coastal Eng.*, Vol. 18, pp. 183-204.

107. Malarkey, J. and A. G. Davies (2002) "Discrete vortex modeling of oscillatory flow over ripples," *Applied Ocean Res.*, Vol. 24, pp. 127-145.

108. Malarkey, J. and A. G. Davies (2004) "An eddy viscosity formulation for oscillatory flow over vortex ripples," *J. Geophysical Res.*, Vol. 109(C12), No. C12016.

109. Mansard, E. P. D. and E. R. Funke (1980) "The measurement of incident and reflected spectra using a least squares method," *Proc. 17th Int. Conf. Coastal Eng.*, ASCE, Sydney, Australia, pp. 154–172.

110. Marin, F. (2004) "Eddy viscosity and Eulerian drift over rippled over beds in waves," *Coastal Eng.*, Vol. 50, pp. 139-159.

111. Massel, S. R. (2001) "Wavelet analysis for processing of ocean surface wave records," *Ocean Eng.,* Vol. 28, pp. 957-987.

112. Masselink, G., M. J. Austin, T. J. O'Hare, and P. E. Russell (2007) "Geometry and dynamics of wave ripples in the nearshore zone of a coarse sandy beach," *J. Geophysical Res.*, Vol. 112, No. C10022.

113. Masuda, A., Y. Y. Kuo, and H. Mitsuyasu (1977) "On the dispersion relation of random gravity waves. Part 1. Theoretical framework," *J. Fluid Mech.*, Vol. 92, pp.

717-730.

114. Mathisen, P. P. and O. S. Madsen (1996a) "Waves and currents over a fixed rippled bed. 1. Bottom roughness experienced by waves in the presence and absence of currents," *J. Geophysical Res.*, Vol. 101, No. C7, pp. 16533-16542.

115. Mathisen, P. P. and O. S. Madsen (1996b) "Waves and currents over a fixed rippled bed. 2. Bottom and apparent roughness experienced by currents in the presence of waves," *J. Geophysical Res.*, Vol. 101, No. C7, pp. 16543-16550.

116. Mathisen, P. P. and O. S. Madsen (1999) "Waves and currents over a fixed rippled bed. 3.Bottom and apparent roughness for spectral waves and currents," *J. Geophysical Res.*, Vol. 104, No. C8, pp. 18447-18461.

117. Matsunaga, N., A. Kaneko, and H. Honji (1981) "A numerical study of steady streamings in oscillatory flow over a wavy wall," *J. Hydraul. Res.*, Vol. 19, No. 1, pp. 29-42.

118. Medina, J. R., J. Aguilar, and J. J. Diez (1985) "Distortions associated with random sea simulations," *J. Waterw., Port, Coast. Ocean Eng.*, ASCE, Vol. 111, pp. 603-628.

119. Mei, C.-C. (1989) *The applied dynamics of ocean surface waves*, World Scientific Publ., Singapore.

120. Miles, M. D. and E. R. Funke (1988) "Numerical comparison of wave synthesis methods," *Proc. 21st Int. Conf. Coastal Eng.*, ASCE, Coata del Sol-Malaga, Spain, Vol. 1, pp.91-105.

121. Mitsuyasu, H., Y. Y. Kuo, and A. Masuda (1979) "On the dispersion relation of random gravity waves. Part 2. An experiment," *J. Fluid Mech.*, Vol. 92, pp. 791-749.

122. Mori, N., and Yasuda, T. (1996) "Weakly non-Gaussian model of wave height distribution for nonlinear random waves," *Proc. 25th Int. Conf. Coastal Eng.*, ASCE, Orlando, Florida, pp. 850-863.

123. Mori, N., and Yasuda, T. (2002) "A weakly non-Gaussian model of wave height distribution for nonlinear random wave train," *Ocean Eng.*, Orlando, Florida, pp. 850-863.

References

124. Myrhaug, D. (1995) "Bottom friction beneath random waves," *Coastal Eng.,* Vol. 24, pp. 259-273.

125. Myrhaug, D. and L. E. Holmedal (2001) "Beload sediment transport rate by nonlinear random waves," *Coastal Eng.*, Vol. 43, No. 3, pp. 133-142.

126. Myrhaug, D. and L. E. Holmedal (2003) "Laminar bottom friction beneath nonlinear random waves," *Coastal Eng. J.,* Vol. 45, pp. 49-61.

127. Myrhaug, D., K. F. Lambrakos, and O. H. Slaattelid (1992) "Wave boundary layer in flow measurements near the seabed," *Coastal Eng.,* Vol. 18, pp.153-181.

128. Myrhaug, D., O. H. Slaattelid, and K. F. Lambrakos (1998) "Seabed shear stresses under random waves: predictions vs. estimates from field measurements," *Ocean Eng.,* Vol 25, pp. 907-916.

129. Nielsen, P. (1981) "Dynamics and geometry of wave-generated ripples," *J. Geophysical Res.*, Vol. 86, No. C7, pp. 6467-6472.

130. Nielsen, P. (1986) "Suspended sediment concentrations under waves," *Coastal Eng.*, Vol. 10, No. 1, pp. 23-31.

131. Nielson, P. (1992) *Coastal Bottom Boundary Layers and Sediment Transport*, Advanced Series on Ocean Engineering, vol. 4. World Scientific, Singapore.

132. Nwogu, O. (1993) "An alternative form of the Boussinesq equations for modeling the propagation of waves from deep to shallow water," *J. Waterw., Port, Coast., Ocean Eng.*, ASCE, Vol. 119, No. 6, pp. 618-638.

133. Nybakken, J. W. and M. D. Bertness (2005) *Marine biology: an ecological approach*, 6th ed., Benjamin Cummings, San Francisco.

134. Ochi, M. K., (1986) "Non-Gaussian random processes in ocean engineering", *J. Prob. Eng. Mech.*, Vol. 1, No. 1, pp. 28-39.

135. O'Donoghue, T., J. S. Doucette, J. J. van der Werf, and J. S. Ribberink (2006) "The dimensions of sand ripples in full-scale oscillatory flows," *Coastal Eng.*, Vol. 53, No. 12, pp. 997-1012.

136. Ohyama, T. (1991) "Development of a numerical wave tank for analysis of nonlinear

and irregular wave field," *Fluid Dyn. Res.,* Vol. 8, pp. 231-251.

137. Ohyama, T., S. Beji, K. Nadaoka, and J. A. Battjes (1994) "Experimental verification of numerical model for nonlinear wave evolutions," *J. Waterw., Port, Coast., Ocean Eng.*, ASCE, Vol. 120, No. 6, pp. 637-644.

138. Ohyama, T. and K. Nadaoka (1994) "Transformation of a nonlinear wave train passing over a submerged shelf without breaking," *Coastal Eng.*, Vol. 24, pp. 1-22.

139. Onorato, M., A. R. Osborne, M. Serio, and L. Cavaleri (2005) "Modulation instability and non-Gaussian statistics in experimental random water-wave trains," *Phys. Fluid*, Vol. 17, No. 078101.

140. Ourmières, Y. and J. R. Chaplin (2004) "Visualizations of the disturbed-laminar wave-induced flow above a rippled bed," *Experiments in Fluid*, Vol. 36, pp. 908-918.

141. Patankar, S. V. (1979) "A calculation procedure for two-dimensional elliptic situations," *Numerical Heat Transfer*, Vol. 2.

142. Peregrine, D. H. (1967) "Long waves on a beach," *J. Fluid Mech.*, Vol. 27, pp. 815-827.

143. Phillips, O. M. (1960) "On the dynamics of unsteady gravity waves of finite amplitude. Part 1. The elementary interactions," *J. Fluid Mech.*, Vol. 9, pp. 193-217.

144. Phillips, O. M. (1977) *The Dynamics of the Upper Ocean*, 2nd ed., Cambridge University Press, New York.

145. Pierson, W. J. and L. Moskowitz (1964) "A proposed spectral form for full-developed wind sea based on the similarity law of S. A. Kitaigorodoskii," *J. Geophysical Res.*, Vol. 69, pp. 5202.

146. Ploeg, J. and E. R. Funke (1980) "A Survey of Random Wave Generation Techniques," *Proc. 17th Int. Conf. Coastal Eng.*, ASCE, Sydney, Australia, Vol. 1, pp. 135-153.

147. Precht, E., and M. Huettel (2004) "Rapid wave-driven advective pore water exchange in a permeable coastal sediment," *J. Sea Res.*, Vol. 51, 93-107.

148. Rambabu, A. C. and J. S. Mani (2005) "Numerical prediction of performance of

submerged breakwater," *Ocean Eng.*, Vol. 32, pp. 1235-1246.

149. Rice, S. O. (1955) Mathematical analysis of random noise. In *Selected Papers on Noise and Stochastic Process*, N. Wax, ed., Dover Publications, Inc., New York, pp. 133-294.

150. Rousseaux, G. (2006) "Physical distinction between rolling-grain ripples and vortex ripples: An experimental study," *Phys. Rev. E*, Vol. 69, No. 066305, p. 7.

151. Rousseaux, G., H. Yoshikawa, A. Stegner and J. E. Wesfried (2004) "Dynamics of transient eddy above rolling-grain ripples," *Phys. Fluids*, Vol. 16, No. 4, pp. 1049-1058.

152. Saffman, P. G. (1992) *Vortex dynamics*, Cambridge University Press, Cambridge.

153. Samad, M. A., H. Tanaka, B. M. Sumer, J. Fredsøe, and C. Lodahl (1998) "Study on bottom shear stress under irregular waves," *Proc. of Coast. Eng.*, JSCE, Vol. 45, pp. 91-95 (in Japanese).

154. Sand, S. E. and E. P. D. Mansard (1986) "Reproduction of higher harmonics in irregular waves," *Ocean Eng.*, Vol. 13, No. 1, pp. 57-83.

155. Sato, S., N. Mimura, and A. Watanabe (1984) "Oscillatory boundary layer flow over rippled beds," *Proc. 25th Int. Conf. Coastal Eng.*, ASCE, Houston, Texas, pp. 2293-2309.

156. Sato, S., K. Shimosako, and A. Watanabe (1987) "Measurements of oscillatory boundary layer flows above ripples with a laser-Doppler velocimeter," *Coastal Eng. Japan*, Vol. 30, pp. 89-98.

157. Schäffer, H. A. (1993) "Second order irregular-wave generation in flumes – computation of transfer function by an asymptotic summation method," *Proc. WAVES '93*, ASCE, New Orleans, pp. 784-797.

158. Schäffer, H. A. (1996) "Second-order wavemaker theory for irregular waves," *Ocean Eng.*, Vol. 23, No. 1, pp. 47-88.

159. Scheibye-Knudsen, K., C. Ellegaard, and F. Bundgaard (2005) "Sand ripples under water with complex wave motion," *Phys. Rev. E*, Vol. 72, No. 016209.

160. Scherer, M., A, F. Melo, and M. Marder (1999) "Sand ripples in an oscillating annular sand-water cell," *Phys. Fluids*, Vol. 11, No. 58, pp. 58-67.

161. Sharma, J. N. (1979) *Development and evaluation of a procedure for simulating a random directional second-order sea surface and associated wave forces*, Ph.D. Dissertation, University of Delaware.

162. Sharma, J. N. and R. G. Dean (1981) "Second-order directional seas and associated wave forces," *J. Soc. Petroleum Eng.*, pp. 129-140.

163. Shen, M.-L. and C.-J. Huang (2005) "Nonlinear random waves and the associated spectra of shear stresses," The Seventh Regional Symposium PACON 2005, Chienkuo Technology University, Changhua, Taiwan (R.O.C.).

164. Sistermans, P. G. J. (2002) *Graded sediment transport by non-breaking waves and a current*, Ph.D. Dissertation, Delft University of Technology, the Netherlands.

165. Sleath J. F. A. (1984) *Sea Bed Mechanics*, Wiley.

166. Sleath, J. F. A. (1995) "Coastal bottom boundary layers," *Appl. Mech. Rev.,* Vol. 48, pp. 589-600.

167. Sulisz, W., and M. Paprota (2008) "Generation and propagation of transient nonlinear waves in a wave flume," *Coastal Eng.*, Vol. 55, No. 4, pp. 277-287.

168. Song, J. B., and Y. H. Wu (1999a) "Statistical distribution of water-particle velocity below the surface layer for finite water depth," *Coastal Eng.*, Vol. 40, No. 1, pp. 1-19.

169. Song, J. B., and Y. H. Wu (1999b) "Statistical distribution of maximum surface displacement in weakly nonlinear random waves," *J. Waterw., Port, Coast., Ocean Eng.*, ASCE, Vol. 125, No. 2, pp. 59-65.

170. Song, J.-B., Y. J. Hou, Y. J. He, Y.-H. Wu, B. S. Yin (2002) "Statistical distribution of wave-surface elevation for second-order random directional ocean waves in finite water depth," *Coastal Eng.*, Vol. 46, No. 1, pp. 51-60.

171. Stamos, D. G. and M. R. Hajj (2001) "Reflection and transmission of waves over submerged breakwaters," *J. Eng. Mech.*, Vol. 127, No. 2, pp. 99-105.

References

172. Stegner, A., and J. E. Wesfreid (1999) "Dynamical evolution of sand ripples under water," *Phys. Rev. E*, Vol. 60, No. R3487, p. 4.

173. Sulisz, W. and R. T. Hudspeth (1993) "Complete second-order solution for water waves generated in wave flumes," *J. Fluids and Structures*, Vol. 7, pp. 253-268.

174. Swart, D. H. (1974) *Offshore sediment transport and equilibrium beach profiles*, Ph.D. Dissertation, Delft University of Technology, the Netherlands. (also: Publication 131. Delft Hydraulics)

175. Tanaka, H. and M. A. Samad (2006) "Prediction of instantaneous bottom shear stress for smooth turbulent bottom boundary layers under irregular waves," *J. Hydraul. Res.,* Vol. 44, pp. 94-106.

176. Tang, C. J., V. C. Patel, and L. Landweber (1990) "Viscous effects on propagation and reflection of solitary waves in shallow channels," *J. Comput. Physics*, Vol. 88, No. 1, pp. 86-113.

177. Tayfun, M. A., (1980) "Narrow-band nonlinear sea waves", *J. Geophysical Res.*, Vol. 85, pp. 1548-1552.

178. Tayfun, M. A., (1994) "Distributions of envelope and phase in weakly nonlinear random waves," *J. Waterw., Port, Coast., Ocean Eng.*, ASCE, vol. 120, No. 4, pp. 1009-1025.

179. Tayfun, M. A., and J. M. Lo (1989) "Envelope, phase, and narrow-band models of sea waves", *J. Waterw., Port, Coast., Ocean Eng.*, ASCE, vol. 115, No. 5, pp. 594-613.

180. Testik, F. Y., S. I. Voropayev, and H. J. S. Fernando (2005) "Adjustment of sand ripples under changing water waves," *Phys. Fluids*, Vol. 17, No. 072104.

181. Thompson, J. F. (1982) *Numerical Grid Generation*, North-Holland (Also published as Vol. 10-11 of *Applied Mathematics and Computation*)

182. Tick, L. J. (1963) "Nonlinear probability models of ocean waves," *Ocean wave spectra :proceedings of a conference*, Easton, Maryland, Prentice-Hall, pp. 163-169.

183. Ting, C. L., M. C. Lin, and C. M. Hsu (2005) "Spatial variations of waves

propagating over a submerged rectangular obstacle," *Ocean Eng.*, Vol. 32, pp. 1448-1464.

184. Ting, F. C. K. and Y.-K Kim (1994) "Vortex generation in water waves propagating over a submerged obstacle," *Coastal Eng.*, Vol. 24, No. 1-2, pp. 23-49.

185. Traykovski, P. (2007) "Observation of wave orbital scale ripples and a nonequilibrium time-dependent model," *J. Geophysical Res.*, Vol. 112, C06026.

186. Traykovski, P., A. E. Hay, J. D. Irish, and J. F. Lynch (1999) "Geometry, migration, and evolution of wave orbital ripples at LEO-15," *J. Geophysical Res.*, Vol. 104, No. C1, pp. 1505-1524.

187. Troch, P. and J. De Rouck (1998) "Development of two-dimensional numerical wave flume for wave interaction with rubble mound breakwaters," *Proc. 25th Int. Conf. Coastal Eng.*, ASCE, Copenhagen, Denmark, pp. 1638-1649.

188. Trowbridge, J. H. and O. S. Madsen (1984) "Turbulent boundary layers: 2. Second-order theory and mass transport," *J. Geophysical Res.*, Vol 89, No. C12, pp. 7999-8007.

189. Tuah, H. and R. T. Hudspeth (1982) "Comparisons of numerical random sea simulations," *J. Waterw., Port, Coast. Ocean Div.*, ASCE, Vol. 108, pp. 569-584.

190. Tucker, M. J., P. G. Challenor, and D. J. T. Capter (1984) "Numerical simulation of a random sea: a common error and its effect upon wave group statistics," *Appl. Ocean Res.*, Vol. 6, pp. 118-122.

191. Tung, C.-C. (1975) "Statistical properties of the kinematics and dynamics of a random gravity-wave field," *J. Fluid Mech.*, Vol. 70, No. 2, pp. 193-217.

192. Tung, C.-C. and Huang, N. E. (1984) "Statistical properties of the kinematics and dynamics of nonlinear waves," *J. Phys. Oceanography*, Vol. 14, No. 3, pp. 594-600.

193. Tunstall, E. B. and D. L. Inman (1975) "Vortex generation by oscillatory flow over rippled surfaces," *J. Geophysical Res.*, Vol. 80, pp. 3475-3484.

194. Vittori, G. and P. Blondeaux (1992) "Sand ripples under sea waves. Part 3. Brick-pattern ripple formation," *J. Fluid Mech.*, Vol. 239, pp. 23-45.

References

195. Van der Werf, J. J. (2003) "Sand ripples in irregular and changing wave conditions: A review of laboratory and field studies," SANDPIT Report, available at http://sandpit.wldelft.nl/reportpage/right/SandpitLiteratureReviewVanDerWerf.pdf, University of Twente, the Netherlands.

196. Van der Werf, J. J., and J. S. Doucette, T. O'Donoghue, J. S. Ribberink (2007) "Detailed measurements of velocities and suspended sand," *J. Geophysical Res.*, Vol. 122, F02012.

197. Van der Werf, J. J., J. S. Ribberink, T. O'Donoghue , and J. S. Doucette, (2006) "Modelling and measurement of sand transport processes over full-scale ripples in oscillatory flow," *Coastal Eng.*, Vol. 53, pp. 657-673.

198. Van Leeuwen, P. J. and G. Klopman (1996) "A new method for the grneration of second-order random waves," *Ocean Eng.*, Vol. 23, No. 2, pp. 167-192.

199. Van Rijn, L. C. (1993) *Principles of Sediment Transport in Rivers, Estuaries and Coastal Seas*, Aqua, Amsterdam.

200. Weber, B. L. and D. E. Barrick (1977) "On the nonlinear theory for gravity waves on the ocean surface. Part 1: Derivations," *J. Phys. Oceanography*, Vol. 7, pp. 1-11.

201. Wiberg, P. L. and C. K. Harris (1994) "Ripple geometry in wave-dominated environments," *J. Geophysical Res.*, Vol. 99, No. C1, pp. 775-789.

202. Williams, J. J., P. S. Bell, P. D. Thorn, N. Metje, and E. Coates (2004) "Measurement and prediction of wave-generated suborbital ripples," *J. Geophysical Res.*, Vol. 109, C02004.

203. Witting, J. M. (1984) "A unified model for the evolution of nonlinear water waves," *J. Comp. Phys.*, Vol. 56, pp. 203-236.

204. Yoshida, A., K. Murakami, M. Yamashiro, and H. Kojima (1996) "Second-order interaction between random wave and submerged obstacle," *Proc. 25th Int. Conf. Coastal Eng.*, ASCE, Orlando, Florida, pp. 927-940.

205. Yasuda, T., T. Yamashita, S. Goto, and Y. Tsuchiya (1982) "Numerical calculations for wave shoaling on a sloping bottom by KdV equation," *Coastal Eng. in Japan*, Vol. 25, pp. 1-23.

206. Young, I. R. (1989) "Wave transformation over coral reefs," *J. Geophysical Res.*, Vol. 94, pp. 9779-9789.

207. Yuen, H. C. and B. M. Lake (1982) "Nonlinear dynamics of deep-water gravity waves," *Advan. Appl. Mech.*, Vol. 22, pp. 67-229.

208. Zedler, E. A. and R. L. Street (2006), "Sediment transport over ripples in oscillatory flow," *J. Hydraulic Eng.*, Vol. 132, No. 2, pp. 180-193.

209. Zhang, H., O. S. Madsen, S. A. Sannasiraj, and E. S. Chan (2004) "Hydrodynamic model with wave-current interaction in coastal regions," *Estuarine, Coastal and Shelf Science*, Vol. 61, pp. 317-324.

210. Zhang, J. and L. Chen (1999) "General third-order solutions for irregular waves in deep water," *J. Eng. Mech.*, Vol. 125, No. 7, pp. 768-779.

References

Index

Index

G

H

N

O

Index

P

R

S

T

Index

U

V

W

Z

自述

個人基本資料:

姓　　名：　沈茂霖 (Mao-Lin Shen)

姓　　別：　男

出生日期：　1977/01/10

學經歷：

畢／肆業學校	系所	學位	起迄
國立成功大學	水系及海洋工程所	博士	2002/9~2008/7
國立成功大學	水系及海洋工程所	碩士	2001/9~2002/6 2001/9 直升博士
國立成功大學	中等學校教育學程	資訊科教師	1999/9~2006/6
國立成功大學	水系及海洋工程學系	學士	1997/9~2001/6
國立成功大學	電機工程學系	21 退學	1995/9~1997/2
國立臺灣師範大學附屬高級中學		高中	1992/9~1995/6

期刊論文

1. 沈茂霖、黃清哲（2007）「不規則波通過潛堤之變形」，*海洋工程學刊*，第 7 卷，第 2 期，第 33-53 頁。

2. Huang, C.-J., Shen, M.-L, and Chang, H. H. (2008) "Propagation of a solitary wave over rigid porous beds," *Ocean Eng.*, (accepted).

研討會討論文

1. 黃清哲、許世盛、<u>沈茂霖</u>、葉智惠、沈建成、吳漢傑、高家俊，2000，*中華民國第二十二屆海洋工程研討會*，中山大學，高雄市，第 487-494 頁。

2. <u>Shen, M.-L.</u>, Chang, H.-H., and Huang, C.-J. (2003) "Numerical study on the propagation of solitary waves over a porous bed," *Proc. 25th Ocean Eng. Conf in Taiwan.*, R.O.C., National Taiwan Ocean University, Keelung, pp. 405-412。

3. <u>Shen, M.-L.</u> and Huang, C.-J. (2004) "Numerical simulation of random waves and the associated spectra of shear stresses," *Proc. 26th Ocean Eng. Conf. in Taiwan*, R.O.C., National Taiwan University, Taipei, pp. 405-412.

4. <u>Shen, M.-L.</u>, Huang C.-J. (2005) "Nonlinear random waves and the associated spectra of shear stresses," *PACON 2005*, Chienkuo Technology University, Changhua, Taiwan (R.O.C.).

5. <u>沈茂霖</u>，黃清哲，2005，不規則波通過潛堤之變形，*中華民國第二十七屆海洋工程研討會*，中興大學，台中市，pp. 393-400。

6. Lee, C.-H., <u>Shen, M.-L.</u>, Huang C.-J. (2007) "Transformation of irregular waves propagating over a submerged breakwater," *ISOPE 2007*, Lisbon, Portugal.